The Pennsylvania State University

The Graduate School

Department of Electrical Engineering

MULTIWAVELENGTH MULTISTATIC OPTICAL SCATTERING FOR AEROSOL CHARACTERIZATION

A Dissertation in

Electrical Engineering

by

Andrea M. Brown

© 2010 Andrea M Brown

Submitted in Partial Fulfillment
of the Requirements
for the Degree of

Doctor of Philosophy

August 2010

The dissertation of Andrea M. Brown was reviewed and approved* by the following:

C. Russell Philbrick
Professor of Electrical Engineering
Dissertation Advisor
Chair of Committee

Julio Urbina
Assistant Professor of Electrical Engineering

Zhiwen Liu
Associate Professor of Electrical Engineering

Anne M. Thompson
Professor of Meteorology

W. Kenneth Jenkins
Professor of Electrical Engineering
Head of the Department of Electrical Engineering

*Signatures are on file in the Graduate School

ABSTRACT

The main focus of this research is the development of a technique to remotely characterize aerosol properties, such as particle size distribution, concentration, and refractive index as a function of wavelength, through the analysis of optical scattering measurements. The proposed technique is an extension of the multistatic polarization ratio technique that has been developed by prior students at the Penn State Lidar Lab to include multiple wavelengths. This approach uses the ratio of polarized components of the scattering phase functions at multiple wavelengths across the visible region of the electromagnetic spectrum to extract the microphysical and optical properties of aerosols. The scattering intensities at each wavelength are vertically separated across the face of the imager using a transmission diffraction grating, so that scattering intensities for multiple wavelengths at many angles are available for analysis in a single image. The ratio of the scattering phase function intensities collected using parallel and perpendicular polarized light are formed for each wavelength and analysis of the ratio is used to determine the microphysical properties of the aerosols.

One contribution of the present work is the development of an inversion technique based on a genetic algorithm that retrieves lognormal size distributions from scattering measurements by minimizing the squared error between measured polarization ratios and polarization ratios calculated using the Mie solution to Maxwell's equations. The opportunities and limitations of using the polarization ratio are explored, and a genetic algorithm is developed to retrieve single mode and trimodal lognormal size distributions from multiwavelength, angular scattering data. The algorithm is designed to evaluate particles in the diameter size range of 2 nm to 60 μm, and uses 1,000 linear spaced diameters within this range to compute the modeled polarization ratio. The algorithm returns geometric mean radii and geometric standard deviations within 2% of the correct value when inverting a single lognormal probability size distribution from simulated

polarization ratios that include random Gaussian noise added to limit the signal-to-noise ratio to 25. The genetic algorithm performed reasonably well when retrieving results using a single complex refractive index for all three wavelengths while finding the lognormal particle size parameters. Three inversion runs of the algorithm on simulated noisy data showed that the algorithm could retrieved a trimodal size distribution and a single complex refractive index that produced a very good fit between the simulated noisy polarization ratios and the forward-calculated polarization ratios.

A significant contribution of the present work is a set of tests conducted at the Environmental Protection Agency's (EPA) Aerosol Test Facility (ATF), which is a controlled environment, where direct measurements of the size distribution and concentration of the scattering volume are available. The aerosol size distribution results obtained from inversion of the measured scattering phase functions, a lognormal size distribution with a geometric mean diameter of ~450 nm and a geometric standard deviation of ~1.3, compare favorably with measurements from an aerodynamic particle sizer and a condensation particle counter. This is one of the first large scale experiments where a comparison between multistatic inversion results and known properties of the interrogated volume of aerosols are made under controlled conditions.

The eventual goal is to develop a prototype sensor and an analysis approach to provide an important and useful tool to better define the atmospheric aerosol properties.

TABLE OF CONTENTS

LIST OF FIGURES vii

LIST OF TABLES xvi

ACKNOWLEDGEMENTS xviii

Chapter 1 Introduction 1

1.1 Significance of Research 3
1.2 Previous Work 5
1.2.1 Multistatic lidar systems 5
1.2.2 Inverting atmospheric aerosol size distributions 12
1.3 Hypotheses 16

Chapter 2 Scattering Theory 18

2.1 Optical Scattering and Atmospheric Aerosols 23
2.1.1 Molecular scattering 23
2.1.2 Particle size distributions 25
2.2 Polarization Ratio 28
2.2.1 Understanding the polarization ratio 31

Chapter 3 Inversion 41

3.1 Genetic Algorithm Terminology 43
3.2 Simple GA Inversion using Polarization Ratio 45
3.2.1 Binary coding 45
3.2.2 Fitness 46
3.2.3 Selection, crossover, and mutation 47
3.2.4 The polarization ratio model 48
3.2.5 Single lognormal with fixed refractive index 56
3.2.6 Single lognormal size distribution with varying refractive index 61
3.2.7 Tri-modal lognormal particle distribution 65

Chapter 4 Multiwavelength-Multistatic Scattering Hardware 70

4.1 Multiwavelength Transmitter 70
4.2 Multistatic Receivers 72
4.3 Images as Data 74
4.4 PSU Chamber Study 76

Chapter 5 EPA Aerosol Wind Tunnel 85

5.1.1 Experimental setup 87
5.1.2 Angle assignment 89
5.1.3 Supporting aerosol measurement instruments 91
5.2 MDG Fog 92
5.2.1 Polarization ratios 95
5.2.2 Inversion parameters and results 99
5.3 Vibrating Orifice Aerosol Generator 111
5.3.1 Producing monodisperse particles 111
5.3.2 Image processing techniques 113
5.3.3 Polarization ratios 116
5.4 Conclusions 121

Chapter 6 Atmospheric Aerosol Measurements 123

6.1 Data Processing 127
6.2 Data Inversion 135
6.3 Conclusions 149

Chapter 7 Future Developments 152

7.1 Supercontinuum scattering 155
7.2 Elimination of assumed particle size distributions 157
7.3 Extension to non-spherical particles 159

Chapter 8 Summary and Conclusions 163

References 170

LIST OF FIGURES

Figure 1-1: Schematic diagram showing the various radiative mechanisms associated with cloud effects that have been identified as significant in relation to aerosols (modified from Haywood and Boucher, 2000) 4

Figure 1-2: Radiative forcing for the climate for the year 2005 relative to 1750 (top of atmosphere; global annual mean); adapted from (Forester et al (IPCC), 2007, Fig. 2-20). 5

Figure 1-3: Bistatic setup used by Stevens (1996) 7

Figure 1-4: (a) Comparison of measured polarization ratio (solid line) to modeled polarization ratio (line with circles) for radiation fog (b) tri-lognormal size distributions used to produce the theoretical polarization ratio shown in (a) (Stevens, 1996, Fig. 5-18) 8

Figure 1-5: Multistatic system used to measure vertical aerosol profiles (Novitsky and Philbrick, 2005) 9

Figure 1-6: Polarization ratios as a function of altitude and scattering angle (Novitsky, 2002, Fig.6-3b). 10

Figure 1-7: Scattering measurements from fog-oil (solid line) under conditions of moderate multiple scattering compared to a single-scatter Mie-calculated polarization ratio (dashed line) (concentration of 60,000 #/cm3 with median diameter of 117 nm) (Park, 2008, Fig. 6.11). 11

Figure 1-8: Effect of multiple scattering on polarization ratio as a function of extinction cross-section (Park, 2008, Fig. 6-17). 11

Figure 2-1: Scattering of polarized light as a function of angle and particle radius. (Born and Wolf, 1980). 21

Figure 2-2: Equivalent dielectric sphere radius as a function of incident wavelength and real refractive index. 24

Figure 2-3: Polarization ratio for 407 nm wavelength as a function of varying equivalent sphere radius and real refractive index. 25

Figure 2-4: Lognormal size distributions for a diameter of 1 μm, a concentration of 1,000 particles/cm^3, and four different values of the geometric standard deviation: 1.01 (black line), 1.5 (blue line), 2.0 (red line), and 3.0 (green line). The left plot shows a linear scale for the particle diameter, while the right plot is a logarithmic scale. 26

Figure 2-5: Trimodal aerosol size distributions from Table 2-2. 28

Figure 2-6: Trimodal particle size distribution used in polarization ratio sensitivity analysis in Fig. 2-7 31

Figure 2-7: Evolution of polarization ratios as each of the nine parameters in the trimodal lognormal size distribution is varied. (Novitsky, 2002, Fig. 3-17). 32

Figure 2-8: Lognormal size distributions used to explore the sensitivity of the model polarization ratio to particle number density. The parameters for each curve are summarized in Table 2-3. 34

Figure 2-9: Polarization ratio for 407 nm as a function of total particle concentration, N_T (#/cm^3), for a lognormal particle size distribution #1, with r_g = 0.01 μm and σ_g = 1.1. .. 36

Figure 2-10: Polarization ratio for 407 nm as a function of total particle concentration, N_T (#/cm^3), for a lognormal particle size distribution #2, with r_g = 0.1 μm and σ_g = 1.1 36

Figure 2-11: Polarization ratio for 407 nm as a function of total particle concentration, N_T (#/cm^3), for a lognormal particle size distribution #3, with r_g = 1.0 μm and σ_g = 1.1 37

Figure 2-12: Polarization ratio for 407 nm as a function of total particle concentration, N_T (#/cm^3), for a lognormal particle size distribution #4, with r_g = 10 μm and σ_g = 1.1 37

Figure 2-13: Trimodal lognormal distribution used to calculate polarization ratios in Fig. 2-14 and Fig. 2-15 38

Figure 2-14: Polarization ratio at 532 nm as a function of real refractive index using the trimodal lognormal size distribution shown in Fig. 2-13 (Novitsky, 2002, Fig. 3-18). 39

Figure 2-15: Polarization ratio change for change in imaginary part of refractive index. Ratios are calculated using trimodal size distribution shown in Fig. 2-13, a wavelength of 532nm, and n_{re}=1.47. 40

Figure 3-1: Example of a flow chart for simple genetic algorithm 44

Figure 3-2: Size distributions used to determine the number of particle sizes to include in the model polarization ratio calculations, see Table 3-1 50

Figure 3-3: Polarization ratios calculated for the first case of a single lognormal size distribution from Table 3-1 as a function of the number of logarithmically-spaced particle radii between 1nm and 30 μm used in the calculations 51

Figure 3-4: Polarization ratios calculated for the first case of a single lognormal size distribution from Table 3-1 as a function of the number of linearly-spaced particle radii between 1nm and 30 μm used in the calculations 52

Figure 3-5: Polarization ratios calculated for the second case of the trimodal lognormal size distribution from Table 3-1 as a function of the number of logarithmically-spaced particle radii between 1nm and 30 μm used in the calculations.. 54

Figure 3-6: Polarization ratios calculated for the second case of the trimodal lognormal size distribution from Table 3-1 as a function of the number of linearly-spaced particle radii between 1nm and 30 μm used in the calculations 55

Figure 3-7: Polarization ratios calculated for trimodal lognormal size distribution from Table 3-1 as a function of scattering angle resolution using 1000 linearly-spaced particle radii. 56

Figure 3-8: (a) Calculated polarization ratio data using a lognormal size distribution (r_g = 0.75 μm, σ_g = 1.5) and a concentration of 1,000 particles/cm^3 (b) polarization ratio with additive white Gaussian noise to create a signal-to-noise ratio of 25 57

Figure 3-9: Calculated polarization ratio for lognormal size distribution (r_g = 0.75 μm, σ_g = 1.5) shown in Fig. 3-8a as a function of particle concentration, N_T. 59

Figure 3-10: (a) Calculated polarization ratios for single lognormal distribution (r_g = 0.75 μm, σ_g = 1.5, N_T = 1000 #/cm^3) and refractive index of 1.465 + i0.01 at 407 nm, 1.460 + i0.01 at 532 nm, and 1.455 + i0.01 at 650 nm (b) same polarization ratios with additive white Gaussian noise used to produce a signal-to-noise ratio of 25. 62

Figure 3-11: Comparison of noisy simulated polarization ratios and modeled polarization ratios using lognormal size distribution with r_g = 0.77 μm, σ_g = 1.48, N_T = 1,780 #/cm^3 (first row of Table 3-4). 63

Figure 3-12: (a) The trimodal size distribution (b) calculated polarization ratios and (c) calculated polarization ratios with additive white Gaussian noise to produce a signal-to-noise ratio of 35. 67

Figure 3-13: Trimodal size distributions inverted from simulated polarization ratios (dashed lines) compared to model trimodal size distribution (black solid line). The parameters for the inverted size distributions are summarized in Table 3-7 68

Figure 3-14: Comparison between 'noisy' simulated polarization ratios (solid lines) and polarization ratios calculated using the trimodal lognormal size distribution retrieved by genetic algorithm in Table 3-7 (dashed lines). 69

Figure 4-1: Picture of the revised transmitter with the waveplate fixed in the transmit path 71

Figure 4-2: Fractional retardance of the half-wave plate response as a function of wavelength. 72

Figure 4-3: Spectral relative response of CCD camera 73

Figure 4-4: CCD camera with lens and diffraction grating mounted 73

Figure 4-5: Spectral response for transmission gratings. 74

Figure 4-6: PSU aerosol chamber setup 77

Figure 4-7: An image of the angular scattering through the 600 lines/mm diffraction grating. 78

Figure 4-8: Data extraction method 78

Figure 4-9: Beam profile of diffracted 532 nm laser at (a) left side of image (column 100) and at (b) right side of image (column 600) 79

Figure 4-10 Scattering intensities collected from PAO fog in the PSU aerosol chamber. Solid lines are parallel scattering intensities and dash lines are perpendicular scattering intensities for 407 nm (blue), 532 nm (green), and 650 nm (red) 80

Figure 4-11: Polarization ratios for PAO fog at 407 nm (blue), 532 nm (green), and 650 nm (red) 80

Figure 4-12: Comparison between measured (solid lines) and modeled (dashed lines) polarization ratios using a lognormal probability density function with d_g = 300 nm σ_g = 1.66 82

Figure 4-13: Comparison between measured (solid lines) and modeled (dashed lines) polarization ratios using a lognormal probability density function with d_g = 300 nm σ_g = 1.66 82

Figure 4-14: Concentration of PAO fog as measured by a condensation particle counter on 8 March. The blue box indicates the time of measurements. 83

Figure 5-1: EPA Aerosol Test Facility Wind Tunnel 86

Figure 5-2: Photograph of the HETS portion of the ATF Wind Tunnel 87

Figure 5-3: (a) Turning mirror and laser path (b) power meter head at end of path. 88

Figure 5-4: Camera setup and aerosol sensor feed tubes 88

Figure 5-5: EPA camera setup.....90

Figure 5-6: Alignment images for camera 1 (300 lines/mm) and camera 2 (600 lines/mm) 90

Figure 5-7: Extraction polynomials for Camera 1 and Camera 2... 90

Figure 5-8: Particle concentration as measured by the CPC and APS. Dotted lines indicated ±20% accuracy for the particle counting instruments. Boxes indicate times that data was taken on 24 November for four different datasets, labeled #1 - #4.....93

Figure 5-9: Raw counts from APS, including counts of coincidence (more than one particle in the measurement chamber. These counts are not included in reported concentration measurements) 94

Figure 5-10: APS particle size distribution for the 4 datasets after removing the lowest 'catch-all' size bin. ... .95

Figure 5-11: Relative scattering intensities for parallel incident light (solid lines) and perpendicular polarized light (dashed lines) at 407 nm (blue lines), 532 nm (green lines), and 650 nm (red lines) 96

Figure 5-12: Polarization ratio for dataset #3 with 5-point moving-average smooth applied.....97

Figure 5-13: Scattering image during the EPA fog experiment..... 97

Figure 5-14: Polarization ratio for datasets #1 and #2 98

Figure 5-15: Polarization ratio for datasets #3 and #4.... 99

Figure 5-16: Solution space for dataset #3 using a fixed refractive index of 1.47 + i0.001 ..100

Figure 5-17: Normalized lognormal size distributions inverted from the polarization ratios (solid lines) and the corresponding normalized size distribution measured by the APS (lines with markers). 103

Figure 5-18: Comparison between measured polarization ratio and model polarization ratio using particle size distribution retrieved by the two-variable genetic algorithm for dataset #1through #4.....105

Figure 5-19: Real refractive index for mineral oil as a function of wavelength (Verkouteren, 2010). 106

Figure 5-20: Fitness (1/squared error) for modeled and measured polarization ratio for dataset #2 using lognormal size distribution retrieved by genetic algorithm (Table 5-4) as a function of complex refractive index.... 107

Figure 5-21: Comparison of measured polarization ratios (x) to modeled polarization ratios using a fixed refractive index of 1.47 + i0.001 for all wavelengths (dashed lines) and modeled polarization ratios using refractive index retrieved from grid search (solid lines) for dataset #3 109

Figure 5-22: Example of possible polarization ratios without errors introduced by background reflections..... 109

Figure 5-23: Effect of variation in polarization retardance as a function of wavelength using retrieved parameters for dataset #3 in Table 5-5 110

Figure 5-24: Concentration of 5 μm oleic acid droplets as measured by the APS. Squares and triangles indicate data images acquired by the two cameras and the blue box indicates the dataset analyzed for this work..... 112

Figure 5-25: Normalized particle size distribution measured by the APS during the collection of the analyzed datasets. 113

Figure 5-26: Scattering images for oleic acid droplets (a) camera 1 and (b) camera 2..... 114

Figure 5-27: (a) 'raw' scattering image (b) dark-count subtraction (c) removed scattering from image (d) interpolated background image..... 115

Figure 5-28: Interpolated background image showing blurring of specular reflections..... 116

Figure 5-29: Number density size distribution measured by APS for analyzed dataset and 'best-fit' lognormal size distribution 117

Figure 5-30: Measured polarization ratios for dataset #1 compared with theoretical polarization ratio for lognormal size distribution (d_g = 5.4 μm, σ_g = 1.05) and concentration of 0.03 particles per cm^3..... 118

Figure 5-31: Picture of operating vibrating orifice from VOAG datasheet (TSI Model 3450 VOAG datasheet). 'Haze' around particle stream could be sub-micron particles.. 119

Figure 5-32: Polarization ratio for bimodal lognormal size distribution ($d_{g,1}$=0.18 μm, $\sigma_{g,1}$=1.3, N_{T1}=1 x 10^4 #/cm^3 and $d_{g,2}$ =5.4 μm, $\sigma_{g,2}$ 1.05, N_{T2}=0.03 #/cm^3)..... 120

Figure 6-1: Scattering image collected using 600 lines/mm diffraction grating showing condensation on the inside of the grating (streaks inside white oval). 124

Figure 6-2: Polarization ratio of scattering data altered by condensation collecting on the inside of the diffraction grating..... 124

Figure 6-3: Temperature, dew point, and relative humidity for night of 20/21 November. Blue lines show times of data collection for datasets analyzed for this work 126

Figure 6-4: CPC concentration for night of 20/21 November with ±20% (dotted lines). Blue boxes indicate times of data collection for analyzed datasets for this work. 126

Figure 6-5: Unfiltered measured scattering intensities for fog at 12:50 AM, 20/21 November. The scattering intensities for the 407 nm and 532 nm have been given constant biases to separate the curves from each other.... 127

Figure 6-6: Unfiltered polarization ratios for fog at 12:50 AM, 20/21 November. 128

Figure 6-7: Scattering intensities and polarization ratios for data collected 20/21 November at 12:50 AM when using an integration cut-off of 50% of the maximum pixel value... 129

Figure 6-8: Scattering intensities and polarization ratios for data collected 20/21 November at 12:50 AM when using an integration cut-off of 75% of the maximum pixel value.... 130

Figure 6-9: Scattering intensities and polarization ratios for data collected 20/21 November at 12:50 AM when using an integration cut-off of 90% of the maximum pixel value 131

Figure 6-10: Location of diffracted beams on the CCD array. 132

Figure 6-11: Depiction of integration of rows to produce scattering intensity as a function of column 132

Figure 6-12: Interline CCD architecture (Spring, Fellers, and Davidson, 2000, Figs. 7 and 8)..... 134

Figure 6-13: Polarization ratio for 650 nm as a function of the number of rows added to calculate the scattering intensity for each scattering angle. The percentage values are the thresholds used in the data processing algorithm to select the number of rows for each wavelength and scattering angle..... 135

Figure 6-14: Unfiltered scattering intensities for fog at 12:50 AM, 20/21 November..... 136

Figure 6-15: Unfiltered scattering intensities for fog at 1:45 AM, 20/21 November 136

Figure 6-16: Time sequence of polarization ratios collected at two times the evening of 20/21 November..... 137

Figure 6-17: (a) Inverted size distribution and (b) modeled (dashed lines) polarization ratios from genetic algorithm using fixed refractive index of 1.35 + i0.001 compared to measured polarization ratios (solid lines) for dataset collected at 12:50 AM, 20/21 November.. 139

Figure 6-18: (a) Adjusted size distribution to produce the (b) best average fit between modeled (dashed lines) and measured (solid lines) polarization ratios for all wavelengths and angles using variable refractive index as a function of wavelength for dataset collected at 12:50 AM, 20/21November. ... 141

Figure 6-19: Comparison between the measured (solid lines) and modeled (dashed lines) polarization ratios for varying refractive indices for dataset collected at 12:50 AM, 20/21 November 143

Figure 6-20: Comparison between the measured (solid lines) and modeled (dashed lines) polarization ratios for varying fine mode concentration, $N_{T,1}$, for dataset collected at 12:50 AM, 20/21 November 144

Figure 6-21: (a) Adjusted size distribution to produce the (b) best average fit between modeled (dashed lines) and measured (solid lines) polarization ratios for all wavelengths and angles using variable refractive index as a function of wavelength for dataset collected at 1:45 AM, 20/21 November 145

Figure 6-22: Comparison of retrieved size distributions for two datasets summarized in Table 6-3 collected the night of 20/21 November 146

Figure 6-23: Comparison of (a) retrieved normalized size distributions from Raleigh, North Carolina multistatic measurements to (b) published normalized size distributions for radiation fog in Albany, New York obtained using an optical particle counter (Meyer *et al*, 1979). 148

Figure 6-24: Comparison between modeled and measured polarization ratios for fog data collected 21/21 November at 12:55 AM, when the inversion algorithm was only required to interpret data for angularly resolved data on two of three wavelengths 150

Figure 7-1: Quantum Efficiency of silicon CCD array. (Spring, 2010) 153

Figure 7-2: High-power supercontinuum from NTK Photonics (Edwards, 2009) 156

Figure 7-3: Scattering image for (a) 3-λ source and (b) 4W supercontinuum source taken using the same camera 157

Figure 7-4: Genetic algorithm inversion of size distribution with no pre-defined distribution function 158

Figure 7-5: Examples of spheroids with varying axial ratios (a/b) (Mishchenko, 2002, Fig. 1) 160

Figure 7-6: Polarization ratios at 1064 nm (black), 650 nm (red), 532 nm (green), and 407 nm (blue), as a function of shape distribution. Gaussian shape distributions were used with the mean and variance shown in the title of each distribution. A fixed Gaussian size distribution was used with a mean radius of 0.5 μm and a variance of 0.05 161

Figure 7-7: Polarization ratios at 1064 nm (black), 650 nm (red), 532 nm (green), and 407 nm (blue), as a function of shape distribution. Gaussian shape distributions were used with the mean and variance shown in the title of each distribution. A fixed Gaussian size distribution was used with a mean radius of 0.5 μm and a variance of 0.05. 162

LIST OF TABLES

Table 2-1: Coefficients for empirical Rayleigh scattering cross section (Bucholtz, 1995). 23

Table 2-2: Values for atmospheric tri-modal lognormal distributions (Jaenicke, 1993) 28

Table 2-3: Lognormal distributions used to investigate the effect of particle number density on the polarization ratio for a scattering wavelength of 407 nm. 34

Table 3-1: Summary of aerosol size distributions selected for algorithm tests. 49

Table 3-2 : Retrieved size distribution for five different runs using the simulated noisy polarization ratio shown in Fig. 3-8b. 58

Table 3-3: Two-variable genetic algorithm results for minimum squared-error of lognormal size distribution with r_g of 0.75 μm and σ_g of 1.5 at a concentration of 1,000 particles/cm^3 60

Table 3-4 : Summary of results for single lognormal distribution with one varying refractive index used for all three wavelengths.....63

Table 3-5: Summary of results for single lognormal distribution with varying refractive index as a function of wavelength.....64

Table 3-6: Ranges used in trimodal lognormal size distribution inversion algorithm …….65

Table 3-7: Summary of retrieved trimodal lognormal size distributions. 67

Table 5-1: Collection information for datasets #1 - #4. 98

Table 5-2 Summary of two-variable inversion of datasets #1-#4 for EPA fog.....100

Table 5-3: Power measurements to calculate extinction for MDG fog……..…..…..102

Table 5-4: Summary of parameters used to calculate normalized particle size distributions shown in Fig. 5-18 for datasets #1-#4 for MDG fog.....103

Table 5-5: Summary of complex refractive indices retrieved by the grid search for dataset #3.

. 108

Table 5-6: Results for five genetic algorithm inversions of dataset #1.....119

Table 6-1: Reconstructed from Shettle and Fenn (1979, Table 4 and Table 6) showing atmospheric aerosol refractive index used in their model as a function of wavelength and relative humidity. 138

Table 6-2: Inversion results from genetic algorithm for datasets collected the evening of 20/21 November.....139

Table 6-3: Ranges of trimodal lognormal inversion parameters for datasets collected the night of 20/21 November using a refractive index of 1.36 + i0.001 for 407 nm, and 1.35+ i0.001 for 532 nm and for 650 nm.. 145

Table 6-4: Extinction coefficients and visibility range for size distributions obtained for datasets collected the evening of 20/21 November. 147

ACKNOWLEDGEMENTS

My sincerest thanks and gratitude-

Dr Philbrick. Your love of science and the world around you is an inspiration to us all. Your words of wisdom, guidance, and encouragement can be seen on every page of this dissertation. Thank you for all of your efforts on my behalf over the years- I am truly grateful.

My committee, Dr. Urbina, Dr. Thompson, and Dr. Liu. Thank you for your guidance and contributions to this work, and your interests in support of my graduate studies.

My sister, Marinda. You are my role model, my support system, and my inspiration in all that I do.

My grandparents. Your love and encouragement kept me going and smiling long after I would have thrown in the towel on my own.

My husband. Your discussions, guidance, and encouragement were instrumental in all that I have done, and will continue to be in all that I do. Not every girl gets to marry a great guy and a great engineer too.

My labmate, Michelle. Without you, I would have spent some really lonely, cold nights in a horse pasture and still have no data. This thesis wouldn't be possible without your help, encouragement, and continuous support.

My labmate, Perry. Thanks for always being there to help. I can't imagine what grad school would have been like without a labmate like you.

Dr. Russell Weiner and the staff at the EPA Aerosol Test Center, for use of their wonderful aerosol wind tunnel, and Tim and Lydia for their help with the data collection.

Dr. Richard Clark for the extended use of his condensation particle counter.

Thank you all for your efforts, support, and guidance.

Chapter 1

Introduction

A considerable effort has been focused over the past decades on understanding the complex dynamics driving the physical and chemical processes of the Earth's atmosphere. The importance of these processes has been highlighted by the Montreal Protocol in 1978 and the creation of the Intergovernmental Panel on Climate Change (IPCC) in 1989. Establishment of both of these entities resulted in large steps forward in recognizing the sensitivity of the Earth's environment, and describing the issues to be addressed in protecting our planet from global climate changes. It is the goal of the IPCC organization that we not only understand these vast and complex processes, but also begin to mitigate the harmful changes that humans have introduced into the natural cycles of our atmosphere. Considerable progress in understanding the climate has been made over the past 20 years, particularly in respect to understanding the chemical processes involving greenhouse gases, such as carbon dioxide and methane. There is still more work to be done; one topic in particular is in the area of understanding physical and chemical processes governing aerosols, and their effects upon climate and the radiation budget. Determining aerosol effects on the global radiation budget is a difficult and daunting task due to the extreme variability in the distribution of aerosols, which depend on physical and chemical environment factors that govern their formation; such as geographic location, season, proximity to urban developments, time of day, *etc*. An article released by the National Ocean and Atmospheric Administration (NOAA) in 2000 states that, "…in order to assess the global impact of aerosols on climate, it is necessary to map their mean properties as functions of latitude, longitude, and altitude, as well as the variability of their properties with time." (Levy, 2000) The study of atmospheric aerosols has traditionally been dominated by direct measurement

techniques, usually performed by mounting point sensing instruments at locations on the surface, on aircraft or on balloons. These approaches are not well-suited for continuous measurements of the spatial and temporal distributions of aerosols over an extended period of time, and such measurements are needed to truly understand atmospheric aerosol distributions. A system is needed that can make continuous measurements over long periods of time, and over a range of heights, in many different types of conditions. Satellite instruments are beginning to provide a global picture of aerosol distributions; however these instruments are so far above the aerosols it is difficult to characterize them with any properties other than the horizontal distribution of backscatter and/or integrated extinction. In order to obtain a global description, vertical profiles from ground based instrument networks capable of better characterization of aerosol properties and their vertical distribution must be obtained and analyzed together with satellite data in order to describe the spatial and temporal variations of the aerosol properties. To collect a large database of information from around the world, the sensor system would also need to be relatively inexpensive, easy to use, and provide information in a standardized format. Multistatic optical scattering is a promising aerosol remote sensing technique that can satisfy many of these requirements. The Lidar Laboratory at Penn State University has been developing this technique for over 15 years, with three prior dissertations focusing on this topic (Stevens, 1996; Novitsky, 2002; Park, 2008). Each has concentrated on different aspects of this problem in order to bring this technique to a level where it can be utilized by the community at large.

The goal of the present work is to extend multistatic techniques to simultaneous multiwavelength measurements; thus increasing the information available for the inversion analysis process. The development of these new techniques has led to another area of focus for this work; namely, the creation of an advanced multi-variable inversion routine. The inversion routine showcased in this work uses measured data to provide information about the aerosol size, size distribution, concentration, and composition (in the form of refractive index information),

while requiring minimal *a priori* information and human interaction. The successful completion of these tasks will do much to further our ultimate goal of developing a standardized aerosol characterization instrument.

1.1 Significance of Research

Aerosols have considerable effects on the climate through direct and indirect radiative forcing, as shown by Fig. 1-1. Direct radiative forcing is caused by absorption and scattering of sunlight. The scattering of sunlight decreases the amount of energy that reaches the Earth's surface and has a cooling effect on the surface and the lower atmosphere. The absorption of sunlight at the ground heats the Earth's surface, and warms the atmosphere by convection and dynamic transport of the latent heat of water vapor. The Earth's system is further warmed by the trapping of radiant energy by greenhouse gases. The net radiative impact on climate can be either a net cooling or a net warming based on absorption and scattering processes caused by the aerosols. For example, increased cloud condensation nuclei lead to high densities of aerosols and cause cloud water droplets to form as higher densities of smaller particles. The higher densities can increase the relative fraction of sunlight reflected back into space by clouds (albedo effect) and increase the lifetime of clouds because the particle growth leading to precipitation is delayed, and results in a cooling of the atmosphere. This effect on cloud formation is indirect radiative forcing.

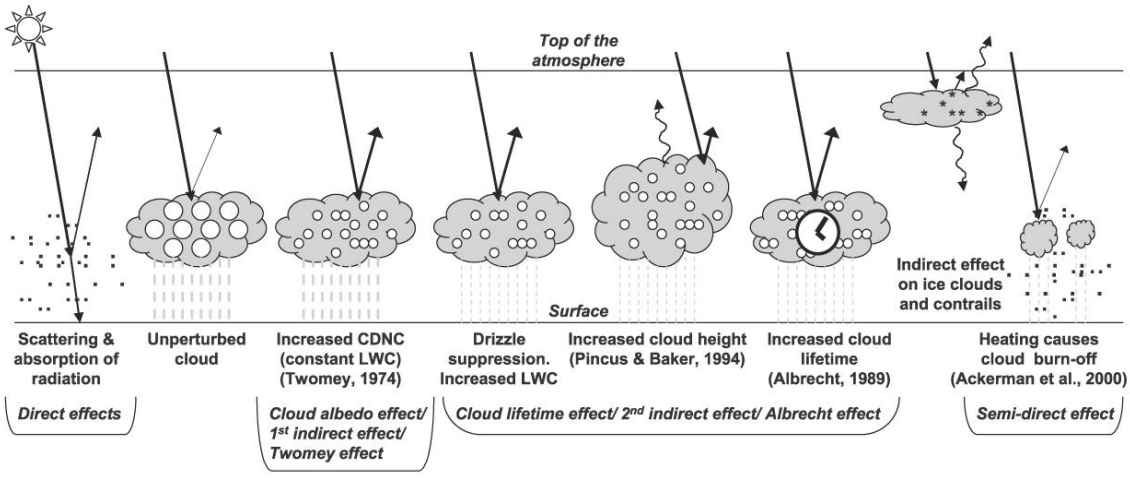


Figure 1-1: Schematic diagram showing the various radiative mechanisms associated with cloud effects that have been identified as significant in relation to aerosols (modified from Haywood and Boucher, 2000). The small black dots represent aerosol particles; the larger open circles cloud droplets. Straight lines represent the incident and reflected solar radiation, and wavy lines represent terrestrial radiation. The filled white circles indicate cloud droplet number concentration (CDNC). The unperturbed cloud contains larger cloud drops as only natural aerosols are available as cloud condensation nuclei, while the perturbed cloud contains a greater number of smaller cloud drops as both natural and anthropogenic aerosols are available as cloud condensation nuclei (CCN). The vertical grey dashes represent rainfall, and LWC refers to the liquid water content. (Forster et al (IPCC), 2007, Fig. 2-10).

It is known that aerosols have an impact on our climate, yet we are unable to confidently model this effect due to a lack of an in-depth understanding of the aerosols themselves (see Figure 1-2). "Atmospheric Aerosol Properties and Climate Impacts," (Chin et al, 2009) a report released by the Climate Change Science Program in January 2009, reports that a significant portion of the uncertainty in climate forecasting is a result of insufficient knowledge of atmospheric aerosols and cloud-aerosol interactions. The chemical composition and optical properties of aerosols vary with their sources and thus, affect the climate differently (e.g. the warming effect of anthropogenic aerosols versus the cooling effect of dust particles). The aerosol lifetime also varies depending on the source and size, from just a few hours to more than a week, and results in extreme spatial and temporal variability on a global scale. This extreme variability makes the description of 'typical' aerosols a difficult task, yet necessary for accurate climate

modeling and forecasting. The ability to accurately characterize and monitor aerosols over the lifetime of the particles will do much to improve our knowledge of aerosol formation and movement, and allow better predictions of the consequences of their presence.

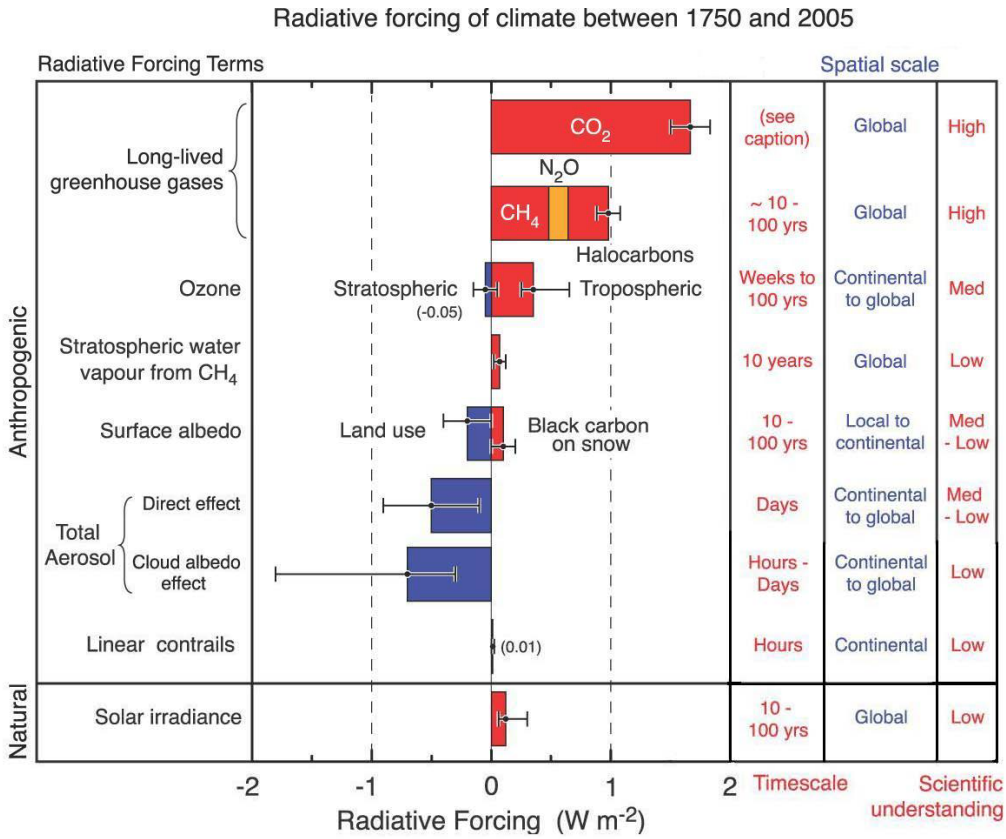


Figure 1-2: Radiative forcing for the climate for the year 2005 relative to 1750 (top of atmosphere; global annual mean); adapted from (Forester et al (IPCC), 2007, Fig. 2-20).

1.2 Previous Work

1.2.1 Multistatic lidar systems

The particle characterization from angular scattering data and the possible benefit of using it to characterize atmospheric aerosols has been recognized since the 60's (see Born and Wolf, 1964 and Reagan, 1982), but the bistatic and multistatic lidar development lagged behind that of monostatic lidar. The bistatic system used by Reagan *et al*. (1982a) required altitude-

azimuth mounts for both the transmitter and the detector to collect scattering angles from 100 degrees to 160 degrees with 0.5 degree accuracy using a pulsed ruby laser at a wavelength of 694.3 nanometers. Size distributions and refractive index of atmospheric aerosols were inverted from the scattering measurements combined with multiwavelength extinction measurements obtained using a solar radiometer (Reagan, 1982b). Two separate research groups in India, the Vikram Sarabhai Space Center (Parameswaran, 1984) and the Indian Institute of Tropical Meteorology (Devara, 1989), operated bistatic scanning lidars in the 80's and 90's. Parameswaran *et al*. used a CW argon laser with the wavelength of 514.5 nm to collect scattering measurements at angles between 90 degrees and 165 degrees, while Devara *et al*. performed measurements across the same angle range using a helium-neon laser at 632.8 nm. Aerosol size distributions and refractive indices were inverted from the data using iterative techniques coupled with many assumptions. In addition to the PSU Lidar Laboratory work that began in 1992, two groups have implemented a bistatic lidar design in recent years. Barnes *et al*. (2003) have operated a bistatic lidar system using a CCD camera as the detector at the Mauna Loa Observatory to obtain aerosol-to-molecular scattering ratios. The CLidar was able to accurately characterize aerosol layers near the ground occurring in the overlap region of traditional backscatter lidar systems. Olofson *et al*. (2008a, 2008b) used a bistatic lidar system to investigate the properties of Nordic clouds by determining the Stoke's parameters I, Q, and U, and calculating the degree of linear polarization. The measured linear polarization values failed to match the theoretical Mie-calculated values; this difference was attributed to the presence of nonspherical ice particles and multiple-scattering processes.

Prior students at Penn State University have contributed significantly to multistatic lidar development. A bistatic lidar system for aerosol characterization was successfully implemented by Stevens (1996a, 1996b) in the early 90's. The angular scattering intensities of two components of polarization (referenced with respect to the plane that contains the laser beam and

the imagers) were measured along a horizontal path of 140 meters through coastal aerosols using a single linear photo-diode array and a 532 nm Nd:YAG laser, as depicted in Fig. 1-3.

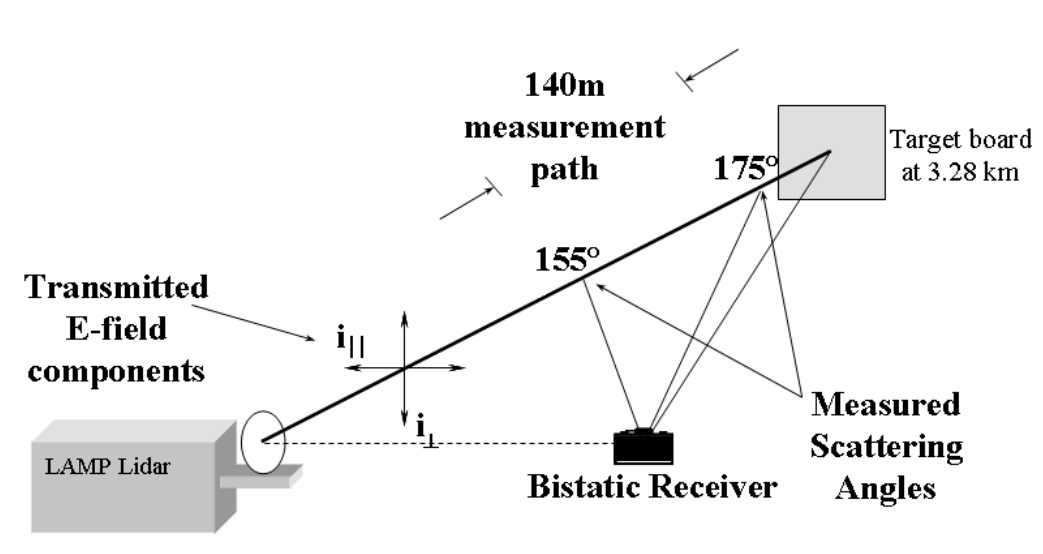


Figure 1-3: Bistatic setup used by Stevens (1996).

The use of the polarization ratio to minimize error and uncertainties across the field-of-view of the receiver was described by Stevens (1996a) along with many advantages of an imaging bistatic lidar including the simplicity of the photo-diode array detector, which does not require scanning in order to capture scattering intensities at multiple angles. While the aerosols along the path of the laser were examined using the imaging bistatic lidar data at scattering angles 155 through 175, the LAMP lidar determined the atmospheric extinction using the monostatic backscatter geometry and standard Raman lidar techniques (inelastic scattering off of N_2 and O_2 in the air.) Stevens was able to simultaneously determine aerosol size distributions using a bistatic measurement during several cases of radiation fog. The polarization ratio measured and analyzed using Mie scatter equations resulted in aerosol extinction measurements that closely matched (within 4%) the measured Raman lidar results (data inset in Fig. 1-4). The measured extinction from the Raman lidar agreed with that which was calculated from the aerosol properties (size, distribution,

number) determined from the bistatic lidar measurements of the scattering phase function and the polarization ratio.

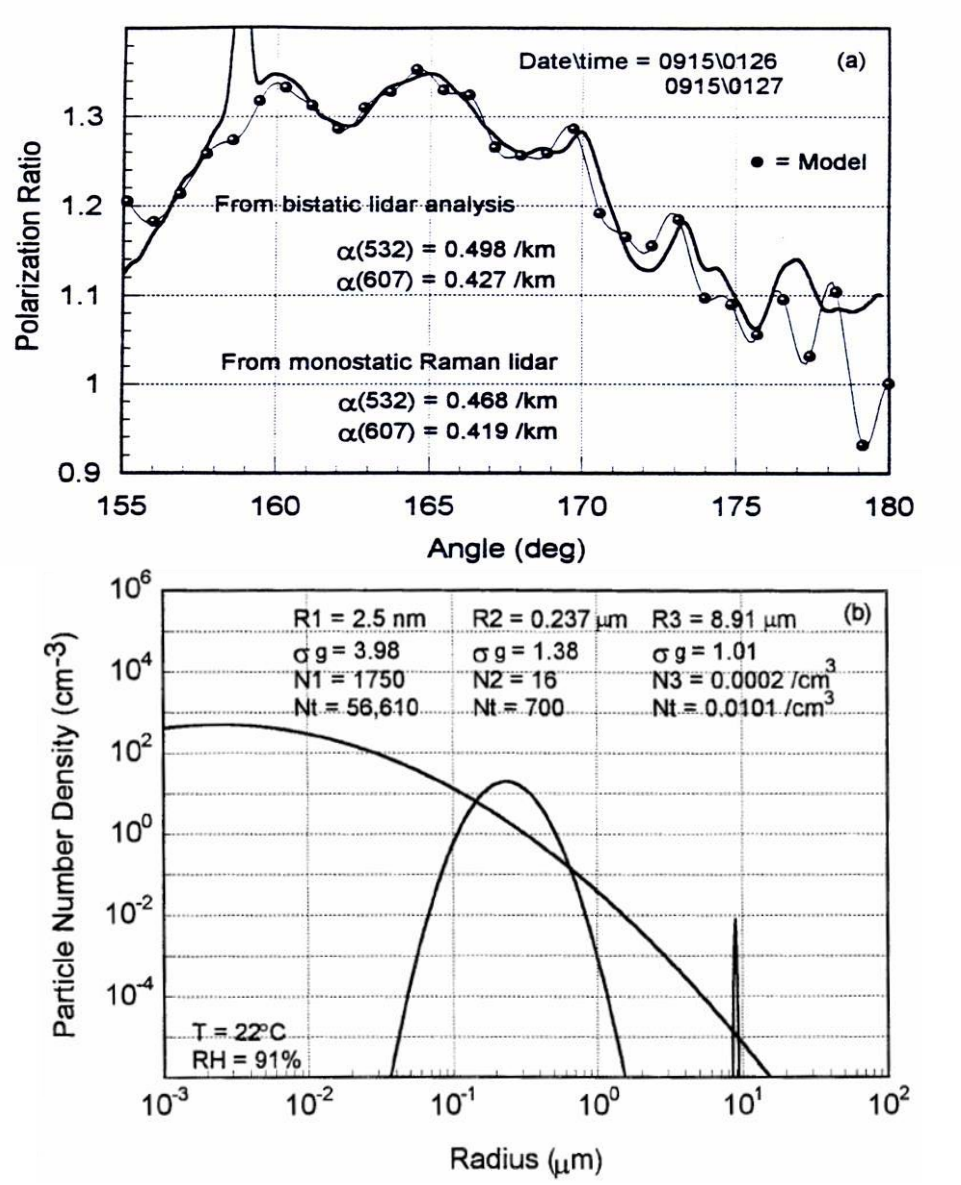


Figure 1-4: (a) Comparison of measured polarization ratio (solid line) to modeled polarization ratio (line with circles) for radiation fog (b) tri-lognormal size distributions used to produce the theoretical polarization ratio shown in (a) (Stevens, 1996, Fig. 5-18).

Novitsky (2002; 2005) extended Stevens' work to vertical profiles of atmospheric aerosols using a multistatic lidar system. Three CCD cameras placed at radial distances from the transmitter were used to image a vertically pointed 532 nm laser, as shown in Fig. 1-5. Much was

learned from this research effort about the retrieval of aerosol size distribution in the regions of strong gradients in altitude dependent layers. The analysis of layers was made possible by simultaneous measurement at several scattering angles for each scattering volume because of the simultaneous measurement at three different angles using the multistatic approach (see Fig.1-6). This variation of aerosols properties as a function of height adds significant complexity to the inversion process as compared to a uniformly mixed volume of aerosols; more information is required for an accurate retrieval of the vertical profile of aerosol size distributions in the presence of strong gradients in aerosol layers. However, this is exactly the data that is needed to study topics such as the growth and dissipation of clouds.

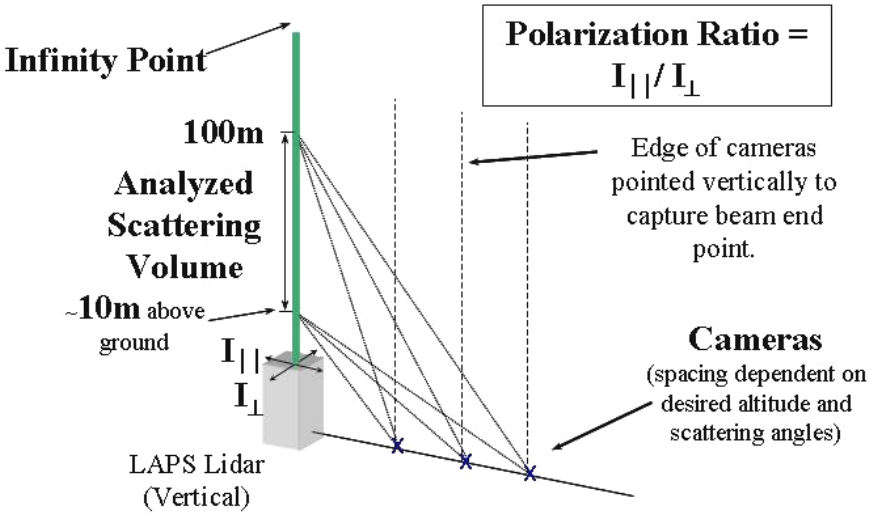


Figure 1-5: Multistatic system used to measure vertical aerosol profiles (Novitsky and Philbrick, 2005).

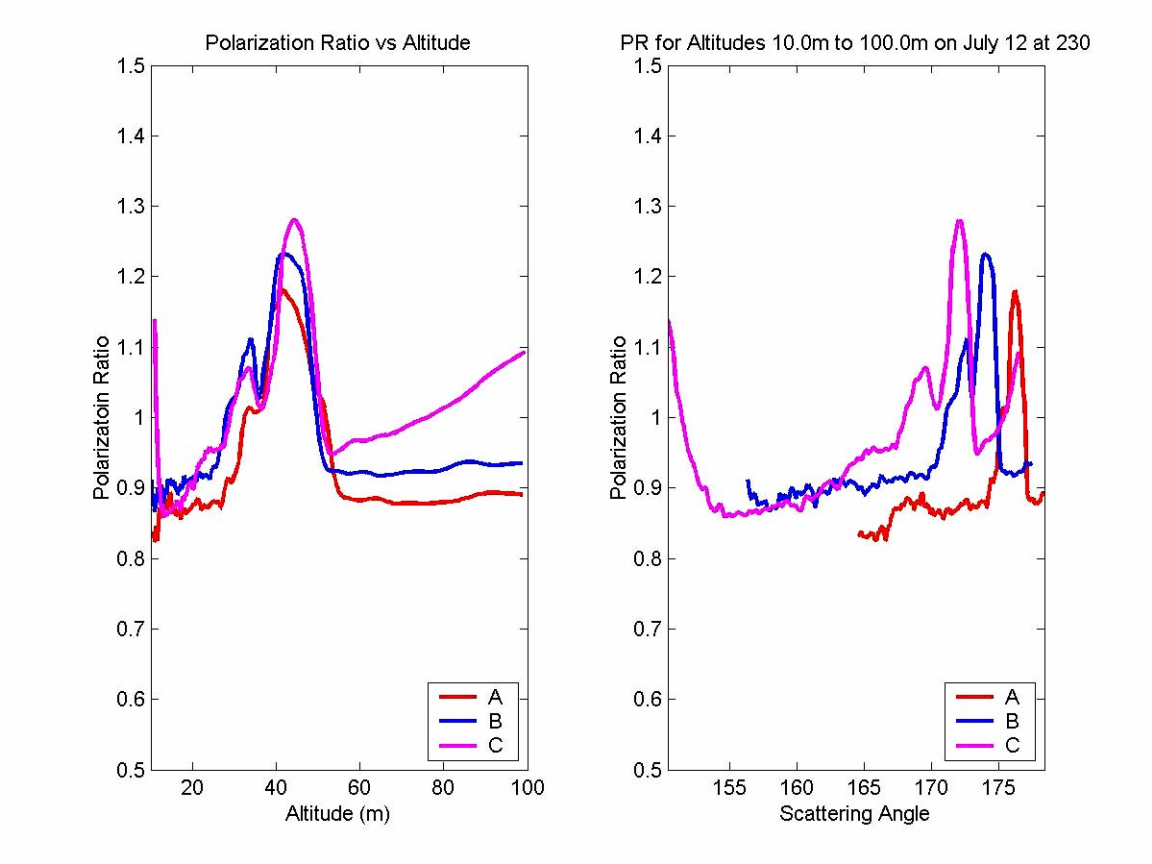


Figure 1-6: Polarization ratios as a function of altitude and scattering angle (Novitsky, 2002, Fig.6-3b).

Jin Park (2008) investigated the effects of multiple scattering on the polarization ratio. An aerosol chamber with an aerosol generator, as well as ambient atmospheric aerosols were studied during investigations of varying concentrations of uniformly mixed aerosols. His research showed that single-scattering Mie equations can be applied to conditions of moderate multiple scattering when examining scattering angles close to the backward direction with a decent level of agreement (Fig. 1-7). In a similar study, Park shows how the measured polarization ratio begins to deviate from the Mie-calculated model for a range of backscattering angles under increasing conditions of multiple scattering (Fig. 1-8). A useful model for the multiple scattering case was proposed.

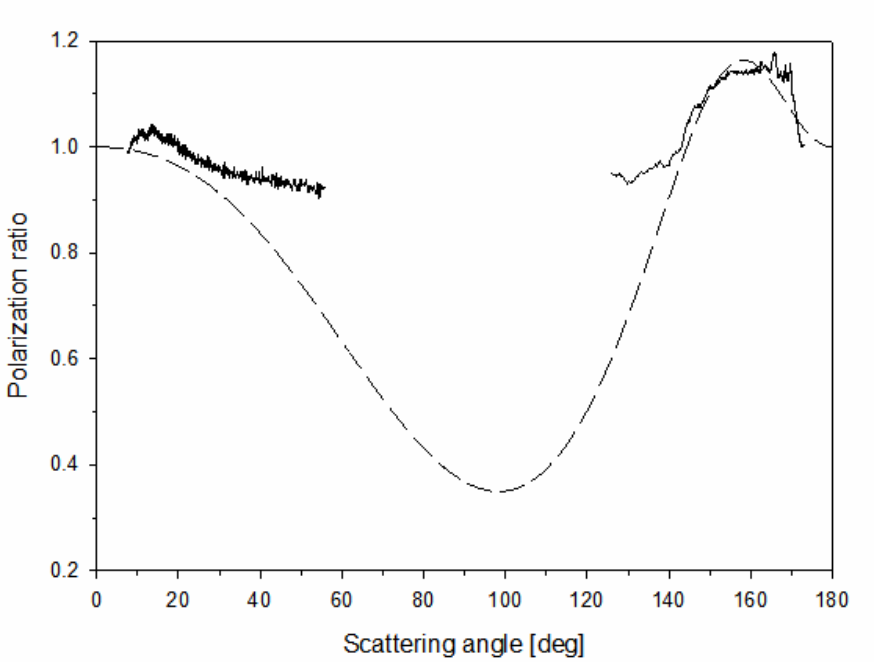


Figure 1-7: Scattering measurements from fog-oil (solid line) under conditions of moderate multiple scattering compared to a single-scatter Mie-calculated polarization ratio (dashed line) (concentration of 60,000 #/cm^3 with median diameter of 117 nm) (Park, 2008, Fig. 6.11).

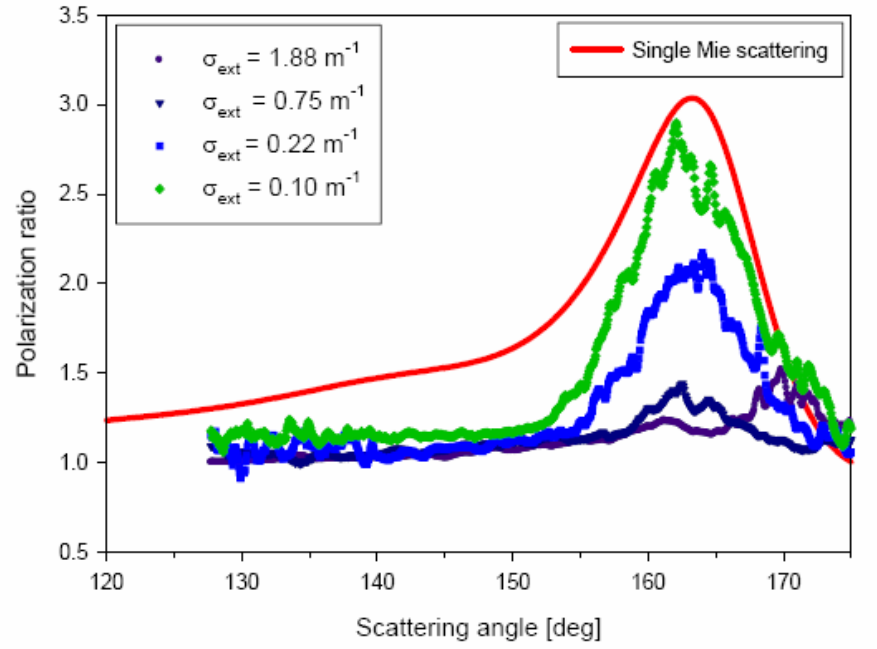


Figure 1-8: Effect of multiple scattering on polarization ratio as a function of extinction cross-section (Park, 2008, Fig. 6-17).

1.2.2 Inverting atmospheric aerosol size distributions

Using scattered intensity data to infer a particle size distribution is an ill-posed problem that requires solving a Fredholm integral of the first kind. The complex problem of solving Fredholm integrals of the first kind for data inversion has been studied for over 40 years. The two first widely-recognized methods, the Phillips-Twomey method and Tikhonov regularization, were developed in the early 60's and are based on constrained linear inversion (Phillips, 1962; Twomey, 1963; Tikhonov, 1963). These techniques rely on introducing additional constraints into the linear equations in order to reduce ambiguity in the solution space and produce an optimal solution (King, 1982). The two constraints introduced by both of the aforementioned algorithms are non-negativity and smoothness. Requiring a positive solution for a measured particle size distribution is obvious and dictated by physical necessity; however, the constraint of requiring the "smoothest' solution in a set of solutions is not as straight-forward, and is very much open to interpretation. An extensive focus of the aerosol remote sensing community for the past 40 years has been on the selection and application of the proper constraints for the linear inversion method. Just a small representation of the literature available on constrained linear inversion for the specific application of aerosol size distribution retrieval includes: Yamamoto and Tanaka (1969), King *et al*. (1978), Walters (1980), Dave (1971), Herman *et al*. (1971), Byrne (1978), Reagan *et al*. (1980), Bockmann (2001), Veselovskii *et al*. (2002), Miecznik *et al*. (2005), and Kolgotin and Muller (2008). An in-depth review of all of these similar inversion methods is too extensive for our purposes, but the point has been made that much attention has been given to this subject over the years. This type of inversion method is attractive for two main reasons: its speed of convergence; and, when it does converge to the global solution, it is mathematically the best solution. All of these methods suffer from similar drawbacks; dependence on initial guesses, high sensitivity to noise, the tendency to be trapped in local

extrema (resulting in an incorrect answer), and the requirement of finding the derivative of the optimized equation, which is not always easy to calculate and oftentimes must be done through numerical techniques.

Stevens (1996) and Novitsky (2002) both utilized a gradient-based optimization technique to invert their measured polarization ratios, and both experienced a high level of frustration with varying-degrees of success. Stevens implemented a Newton-Rhaphson optimization routine to retrieve the geometric means and geometric standard deviations of his tri-modal lognormal size distributions. Stevens found that this method often did not converge to a global solution, and he eventually resorted to a brute-force guess-and-check method. Many helpful ideas were gleaned from Stevens' inversion work, particularly his approach to modeling molecular scattering which will be explained in Chapter 2. Novitsky invested a considerable amount of time and energy in a non-linear least-squares (NLS) inversion routine to retrieve tri-lognormal size distributions. Novitsky found that the NLS routine was able to adequately fit simulated parallel and perpendicular scattering phase functions, provided that the initial 'first-guesses' for the nine lognormal parameters were within an approximate range of the correct parameters (which were known in the case of simulated data). When attempting to use the NLS routine to fit the polarization ratio, the program "failed" after a single iteration even for cases where the initial starting point closely resembled the lognormal parameterized solution. The approach struggles to converge to an appropriate solution in many cases due to asymptotes in the denominator of the polarization ratio, i.e. the derivative of the polarization ratio heads to infinity at points along such a curve. While the NLS routine did prove to be impressive in its curve-fitting abilities, it was not able to invert the polarization ratio data obtained from the multistatic approach and Novitsky was forced to resort to manual intervention to arrive at the final inversion of the data. Novitsky points out that another drawback of utilizing a gradient-based inversion routine is the difficulty of calculating analytical derivatives of the polarization ratio, specifically

in the case of a varying refractive index. This work on the NLS routine presented by Novitsky had a considerable impact on the selection of an inversion routine for the multiwavelength-multistatic scattering data; specifically, it was determined that a non-gradient-based inversion routine should be implemented. The search for such an algorithm revealed the genetic algorithm as a promising alternative to the gradient-based approach.

The use of stochastic search techniques as inversion methods for retrieval of aerosol size distributions started receiving attention during the past decade. These types of algorithms, such as Monte Carlo methods, simulated annealing, and genetic algorithms, have the advantage of exploring the global solution space without using any derivative information. These techniques are not generally caught in local extrema of the solution space, and they are stable under conditions of random noise because they do not operate on the steepest descent principle. The simplicity of the algorithms, to both understand and implement, make them popular across a wide-range of applications. The main drawbacks of these types of optimization algorithms are: the amount of time that is takes to converge and the lack of mathematical justification for the actual global solution found. The convergence time has become less of a concern as computer technology has grown rapidly with multi-core computers. The stochastic search algorithms are highly parallel in nature and are easily extended to multi-core processing, greatly increasing the speed at which these algorithms converge.

Genetic algorithms (GA) are an attractive search technique over the purely random Monte Carlo techniques because they use information from previously tried solutions of the problem to search for a global solution. GA's produce solutions using a process of selection, reproduction, and mutation that is modeled on the theory of natural selection and survival of the fittest. A limited amount of information on applying genetic algorithms to retrieve particle size distributions and refractive indices from measured scattering data is available in the literature, all showing promising results. Ye *et al*. (1999) applied a genetic algorithm to multiple sets of

simulated angular scattering data to invert aerosol size distributions with a high level of success. No predefined probability density functions were used in the inversion process, but rather 'bins' of radii ranging between 1 μm and 40 μm are allowed to assume concentration values. The result was found to strongly depend on the real part of the refractive index, and indicates that the real refractive index should be a parameter that can be extracted by the inversion routine (i.e. changing the refractive index will either increase or decrease the fit between the model and the measured polarization ratio). Hodgeson (2001) also applied a genetic algorithm to simulated light scattering data in determining particle size distributions for a particle size ranges between 100 nm to 4 μm. This paper focuses on the ability of the algorithm to extract unimodal, bimodal, and trimodal distributions of spheres with well-defined diameters from a discrete set of simulated angular scattering measurements. It was found that the GA performed well in this extremely simplified optical scattering scenario. Another interesting study of genetic algorithm performance on simulated data was conducted by Xu *et al*. (2004) using multispectral extinction. Simulated extinction data was used at 16 different wavelengths across the mid-wave and longwave infrared region of the electromagnetic spectrum to determine particle size distributions described by a probability density function. A comparison of the results obtained by the genetic algorithm to those obtained by two different gradient-based techniques showed that the GA outperformed the other two algorithms in the presence of noise, and produced similar results in low-noise datasets (Xu, 2004). Lienert, Porter, and Sharma (2003) apply a genetic algorithm to invert particle size distributions from polar nephelometer data at 532 nm using a predefined lognormal probability density function. Comparison of inverted size distributions to measurements made by particle sizers showed good agreement for particle diameters on the order of the wavelength and larger, but inversion of the single wavelength data was unable to accurately place constraints on the smaller sizes of accumulation-mode particles. A genetic algorithm combined with polar nephelometer measurements also has been used to determine aerosol

refractive indices from angular scattering data (Barkey *et al*, 2007). Parallel- and perpendicular-polarized scattering measurements at 670 nm were used to retrieve the real refractive index of polystyrene latex spheres and ammonium sulfate droplets, with the inverted results falling within the expected range.

1.3 Hypotheses

As previously mentioned, this work is really a continuing effort that heavily utilizes the work and contributions of prior students. The main goals of this research are to extend the multistatic polarization ratio technique to multiple wavelengths and development of a robust inversion algorithm that can be used to infer particle size distributions, concentrations, and complex refractive indices as a function of wavelength from the collected data. Three primary hypotheses are tested through this work:

1) *Adding multiple wavelength data to a multistatic lidar system aids in accurately determining the size distribution and number density of the aerosols.* Multiple wavelength data are expected to be particularly useful in situations where a wide range of aerosol sizes and/or non-spherical aerosols are present. Each wavelength scatters more effectively from particles corresponding to a specific range of sizes and shapes. Multiwavelength-multistatic data should also be beneficial in regions where the aerosols are non-uniformly mixed by providing multiple simultaneous measurements at each spatial element over a range of angles.

2) *A multiwavelength-multistatic system provides the capability to determine the refractive index of aerosols as a function of wavelength.* The refractive index of aerosols is dependent on their chemical composition, so multiwavelength complex refractive indices will tell us information about what materials are most likely present in the interrogated aerosols.

3) *A genetic algorithm accurately and robustly inverts the multiwavelength-multistatic data to determine aerosol characteristics.* An effort will be made to explore the robustness of the inversion technique and to describe some of the errors associated with its use on the multiwavelength-multistatic data.

A shared conclusion by both Stevens and Novitsky was the need for a controlled experiment where the microphysical properties of the scattering medium were known in order to validate the results obtained by applying the Mie calculations to perform the analysis. A significant contribution of the present work is a controlled experiment conducted at the Environmental Protection Agency's (EPA) Aerosol Test Facility (ATF) where *in situ* aerosol size and concentration information is available to compare with the results from the optical scattering measurements.

Chapter 2

Scattering Theory

The key to an accurate inversion is an accurate description of the forward problem. The intensity distribution of a beam of light scattered from a collection of particles is dependent on the microphysical properties of the particles, including the size, concentration, shape, and composition. The large number of variables makes the remote sensing of aerosols by scattered light impossible without the use of some careful observations and intelligent constraints to narrow the allowable solutions to physically possible and reasonable ranges. One constraint that significantly simplifies the description of an ensemble of scatterers is limiting their allowable shape to be spherical. While not all atmospheric aerosols can be viewed as spheres (dust and ice definitely can not be), it has been found that Mie calculations, which are based on spherical scatterers, can describe optical scattering from fogs, clouds, and even dust, rather well. Gustav Mie solved Maxwell's equations using the necessary boundary conditions for the interaction between a homogenous dielectric sphere and an electromagnetic plane wave (Mie, 1908). The so-called Mie equations are well-known within the electromagnetic community, and describe fully the interaction of the electromagnetic fields, both internal and external to the dielectric sphere, as incident radiation is scattered. The complete derivation is rather intensive and is available in many excellent texts devoted to optical scattering (van de Hulst, 1957; Kerker, 1969; Bohren and Huffman, 1983). There are a number of conditions that must be satisfied in order for these equations to accurately describe a volume of scatterers, with the most significant condition being that the process must be dominated by single, independent scattering events. In other words, the scattered light must only strike a single particle and then be scattered into the field of view of the receiver with out interacting with any other particle (or the radiation from another

particle, meaning the process must be incoherent). The relationship between scattered and incident electromagnetic fields from a sphere can be expressed as (Bohren and Huffman, 1989, pg. 65),

$$\begin{bmatrix} \vec{E}_{\parallel}^{s} \\ \vec{E}_{\perp}^{s} \end{bmatrix} = \frac{e^{jk(R-z)}}{-ikR} \begin{bmatrix} S_2 & 0 \\ 0 & S_1 \end{bmatrix} \begin{bmatrix} \vec{E}_{\parallel}^{i} \\ \vec{E}_{\perp}^{i} \end{bmatrix}, \tag{2-1}$$

where the 2 x 2 matrix S can be calculated using Mie's solution to the Maxwell equations. The S_i elements of the matrix are the complex amplitude scattering coefficients that can be used to calculate the magnitude of a scattered electromagnetic wave. The intensity of an electromagnetic wave is proportional to the square of the magnitude, and is the characteristic of the scattered field that will be measured and analyzed in this work. A matrix equation similar to Eqn. 2-1 can be used to represent the intensity of polarized light scattered from a sphere using Stoke's vectors and a Mueller matrix,

$$\begin{bmatrix} I_s \\ Q_s \\ U_s \\ V_s \end{bmatrix} = \frac{1}{k^2 R^2} \begin{bmatrix} S_{11} & S_{12} & 0 & 0 \\ S_{21} & S_{22} & 0 & 0 \\ 0 & 0 & S_{33} & S_{34} \\ 0 & 0 & -S_{34} & S_{44} \end{bmatrix} \begin{bmatrix} I_i \\ Q_i \\ U_i \\ V_i \end{bmatrix}. \tag{2-2}$$

A Mueller matrix is a transfer matrix that can be used to describe the manipulation of incoherent light. The S_{ii} elements of the Mueller matrix describe the polarization properties of scattered light and are related to the amplitude scattering coefficients as (Bohren and Huffman, 1989, pg. 112),

$$S_{11} = \frac{1}{2}\left(|S_2|^2 + |S_1|^2\right), \qquad S_{12} = \frac{1}{2}\left(|S_2|^2 - |S_1|^2\right) \tag{2-3}$$

$$S_{33} = \frac{1}{2}\left(S_2^* S_1 + S_2 S_1^*\right), \qquad S_{34} = \frac{i}{2}\left(S_1 S_2^* - S_2 S_1^*\right).$$

The Stoke's parameters I, Q, U, and V describe fully the scattered light polarization. *I* is the total irradiance of the electromagnetic wave, *Q* is the polarized component of irradiance in the horizontal (+) and vertical (-) directions, *U* is the irradiance 45° from vertical in the clockwise (+) or counterclockwise (-) directions, and *V* is the irradiance in a circularly polarized state, either left-handed (-) or right-handed (+). The sign of the component is defined by the direction observed when looking back at the source of the electromagnetic wave. Under the conditions of a fully polarized electromagnetic wave, the Stoke's parameters follow the relationship,

$$I^2 = Q^2 + U^2 + V^2 . \tag{2-4}$$

Stoke's vectors are generally normalized by the total irradiance I, which transforms the previous equation to the form of a unit sphere, and provides an elegant representation of the polarization state of an electromagnetic wave. For example:

$$\begin{bmatrix} 1 \\ 0 \\ 0 \\ 0 \end{bmatrix} \text{unpolarized} \qquad \begin{bmatrix} 1 \\ 1 \\ 0 \\ 0 \end{bmatrix} \text{horizontal} \qquad \begin{bmatrix} 1 \\ -1 \\ 0 \\ 0 \end{bmatrix} \text{vertical} \tag{2-5}$$

The normalized Stoke's vectors and the Mueller matrix can be used to develop equations for the scattered intensity per incident unit intensity for parallel and perpendicular polarized (with respect to the scattering plane) light as (Bohren and Huffman, 1989, pg. 113),

$$I_{s,\|} = \frac{1}{k^2 R^2}\left(S_{11} + S_{12}\right) I_{i,\|} \qquad \text{and} \qquad I_{s,\perp} = \frac{1}{k^2 R^2}\left(S_{11} - S_{12}\right) I_{i,\perp} . \tag{2-6}$$

Expressions for the parallel and perpendicular scattering intensities per unit intensity can be written by normalizing Eqn. 2-6 by the incident intensities and omitting the propagation scaling factor $1/k^2r^2$,

$$i_{\|} = \left(S_{11} + S_{12}\right) = \left|S_2\right|^2 \qquad \text{and} \qquad i_{\perp} = \left(S_{11} - S_{12}\right) = \left|S_1\right|^2 \tag{2-7}$$

These unitless equations form the basis of the scattering equations used to calculate the polarization ratio (explained in the next section). At first glance the equations look deceptively simple, but the amplitude scattering coefficients are actually dependent on the wavelength of incident light (λ), the complex refractive index of the particle (n_{re}+in_{im}) which is also wavelength dependent, the radius of the particle (a), and the scattering angle (θ), i.e. $S_{1,2}\left(\lambda, n_{re}(\lambda) + in_{im}(\lambda), a, \theta\right)$. A vectorized MATLAB version of the popular BHMIE code provided in the Bohren and Huffman appendix (1989) is used to compute the amplitude scattering matrix coefficients, S_1 and S_2 for all calculations presented in this work and in the inversion algorithm explained in Chapter 4.

Figure 2-1 shows the intensity distributions of the scattering phase function for perpendicular polarized light, i_1, and parallel polarized light, i_2, as the parameter *ka* increases. The quantity *ka* relates the incident propagation number ($k = 2\pi/\lambda$) to the radius of the aerosol, *a*.

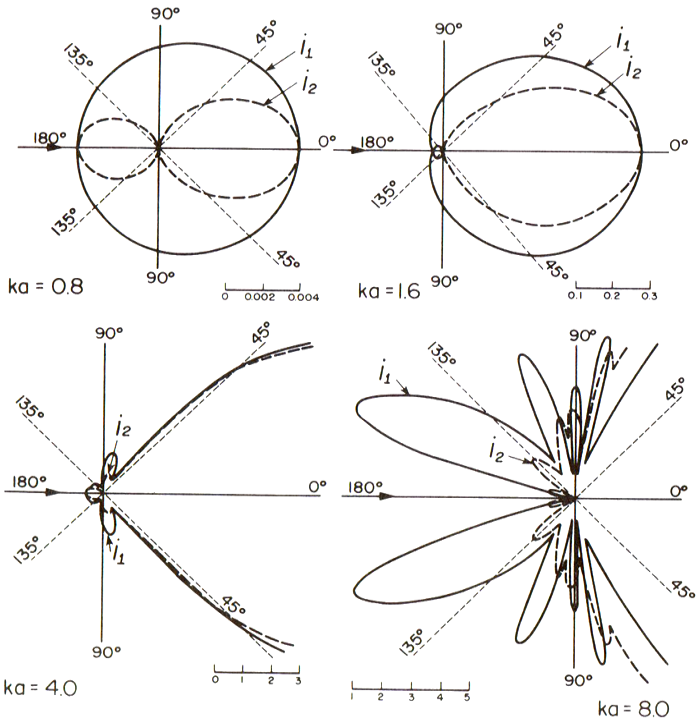


Figure 2-1: Scattering of polarized light as a function of angle and particle radius. i_1 is perpendicular polarized light and i_2 is parallel polarized light. (Born and Wolf, 1980)

When the particle is much smaller than the wavelength ($a < 0.1\lambda$), the particle scatters as a dipole and it is referred to as Rayleigh scattering. In this case, the presence of small particles is difficult to distinguish from background molecules. When the particle size and the wavelength are on the same order, distinctive scattering patterns are formed, which are represented by calculations using the Mie solutions of Maxwell's equations. As the size parameter (ka) of the particle increases, the angular scattering pattern changes from the simple dipole pattern to a highly-structured pattern with multiple peaks and nulls. When the particle is much larger than the wavelength of incident light ($a > 10\lambda$), the scattering structure becomes highly complex, and defining features of the scattering pattern become difficult to discern. The focus of this work uses these lobed structures, and knowledge of the wavelength and polarization of the incident wavelength, to retrieve the size and refractive index information about the scattering particles. The examination of multiple wavelengths in this study is intended to show that use of a range of wavelengths, specifically a broad range that covers regions of the UV, VIS, and IR spectra, can extend the applicability of the technique for multistatic aerosol characterization technique to include essentially all sizes of atmospheric aerosols. Three wavelengths that span the visible spectrum are used in this work; 407 nm (blue/violet), 532 nm (green), and 650 nm (red). These wavelengths were selected based on price and to provide the widest wavelength spread that could be analyzed using the optics and CCD imagers that were available for these multistatic measurements.

2.1 Optical Scattering and Atmospheric Aerosols

2.1.1 Molecular scattering

Molecular optical scattering is a well-known phenomenon and is responsible for the appearance of a blue sky. Molecules are much smaller than aerosols, but still contribute to atmospheric scattering because of their abundance (on the order of 10^{19} molecules/cm^3). In order to calculate the contribution of molecules to the polarization ratio, an equivalent spherical radius is computed as explained by Stevens (1996, pg. 68) and Novitsky (2002, pg. 83). The equivalent radii, a_{eq}, are dependent on the Rayleigh cross-section, σ, and the real part of the index of refraction, n, and are computed for each wavelength as,

$$a_{eq} = \left[\frac{3\sigma_\lambda}{8\pi} \left(\frac{\lambda}{2\pi} \right)^4 \frac{n_\lambda^2 + 2}{\left(n_\lambda^2 - 1 \right)^2} \right]^{\frac{1}{6}}. \tag{2-8}$$

The Rayleigh cross section for standard air can be calculated using the empirical formula,

$$\sigma_\lambda = A \cdot \lambda^{-\left(B + C\lambda + \frac{D}{\lambda} \right)} \tag{2-9}$$

where the coefficients A through D are given in Table 2-1 (Bucholtz, 1995).

Table 2-1: Coefficients for empirical Rayleigh scattering cross section in air (Bucholtz, 1995)

Wavelength range	A	B	C	D
0.2 μm≤ λ < 0.5 μm	3.01577 x 10^{-28}	3.55212	1.35579	0.11563
0.5 μm≤ λ < 4.0 μm	4.01061 x 10^{-28}	3.99668	0.00110298	0.0271393

Using Eqn. 2-9, the Rayleigh scattering cross sections are 3.297 x 10^{-26} cm^2 at 407 nm, 5.126 x 10^{-27} cm^2 at 532 nm, and 2.285 x 10^{-27} cm^2 at 650 nm, which are the three wavelengths used for the experimental measurements analyzed in this work. These wavelength-dependent cross-sections are used in Eqn. 2-8 to calculate an equivalent size dielectric sphere. The Mie equations

are used to calculate the scattering intensity from these equivalent dielectric spheres to approximate the intensity of optical scattering from nitrogen and oxygen in the atmosphere. Figure 2-2 shows the equivalent sphere radius as a function of incident wavelength and the real refractive index of the dielectric sphere.

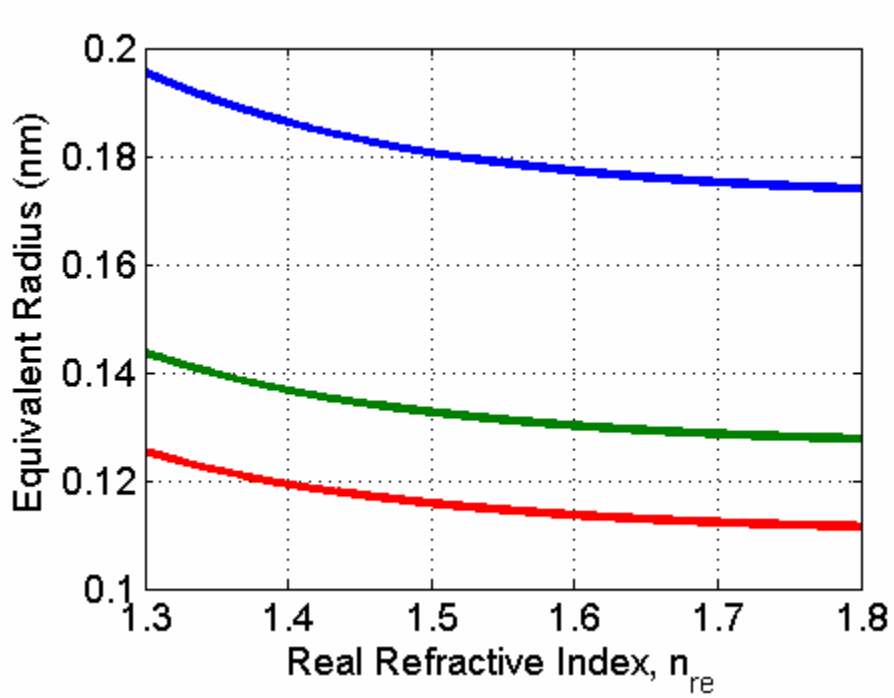


Figure 2-2: Equivalent dielectric sphere radius as a function of incident wavelength and real refractive index.

Novitsky (2002) points out that even though the real part of the index of refraction is included in the equivalent radius calculation, and the refractive index is allowed to vary in the inversion algorithm, this results in no change to the amplitude scattering coefficients because the resulting radii are so small compared to the incident wavelength (2002, pg. 83-84). This point is confirmed by Fig. 2-3, which shows the polarization ratio for 407 nm incident light scattering from dielectric spheres of six different radii and real refractive indices (values from 407 nm curve shown in Fig. 2-2), yet it appears as a single curve.

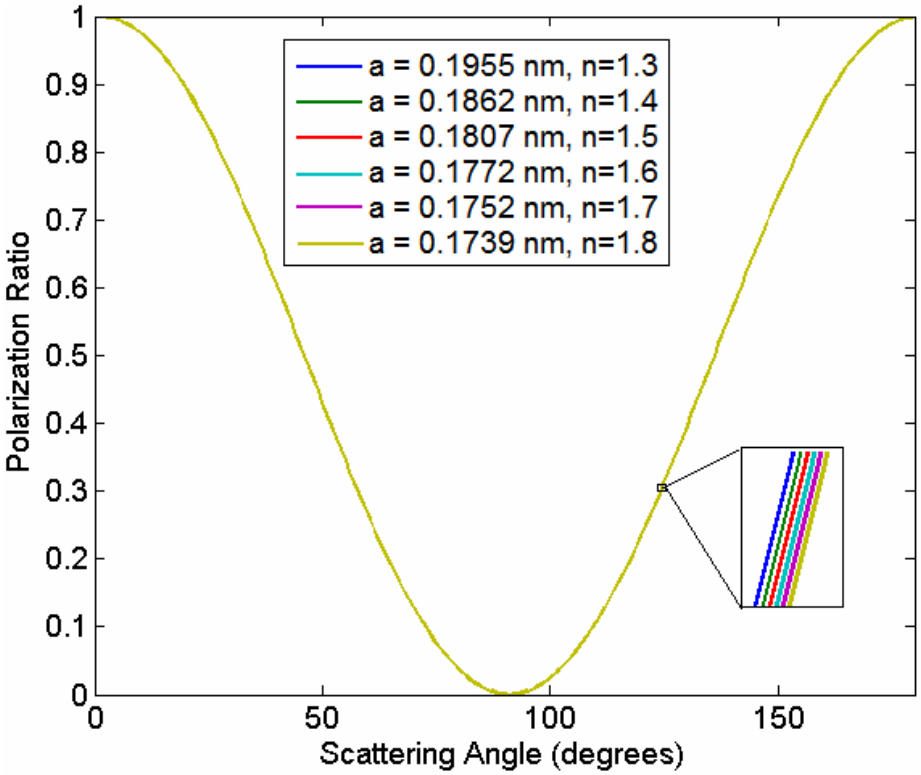


Figure 2-3: Polarization ratio for 407 nm wavelength as a function of varying equivalent sphere radius and real refractive index.

2.1.2 Particle size distributions

Aerosols in the atmosphere are present in many sizes, ranging in diameter from single nanometers to hundreds of microns (Seinfeld and Pandis, 1998). Many different probability density functions have been used to describe aerosols over the past 50 years. A lognormal distribution is often used to describe aerosols that originate from a single source and is expressed as,

$$\frac{dN}{d\log(d_p)} = \frac{N_T}{\sqrt{2\pi}\log(\sigma_g)}\exp\left(\frac{-(\log(d)-\log(d_g))^2}{2\log^2(\sigma_g)}\right), \qquad (2\text{-}10)$$

where N_T is the total number concentration, d_g is the geometric mean diameter, and σ_g is the geometric standard deviation. Figure 2-4 shows four lognormal size distributions, each with a constant geometric mean diameter of 1 μm, a constant concentration of 1,000 particles/cm^3, and four different values of the geometric standard deviation: 1.01, 1.5, 2.0, and 3.0. A thorough description of the lognormal particle distribution is given by Novitsky (2002, Chapter 2).

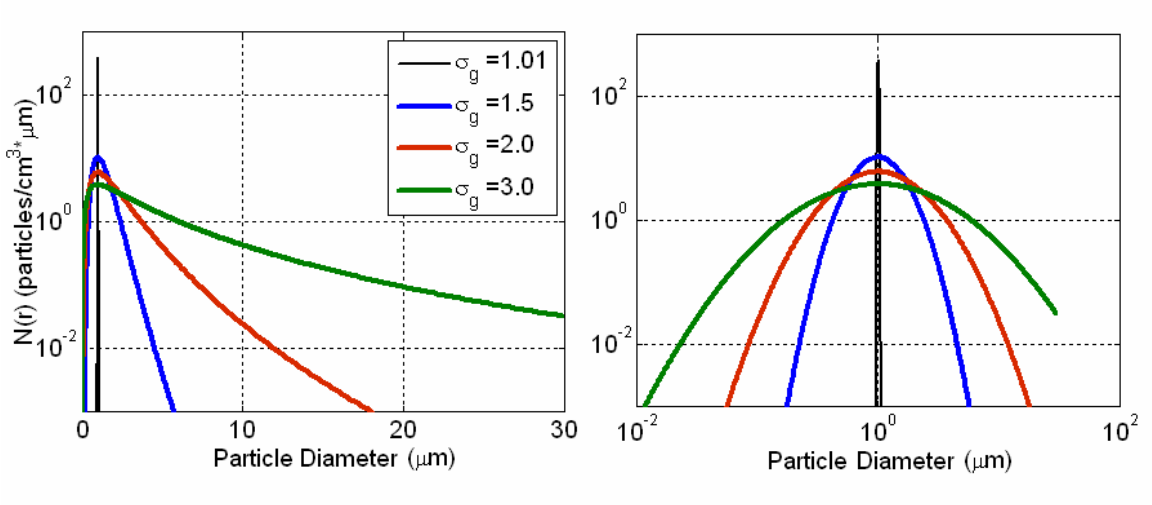


Figure 2-4: Lognormal size distributions for a diameter of 1 μm, a concentration of 1,000 particles/cm^3, and four different values of the geometric standard deviation: 1.01 (black line), 1.5 (blue line), 2.0 (red line), and 3.0 (green line). The left plot shows a linear scale for the particle diameter, while the right plot is a logarithmic scale.

The trimodal lognormal distribution has found the most success in describing the total concentration of atmospheric aerosols, modeling the fine mode (d_p < 0 .1 μm), accumulation mode (0.1 μm < d_p < 1 μm), and course mode (d_p > 1 μm) of aerosols with a separate lognormal distribution (Seinfeld and Pandis, 1998). The use of three lognormal distributions to describe atmospheric aerosols grew out of data published observations on Los Angeles smog (Whitby, 1972). The measured particle sizes did not fit the power law that had previously been used to describe aerosol size distributions and Whitby theorized that the size distributions should be broken up into subranges. Kelkar and Joshi (1977) fit three lognormal size distributions to the smog data using the justification that the aerosols were produced through three mechanisms: gas-

particle conversion (fine mode), condensation (accumulation mode), and disruption of bulk material and resuspension of settled particles (course mode). The trimodal lognormal size distribution is expressed as the sum of three lognormal distributions:

$$\frac{dN}{d\log(d_p)} = \sum_{i=1}^{3} \frac{N_{T,i}}{\sqrt{2\pi}\log(\sigma_{g,i})} \exp\left(\frac{-(\log(d)-\log(d_{g,i}))^2}{2\log^2(\sigma_{g,i})}\right). \quad (2\text{-}11)$$

The total aerosol concentration is then calculated by adding the concentration of each mode, $N_{T,i}$. Jaenicke (1993) presents a description of 'typical' trimodal lognormal particle size distributions for different global regions, which was reproduced by Seinfeld and Pandis (1998), and displayed in Table 2-2. The trimodal lognormal particle size distributions for urban, rural, and remote continental regions are shown in Fig. 2-5. These models are useful for making general comparisons between the 'typical' aerosol size distributions based on geographic location. In general, an urban environment will have a higher concentration of smaller particles and a rural environment will show two distinct lognormal modes. It is important to remember that aerosols exhibit extreme variability over time and location, and applying one model of the 'typical' aerosol size distribution to locations anywhere around the world, at all times of the day, seasons, etc., based on geographic location is not possible. For this reason, it should be expected that measured size distributions will differ significantly from the models presented in Table 2-2 most of the time.

Table 2-2: Values for atmospheric tri-modal lognormal distributions. (Jaenicke, 1993)

	Mode 1			Mode 2			Mode 3		
	N ($\#/cm^3$)	d_p (μm)	σ_g	N ($\#/cm^3$)	d_p (μm)	σ_g	N ($\#/cm^3$)	d_p (μm)	σ_g
Urban	9.93×10^4	0.013	1.758	1.11×10^3	0.014	4.634	3.64×10^4	0.05	2.173
Marine	133	0.008	4.539	66.6	0.266	1.622	3.1	0.58	2.489
Rural	6650	0.015	1.679	147	0.054	3.606	1990	0.084	1.845
Remote Continental	3200	0.02	1.449	2900	0.116	1.648	0.3	1.8	2.399
Free Troposphere	129	0.007	4.416	59.7	0.25	1.791	63.5	0.52	2.661
Polar	21.7	0.138	1.758	0.186	0.75	1.995	3×10^{-4}	8.6	1.954
Desert	726	0.002	1.766	114	0.038	5.888	0.178	21.6	2.742

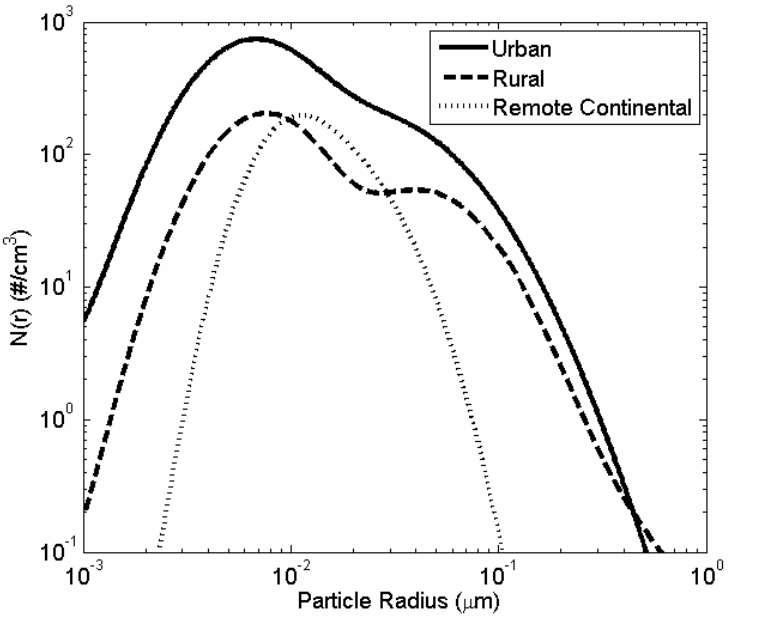


Figure 2-5: Trimodal aerosol size distributions from Table 2-2. (Jaenicke, 1993)

2.2 Polarization Ratio

For the case of independent, single-scattering, the angular intensity distribution of scattered light is a summation of the scattered light from each particle in the scattering volume. A

Fredholm integral equation of the first-kind relates the total scattered intensity to the particle size distribution, *f(a)*,

$$I_{\|,\perp}(\lambda, n+ik, a, \theta) = N_T \int_{a_{\min}}^{a_{\max}} i_{\|,\perp}(\lambda, n+ik, a, \theta) f(a) da \,, \tag{2-12}$$

where N_T is the total number concentration of particles and $i_{\|,\perp}(\lambda, n+ik, a, \theta)$ are the unit scattering intensities per incident intensity equations (Eqn. 2-7). The polarization ratio, which is the parameter used to determine the aerosol characterization, is formed by dividing the total scattering intensity from incident parallel polarized light by the total scattering intensity from perpendicular polarized light. The advantages of using the polarization ratio are highlighted in the next few paragraphs. A mathematical expression for the polarization ratio can be written by combining Eqns. 2-7 and 2-11 (Novitsky, 2002, pg. 82),

$$PR(\lambda, \theta) = \frac{I_{s,\|}(\lambda, \theta)}{I_{s,\perp}(\lambda, \theta)} = \frac{\int_{a_{\min}}^{a_{\max}} \left|S_2(\lambda, n+ik, a, \theta)\right|^2 f(a) da + molecular_{\|}}{\int_{a_{\min}}^{a_{\max}} \left|S_1(\lambda, n+ik, a, \theta)\right|^2 f(a) da + molecular_{\perp}}, \tag{2-13}$$

where

$I_{s,\|}(\lambda, \theta)$ is the total scattered intensity from parallel incident polarization,

$I_{s,\perp}(\lambda, \theta)$ is the total scattered intensity from incident perpendicular polarization,

$\left|S_{1,2}(\lambda, n+ik, a, \theta)\right|^2$ are the amplitude scattering coefficients calculated using the Mie solution of Maxwell's equations,

f(a) is the particle size(radius) number distribution ($N(a_i)$ vs. a_i), and

$molecular_{\|,\perp}$ are the intensities contributed by molecular scattering.

The number-density particle size distribution, $N(a_i)$, is calculated by multiplying the normalized lognormal distribution, $dN/d\log(a_i)$ (Eqns. 2-10 and 2-11), by the logarithm of the bin width for each radii, $d\log(a_i)$,

$$f(a) = N(a_i) = \frac{dN}{d\log(a_i)} \cdot \left(\log(a_{i,\max}) - \log(a_{i,\min})\right). \tag{2-14}$$

Examining the properties of the polarization ratio reveals why it is used in the inversion process rather than the intensity of the parallel or perpendicular phase functions. The power of the received signal by the multistatic system can be calculated as,

$$P_r(\theta) = P_t \frac{C}{D} \beta(\theta) T^2 d\theta\,, \tag{2-15}$$

where C is the optical efficiency of the system, D is the linear distance from the detector to the imaged aerosol volume, β is the scattering coefficient, and T^2 is the two-way atmospheric transmittance (Meki, 1996). In the case of a stationary receiver imaging a scattered beam (which is the case of the multiwavelength-multistatic system used in this work), the linear distance to the scattering volume (D) and the two-way transmittance (T^2) will vary with the scattering angle θ, making range correction of the data rather involved. When the system design is such that only the scattering coefficients contain polarization dependence, then the equation for describing the polarization ratio reduces to,

$$PR = \frac{P_{r,\|}}{P_{r,\perp}} = \frac{\beta_\|(\theta)}{\beta_\perp(\theta)}. \tag{2-16}$$

The system parameters (such as the spectral response of the transmitter optics and the detector and nonlinearities across the field-of-view of the detector) and the path extinction between the scattering volume and the imager are all cancelled by forming a ratio of the two intensities; thus significantly simplifying the data analysis procedure as well as eliminating many measurement uncertainties.

2.2.1 Understanding the polarization ratio

Before designing an inversion algorithm based on the polarization ratio, it is necessary to understand how the function changes as the different descriptors of the scattering particles vary. In other words, it is important to understand how the polarization ratio changes as a function of the particle size to wavelength ratio, the size distribution, and the complex refractive indices of the particles. Novitsky (2002, pgs. 87-97) performed such a study prior to attempting a non-linear least-squares (NLS) inversion on collected polarization ratio data. Calculations for the single wavelength of 532 nm are performed, using the trimodal size distribution shown in Fig. 2-6, and using a real refractive index of 1.38. Novitsky presents plots, shown in Fig. 2-7, that show the variations in the polarization ratio as each of the nine lognormal parameters of the trimodal size distribution are varied.

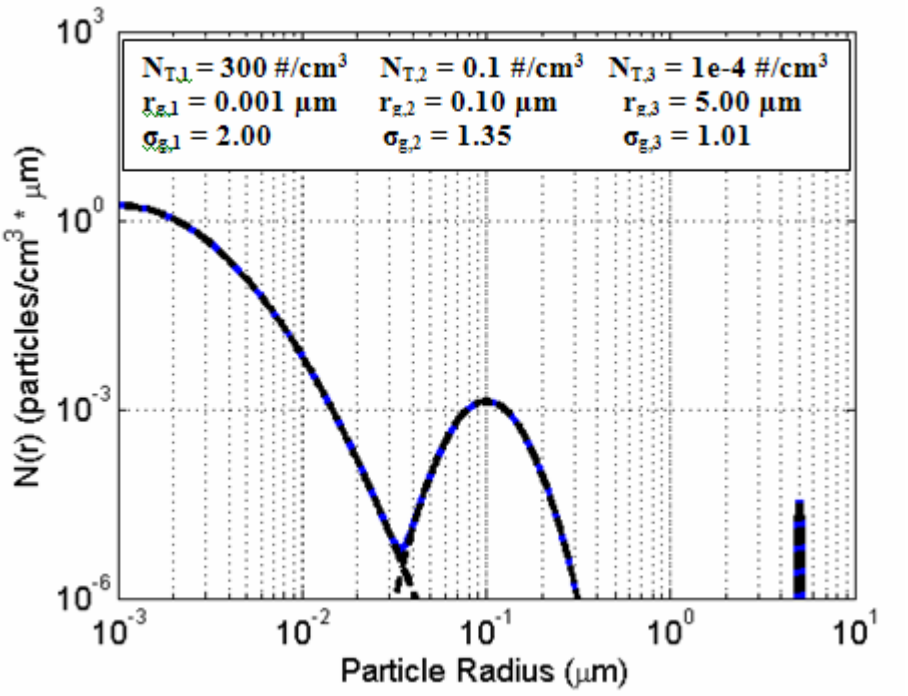


Figure 2-6: Trimodal particle size distribution used in polarization ratio sensitivity analysis in Fig. 2-7.

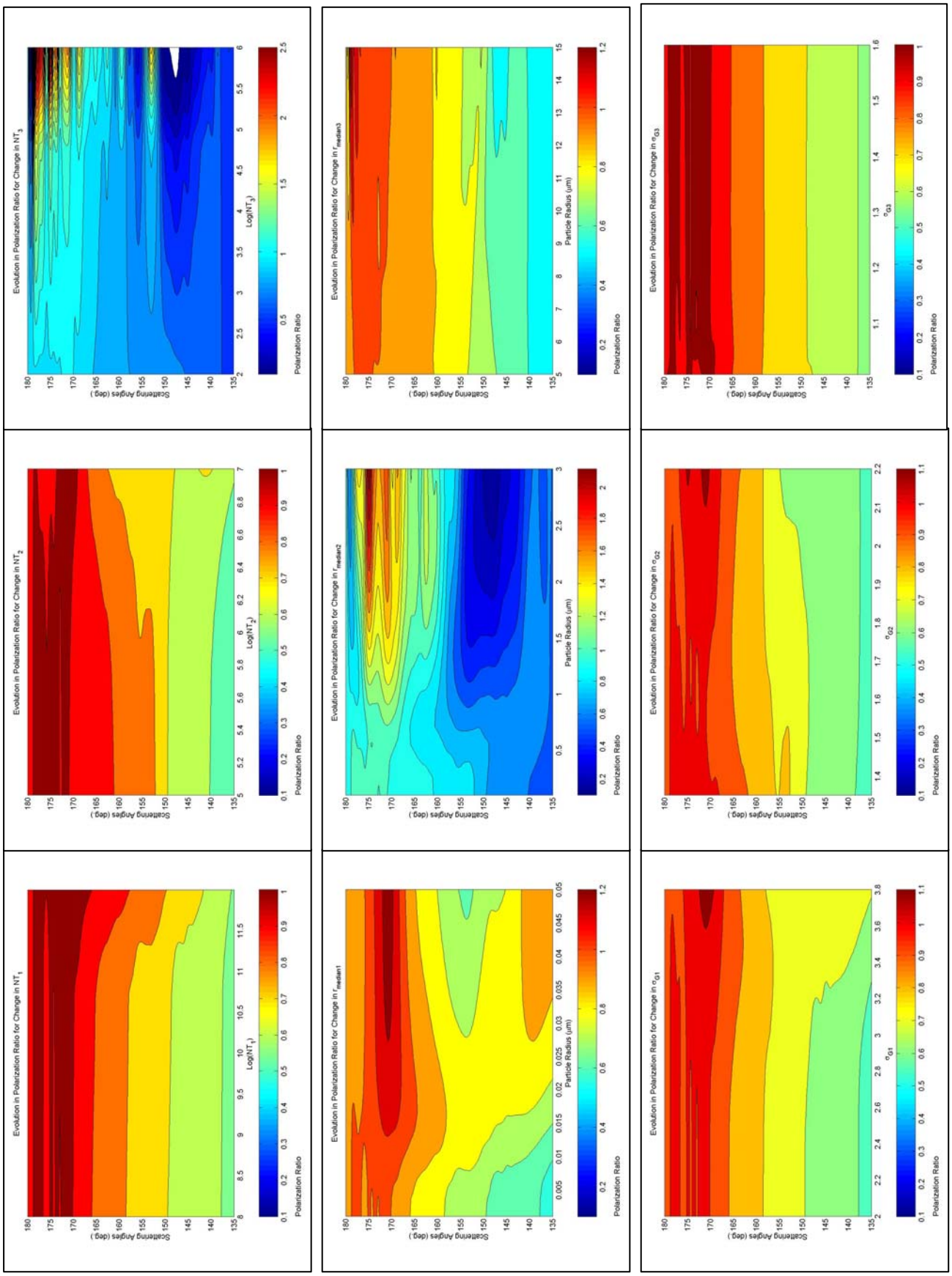


Figure 2-7: Evolution of polarization ratios at 532 nm as each of the nine parameters in the trimodal lognormal size distribution is varied. (Novitsky, 2002, Fig. 3-17).

Some important observations can be made from these plots that help shape the design of the inversion algorithm used in this work. These plots show that the 532 nm polarization ratio appears to be the quite sensitive to changes in the geometric mean radius of the accumulation mode, $r_{g,2}$, and the number density of the course mode, $N_{T,3}$. This dependence should be expected, when the physics of optical scattering from particles with diameters on the same order of size as the wavelength is considered; however, what is surprising is the apparent lack of sensitivity to the geometric mean radius of the course mode, $r_{g,3}$, and the number density of the accumulation mode, $N_{T,2}$. Additional simulations are performed to better understand the behavior of the polarization ratio in response to changing particle concentrations of each lognormal mode.

The concentrations used to scale the lognormal size distributions are only significant in their relation to the concentration of the modeled molecular scatterers, 2.54×10^{19} particles/cm^3 at STP. Analysis of Eqn. 2-13 reveals that the particle concentration, N_T, would cancel out of the mathematical equation for the polarization ratio if not for the addition of the molecular scattering intensity which is also within the integral. Because we know the molecular density (from pressure and temperature) and the Rayleigh scatter cross-section, we can calculate the range of particle concentrations that will produce discernable changes from the pure dipole contribution to the polarization ratio. The polarization ratio will only vary in a range of concentration values where the molecular scattering intensity is a sizable fraction of the total scattering intensity, but not dominating it. A set of four single lognormal size distributions, whose parameters are summarized in Table 2-3 and are plotted in Fig. 2-8, are used to explore the sensitivity of the modeled polarization ratio to particle number density. The simulations are performed using a complex refractive index of 1.38 + i0.

Table 2-3: Lognormal distributions used to investigate the effect of particle number density on the polarization ratio for a scattering wavelength of 407 nm.

	Geometric mean radius, r_g (μm)	Geometric standard deviation, σ_g	Concentration shown in Fig. 2-7 (#/cm^3)	Simulated concentration range (#/cm^3)	Unique concentration range (#/cm^3)
Lognormal #1	0.01	1.10	10^5	10^{-4} to 10^{10}	-
Lognormal #2	0.10	1.10	10^3	1 to 10^6	10^2 to 10^5
Lognormal #3	1.0	1.10	10	10^{-3} to 10^5	10^{-1} to 10^3
Lognormal #4	10	1.10	10^{-2}	10^{-5} to 10	10^{-4} to 10

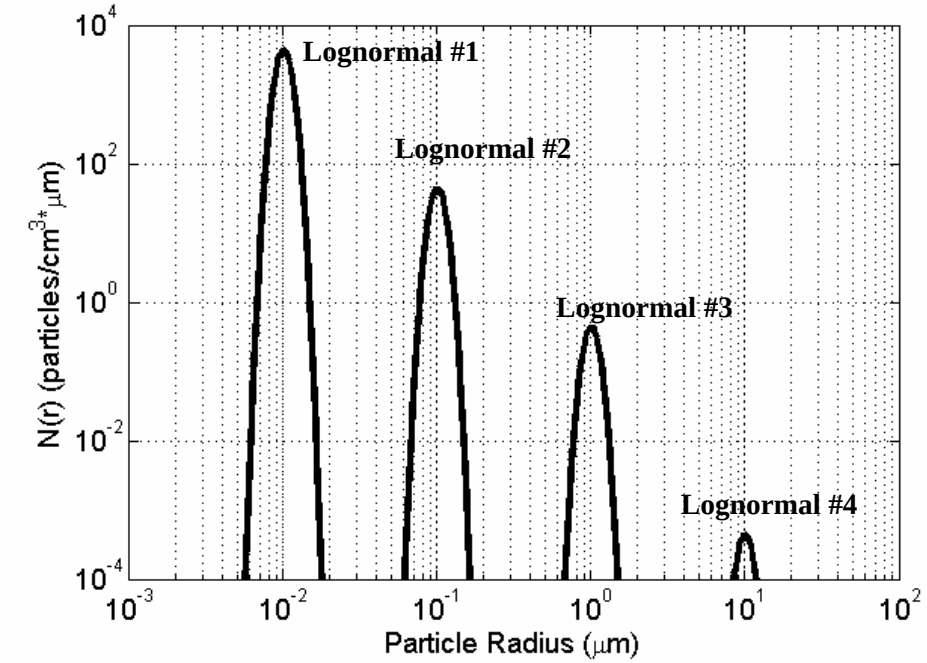


Figure 2-8: Lognormal size distributions used to explore the sensitivity of the model polarization ratio to particle number density. The parameters for each curve are summarized in Table 2-3.

The retrievable concentration range of the fine mode was examined first using a lognormal distribution with a mean particle diameter of 0.01 μm and $\sigma_g = 1.1$. The total concentration of the distribution, N_T, was varied from 10^{-4} particles/cm^3 to 10^{10} particles/cm^3 and combined with the scattering from the STP molecular density at the surface. The resulting

polarization ratio for a wavelength of 407 nm is shown in Fig. 2-9. Eight different polarization ratio curves are plotted in Fig. 2-9, corresponding to eight different fine-mode concentrations (plus the molecular density), but only one distinct curve can be seen. This is due to the fact that scattering from particles in this size range are dominated by the molecular scattering at 407 nm for all realistic atmospheric particle concentrations. This indicates that to retrieve accurate concentration information on particles less than several tens of nanometers, it is necessary to use a shorter wavelength than 407 nm. Fig. 2-10 shows the polarization ratio at 407 nm for a lognormal size distribution with a geometric mean radius of 0.1 μm and $\sigma_g = 1.1$. This figure shows that polarization ratios for particle concentrations less than 100 particles/cm^3 and greater than 100,000 particles/cm^3 are not unique, and thus accurately retrieving these concentrations is not possible. Likewise, examination of Figs. 2-11 and 2-12 show that the retrievable concentration range for a lognormal particle distribution with a mean radius of 1 μm and 10 μm is roughly 0.1 to 1000 particles/cm^3 and 0.001 to 10 particles/cm^3 respectively, when using the polarization ratio at 407 nm (532 nm and 650 nm produce similar concentration sensitivity results). The ranges are summarized in Table 2-3, and provide some insight into the range of accurate concentrations that can be obtained through the inversion process. The ranges obtained from these simulations pertain to four narrow lognormal size distributions and the obtained results should not be considered concrete ranges for all possible size distributions. The size range sensitive for concentration measurements can be changed or extended to both smaller and larger sizes by using wavelengths in the ultraviolet and infrared. The atmospheric window wavelengths between 300 nm and 30 μm will extend the ranges of particle sizes and the particle densities that can be measured. This study helps in visualizing the errors to be assigned to the results.

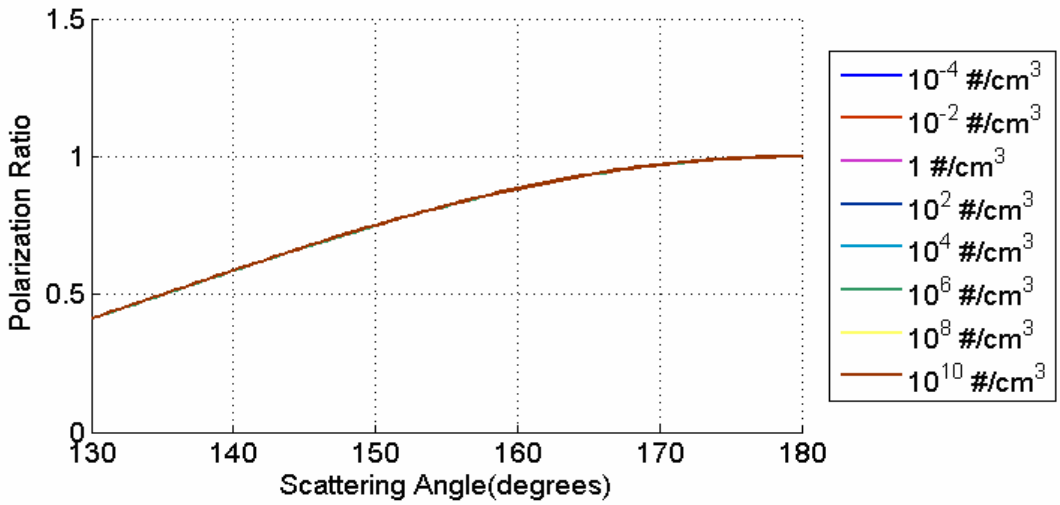


Figure 2-9: Polarization ratio for 407 nm as a function of total particle concentration, N_T (#/cm^3), for a lognormal particle size distribution #1, with r_g = 0.01 μm and σ_g = 1.1.

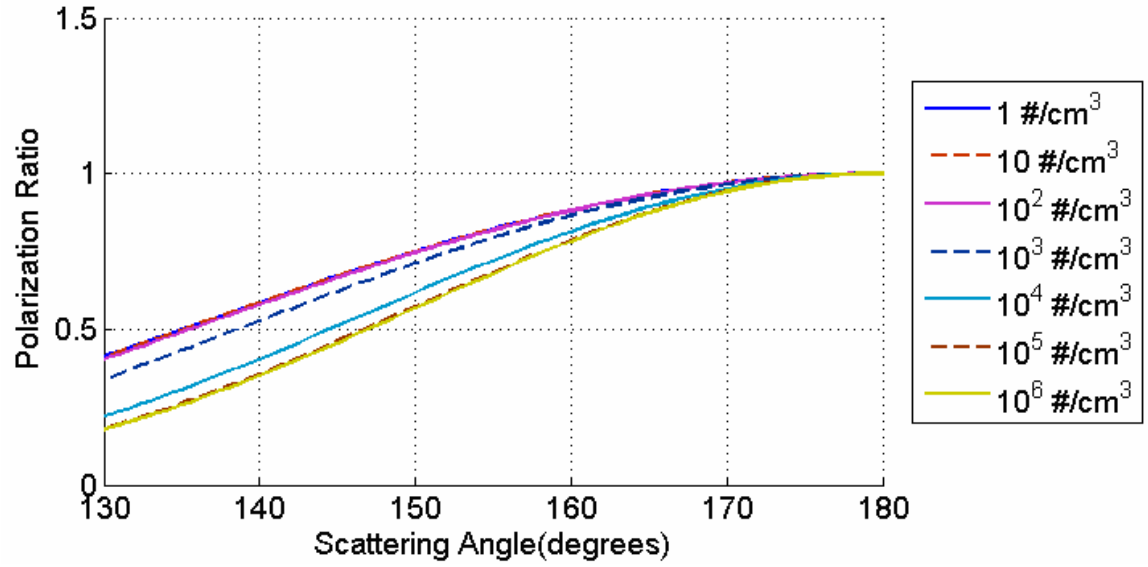


Figure 2-10: Polarization ratio for 407 nm as a function of total particle concentration, N_T (#/cm^3), for a lognormal particle size distribution #2, with r_g = 0.1 μm and σ_g = 1.1.

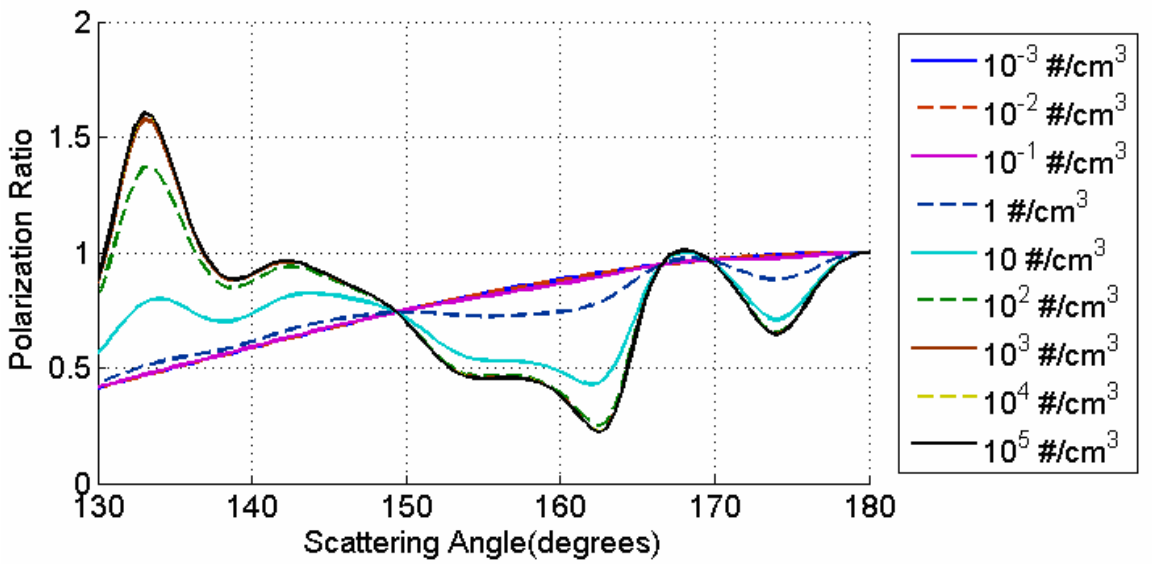


Figure 2-11: Polarization ratio for 407 nm as a function of total particle concentration, N_T (#/cm^3), for a lognormal particle size distribution #3, with r_g = 1.0 μm and σ_g = 1.1.

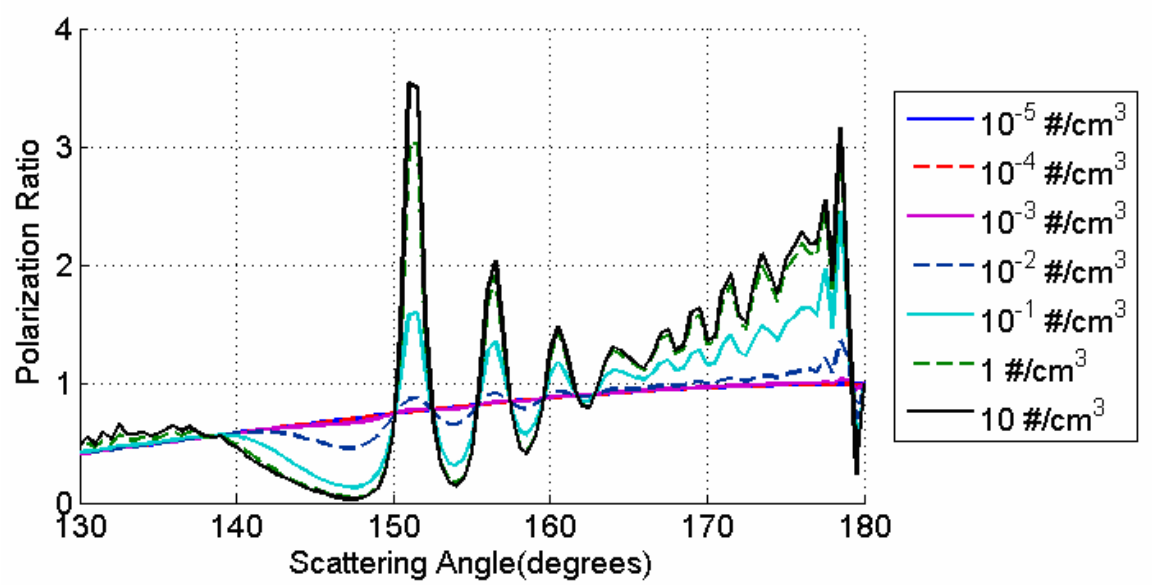


Figure 2-12: Polarization ratio for 407 nm as a function of total particle concentration, N_T (#/cm^3), for a lognormal particle size distribution #4, with r_g = 10 μm and σ_g = 1.1.

One goal of the present work is to determine complex refractive indices of aerosols as a function of wavelength from the polarization ratio. The feasibility of extracting the complex refractive information from the polarization ratio is first studied through simulation. Novitsky

performed simulations at a single wavelength to study the effect of the refractive index on the polarization ratio (Novitsky, 2002, pg. 95). The polarization ratio for the tri-modal lognormal size distribution shown in Fig. 2-13 was calculated at a wavelength of 532 nm using a real refractive index range from 1.33 to 1.8 in steps of 0.002 (the imaginary part of the refractive index was constant at zero). Figure 2-14 shows that a small change in the refractive index of the scattering volume results in a noticeable change in the polarization ratio, which supports the hypothesis that the real refractive index can be retrieved from the scattering measurements.

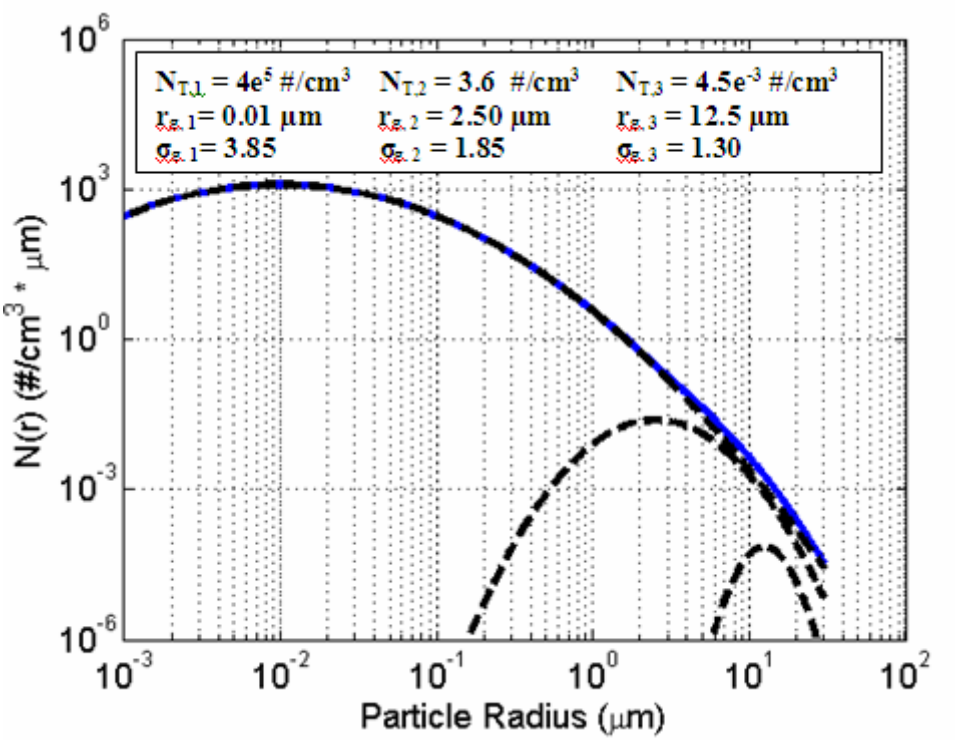


Figure 2-13: Trimodal lognormal distribution used to calculate polarization ratios in Fig. 2-14 and Fig. 2-15.

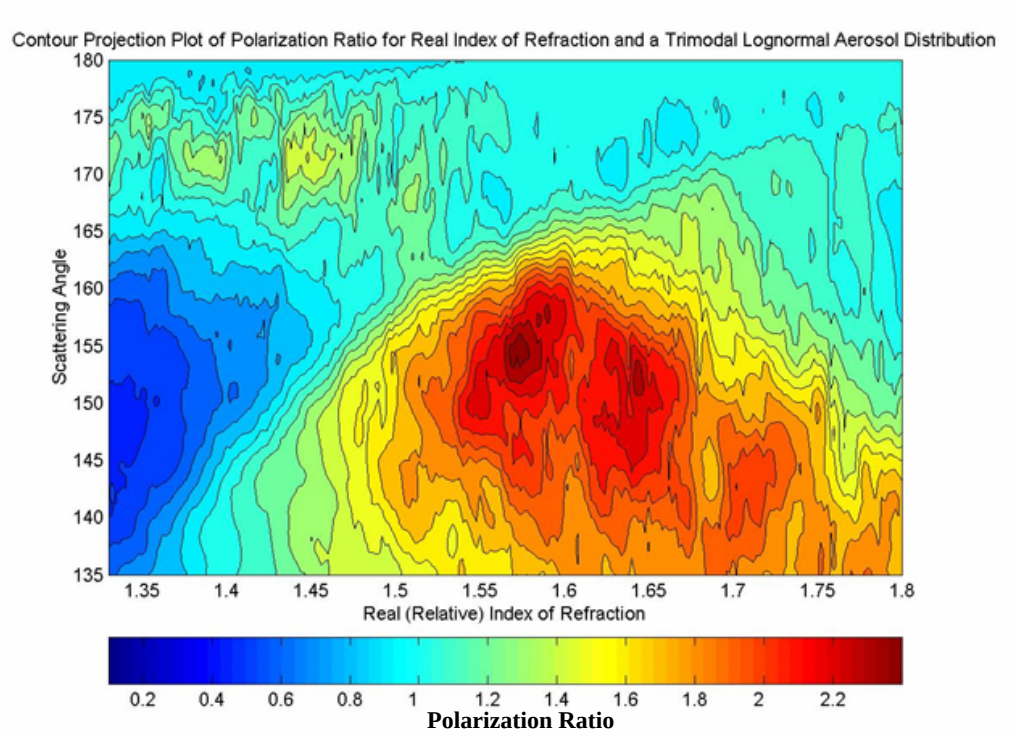


Figure 2-14: Polarization ratio at 532 nm as a function of real refractive index using the trimodal lognormal size distribution shown in Fig. 2-13 (Novitsky, 2002, Fig. 3-18).

Novitsky also considered the effect of the imaginary part of the refractive index and concluded that it should not be included in the inversion process (2002, pg. 88). Novitsky contended that the polarization ratio is indifferent to the imaginary part of the refractive index, which is true for a large range of index values. Figure 2-15 shows the polarization ratios for the trimodal lognormal size distribution shown in Fig. 2-13, a wavelength of 532 nm, and a fixed real refractive index of 1.47, as the imaginary part of the refractive index varies logarithmically from 10^{-10} to 1. For the range of 10^{-10} to 10^{-4}, the polarization ratios are unchanged, however; as n_{im} continues to increase the polarization ratio curves start changing, particularly in the backscattering directions. This is important to know, as some aerosols, such as carbon, do have high imaginary refractive indices. The oleic acid and fog oil, which we used in the EPA aerosol chamber tests, also have n_{im} values that fall within this range, and the polarization ratios are

altered by the imaginary part of the refractive index. This knowledge of the polarization ratio behavior in response to changing n_{im} values is used to restrict the inversion algorithm to imaginary refractive index values from 10^{-4} to 0.1. If a value of 10^{-4} is retrieved by the algorithm, it is noted that the imaginary part of the refractive index is a value equal to or less than the retrieved index.

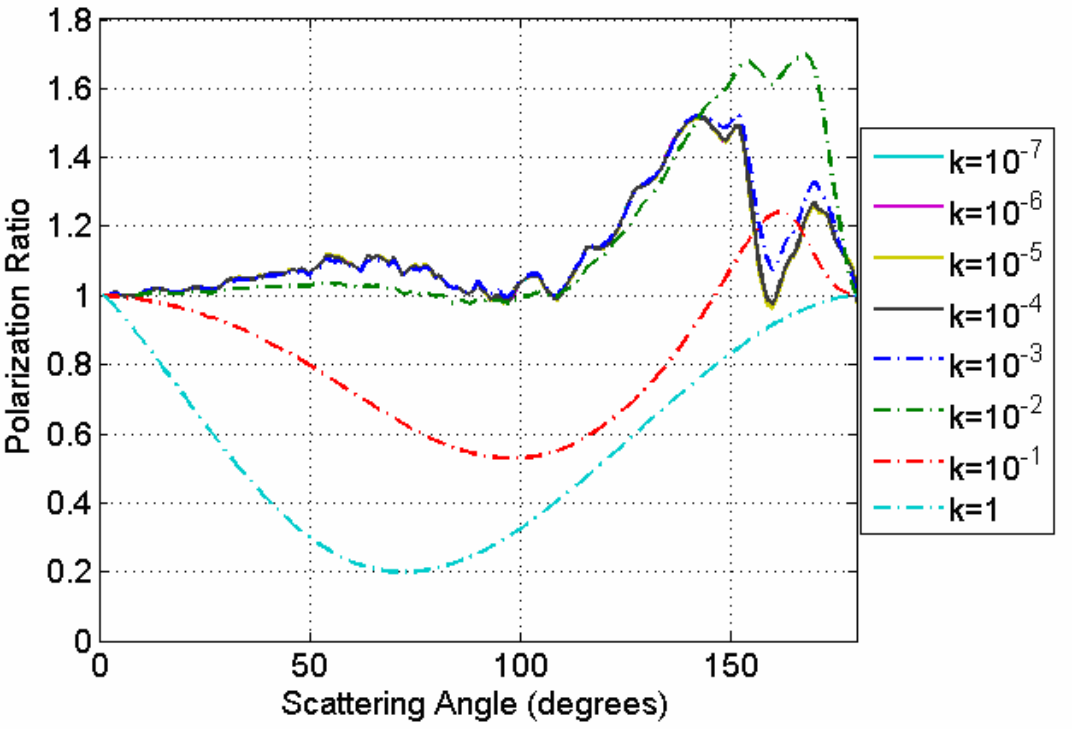


Figure 2-15: Polarization ratio change for change in imaginary part of refractive index. Ratios are calculated using trimodal size distribution shown in Fig. 2-13, a wavelength of 532nm, and n_{re}=1.47.

Chapter 3

Inversion

Retrieving aerosol characteristics from scattering measurements requires a method of mapping the measured data to the desired aerosol characteristics. This 'mapping' method can then be used to 'invert' the data, i.e. use light scattering measurements to determine characteristics about the aerosols that scattered the light. The 'mapping' is generally referred to as the forward model, and the retrieval of the aerosol characteristics from the measurements is called the inversion process. While it is relatively straight forward to select the 'best' forward model for a given application, it is a bit more ambiguous to select the 'best' inversion algorithm. Dubovik and King (2000) explained it well:

> "…forward models differ mainly in the accuracy of describing a physical phenomenon and the speed of calculation. Correspondingly, for practical applications, one always chooses the most accurate model provided it satisfies the time standards. Choosing the best inversion method, on the other hand, is a more complicated task, in that the evaluation of inversion accuracy is an ambiguous question, especially for a case of the simultaneous retrieval of several variables. For example, replacing a scalar model of light scattering by a model accounting for polarization, results in doubtless improvement in the accuracy of describing any characteristic of scattered light. In contrast, retrieval errors are not so well correlated for different retrieved parameters. Due to a change of inversion methods the retrieval accuracy may improve for one parameter but degrade for another parameter. Correspondingly, the preference between inversion methods is always rather uncertain."

The inversion algorithm can only be as good as the accuracy of the measurements and the forward model. Theoretically, the best possible inversion would retrieve a model that creates an error of zero between the modeled and measured data. This can only be done if the forward model exactly matches the conditions of the measurements, and the errors and noise in the data are understood and quantified. The best inversion algorithm that can practically be applied to

measured data, takes into account the accuracy, and noise of the measured data. The 'best' inversion algorithm would then minimize the error to within the error bars of the measured data.

Mie scatter analysis can be used to accurately describe the angular scattering intensity of collimated light from a volume of spherical particles provided that the scattering volume is optically thin, that is particles are widely spaced and single, independent scattering processes dominate. Applying Mie scattering equations to spherical aerosols has been well studied and is known to the aerosol community as a feasible approach for describing many atmospheric aerosols, specifically fogs, clouds, and other water-based aerosols. For these reasons, and the general speed of the calculations, the Mie scattering equations are used to calculate the forward model. The ensemble-averaged angular scattered intensity, $I(\theta)$, is expressed as a Fredholm integral of the first kind:

$$I(\theta) = N\int i(\theta, \alpha, m')f(r)dr \qquad (3\text{-}1)$$

where N is the number of particles, $f(r)$ is the particle size distribution function, r is the particle radius, $\alpha=2\pi r/\lambda$ is the size parameter, λ is the wavelength of the incident light, m' is the complex refractive index of the particle relative to the surrounding media, and $i(\theta, \alpha, m')$ is the intensity of the scattered light of a single spherical particle. Due to the oscillatory nature of the Mie scattering intensity $i(\theta, \alpha, m')$, the solution to Eqn. 3-1 lacks uniqueness, and is an ill-posed problem. Many techniques have been used over the years to invert particle size distributions from scattering data, and these have been reviewed in Chapter 1. Recently, stochastic search techniques have entered the scene as promising alternatives to the linear search methods (Ye, 1999; Lignon, 1998). A genetic algorithm was used by Ye, *et al*. (1999) to invert particle size distributions from simulated angular scattering data with promising results. Genetic algorithms offer many advantages over traditional numerical optimization techniques including the ability to use both continuous and discrete parameters, search across a wide sampling of the solution space,

and handle a large number of variables. Derivative information of the performance surface is not needed, which eliminates many of the difficulties associated with traditional gradient-based algorithms. For these reasons, and the overall simplicity to both understand and implement, a genetic algorithm is selected as the inversion algorithm of choice for these investigations.

3.1 Genetic Algorithm Terminology

Genetic algorithms (GA) are modeled after the processes of evolution and genetic recombination so the building blocks of the algorithms are named after genetic elements. *Genes* are the binary encoding of each problem variable, and all of the genes are referred to as a *chromosome*. A set of chromosomes is called a *population*. Each chromosome in a population has a *fitness* associated with it that is calculated through a *fitness function*. The chromosomes in each population are ranked from best to worst based on their fitness. The higher ranked chromosomes are *mated* to produce a new population that exhibits characteristics of the better individuals from the previous generation. *Mutation* is allowed to occur at a small probability. This process repeats until either a desired fitness has been achieved or a set number of generations have occurred. A simple GA has the following steps:

1. Generate an initial random population of chromosomes.
2. Evaluate the fitness of each population member.
3. Rank the individuals based on fitness.
4. Generate offspring by mating good individuals.
5. Mutate selected members of the offspring.
6. Terminate if conditions have been met or continue back to step 2.

The flow chart of a basic genetic algorithm just described is shown in Fig. 3-1.

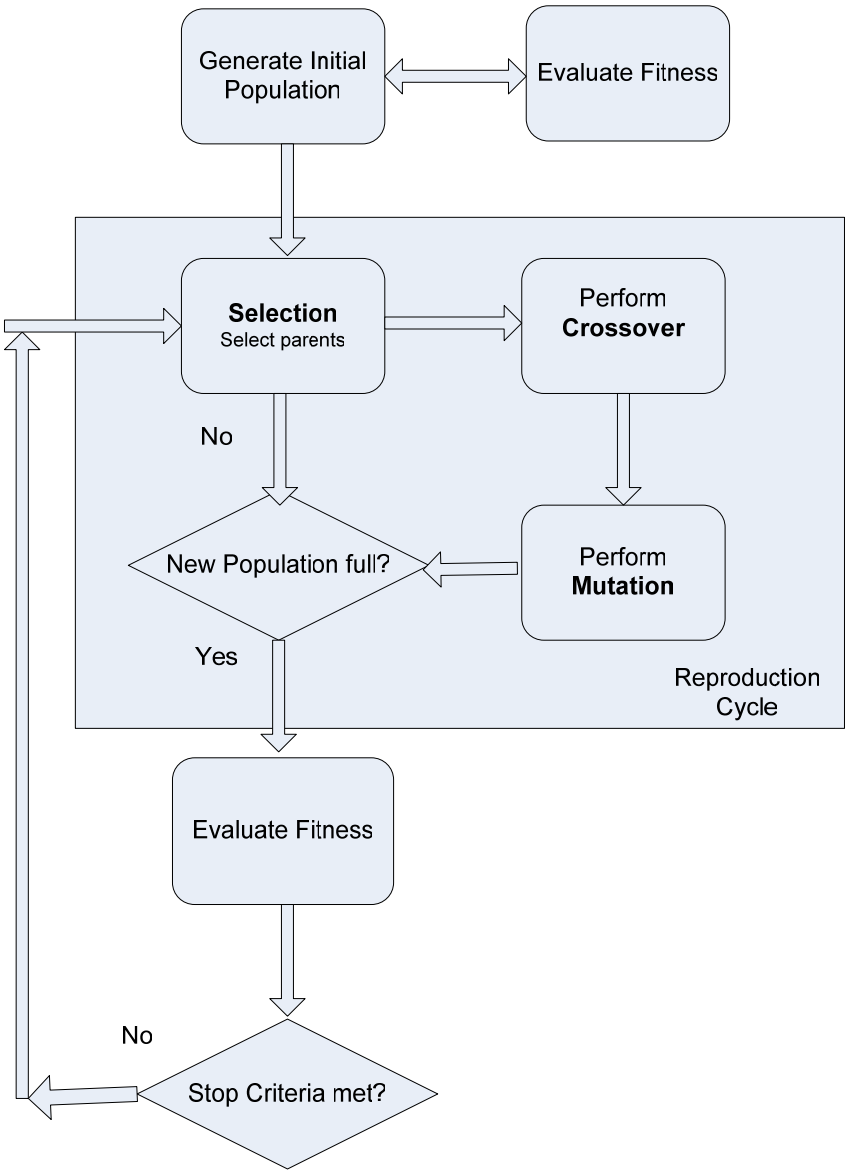


Figure 3-1: Example of a flow chart for simple genetic algorithm.

3.2 Simple GA Inversion using Polarization Ratio

3.2.1 Binary coding

Atmospheric aerosol size distributions are commonly modeled as lognormal distributions or a combination of lognormal distributions as described in Chapter 2. Lognormal size distributions are fully characterized using three parameters, the total particle concentration (N_T), the geometric mean particle radius (r_g), and the geometric standard deviation (σ_g).

In the genetic algorithm, the concentration, geometric mean and the geometric standard deviation of the lognormal distributions are represented as a binary string of zeros and ones. The binary string is translated to a physical quantity using the generalized formula,

$$n' = n * n'_{res} + n'_{\min} \tag{3-2}$$

where *n'* is either the concentration, the geometric mean particle radius or the geometric standard deviation. The value of *n* is the decimal equivalent of the binary string, n'_{res} is the resolution of the variables, and n'_{min} is the minimum decimal value that the variable is allowed to assume. Selecting the correct range and resolution for the size distribution variables is essential to the success of the inversion algorithm. If the resolution is too course, the algorithm may never find an optimal answer and if the resolution is too fine the algorithm may take too long to search the solution space. The radii used to calculate the theoretical polarization ratio is limited to the range of 1 nm to 30 μm (see Chapter 2), so the inversion algorithm should not search for a geometric mean radius outside this range.

3.2.2 Fitness

The fitness function is the most important part of a genetic algorithm, as it is the part of the algorithm that forms the connection to the physical problem being optimized. The success of the algorithm is dependent on how well the fitness function evaluates each solution in relation to the overall objectives of the optimization problem. The measured polarization ratio, which will be used as the principle data for the aerosol characterization, is formed by dividing the received scattering intensity from parallel polarized incident light by the received scattering intensity from perpendicular polarized incident light.

As discussed in Chapter 2, the theoretical polarization ratio used in the genetic algorithm as the measure of each size distributions' fitness is calculated using the following equation,

$$PR(\theta,\lambda)=\frac{\sum_{i=r\min}^{r\max} w_i\cdot|S_2|^2}{\sum_{i=r\min}^{r\max} w_i\cdot|S_1|^2}=\frac{I_{\parallel}(\theta,\lambda)}{I_{\perp}(\theta,\lambda)}, \tag{3-3}$$

where w_i are the weights for each particle radius, r_i, determined by the particle size distribution generated by the genetic algorithm, and S_1 and S_2 are the amplitude scattering coefficients described in Chapter 2. The calculation of the total scattering intensity for parallel or perpendicular polarized incident light is shown below, and the point-by-point division of the two calculated intensities forms the model polarization ratio, PR(θ, λ).

$$\begin{bmatrix} I_{\theta_{\min}} \\ . \\ . \\ I_{\theta_{\max}} \end{bmatrix}^{s} = \begin{bmatrix} i(a_{\min})_{\theta_{\min}} & . & . & i(a_{\max})_{\theta_{\min}} \\ . & . & & . \\ . & & . & . \\ i(a_{\min})_{\theta_{\max}} & & & i(a_{\max})_{\theta_{\max}} \end{bmatrix} \begin{bmatrix} N(a_{\min}) \\ . \\ . \\ N(a_{\max}) \end{bmatrix} + \begin{bmatrix} I_{\theta_{\min}} \\ . \\ . \\ I_{\theta_{\max}} \end{bmatrix}^{molecular}$$

The squared error between the measured polarization ratios and the polarization ratios calculated using Mie theory will be used as the measure of each generated size distributions' fitness, *F*,

$$F = \sum_{k=1}^{M}\left(\sum_{j=1}^{N}\left(PR\left(\theta_j,\lambda_k\right) - \frac{I_{\parallel}\left(\theta_j,\lambda_k\right)}{I_{\perp}\left(\theta_j,\lambda_k\right)}\right)^2\right). \tag{3-4}$$

3.2.3 Selection, crossover, and mutation

Stochastic universal sampling (Baker, 1987) and sigma scaling (Goldberg, 1991) were implemented in the algorithm. This fitness-proportionate selection method gives every individual a chance of being selected, while still ensuring that fitter candidates are more likely to be chosen than weaker individuals. The individuals are mapped to a wheel, such that each individual's segment is proportional in size to its fitness. A single random spin of the roulette wheel determines the first selected individual. The selection process then proceeds by advancing all the way around the wheel in equal sized steps, where the step size is determined by the number of individuals to be selected. Selection pressure is the probability of the best individual being selected compared to the average probability of selection of all individuals. Sigma scaling attempts to moderate selection pressure over time so that it is not too strong in early generations and not too weak once the population has stabilized and fitness differences are smaller. The standard deviation of the population fitness is used to scale the fitness values so that the selection pressure is relatively constant over the lifetime of the evolutionary program.

Uniform crossover was used to generate two new offspring from two selected individuals by exchanging a random number of bits. Uniform crossover is accomplished through the use of a randomly generated mask that contains the same number of binary bits as the parent

chromosomes. The numbers in the mask indicate whether the bit from parent one or parent two should be translated to each child. For example, if the two chromosomes of the parents are '1 1 1 1 1 1' and '0 0 0 0 0 0', and the uniform crossover mask is '0 0 0 1 0 1' then the two offspring will be '1 1 1 0 1 0' and '0 0 0 1 0 1'. Mutation is a random flipping of a bit after crossover has occurred. It is used to prevent premature convergence to a local minimum.

3.2.4 The polarization ratio model

The run-time of the inversion algorithm is drastically reduced by using pre-calculated look-up tables of the unit scattering intensity kernels, $i_{\parallel}$ and $i_{\perp}$. The look-up tables of unit scattering intensities, *i*, used within the model are functions of the polarization of the incident light, and the real and imaginary refractive index of the scattering particle. The size of the table is dependent on the resolution and range of the particle radii and the resolution of the scattering angles. A finer resolution of particle radii (i.e. more particle radii used in the calculation) will increase the accuracy of the polarization ratio calculation and a finer resolution of scattering angles will theoretically improve the fit between the measured and modeled polarization ratios by increasing the number of points to minimize the mean squared error between them. Increasing the resolution of the particle radii and/or the scattering angle resolution improves the inversion, but at the expense of longer computation times.

The range of radii to include in the model was determined by considering the residency time of particles in the atmosphere, and the limitations of differentiation for visible-wavelength optical scattering from small particles. The upper radii limit of 30 μm (or 60 μm diameter) was selected based on arguments presented by Novitsky (2002, pg. 110) and include consideration of the settling time of large particles, and the time scale of the multistatic scattering measurements. Particles larger than 30 μm will fall out of the field of view of the multistatic detectors faster than

the data is typically collected. The lower limit of the range was selected based on the condition for Rayleigh scattering, $\frac{m \cdot 2\pi \cdot r}{\lambda} < 0.05$. Using the shortest wavelength of 407 nm and the highest reasonable refractive index of 1.8, the radii of a particle must be less than 2 nm to be modeled as Rayleigh scattering. Particles with radii below 2 nm will have essentially identical polarization ratios (that of a dipole scatterer) and it will be impossible to differentiate between particle sizes based on the polarization ratio.

Simulations were performed to determine the radii and scattering angle resolution that is required within the model to produce accurate polarization ratios, while minimizing computation time. Two different size distributions representative of those we expect during our measurements were examined, and these are summarized in Table 3-1. The first size distribution is a single lognormal distribution of submicron particles, similar to the size distribution expected from the aerosols produced by a commercial fog generator. The second distribution is a trimodal lognormal size distribution that was retrieved from coastal aerosol scattering measurements by Stevens (1996, pg. 124) using the multistatic technique at the single wavelength of 532 nm. Figure 3-2 shows the two size distributions used in the following calculations to determine the necessary number of particle sizes and scattering angles to include in the polarization ratio models.

Table 3-1: Summary of aerosol size distributions selected for algorithm tests.

$n_{re} + in_{im}$	r_{g1} (μm)	σ_{g1}	N_{T1} (#/cm^3)	r_{g2} (μm)	σ_{g2}	N_{T2} (#/cm^3)	r_{g3} (μm)	σ_{g3}	N_{T3} (#/cm^3)
1.33 + i0	0.30	1.75	1,000	-	-	-	-	-	-
1.38 + i0	0.0025	3.98	56,610	0.237	1.38	700	8.91	1.01	0.0101

The polarization ratios expected for wavelengths of 407 nm, 532 nm, and 650 nm for the first case of the single lognormal distribution are shown in Figs. 3-3 and 3-4, and show the dependence as a function of the number of particle sizes used in the calculations. Figure 3-3

shows the polarization ratios computed for a different number of samples that are logarithmically spaced radii, while Fig. 3-4 shows the polarization ratios computed for a different number of samples that are linearly-spaced radii. Examination of Figs. 3-3 and 3-4 show that the polarization ratio calculation has basically converged when using 500 to 750 logarithmically-spaced particles sizes or when using about 1,500 linearly-spaced particle sizes. The logarithmically-spaced calculation converges quicker in this case of a single lognormal distribution of small particles, because the logarithmic scale concentrates the sampled particle radii at the smaller particle sizes where the distribution is centered. The linearly-spaced radii are equally spread across the whole range from 1 nm to 30 μm, so it takes more linearly-spaced points to adequately sample this lognormal size distribution.

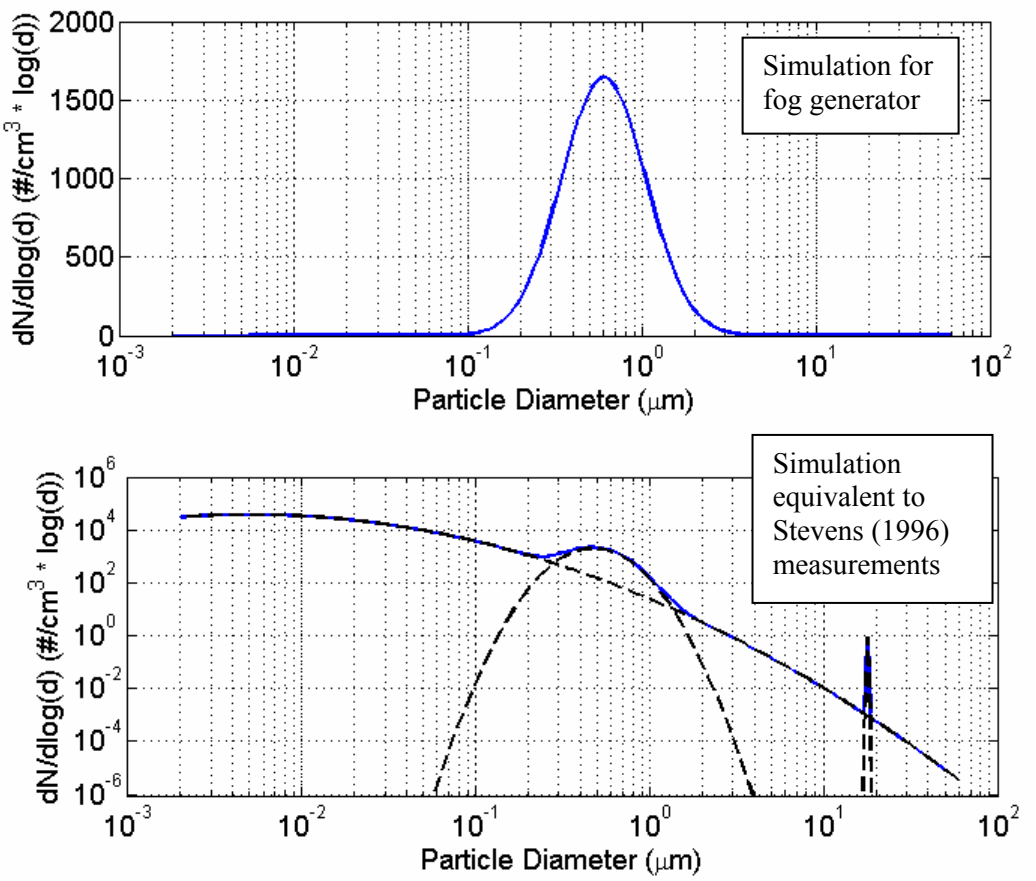


Figure 3-2: Size distributions used to determine the number of particle sizes to include in the model polarization ratio calculations, see Table 3-1.

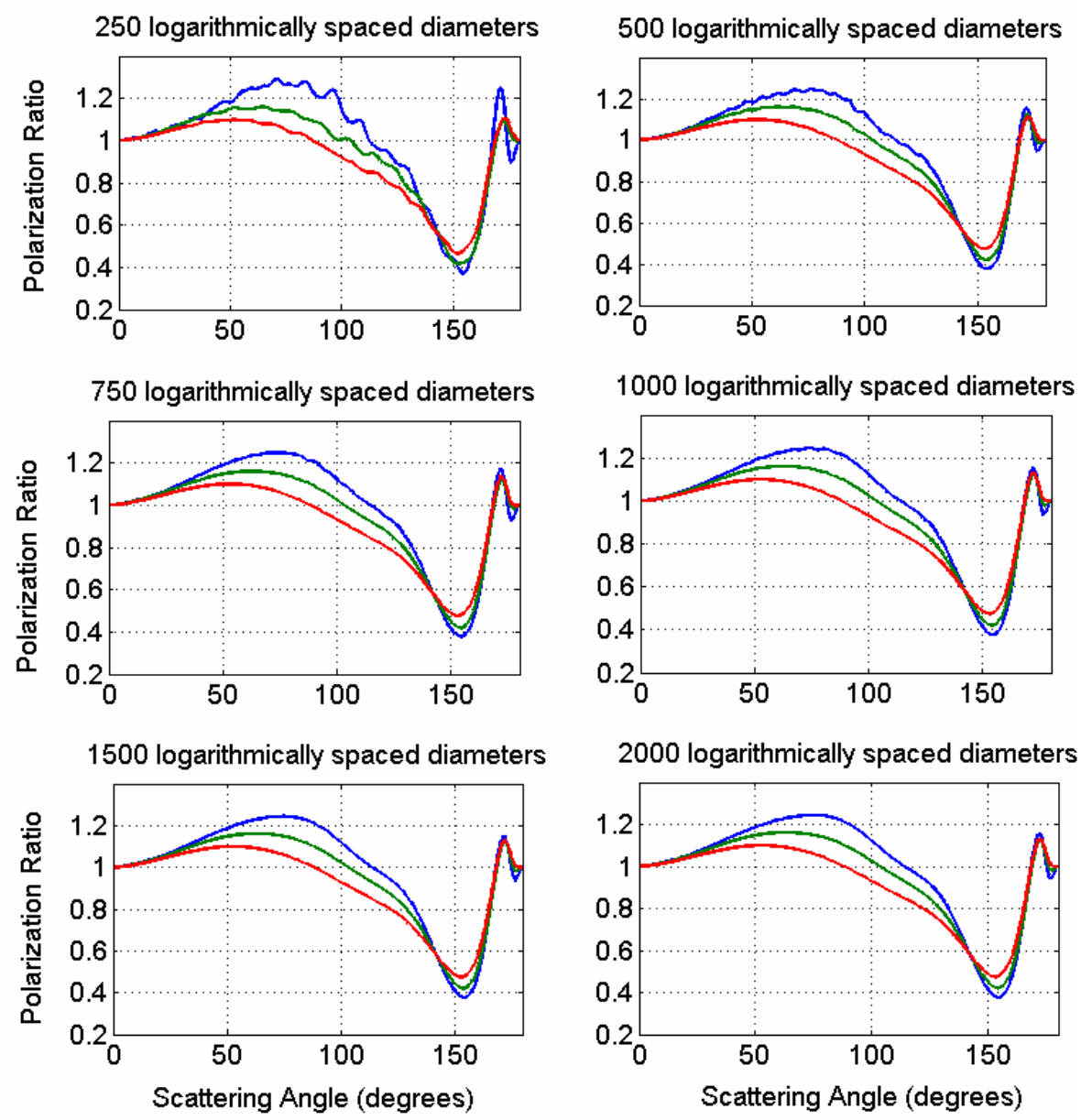


Figure 3-3: Polarization ratios calculated for the first case of a single lognormal size distribution from Table 3-1 as a function of the number of logarithmically-spaced particle radii between 1nm and 30 μm used in the calculations.

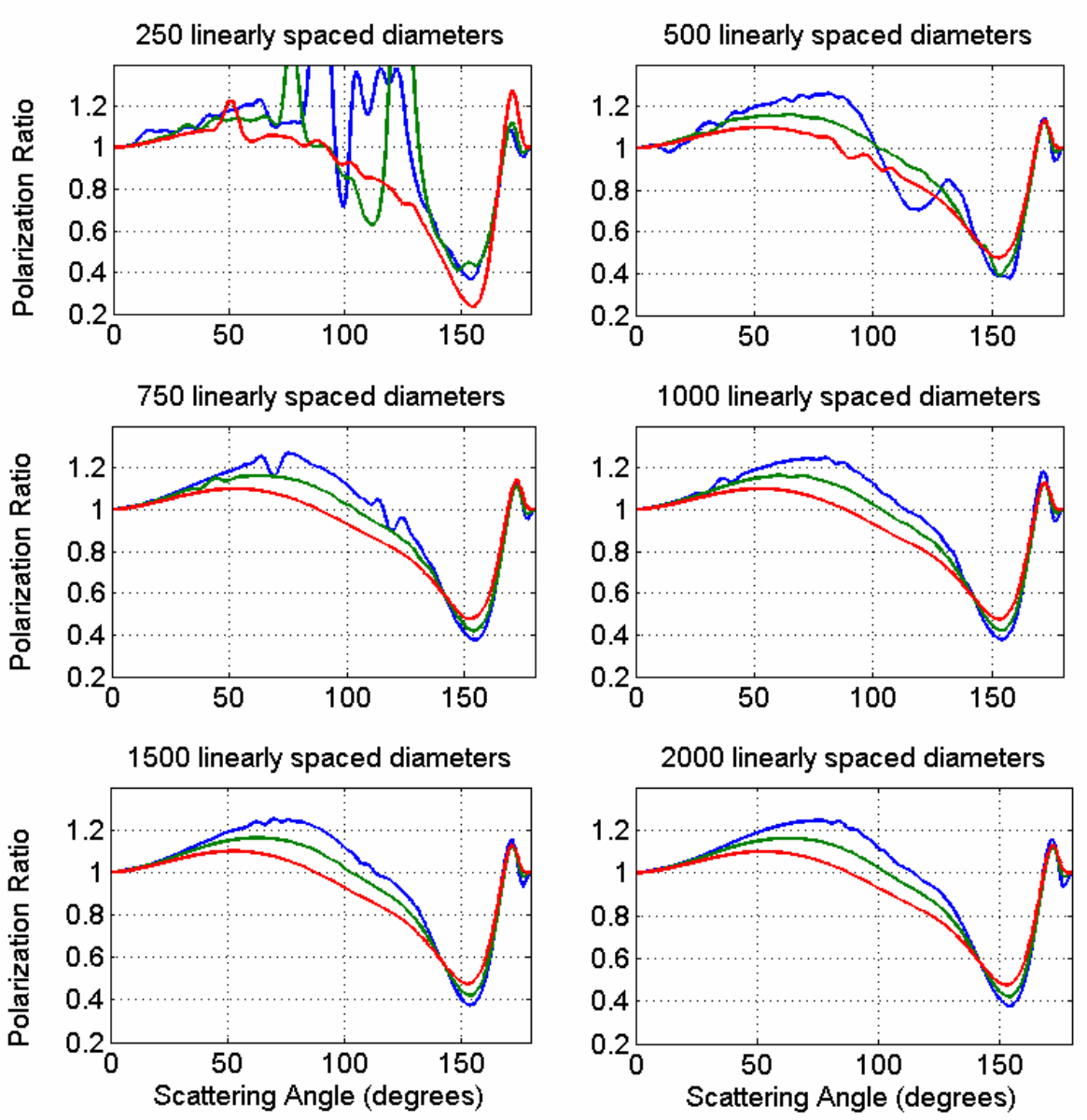


Figure 3-4: Polarization ratios calculated for the first case of a single lognormal size distribution from Table 3-1 as a function of the number of linearly-spaced particle radii between 1nm and 30 μm used in the calculations.

Polarization ratios at 407 nm, 532 nm, and 650 nm are calculated for the second case of the trimodal lognormal size distribution in Fig. 3-2b using different resolutions of particle sizes to determine the necessary number of particle size to include in the polarization ratio inversion model. The resulting polarization ratios are shown in Figs. 3-5 and 3-6. The fine structure of

peaks and troughs in the scattering angle range between 130 and 180 degrees changes significantly as the resolution varies. This structure is caused by combining several highly structured phase functions created by the scattering from large particles of similar sizes. This pattern converges when the course mode lognormal distribution is adequately sampled so that the rippled pattern stabilizes. It appears to stabilize for approximately 1,000 logarithmically-spaced or 750 linearly-spaced particle sizes. Figures 2-3 though 2-6 show that the results from using 1,000 logarithmically-spaced or 1,000 linearly-spaced particle sizes should be adequate to reach convergence in the model polarization ratio calculation of the single and trimodal lognormal size distributions. The two cases examined should be representative of the aerosol size distributions that will be encountered during the multiwavelength-multistatic measurements. The polarization ratios do not vary widely with changing concentration of smaller particles (see Figs. 2-7 and 2-8), but do change significantly with small changes in the concentration of large particles (see Fig. 2-10). This knowledge is used in combination with the previous four figures to select the resolution of particle sizes to use within the polarization ratio model. The polarization ratio model is implemented using 1,000 linearly-spaced particle sizes in order to equally represent all particle sizes, and not concentrate the particle sizes used in the calculation in the smaller particle range where the polarization ratio does not change significantly with changing radius or concentration.

The scattering angle resolution to use within the model is determined by examining the polarization ratio calculated for the trimodal lognormal size distribution using 1,000 linearly spaced particle sizes. The polarization ratios are calculated at one degree, half degree, quarter degree, and eighth degree, intervals between the angles of 130 and 180 degrees and are displayed in Fig. 3-7. Examination of Fig. 3-7 reveals that no extra information is added to the polarization ratio beyond a resolution of half-degree scattering angle steps. Half-degree steps are selected to use within the model to minimize the number of calculation points and thus maximize the speed of the model calculation.

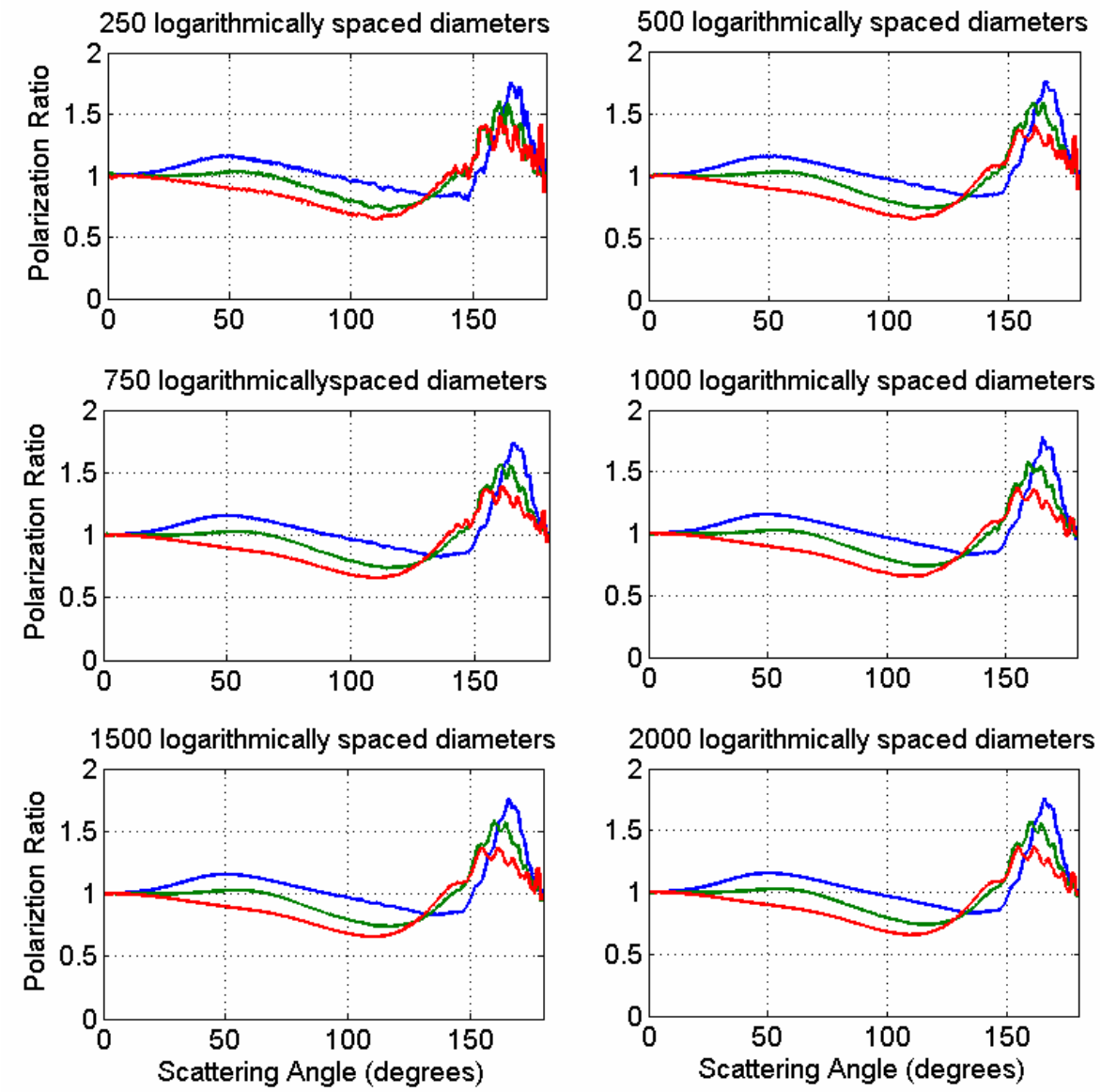


Figure 3-5: Polarization ratios calculated for the second case of the trimodal lognormal size distribution from Table 3-1 as a function of the number of logarithmically-spaced particle radii between 1nm and 30 μm used in the calculations.

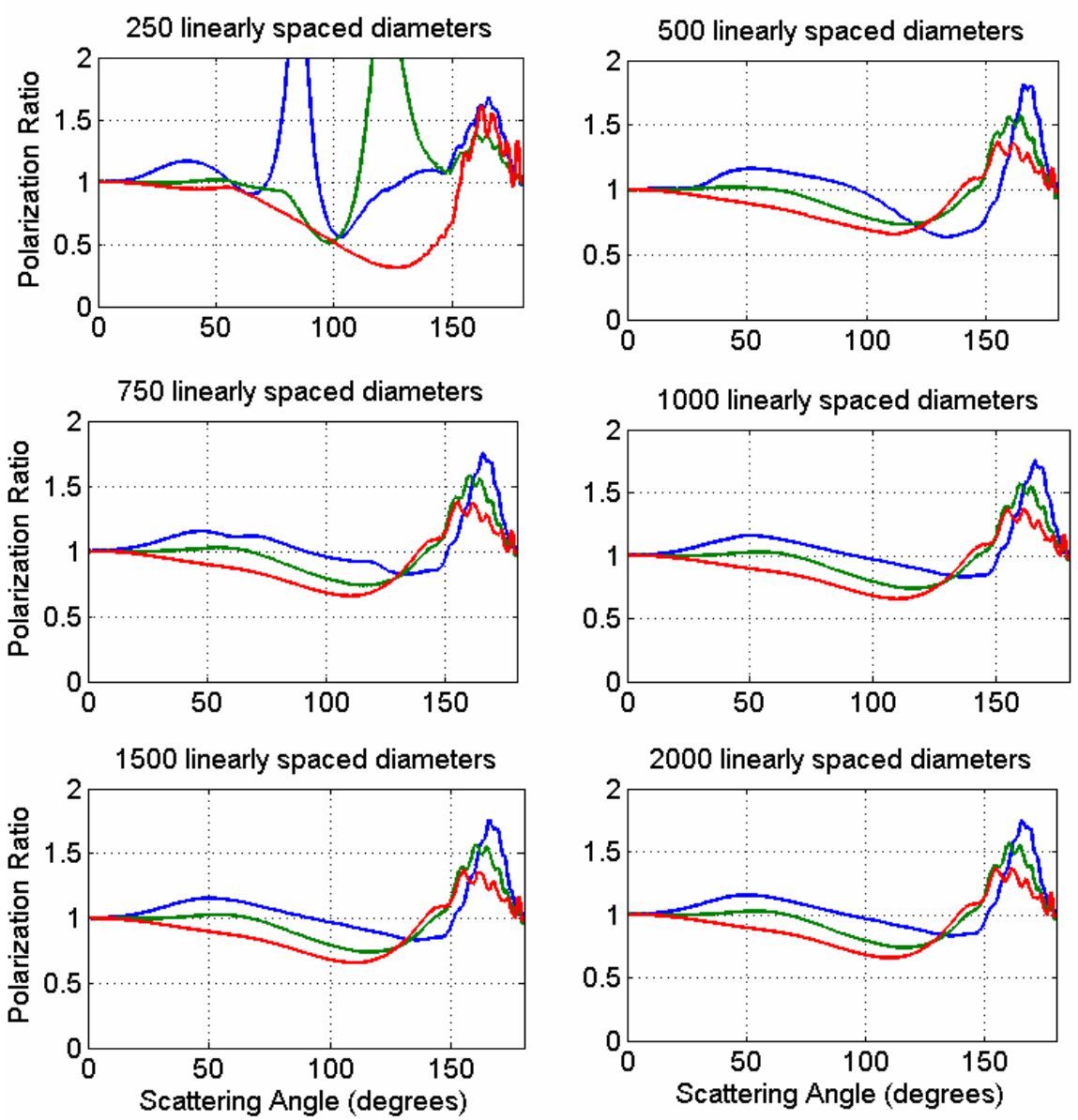


Figure 3-6: Polarization ratios calculated for the second case of the trimodal lognormal size distribution from Table 3-1 as a function of the number of linearly-spaced particle radii between 1nm and 30 μm used in the calculations.

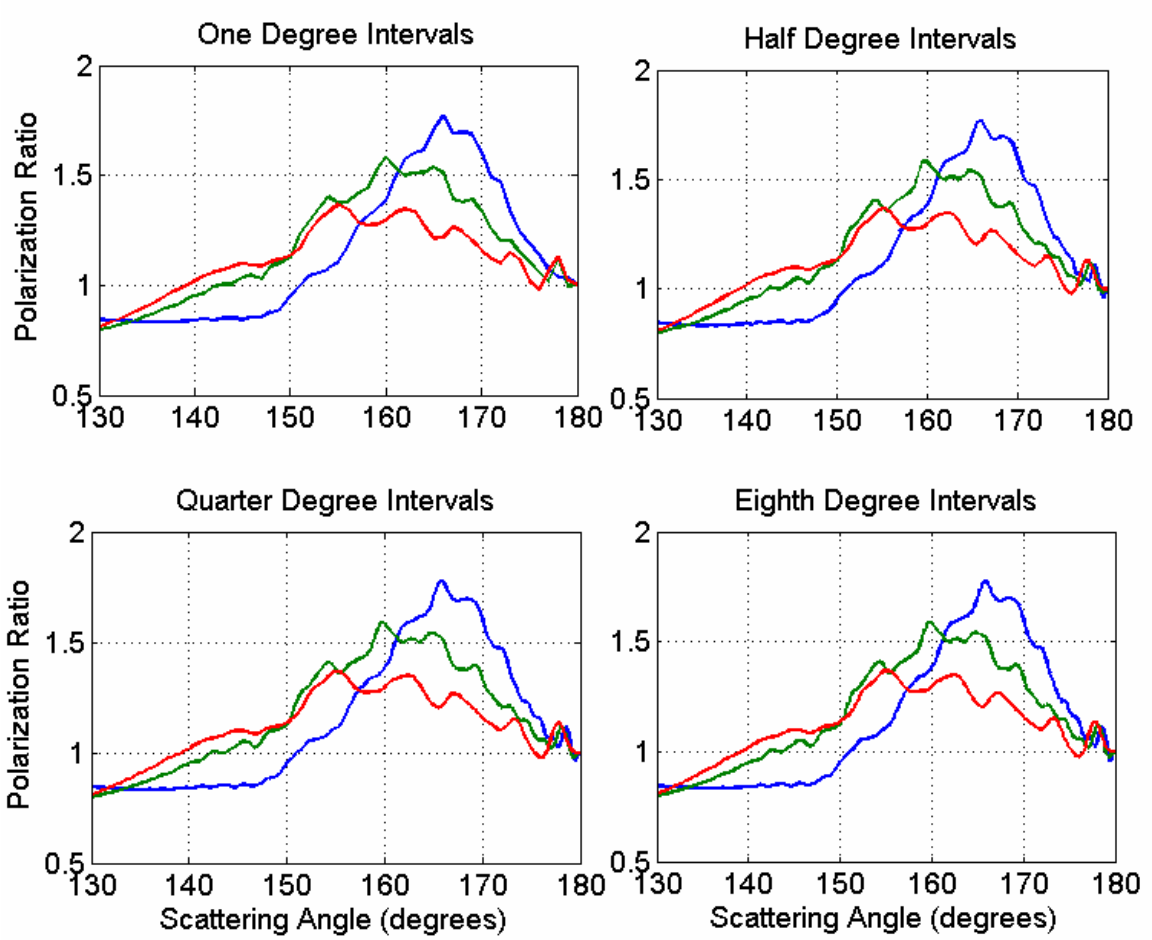


Figure 3-7: Polarization ratios calculated for trimodal lognormal size distribution from Table 3-1 as a function of scattering angle resolution using 1000 linearly-spaced particle radii.

3.2.5 Single lognormal with fixed refractive index

The design and testing of the algorithm progressed in steps. The first task was to determine if the genetic algorithm could invert the concentration, geometric mean and geometric standard deviation of a lognormal particle size distribution from simulated polarization ratio data. A lognormal size distribution with a concentration of 1,000 particles/cm^3, a mean radius of 0.75 μm, and a geometric standard deviation of 1.5 was used in the model to test the algorithm. The resulting polarization ratios, calculated using 1000 linearly spaced radii from 1 nm to 30 μm, and a refractive index of 1.35 + i0, are shown in Fig. 3-8. Figure 3-8a are the calculated polarization

ratios and 3-8b are the calculated ratios combined with additive white Gaussian noise to provide a signal to noise ratio (SNR) of 25. The noisy polarization ratios are used as the 'measured' data to test the inversion algorithm. This signal-to-noise was selected through visual inspection of the polarization ratios curves. It was desired that the inversion algorithm be tested with a high level of noise, but still be able to pull out the original signal. Increasing levels of noise were added to calculated polarization ratios curves until the average shape of the resulting 'noisy' polarization ratios started to deviate from the 'clean' signal.

An 11 bit binary number is used within the genetic algorithm to represent the geometric mean radius with a minimum radius value of 0.01 microns and a resolution of 0.01 microns. Utilizing all 11 bits of the binary number allows the mean radius to assume a maximum radius value of 20.48 microns (see Eqn. 3-2). The geometric standard deviation was represented by a nine bit binary number with a minimum value of 1.01, a resolution of 0.01, and a utilization of all nine bits allows a maximum value of 6.12.

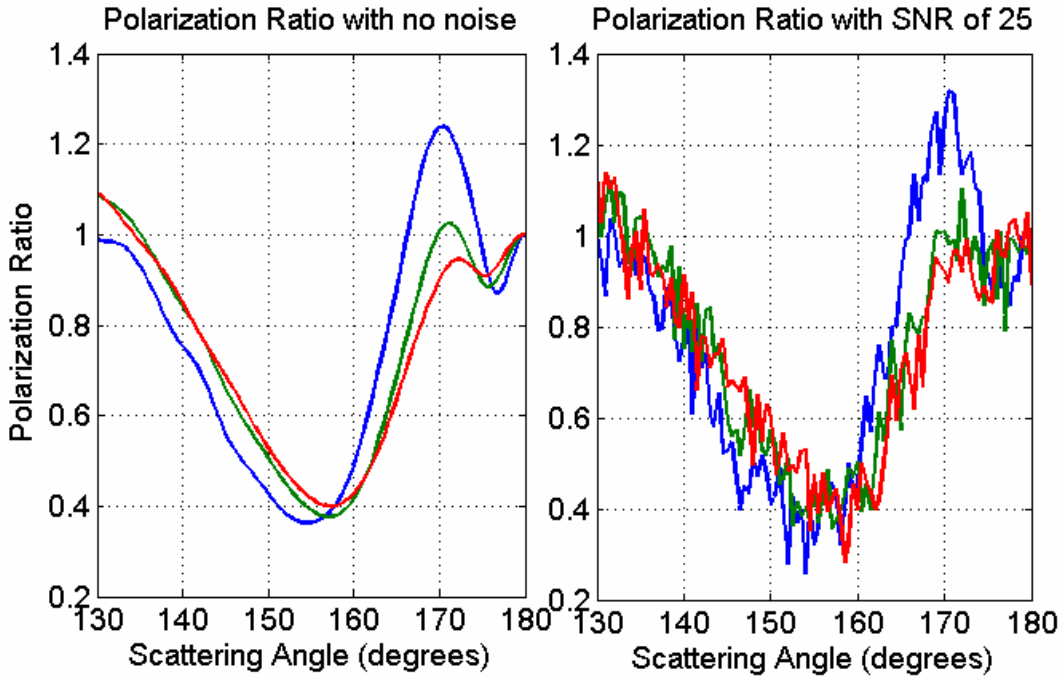


Figure 3-8: (a) Calculated polarization ratio data using a lognormal size distribution ($r_g = 0.75$ µm, $\sigma_g = 1.5$) and a concentration of 1,000 particles/cm^3 (b) polarization ratio with additive white Gaussian noise to create a signal-to-noise ratio of 25.

The analysis was run multiple times to explore the uniqueness of the results produced by the algorithm. The first set of runs produced the five lognormal size distributions summarized in Table 3-2. The algorithm is consistently inverting the correct geometric mean radius and geometric mean standard deviation of the model size distribution to within 2% error for the mean radius and 1% error for the geometric standard deviation. The concentration of the particles is not converging to the same value every time, and is frequently producing a value that is off by over 100% error. This lack of convergence for the concentration is due to the previously explored (see Chapter 2) lack of sensitivity in the polarization ratio to varying concentration levels outside a certain range. The polarization ratio for this lognormal size distribution, with a geometric mean radius of 0.75 μm and a geometric standard deviation of 1.5 is calculated for a large range of concentrations, shown in Fig. 3-9. This figure helps explain why the algorithm can not differentiate between concentrations of 1,000 particles/cm^3 or greater. Calculations similar to this should be performed for all inversions involving a large concentration of small particles to add upper and lower bounds to the retrieved concentration range.

Table 3-2: Retrieved size distribution for five different runs using the simulated noisy polarization ratio shown in Fig. 3-8b.

Minimum Squared Error	Concentration (#/cm^3)	N_T % error	Geometric Mean Radius (μm)	r_g % error	Geometric Standard Deviation	σ_g % error
10.810	5,120	+412%	0.74	-1.3%	1.51	+0.67%
10.803	1,585	+58.5%	0.74	-1.3%	1.51	+0.67%
10.796	1,000	0%	0.76	+1.3%	1.49	-0.67%
10.797	1,585	+58.5%	0.75	0%	1.50	0%
10.805	2,512	+151%	0.74	-1.3%	1.51	+0.67%

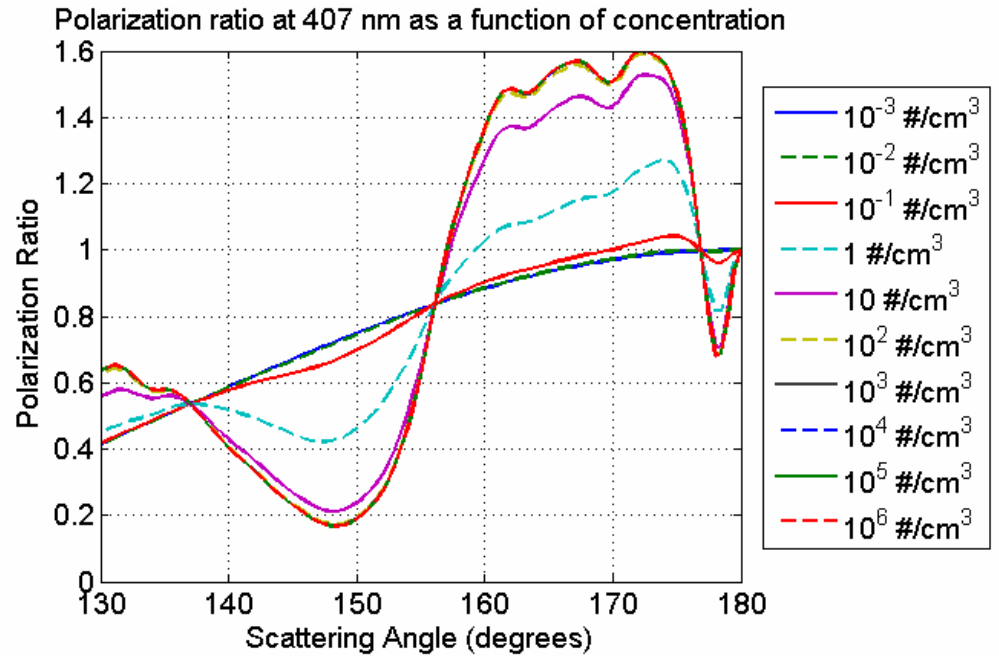


Figure 3-9: Calculated polarization ratio for lognormal size distribution (r_g = 0.75 μm, σ_g = 1.5) shown in Fig. 3-8a as a function of particle concentration, N_T.

After experiencing difficulties with concentration convergence, a second algorithm was designed that did not include the concentration as a retrievable variable. This version of the genetic algorithm uses a lognormal probability density function with a normalized area of 1. The retrieved lognormal probability density function can then be scaled by the concentration in order to produce number density particle size distributions. This two-variable version of the genetic algorithm searches for a geometric mean diameter and geometric standard deviation for a single lognormal probability density distribution that fits the measured polarization the best in the mean-squared-error sense. The same polarization ratios calculated from the lognormal size distribution with a mean radius of 0.75 μm and a standard deviation of 1.5 and a concentration of 1000 particles/cm^3 are used in the genetic algorithm for the scattering angles 130 to 175 degrees (Fig. 3-8b). The two-variable genetic algorithm is run five different times and the retrieved lognormal probability density functions are summarized in Table 3-3.

Table 3-3: Two-variable genetic algorithm results for minimum squared-error of lognormal size distribution with r_g of 0.75 μm and σ_g of 1.5 at a concentration of 1,000 particles/cm^3

Geometric Mean Radius (μm)	Percent Error for r_g	Geometric Standard Deviation	Percent Error for σ_g
0.75	0%	1.48	-1.3%
0.73	-2.7%	1.50	0%
0.73	-2.7%	1.50	0%
0.72	-4.0%	1.53	+2.0%
0.75	0%	1.48	-1.3%

The inversion algorithm produces consistent geometric mean radius and geometric standard deviation results within 4% error, even under conditions of significant random noise. This two-variable genetic algorithm converged to lognormal probability density functions in approximately 60 seconds on a Pentium D processor. This is considerable faster than the five minutes on-average that it took for the model to converge that included the concentration as a retrievable variable.

The variation in retrieved lognormal size distribution parameters in Tables 3-2 and 3-3 is a good example of why it is important to run the genetic algorithm multiple times on any given set of data. This variation occurs because the algorithm is sampling random points inside the entire solution space and then is concentrating in areas with the highest fitness as the algorithm continues to produce new populations. The absolute best-solution may never be tried by the genetic algorithm, depending on the crossover and mutation process. The important point is that all of the solutions retrieved by the genetic algorithm are in the same general area within the solution space, clustered around the global maximum. A second more exact method, such as a grid search, where every possible combination of variables is tried, can be used to find the solution that produces the lowest mean squared error within this much smaller solution space.

3.2.6 Single lognormal size distribution with varying refractive index

The second step in the inversion testing process was to allow the complex refractive index to vary as function of wavelength. Mie scattering intensity look-up tables are generated for real refractive indices from 1.3 to 1.8 by steps of 0.005, and the imaginary refractive index is allowed to assume eight different values: 0, 0.1, 0.05, 0.01, 0.005, 0.001, 0.0005, and 0.0001. This requires 707 different look-up tables of unit scattering intensities, with each table containing the parallel and perpendicular unit scattering intensity for 1000 linearly spaced radii between 1nm and 30 μm at the three wavelengths of 407 nm, 532 nm, and 650 nm. The entire directory of look-up tables requires five gigabytes of memory and takes an entire day to generate on a 4-core 2 GHz processor. The requirement of loading a different look-up table for every combination of inversion variables significantly reduces the speed of the genetic algorithm. The extension of the genetic algorithm code to multi-core processing would be an extremely rewarding effort if this algorithm were to be used to process a large volume of scattering data.

The single lognormal size distribution with a geometric mean radius of 0.75 μm and a geometric standard deviation of 1.5 is used to calculate polarization ratios using three different complex refractive indices for each wavelength. The calculated polarization ratios are shown in Fig. 3-10 using a complex refractive index of 1.465 + i0.01 for 407 nm, 1.46 + i0.01 for 532 nm, and 1.455 + i0.01 for 650 nm. White Gaussian noise is added to the calculated polarization ratios to produce curves with a signal-to-noise ratio of 25, as shown in Fig. 3-10b. The range of scattering angles between 130 and 175 degrees are used as the input to the inversion algorithm.

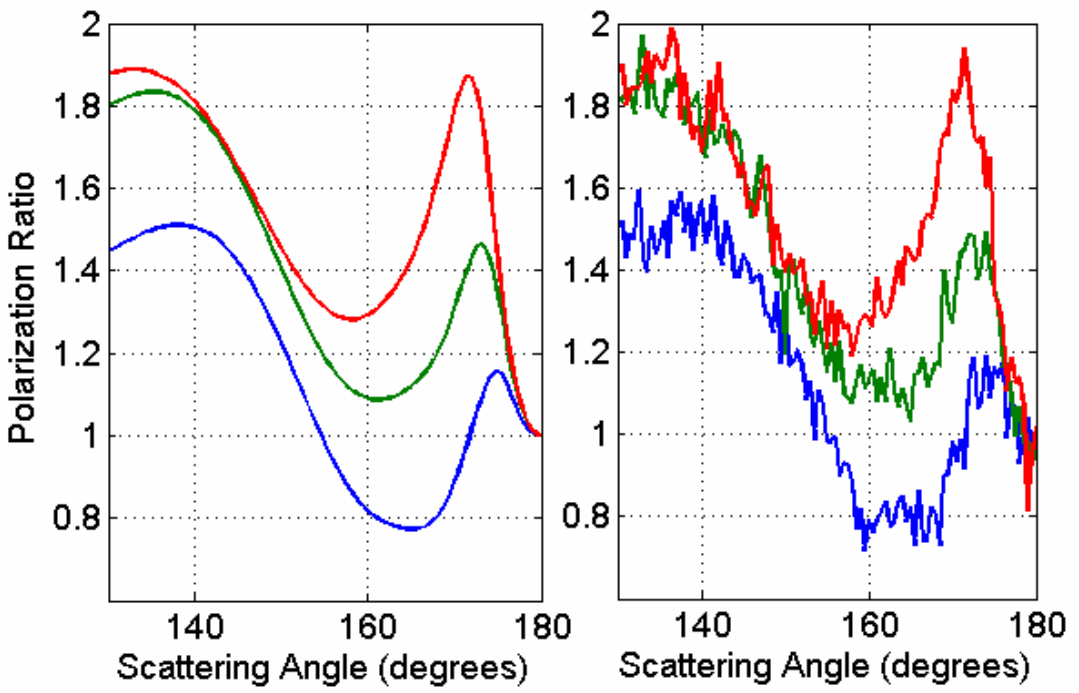


Figure 3-10: (a) Calculated polarization ratios for single lognormal distribution with r_g = 0.75 µm, σ_g = 1.5, N_T = 1000 #/cm^{3}and refractive index of 1.465 + i0.01 at 407 nm, 1.460 + i0.01 at 532 nm, and 1.455 + i0.01 at 650 nm (b) same polarization ratios with additive white Gaussian noise used to produce a signal-to-noise ratio of 25.

The genetic algorithm is then used to retrieve a single lognormal size distribution and a single complex refractive index for all three wavelengths from the simulated polarization ratio. On average, it took about 1 hour and 15 minutes for the algorithm to produce a size distribution and refractive index combination that resulted in a small squared-error between the simulated noisy polarization ratios and the model. Results from five runs are summarized in Table 3-4 below. The polarization ratios calculated using the retrieved lognormal size distribution and complex refractive index from the first inversion run (first row of Table 3-4) are shown in Fig. 3-11 along with the 'noisy' polarization ratios used as the data input to the algorithm. The inverted polarization ratios (dashed lines in Fig. 3-11) match quite well to the average of the noisy polarization ratios.

Table 3-4: Summary of results for single lognormal distribution with one varying refractive index used for all three wavelengths.

r_{g1} (μm)	Percent Error for r_g	σ_{g1}	Percent Error for σ_g	N_{T1} (#/cm^3)	Percent Error for N_T	$n_{re} + in_{im}$
0.77	+2.67%	1.48	-1.35%	1780	+78%	1.460 + i0.01
0.77	+2.67%	1.48	-1.35%	1120	+12%	1.460 + i0.01
0.75	0%	1.51	+0.67%	1260	+26%	1.460 + i0.01
0.74	-1.33%	1.48	-1.35%	1410	+41%	1.460 + i0.01
0.76	+1.33%	1.49	+0.67%	1120	+12%	1.460 + i0.01

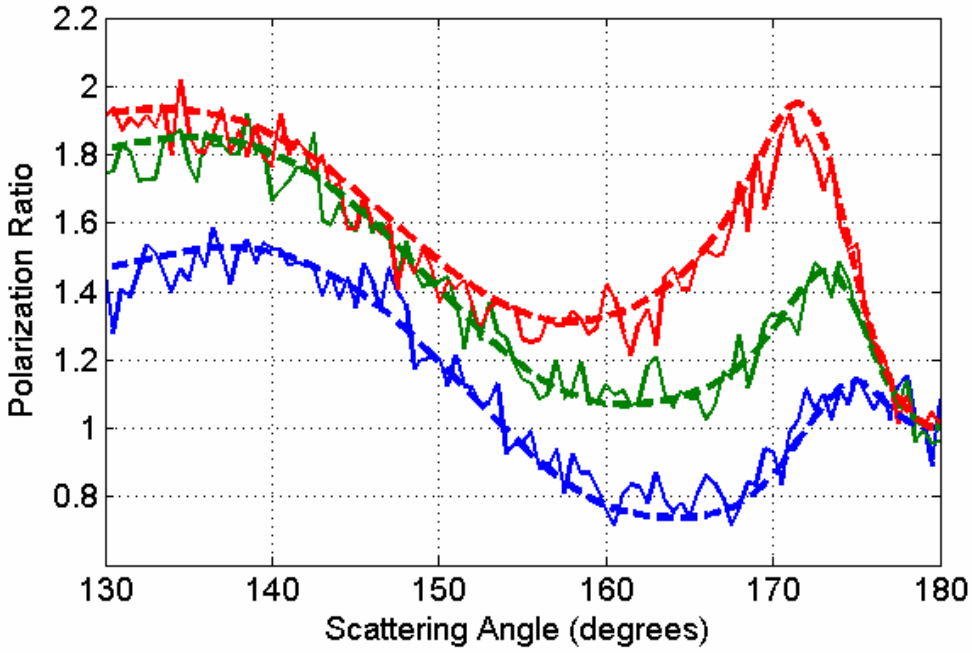


Figure 3-11: Comparison of noisy simulated polarization ratios and modeled polarization ratios using lognormal size distribution with r_g = 0.77 μm, σ_g = 1.48, N_T = 1,780 #/cm^3 (first row of Table 3-4).

After successfully retrieving a single refractive index, the algorithm is extended to retrieve a complex refractive index for each wavelength. The noisy polarization ratios shown in Fig. 3-10b, are used as the input to the extended version. Results from five different inversion runs are shown in Table 3-5.

Table 3-5: Summary of results for single lognormal distribution with varying refractive index as a function of wavelength.

r_{g1} (μm)	% error	σ_{g1}	% error	N_{T1} (#/cm^3)	% error	$n_{re} + in_{im}$ for 407 nm	$n_{re} + in_{im}$ for 532 nm	$n_{re} + in_{im}$ for 650 nm
0.72	-4.0%	1.56	+4.0%	1260	+26%	1.460 + i0.005	1.445 + i0.005	1.450 + i0.005
0.75	0%	1.5	0%	1410	+41%	1.460 + i0.01	1.460 + i0.005	1.445 + i0.001
0.74	-1.3%	1.53	+2.0%	708	-29%	1.465 + i0.01	1.46 + i0.01	1.455 + i0.01
0.77	+2.7%	1.48	-1.4%	1780	+78%	1.460 + i0.01	1.445 + i0.005	1.465 + i0.001
0.74	-1.3%	1.52	+1.4%	1550	+55%	1.460 + i0.01	1.465 + i0.001	1.440 + i0.05

The lognormal distribution parameters retrieved are not significantly improved from the values retrieved when including only one complex refractive index value as an inversion variable. The geometric mean radii and geometric mean standard deviations retrieved by the algorithm are all within 4% error. The retrieved concentration values vary considerably around the 1,000 particles/cm^3 concentration value that was used to generate the data, but the range of concentration values can be explained by the fact that the molecular scattering contribution is dominated by the aerosol scattering for this size distribution (see Fig. 3-9). The complex refractive indices retrieved by the algorithm also show a variation between the five runs. The complex refractive indices are close to the values used to calculate the noisy polarization ratios, especially considering the fact that the solution space spanned 101 real refractive index values (1.3 to 1.8 by 0.005) and eight imaginary refractive index values. The real refractive indices produced by the inversion algorithm are all within ±0.015 (~10%) of the correct value, and the imaginary refractive indices are within a magnitude (step size used was half-magnitude) of the 0.01 value used to simulate the data. While the retrieved values are reasonably close to the correct values, the complex refractive indices retrieved by the previous inversion algorithm, one that inverts a single value for all three wavelengths, are actually more accurate than these values.

The better accuracy of the single-complex refractive index inversion algorithm also comes with the advantage of decreased computation time. The genetic algorithm that retrieves a single complex refractive index value for all three wavelengths is used to invert measured data in Chapter 5 of this work. The complex refractive index produced by the genetic algorithm is then slightly altered as a function of wavelength to produce the best fit between the measured and modeled polarization ratios.

3.2.7 Tri-modal lognormal particle distribution

The genetic algorithm was expanded to retrieve trimodal lognormal size distributions at a single, fixed refractive index. The geometric mean radius ranges for each of the lognormal distributions is assigned based on mode models: the fine mode (1 nm – 100 nm), the accumulation mode (0.1 μm – 1 μm), and the course mode (1 μm – 30 μm). The ranges for the geometric standard deviations, shown in Table 3-6, are selected based on the values reported in the literature, specifically in Novitsky (2002) and Stevens (1996) work. In general, it appears that in an urban environment, the fine mode has a broad distribution, and the other two modes are much narrower. The concentration ranges for each of the modes are selected based on the simulations in Chapter 2 that explore the effect of changing concentration levels on the polarization ratio for various sized particles, shown in Figs. 2-9 though 2-12.

Table 3-6: Ranges used in trimodal lognormal size distribution inversion algorithm.

Mode	r_g (μm)	σ_g	N_T (#/cm^3)
Fine	0.001 - 0.10	1.01 -5.01	10^2 - 10^5
Accumulation	0.1 -1.0	1.01 - 3.55	10^{-1} - 10^3
Course	1 - 30	1.01 - 3.55	10^{-4} - 10

The inversion algorithm retrieves the concentration, geometric mean radius, and geometric standard deviation for each of the three lognormal distributions that form the trimodal size distribution, based on the squared error between the measured and modeled polarization ratio. A trimodal size distribution is used to generate simulated data to test the trimodal inversion algorithm. This trimodal lognormal size distribution was retrieved from coastal aerosol scattering measurements by Stevens (1996, pg. 124) using the multistatic technique at the single wavelength of 532 nm. The polarization ratios at 407 nm, 532 nm, and 650 nm are calculated using the complex refractive index of 1.38 + i0 for each wavelength and white Gaussian noise is added to create a signal-to-noise ratio of 35. The trimodal size distribution, calculated polarization ratios, and polarization ratios with Gaussian noise are shown in Fig. 3-12. The 'noisy' polarization ratios shown in Fig. 3-12b are used as input data to the genetic inversion algorithm; the trimodal size distribution parameters and a single complex refractive index are retrieved by the algorithm. Each trimodal genetic algorithm inversion took approximately two hours to converge on a Pentium D processor. Results from three inversions runs are summarized in Table 3-7. The complex refractive index retrieved by the algorithm is extremely close to the correct value of 1.38 + i0 for all three inverted cases. The nine parameters for the trimodal lognormal distributions agree very well with the values used to generate the noisy data. Small variations are seen in each of the retrieved trimodal parameters, but the overall size distributions are extremely similar. The three retrieved trimodal size distributions are shown in Fig. 3-14 (dashed lines) along with the model trimodal size distribution (black line).

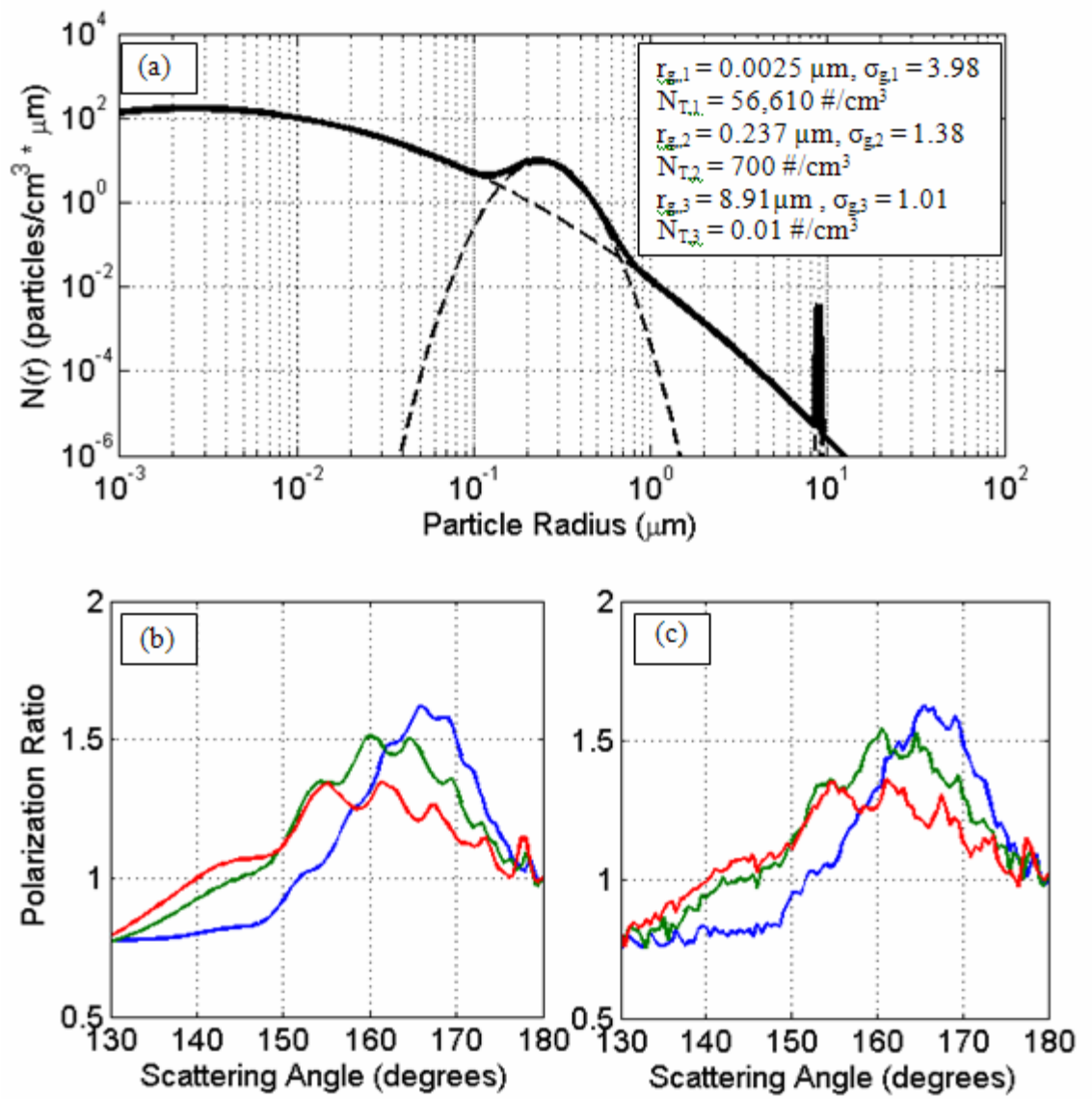


Figure 3-12: (a) The trimodal size distribution (b) calculated polarization ratios and (c) calculated polarization ratios with additive white Gaussian noise to produce a signal-to-noise ratio of 35.

Table 3-7: Summary of retrieved trimodal lognormal size distributions.

	r_{g1} (µm)	σ_{g1}	N_{T1} (#/cm^3)	r_{g2} (µm)	σ_{g2}	N_{T2} (#/cm^3)	r_{g3} (µm)	σ_{g3}	N_{T3} (#/cm^3)	$n_{re} + n_{im}$
Run #1	0.004	3.70	50,119	0.236	1.35	708	8.90	1.02	0.0089	1.38 + i0.0001
Run #2	0.003	3.93	63,096	0.234	1.40	891	8.91	1.01	0.0089	1.38 + i0.0
Run #3	0.002	3.95	58,119	0.237	1.38	708	8.87	1.04	0.0112	1.385 + i0.0001
Model	0.0025	3.98	56,610	0.237	1.38	700	8.91	1.01	0.01	1.38 + i0

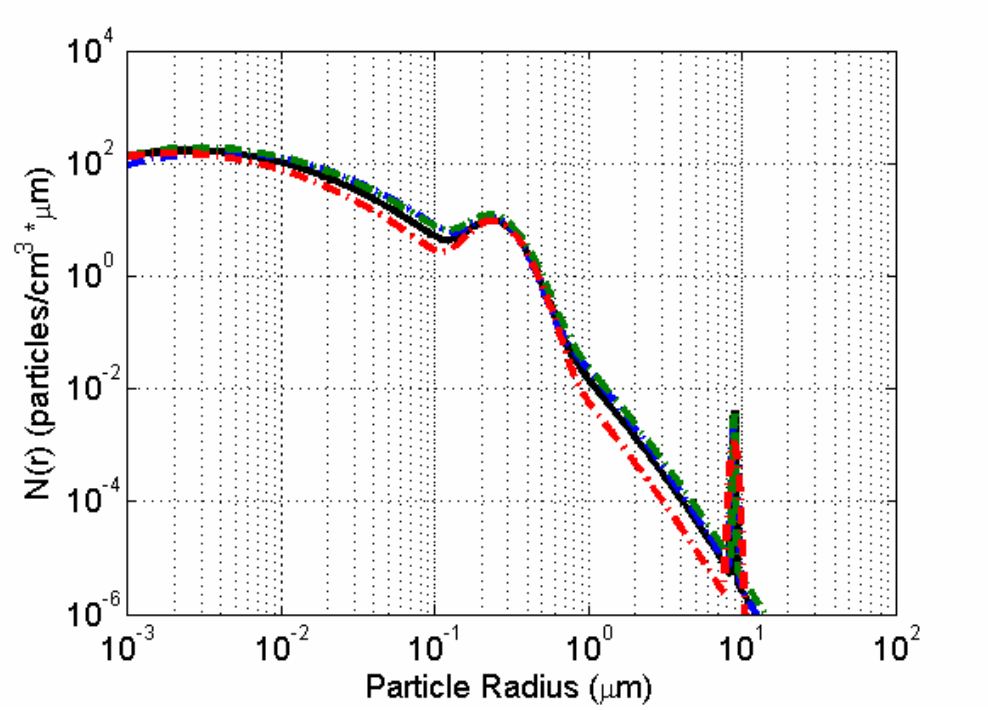


Figure 3-13: Trimodal size distributions inverted from simulated polarization ratios (dashed lines) compared to model trimodal size distribution (black solid line). The parameters for the inverted size distributions are summarized in Table 3-7.

The comparison between the modeled polarization ratios calculated using the retrieved trimodal size distributions and complex refractive index in Table 3-7, and the 'noisy' polarization ratio used as input for the inversion algorithm are shown in Fig. 3-14. An impressive fit of the polarization ratios are achieved, given the number of inversion variables and the presence of Gaussian noise that is corrupting the input data. The results obtained from this test run indicate that reasonably accurate trimodal size distributions and a complex refractive index can be retrieved using this 10-variable genetic algorithm. The results obtained from the algorithm should only require minimal optimization of the parameters to obtain the best fit between the modeled and measured data.

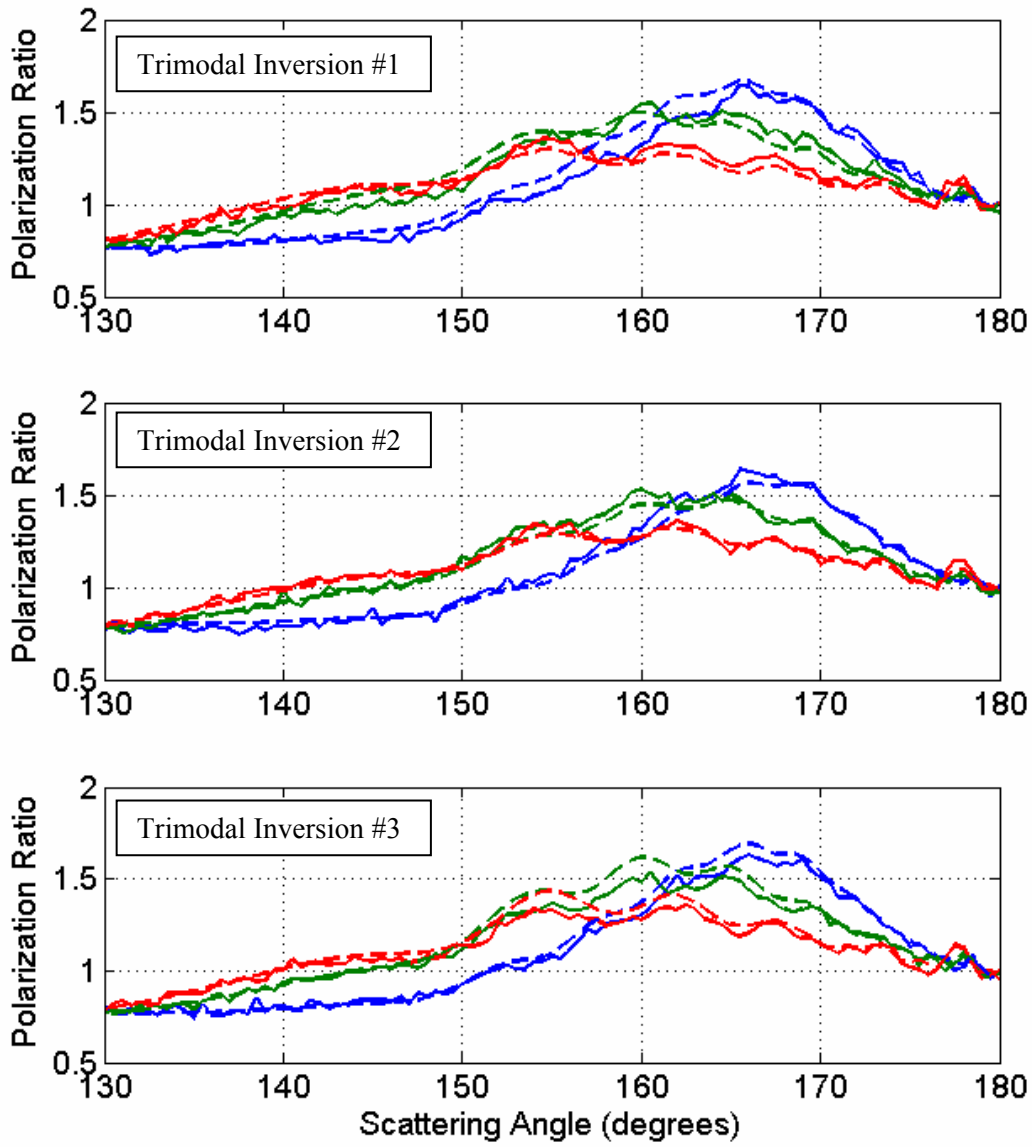


Figure 3-14: Comparison between 'noisy' simulated polarization ratios (solid lines) and polarization ratios calculated using the trimodal lognormal size distribution retrieved by genetic algorithm in Table 3-7 (dashed lines).

Chapter 4

Multiwavelength-Multistatic Scattering Hardware

The main objective of this work is to analyze scattering measurements at multiple wavelengths and angles to determine microphysical properties of the scattering aerosols. This analysis uses simultaneous measurements of multiple wavelengths at different angles to examine the same scattering volume, thus providing a more robust analysis in complex aerosol layers. These measurements combine three continuous-wave (CW) laser wavelengths in one transmitted beam that is imagined using CCD cameras with wide field-of-view focusing lenses. A transmission diffraction grating is placed in front of the focusing lens; thereby spreading the different wavelengths across the CCD array and creating two-dimensional data. The angle-dependent scattering is spread across the columns of the CCD and the wavelength-dependent scattering is spread across the rows.

4.1 Multiwavelength Transmitter

Three 100 mW diode lasers at wavelengths of 407 nm, 532 nm, and 650 nm are overlapped and co-aligned into a single transmitted beam. Visible wavelengths were selected based on the sensitivity of the CCD cameras that we had available and for the ease of alignment. The specific laser diode wavelengths were selected based on availability, price, and to provide a large wavelength spread. The co-alignment ensures that the lasers are interrogating the same volume of aerosols and that scattering from each beam is located in the same horizontal plane imaged by the CCD camera. The lasers beams are combined using dichroic mirrors, which will either transmit or reflect light based on its wavelength.

The polarization state of the combined lasers is important, as our technique is dependent on using two orthogonal polarizations of the incident light. To ensure that all of the transmitted light is in the same plane of polarization, the combined beam is sent through a polarizing beamsplitter, which transmits only the polarization component that is parallel to the scattering plane. The polarization of the combined laser beam is adjusted by manually rotating a broadband half-waveplate back and forth between two predetermined angles to produce parallel and perpendicular polarization with respect to the scattering plane. The multiwavelength transmitter is shown in Fig. 4-1 and the retardance of the waveplate as a function of wavelength is shown in Fig. 4-2. The small variance of the retardance around the desired 0.5 will introduce a polarization rotation error of +3.6 degrees for 532 nm, -3.6 degrees for 650 nm, and -7.2 degrees for 407 nm. This variation in the retardance will introduce a small level of uncertainty in the orientation of the polarized light exiting the transmitter. This uncertainty later transfers to error in our measured polarization ratios, because the incident laser beams are not perfectly polarized parallel or perpendicular to the scattering plane of incidence. The impact of the polarization ratio error introduced by the inherent uncertainty of the half waveplate retardance is explored in Chapter 5.

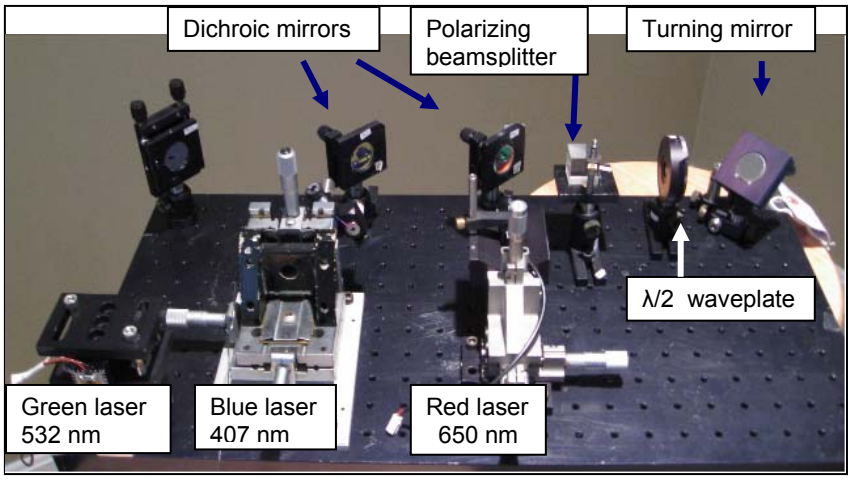


Figure 4-1: Picture of the revised transmitter with the waveplate fixed in the transmit path.

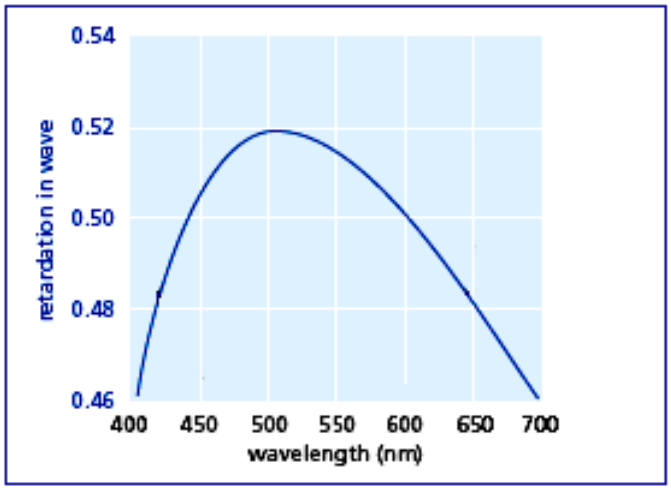


Figure 4-2: Fractional retardance of the half-wave plate response as a function of wavelength (CVI Melles Griot datasheet).

4.2 Multistatic Receivers

One great advantage to this multistatic approach is the simplicity of the setup. All that is required is a laser beam with a polarization rotator and a CCD camera and a wide-angle lens to capture a range of angular scattering. This makes the system extremely portable and flexible for use in many different scenarios. The multistatic receivers described here were used in a laboratory setting, in an aerosol wind tunnel, and outdoors across a farm pasture with no modifications to the setup.

Two Meade Deep Sky Imager PRO™ II monochromatic CCD cameras were used during the scattering experiments. The camera uses a 16-bit CCD chip, Sony's ICX429ALL, which exhibits the spectral response characteristics shown in Fig. 3-3. The chip has 752 x 582 pixels, with each pixel having dimensions of 8.3 µm x 8.6 µm. An 8 mm focal length lens with a 45 degree field-of-view is mounted in front of each CCD camera. The cameras are mounted on 3-axis tripods with horizontal levels for ease of alignment relative to the transmitted beams. A

transmission grating mounted in front of the camera lens, as shown in Fig. 3-4, spreads the wavelengths down across the CCD array.

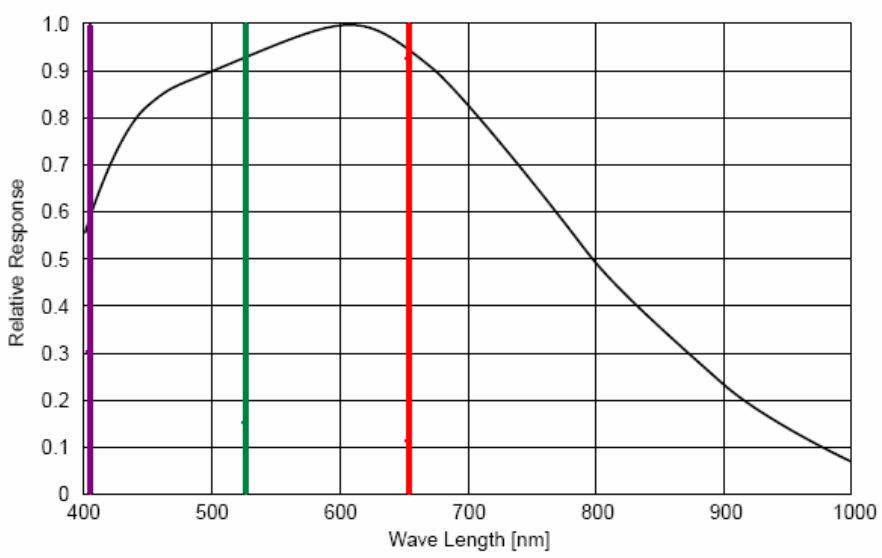


Figure 4-3: Spectral relative response of CCD camera (ICX429ALL).

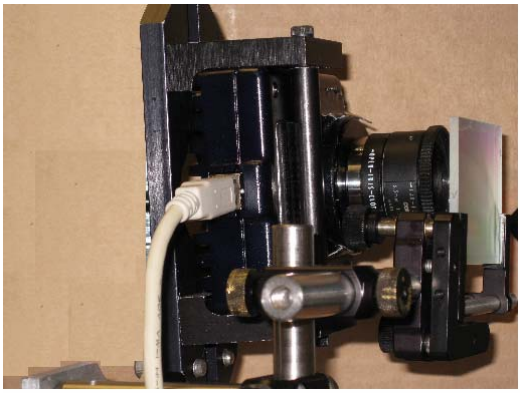


Figure 4-4: CCD camera with lens and diffraction grating mounted.

Two transmission gratings were used for the scattering measurements. The spectral response characteristics of both the 300 lines/mm and 600 lines/mm grating are shown in Fig. 4-5. The 300 lines/mm grating offers less wavelength spread but has a higher transmission efficiency across the wavelength range.

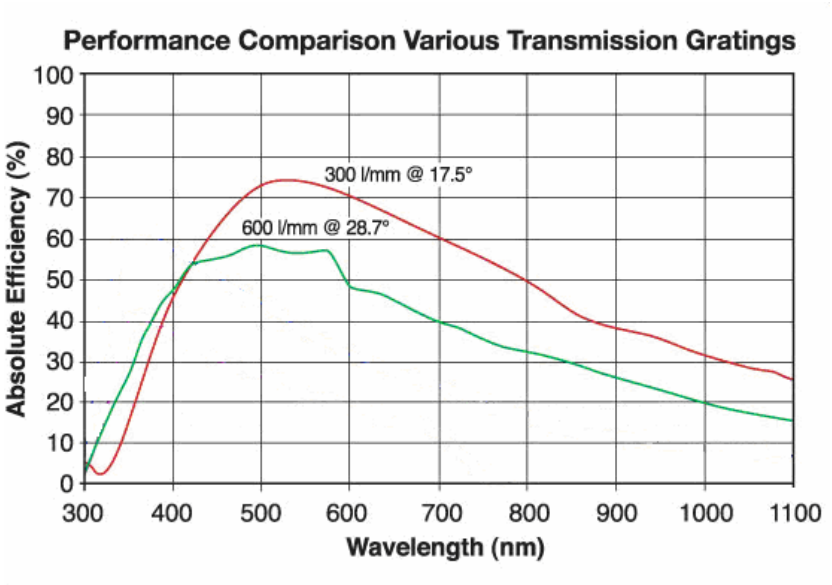


Figure 4-5: Spectral response for transmission gratings (Thorlabs).

4.3 Images as Data

Using a CCD imager as a detector requires care during operating periods to remain below the saturation level of the camera's pixels while maintaining reasonably high signal strength. It is important to ensure that the scattering data is well above the noise floor of the camera, so that it is not washed-out by noise. This was accomplished by monitoring a histogram of the pixel intensities and adjusting the integration time of the camera. The target level used to adjust the integration time was typically 50%-70% of the full range of the camera pixels. This level is well above the noise floor and safely below the saturation point. It is also beneficial to average multiple images of the same exposure time, called stacking, in order to further increase the signal to noise by averaging out random noise. There are sources of noise when using a CCD that can not be eliminated during the operation of the camera or through averaging. These noise sources are related to the electronics operating the CCD and can be mostly removed by using image processing techniques.

Ideally, the number of electrons stored in a CCD array would be only dependent on the number of photons 'seen' by each pixel during exposure, and every pixel in the array would have the exact same response to all wavelengths. Unfortunately, this is never the case. CCD images are often corrupted by dark noise, bias offset noise, and readout noise. CCD imagers can exhibit varying pixel sensitivities which also contribute error to the data depending on the data analysis techniques employed. Another common error introduced in data images is uneven illumination of the pixels, which may be caused by the focusing optics or by dust in the optical path. There are a number of techniques used to minimize these sources of noise and error when using images as data.

Dark current is the generation of electrons through thermal vibration. Dark current fills each pixel with electrons at a relatively steady rate dependent on the temperature of the CCD chip and the length of the exposure. Dark current noise is a linear response and repeatable, which means that correction for this type of noise is rather simple. A dark frame is taken with the CCD imager at the same temperature and using the same exposure as used for the data collection. This dark frame is then subtracted from each data image to remove the dark current noise. As this subtraction is done pixel by pixel, it will also remove error introduced into the image by hot pixels, which are pixels that record high intensities regardless of the photon flux impinging on them. Bias offset is a constant value added to each pixel caused by the electric 'pre-charge' applied to the CCD chip by the camera electronics to activate its photon-collecting ability. Readout noise is structured noise introduced by the voltages applied to each pixel by the camera electronics in order to collect the image from the CCD array. Both bias offset and readout noise are removed from an image when a dark frame is taken at the same temperature and the same exposure length, and is then subtracted from the data image.

Varying pixel sensitivities and uneven illumination of the CCD can be corrected using flat field frames. Flat field calibration, sometimes referred to as a grayscale calibration, is a little

more complicated than dark current correction and involves illuminating the CCD array with a uniform white light source. The exposure length should be long enough to reach roughly 50% of the saturation level. A dark frame must be subtracted from the flat field frames and multiple flat frames should be averaged together to create a master flat field frame. Then each pixel value in the image is divided by the maximum pixel value to produce a scaling factor for each pixel. Dividing your original data frame by these scaling factors should produce a uniform image with the same value for every pixel. The scaling factors for each pixel are then applied to subsequent data images to correct for varying pixel sensitivities.

Flat field corrections were not necessary for our measurements due to the ratio technique utilized in forming the polarization ratio during the data analysis. Varying pixel sensitivities do not add error to our data because we are primarily creating a ratio of data collected at the same pixel in two images, and only the polarization of the light changes between the two images. The application of this ratio technique does depend on the polarization bias of the receiver, which ideally would be zero, indicating that there is no variation in pixel sensitivities based on the polarization of the incident light. An experiment using a uniform white-light source and polarization gratings was conducted to investigate the polarization bias of the camera and the transmission grating. Results from the experiment indicate that there is very little polarization bias in the receiver, which is supported by the information presented by the manufacture.

4.4 PSU Chamber Study

The first experimental study investigates the feasibility of expanding the multistatic polarization ratio technique, which was demonstrated by Stevens (1996), Novitsky (2002) and Park (2008) using a single wavelength, to multiple wavelengths across the visible spectrum. The intent of this experiment was to ensure that multiple wavelengths could be detected

simultaneously using a monochromatic CCD array and a transmission diffraction grating, and to demonstrate the advantages of multiple wavelengths in determining aerosol properties. The scattering experiments were performed using an aerosol generator which produced a size distribution of smoke particles that had been characterized by Park (2008). This will give us a theoretical comparison to help determine if the system is operating as designed.

The artificially generated polyalpha olefin (PAO) smoke is held by an aerosol chamber that is 122 cm long, 122 cm wide, and 21 cm high. A viewing window is located on the entrance-side of the chamber to measure scattering angles between approximately 127 through 170 degrees, as shown in Figure 4-6

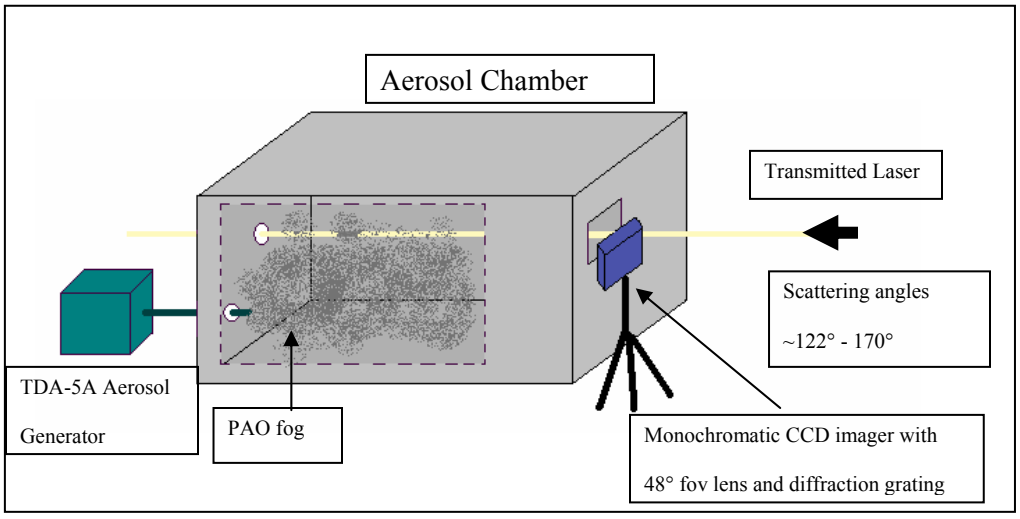


Figure 4-6: PSU aerosol chamber setup.

An example of the angular scattering imaged using a 300 lines/mm grating is shown in Fig. 4-7. Although it is difficult to perceive from viewing the image of raw data shown in Fig. 4-7, variations in the scattering phase function along the beam can be extracted through a series of processing techniques. Examination of Fig. 4-7 reveals a slight bend to each of the 'rows' of scattering intensities and a de-focusing of the scattered beams from the left side of the image to the right side. The bend is due to imaging off-axis points through the diffraction grating, and the de-focusing is a near-field effect; both add some complexity to the analysis of the image.

An image alignment procedure was used to accurately extract the intensities as a function of wavelength and angle from the image. Vertical strings were equally spaced along the length of the chamber at 10 centimeter intervals and an image was taken of the lasers striking the strings. A second order polynomial is fit to the bright laser spots, as shown in Fig. 4-8. The polynomials are then used to extract the scattering data and assign scattering angles to pixel locations for each wavelength from the polarized scattering images.

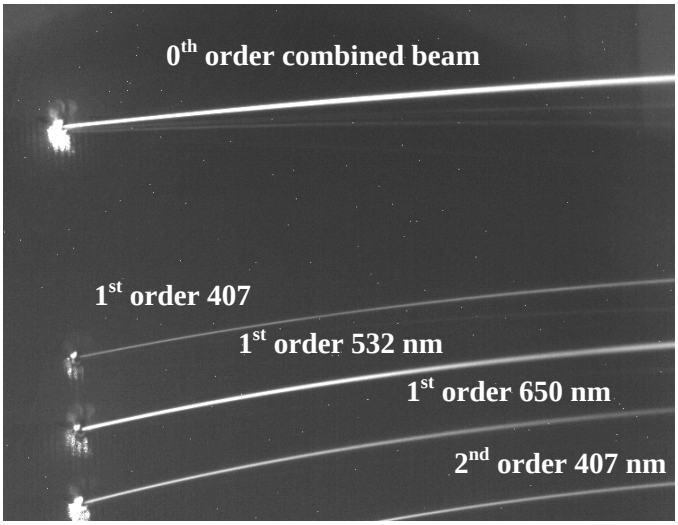


Figure 4-7: An image of the angular scattering through the 600 lines/mm diffraction grating.

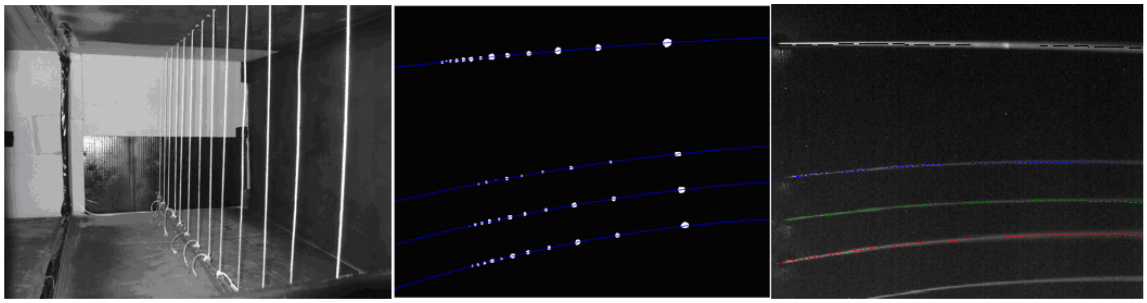


Figure 4-8: Data extraction method.

The scattering information for each wavelength falls on multiple rows of the CCD array, and the number of rows that contain scattering information changes as a function of CCD column due to the defocusing of the beam in the near-field of the camera. The beam profile is examined for each wavelength as a function of column in order to determine the number of rows to sum for

calculating the total scattered intensity in each column of the CCD. The 25% intensity point on each side of the maximum intensity pixel is used to determine the number of rows to integrate across for each diffracted laser beam. This value was selected to minimize the noise in the signal while still collecting a large majority of the scattered light. This process is depicted in Fig. 4-9, where the red asterisks indicate the pixel that has fallen below 25% of the maximum pixel value. In Fig. 4-9, the values from eight pixels are added together to calculate the 532 nm scattered intensity at CCD column 100, and the values from 21 pixels are added to calculate the intensity at column 600. The integrated scattered intensities for the three wavelengths for parallel and perpendicular polarized incident light are shown in Fig. 4-10. The polarization ratios formed by dividing the parallel scattering intensities by the perpendicular scattering intensities for the PAO fog are shown in Fig. 4-11.

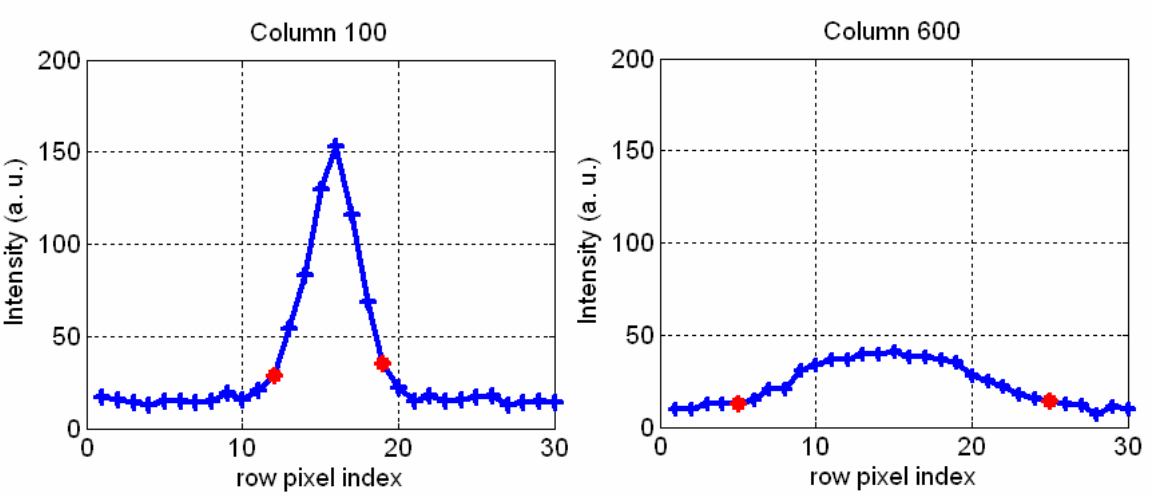


Figure 4-9: Beam profile of diffracted 532 nm laser at (a) left side of image (column 100) and at (b) right side of image (column 600).

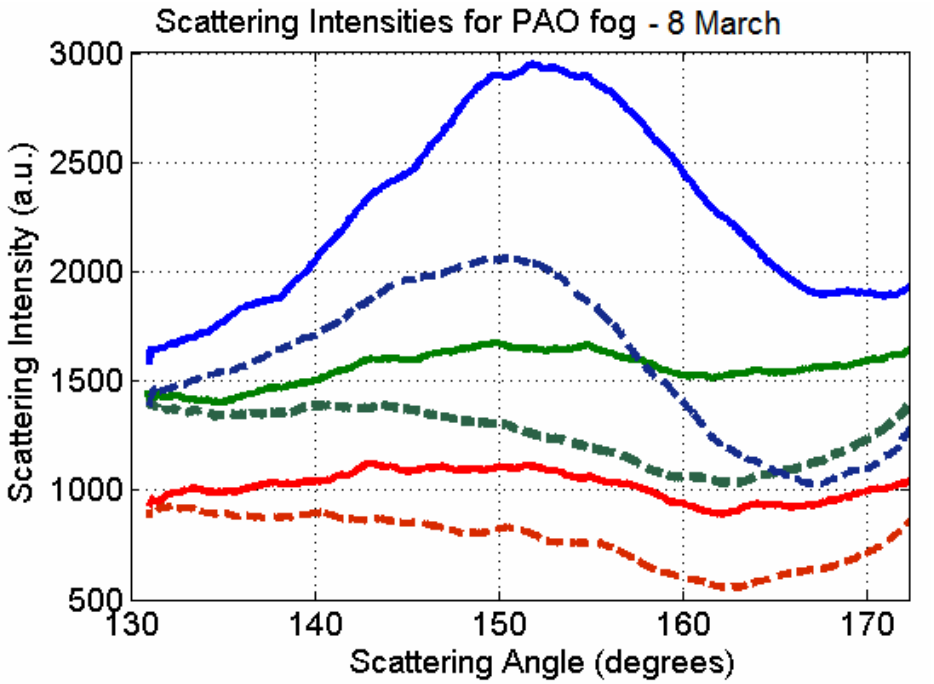


Figure 4-10: Scattering intensities collected from PAO fog in the PSU aerosol chamber on 8 March. Solid lines are parallel scattering intensities and dash lines are perpendicular scattering intensities for 407 nm (blue), 532 nm (green), and 650 nm (red).

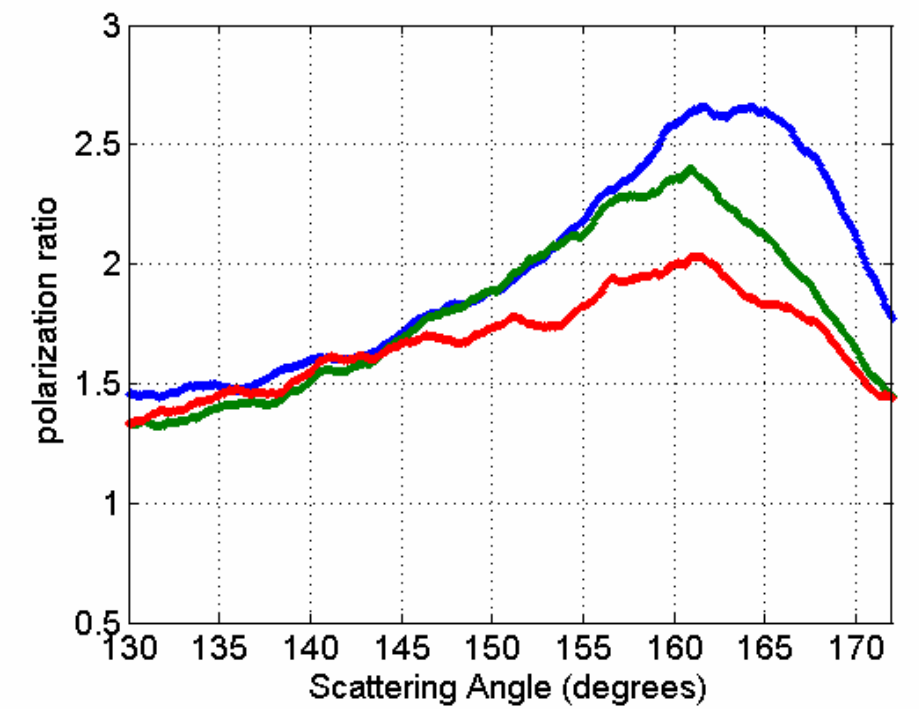


Figure 4-11: Polarization ratios for PAO fog at 407 nm (blue), 532 nm (green), and 650 nm (red)

The genetic algorithm is used to obtain a lognormal size distribution and complex refractive indices as a function of wavelength from the multiwavelength-multistatic data. The lognormal size distribution retrieved by the genetic algorithm that produces the lowest-squared error between the modeled and measured polarization ratios has a geometric mean diameter of 300 nm and a standard deviation of 1.66. Figure 4-12 shows the comparison between the measured polarization ratio and the best-fit model calculated using the retrieved best-fit lognormal size distribution. The refractive indices used to calculate the best-fit polarization ratios are 1.465 + i0.001 for 407 nm and 1.455 + i0.0005 for 532 nm and 650 nm. The size distribution of the PAO fog produced by the TDA-5A aerosol generator was measured 30 times by Park (2008, pg. 120) using a scanning mobility particle sizer, with one of the measurements shown in Fig. 4-13. A lognormal distribution was fit to the averaged data to find a geometric mean diameter of 317 nm ± 6.95 nm and a geometric standard deviation of 1.66 ± 0.04. The mean diameter and standard deviation of the particle size distribution measured by the scanning mobility particle sizer is consistent with the multiwavelength-multistatic measurement and algorithmic result.

The differences in magnitude of the polarization ratios are most likely caused by a few factors, particularly the quickly changing concentration of the particles. A condensation particle counter was used to monitor the concentration of the PAO fog during the measurement. The measured concentration is plotted in Fig. 4-14, and shows that the concentration fell from ~225,000 to ~220,000 particles/cm^3 throughout the course of the measurements.

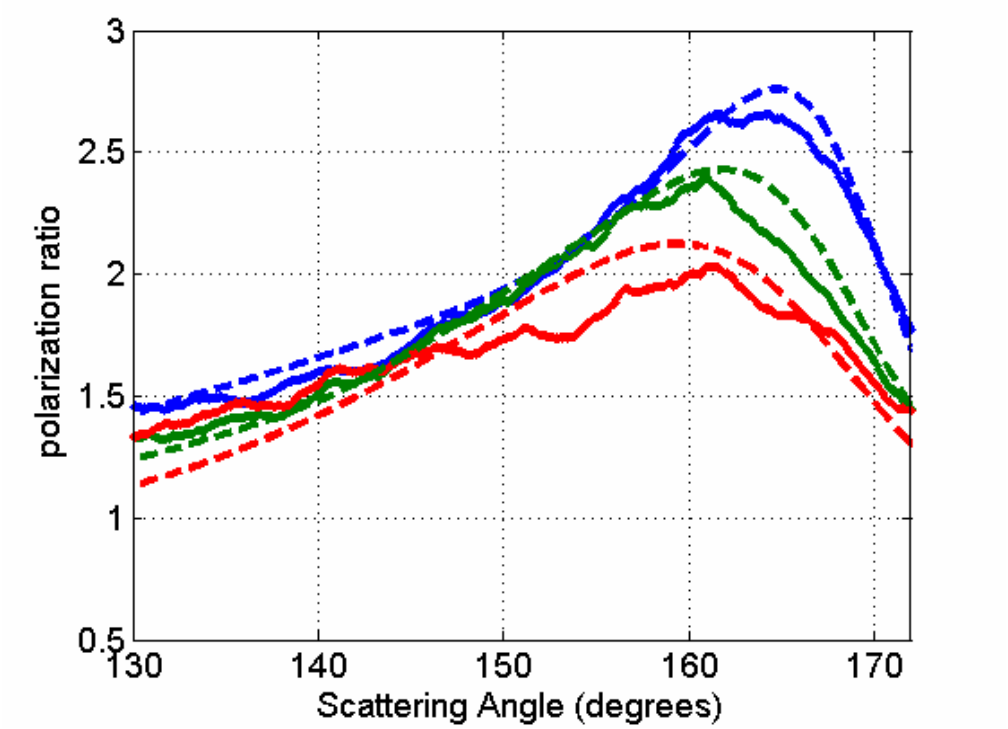


Figure 4-12: Comparison between measured (solid lines) and modeled (dashed lines) polarization ratios using a lognormal probability density function with d_g = 300 nm σ_g = 1.66.

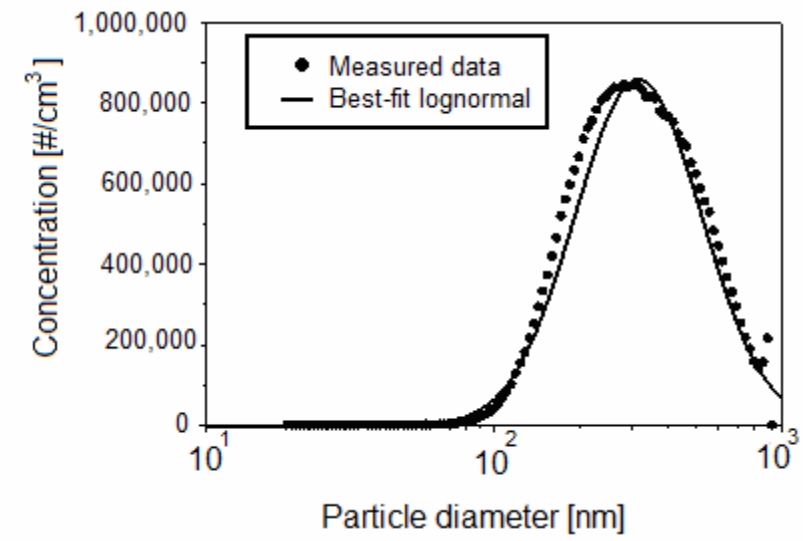


Figure 4-13: Particle size distribution of PAO fog generated with TDA-5A aerosol generator measured by Park (2008, Fig. 3.13) using scanning mobility particle sizer.

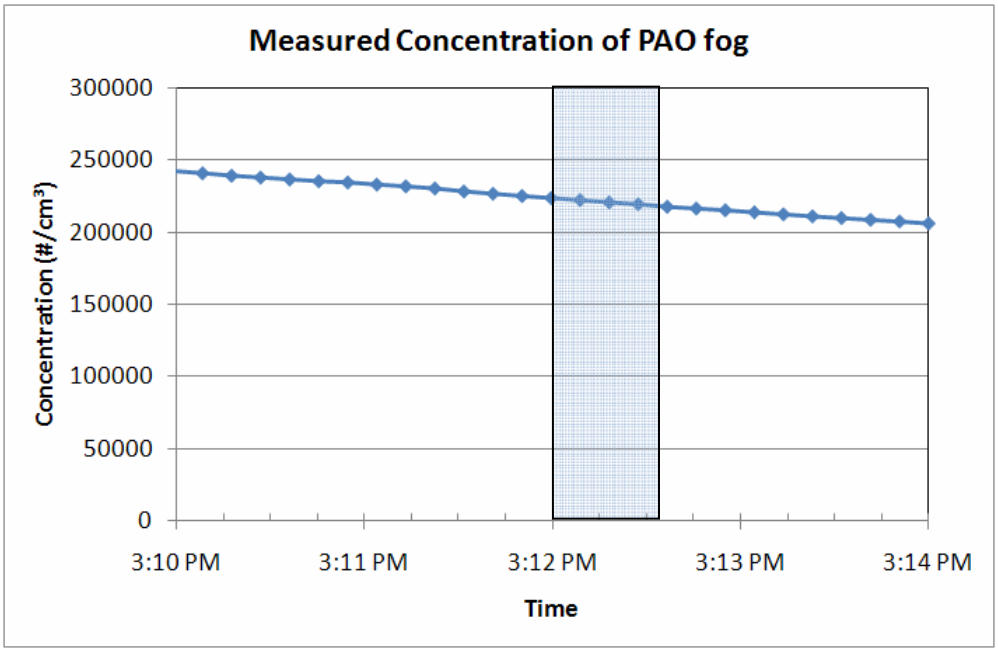


Figure 4-14: Concentration of PAO fog as measured by a condensation particle counter on 8 March. The blue box indicates the time of measurements.

The perpendicular scattering measurements were made first, indicating that the perpendicular scattering intensities will be slightly higher than the corresponding parallel measurements collected from a lower concentration of particles. The ability to robustly retrieve lognormal size distributions from data containing non-uniformities along the measurement path was a primary goal of this work. In this case, the multiwavelength-multistatic technique and coupled genetic inversion algorithm arrived at a mean particle diameter solution that was within 6% of that measured by the SMPS. The inverted result for the width of the particle size distribution was exactly what was measured by the SMPS with a small degree of uncertainty (less than 3%).

The extinction cross sections of a lognormal size distribution with a mean diameter of 300 nm and a geometric standard deviation of 1.66 are 0.1876 μm^2, 0.1290 μm^2, and 0.09132 μm^2, for 407 nm, 532 nm, and 650 nm respectively, using a refractive index of 1.455 + i0.001. The extinction coefficients for 407 nm, 532 nm, and 650 nm for a lognormal size distribution of

225,000 particles/cm^3 with a geometric mean diameter of 300 nm and a geometric standard deviation of 1.66 are 0.0421 m^{-1}, 0.0290 m^{-1}, and 0.0205 m^{-1}, respectively. The longest path length between the scattering volume and the camera is roughly 1.5 meters, and using the highest extinction coefficient of 0.0422 m^{-1} for 407 nm, the highest optical depth encountered during the scattering measurements is 0.063 m^{-1}. Multiple scattering should not be a significant factor in the scattering measurements, as the optical depths are below the value of 0.1 (van de Hulst, 1957).

Chapter 5

EPA Aerosol Wind Tunnel

Multistatic-multiwavelength scattering measurements were performed at the U.S. Environmental Protection Agency's (EPA) Aerosol Test Facility (ATF) in Research Triangle Park, North Carolina. The aerosol wind tunnel in the ATF is unique in the world; the special features are its size, fluid parameter (temperature, humidity, velocity, and turbulence) control, and integration of multiple state-of-the-art aerosol generation and measurement systems. The aerosol generation system was designed specifically for this tunnel and is capable of producing monodisperse aerosols while maintaining uniform particle size, shape, and density. The ability to stabilize and control the scattering environment while simultaneously monitoring the aerosol size and number concentration made this a great facility for testing the multiwavelength-multistatic scattering technique, and evaluating the inversion algorithm. A layout of the aerosol wind tunnel is shown in Fig. 5-1 and a side view of the tunnel during our test is shown in Fig. 5-2. There are two different sections of the tunnel that can be used for aerosol testing, the Human Exposure Test Section (HETS) and the Sampler Test Section (STS). The HETS, with dimensions of 12 feet x 10 feet x 30 feet, can easily accommodate several people, which is convenient for setting up test equipment. There are three aerosol distribution points in the aerosol tunnel, though only two were used for the scattering experiments. The aerosols generated by TSI's Vibrating Orifice Aerosol Generators (VOAG) entered at the location labeled Aerosol Distribution 1, and the fog produced by MDG's Fog Generator entered the tunnel Aerosol Distribution 2 in Fig. 5-1. The wind speed, temperature, and humidity of the entire tunnel were automatically controlled, and constantly monitored to provide stable conditions throughout the scattering measurements.

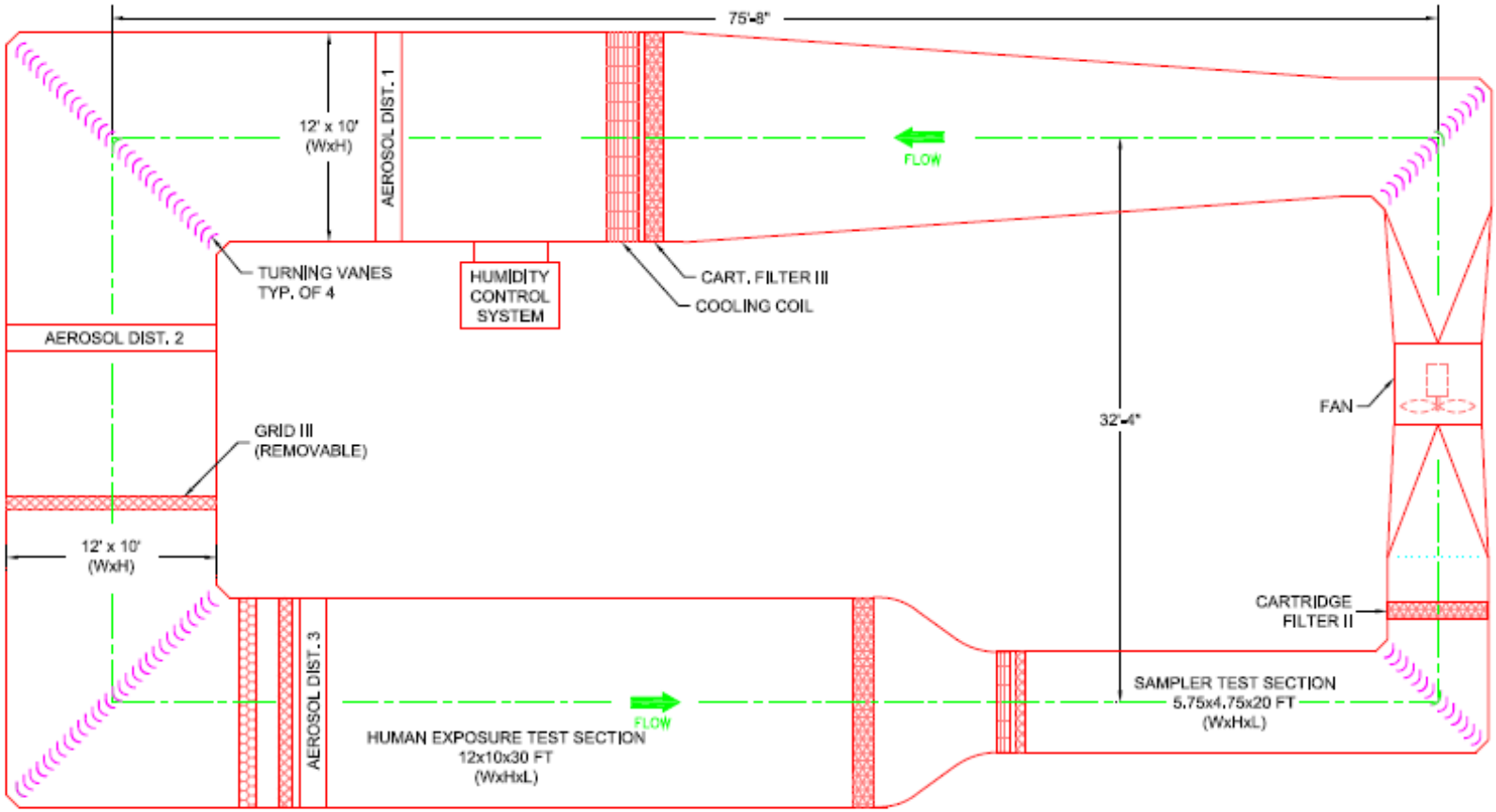


Figure 5-1: EPA Aerosol Test Facility Wind Tunnel.



Figure 5-2: Photograph of the HETS portion of the ATF Wind Tunnel.

5.1.1 Experimental setup

The multiwavelength-multistatic scattering measurements were conducted in the HETs portion of the wind tunnel (Figs. 5-1 and 5-2) because the larger area made it easy to set up the cameras and the extra equipment necessary for instrument alignment. The combined laser beams entered the chamber through a hole in the floor of the HETS and reflected out across the chamber using a 45-degree turning mirror as shown in Fig. 5-3a. This was done to protect the transmitter optics from the different oils in the fog fluids and to ensure that no unnecessary turbulence was added to the aerosol flow by objects encountered as it traversed the wind tunnel. An optical power meter head was placed approximately 8.5 m away from the turning mirror (Fig. 5-3b). The power meter served the dual purpose of monitoring the power of the lasers throughout the experiments and as a termination/collection point for the combined beams.

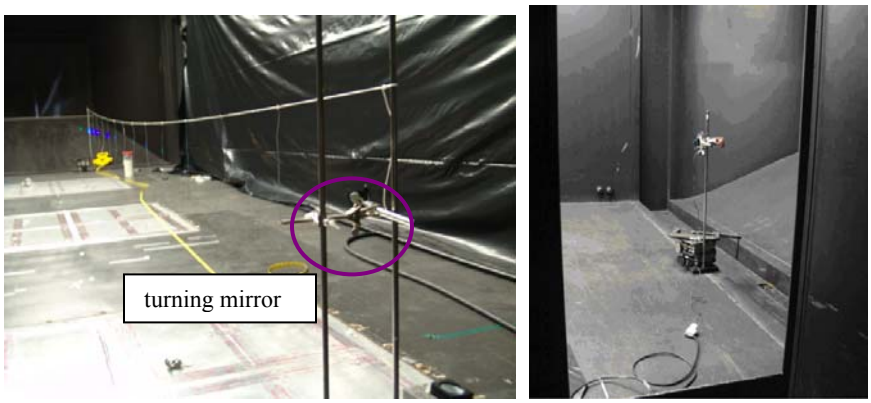


Figure 5-3: (a) Turning mirror and laser path (b) power meter head at end of path.

The receiver CCD cameras were placed parallel with the entry point for the lasers to collect backscattering angles. The USB cables that connect the cameras to the computer were routed through a hole in the floor, which was also used as the entry for the tubes that fed two point sensors used to monitor the aerosols in the tunnel. These sensors are explained in depth in section 5.1.3. The camera set-up and tubes that feed the aerosol sensors are shown in the photograph in Fig. 5-4.

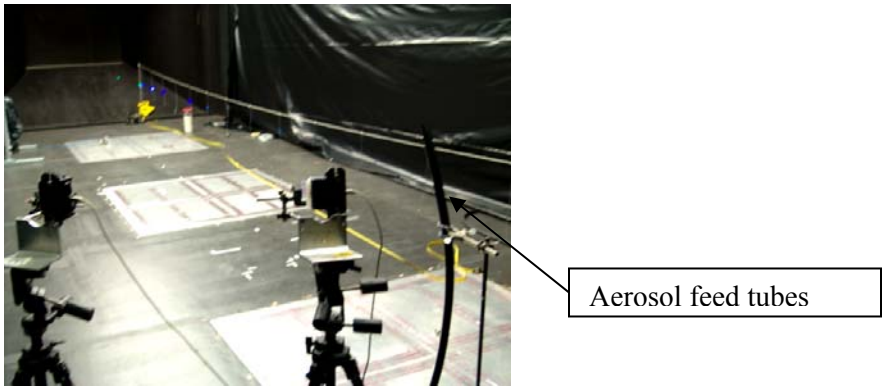


Figure 5-4: Camera setup and aerosol sensor feed tubes.

5.1.2 Angle assignment

An alignment image was used to accurately extract the spatial location and assign a scattering angle to the intensities from the scattering images. Vertical wires were equally spaced at 61 cm intervals (2 feet) along the length of the wind tunnel section and an image is taken of the laser beams striking the wires. The perpendicular distances from each camera to the laser beams are recorded, as well as the linear distance to the first dangling wire in each camera's field of view. These distances are used to calculate the scattering angles imaged by each camera. The general setup for the two cameras is depicted in Fig. 5-5. An alignment image taken with both cameras is shown in Fig. 5-6. The bend in the diffraction pattern image of the scattered beams is caused by imaging off-axis points through the diffraction grating, and adds some complexity to the analysis of the image. The bend could have been minimized by using a confocal configuration but optics to accomplish this were not available. Second order polynomials are fit to the center pixels for each wavelength and used to extract the scattering intensity from the images (Fig. 5-7). The polynomial equation is used to locate a 'starting' point as a function of wavelength for each column. The beam profile is examined for each laser wavelength as a function of column and the 10% intensity point on each side of the maximum intensity point is used to determine the number of rows to integrate across for each diffracted wavelength. The scattering intensities are then smoothed using a 5-point moving filter. The angle-dependent polarization ratio is calculated by dividing the integrated scattering intensity for incident parallel polarization by the integrated scattered intensity for incident perpendicular polarization on a column-by-column basis. The polarization ratio is then resampled at half-degree intervals and used by the genetic algorithm to determine the corresponding size distribution of particles in the scattering volume.

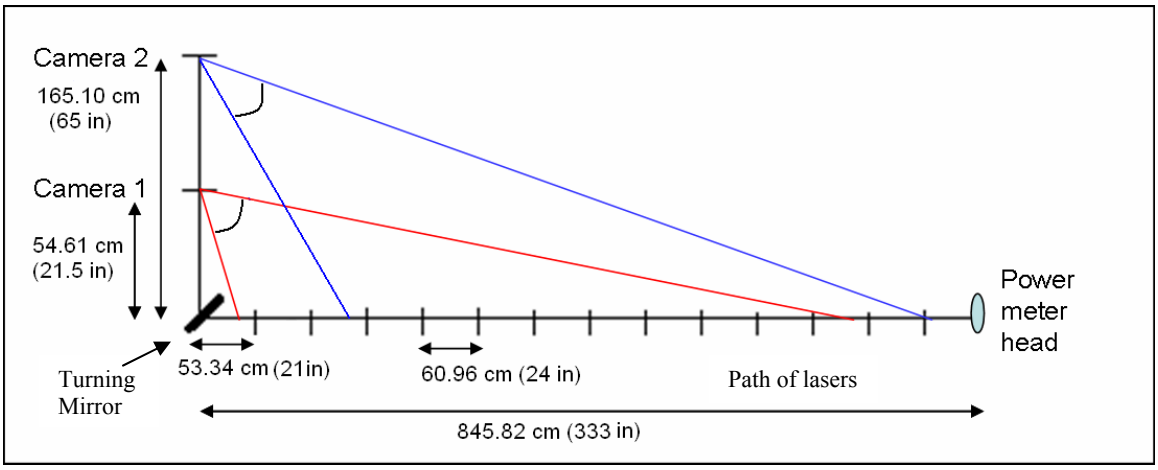


Figure 5-5: EPA camera setup.

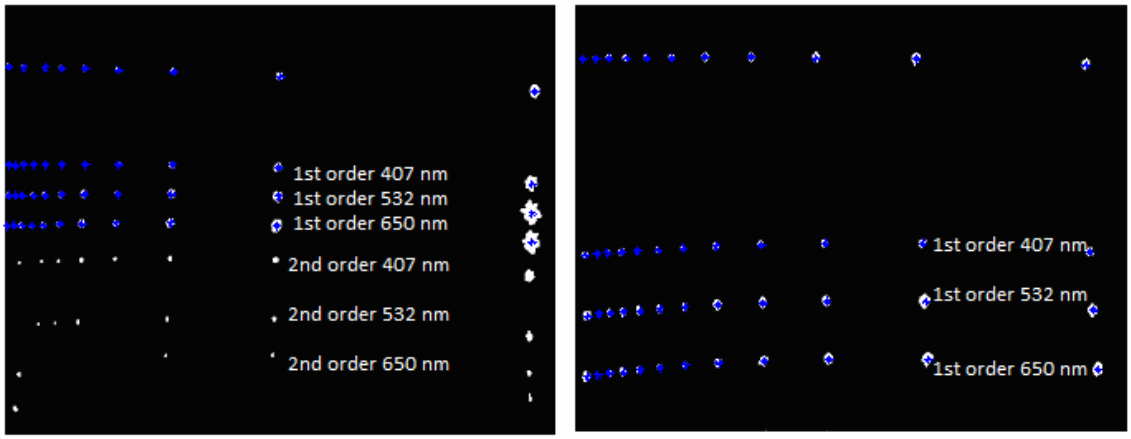


Figure 5-6: Alignment images for Camera 1 (300 lines/mm) and Camera 2 (600 lines/mm).

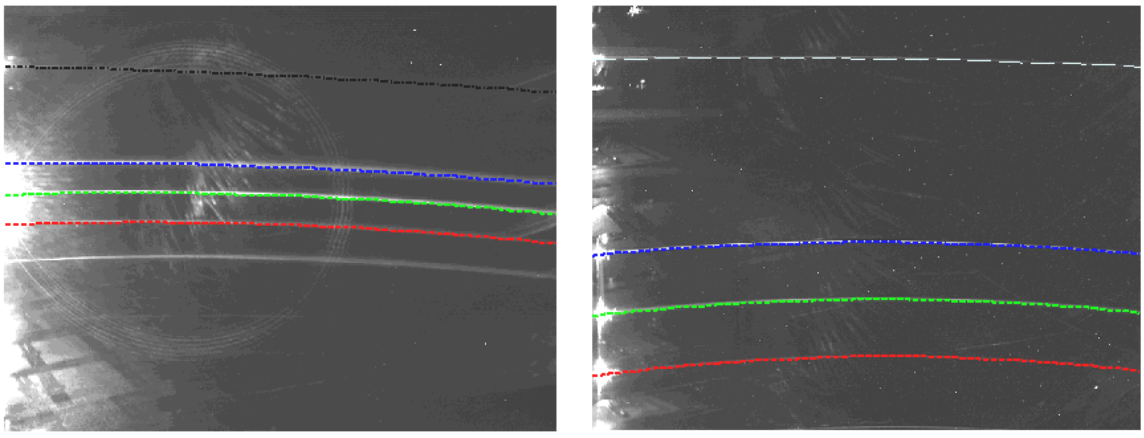


Figure 5-7: Extraction polynomials for Camera 1 and Camera 2.

5.1.3 Supporting aerosol measurement instruments

The aerosols in the wind tunnel were simultaneously monitored by a TSI Model 3321 Aerodynamic Particle Sizer® spectrometer (APS) and a TSI Model 3007 Condensation Particle Counter (CPC). The APS sizes particles into 52 bins in the range from 0.5 to 20 microns using a time-of-flight technique that measures aerodynamic diameter. Aerodynamic diameter is defined as the physical diameter of a unit density (1 gm/cm^3) sphere that settles through the air with a velocity equal to the particle under measure. The APS accelerates the aerosol sample flow and then measures the time it take to cross two points, with larger particles accelerating slower due to their inertia. An advantage to this sizing technique is that the measurement is independent of aerosol type (refractive index). The APS can be programmed to record averaged size distributions at any interval between one second and 18 hours. The maximum particle concentration recommended by the TSI Model 3321 user's manual for approximately ±10% accuracy is 1,000 particles/cm^3, and suggests that collected data is "usable" up to concentrations of 10,000 particles/cm^3. The APS reports size distributions as normalized number concentrations (dN/dlog(d_a)), which means that the particle number concentrations have been divided by the logarithm of the particle size. Normalized number concentrations are converted to number concentrations (dN/dd_a) by multiplying each concentration value by the difference between the logarithm of the size bins lower and upper edge,

$$\frac{\Delta N}{\Delta d_a} = \frac{\Delta N}{\Delta \log(d_a)} \times \left(\log(d_{a,upper}) - \log(d_{a,lower})\right) \tag{5-1}$$

Aerodynamic particle diameter (d_a) is then converted to geometric particle diameter (d_g) using the formula:

$$d_g = \frac{d_a}{\sqrt{SG}}, \tag{5-2}$$

where SG is the specific gravity of the spherical particles.

The CPC can detect particles in the size range of 0.01 to greater than 1.0 micron, at concentrations between 1 and 100,000 particles/cm^3 with ±20% accuracy (TSI model 3007 CPC user's manual). The CPC counts particles by drawing the aerosol sample through vaporized alcohol and then into a cooled condenser. The aerosols act as condensation sites for the vaporized alcohol, so that the aerosols quickly grow to a size where they can be counted by an optical detector. This instrument can detect much smaller particles and much higher particle concentrations than the APS, though it lacks the capability to determine the size distributions.

5.2 MDG Fog

The first test examined the multiwavelength-multistatic scattering from fog particles generated by the MDG MAX APS 3000 fog generator. The amount of fog that is produced by the generator is controlled by adjusting the pressure on the compressed nitrogen tank that feeds the generator. The concentration of the fog was monitored by the APS and the CPC as shown in Fig. 5-8. The dark dashed lines above and below the concentration measurements from the two instruments show the ±20% concentrations, which are the concentration accuracies indicated by the manufacturer. Figure 5-8 also shows the time stretches that data images are recorded during the fog experiment. The difference in concentration reported by the two instruments is due to their different capabilities to detect particles in different size ranges. The APS can only size particles down to aerodynamic particle diameters of 0.5 μm, while the CPC can detect particles down to a single nanometer. The differences in the reported concentrations indicate that roughly half of the particles generated by the MDG fog generator are smaller than the lowest detectable diameter of the APS.

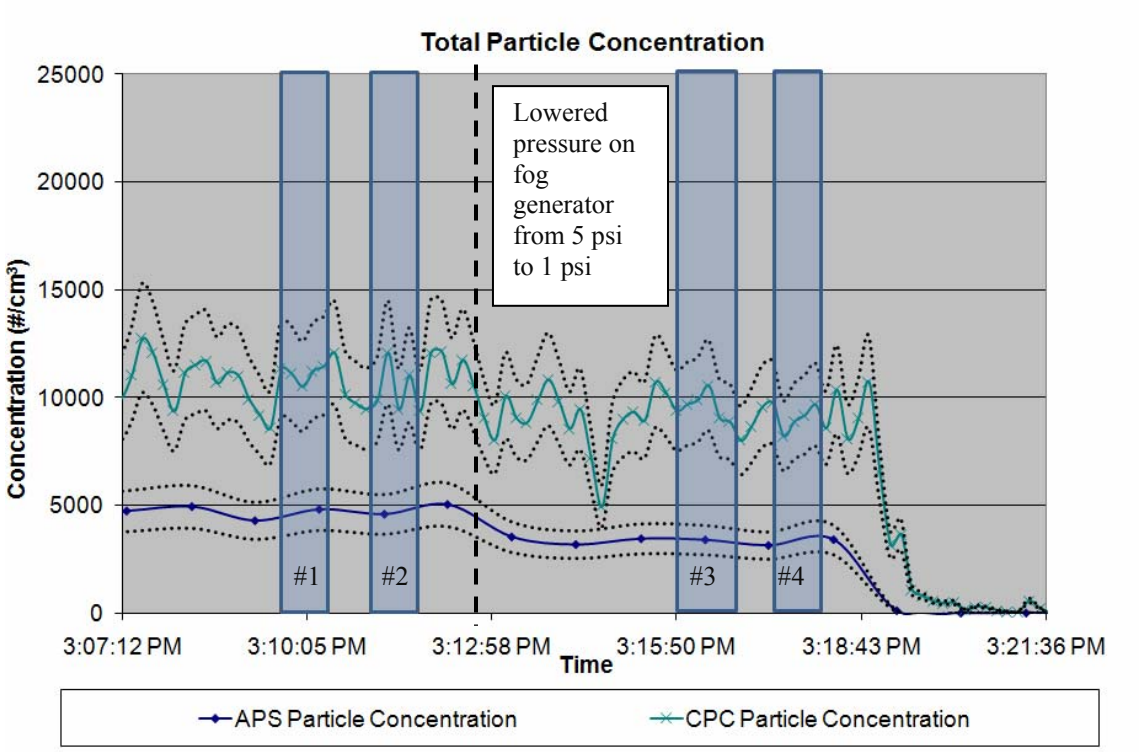


Figure 5-8: Particle concentration as measured by the CPC and APS. Dotted lines indicated ±20% accuracy for the particle counting instruments. Boxes indicate times that data was taken on 24 November for four different datasets, labeled #1 - #4.

It is also important to bear in mind that the recommended maximum concentration level for the APS is 1,000 particles/cm^3 and the concentration of the MDG fog is well above this range. The effect of operating the APS at this concentration level can be seen in the number of times that the APS rejected particle counts due to coincidence. Coincidence occurs when more than one particle is inside the APS measurement chamber during a measurement, and is categorized by the APS read-out record as an 'event 3'. When an 'event 3' is detected, the particle count and size obtained from that measurement is not included in the reported APS size distribution or concentration level. A high number of coincidences skews the concentration level to a value much less than it actually is, and would also change the shape of the size distribution. Figure 5-9 shows the raw counts measured by the APS during the time that dataset #3 was collected. Notice

that a significant number of particles were classified as <0.5 μm (aerodynamic diameter), showing that a large part of the size distribution falls below the range of the APS. The number of coincidence counts, 114,835, is on the same order as the number of counts that get 'binned' into each defined size interval. This will contribute to an under-reporting of the aerosol number concentration by the APS unit. The particle number size distributions (radius) measured by the APS, after correcting for geometric particle size and scaling the distribution by the logarithm of the bin widths, during the same approximate time as the data collection for the four datasets in Fig. 5-8 are shown in Fig. 5-10.

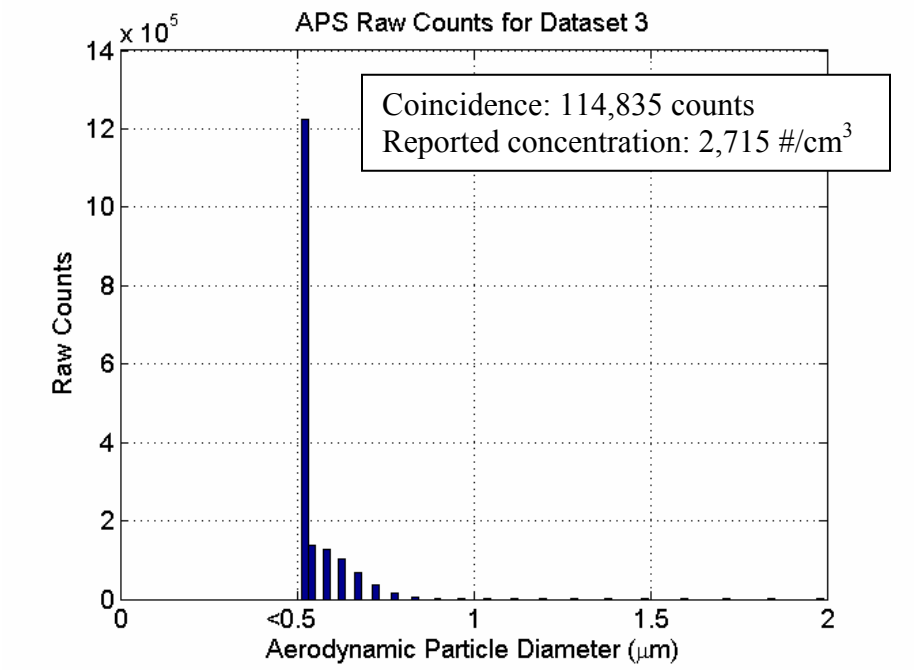


Figure 5-9: Raw counts from APS for 24 Novemeber at ~3:16 PM, including counts of coincidence (more than one particle in the measurement chamber. These counts are not included in reported concentration measurements).

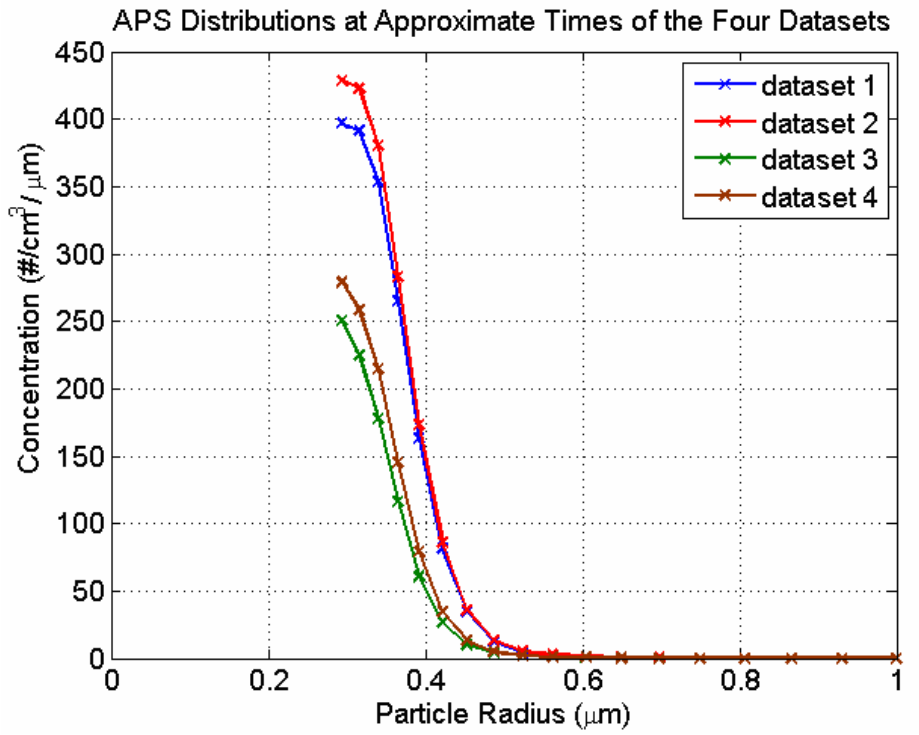


Figure 5-10: APS particle size distribution for the 4 datasets after removing the lowest 'catch-all' size bin.

5.2.1 Polarization ratios

The background image and dark counts were subtracted from the 'raw' scattering images to produce a 'processed' image used for data extraction. The extraction algorithm for the EPA fog used 10% of the maximum intensity in each column as the cut-off point to determine how many rows to integrate across for each wavelength and column. The integrated quantities represent scattered intensities for each wavelength as a function of scattering angle and polarization. Examples of these scattering intensities are shown in Fig. 5-11 with a five-point moving-average smoothing applied. Only the pairs of parallel and perpendicular intensities for each wavelength can be compared, not the relative intensities between wavelengths because each laser diode had different power levels and transmission efficiencies through the transmission and collection optics.

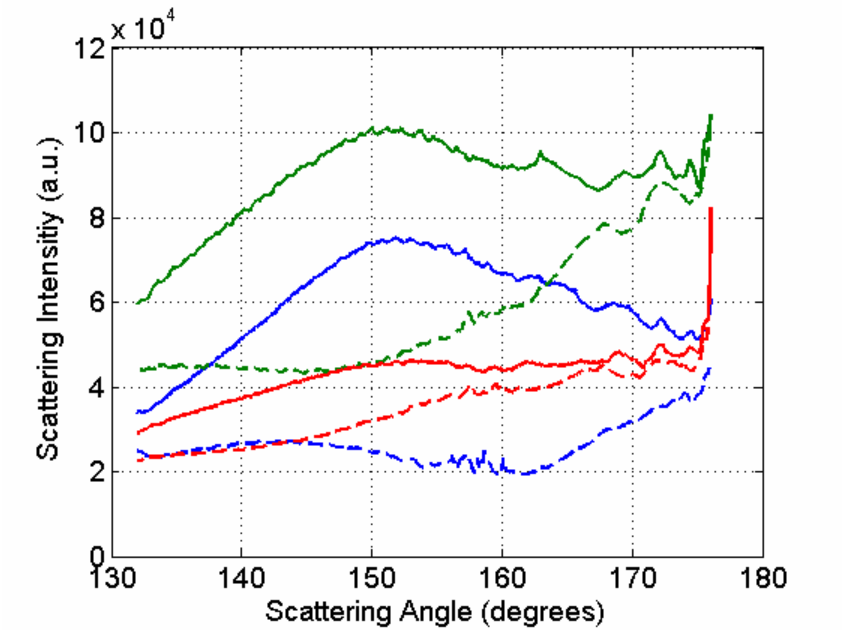


Figure 5-11: Relative scattering intensities for parallel incident light (solid lines) and perpendicular polarized light (dashed lines) at 407 nm (blue lines), 532 nm (green lines), and 650 nm (red lines).

The extracted parallel scattering intensities are divided by the extracted perpendicular intensities to form the polarization ratio as a function of wavelength and CCD column. The alignment images are used to map each column of the CCD array to a scattering angle (Fig. 5-11) to produce an angle-dependent polarization ratio (Fig. 5-12). The spurious spikes at the peak of the 407 nm polarization ratio curve between 155 and 160 degrees in Fig. 5-12 are caused by reflections off of the back wall, as shown by the scattering image in Fig. 5-13. A 5-point moving-average filter is applied to the scattering intensities prior to the division. The number of points to use in the filter was selected based on the knowledge that the inversion algorithm computed the error between the polarization ratios at half degree intervals. Due to the geometry of our focusing lens and CCD array, seven columns or horizontal points corresponds to a half degree (i.e. scattering angle) smooth.

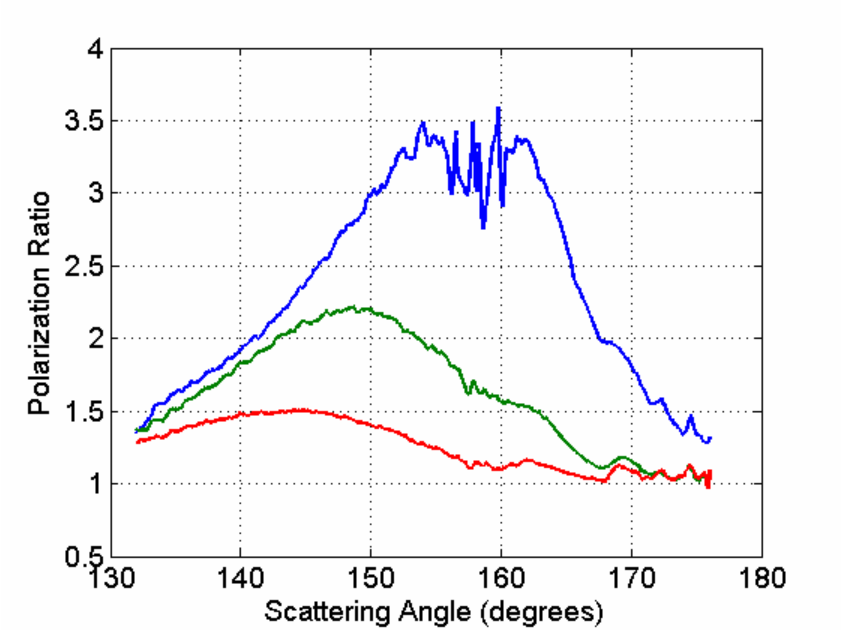


Figure 5-12: Polarization ratio for dataset #3 with 5-point moving-average smooth applied.

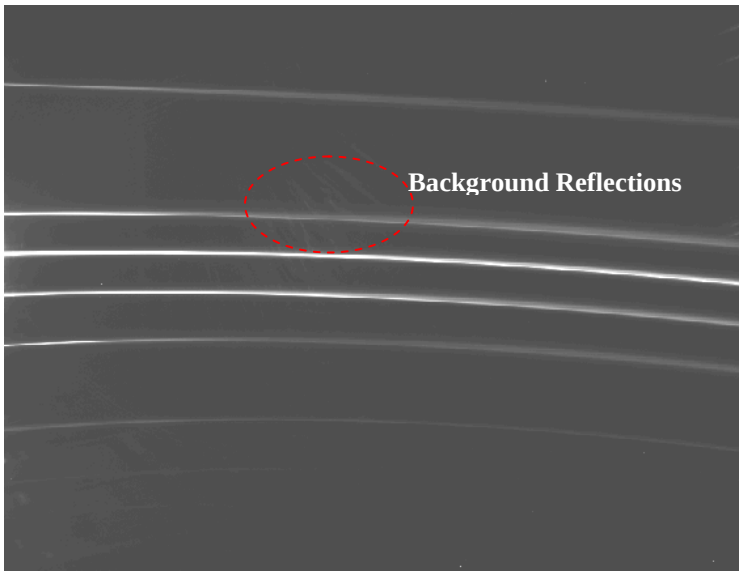


Figure 5-13: Scattering image during the EPA fog experiment.

The measured polarization ratios for datasets #1 - #4 are shown in Figs. 5-14 and 5-15, and information regarding the collection of each dataset are summarized in Table 5-1. The location and magnitude of the peaks are similar for all four datasets, which lends confidence to the measurement. There are distinct differences between the polarization ratios collected when

the fog generator was set at the higher pressure setting of 5 psig (datasets #1 and #2) and the polarization ratio curves measured using the lower pressure setting of 1 psig (dataset #3 and #4). This shows that the particle size distribution generated may change as a function of the pressure setting of the instrument.

Table 5-1: Collection information for datasets #1 - #4.

Dataset	Angle Range	Acquisition Start Time	Integration Time	Fog Pressure	Diffraction Grating
#1	126° - 169°	3:09:58 PM	1.3 s	5 psig	600 lines/mm
#2	132° - 176°	3:11:20 PM	0.3 s	5 psig	300 lines/mm
#3	132° - 176°	3:16:10 PM	0.3 s	1 psig	300 lines/mm
#4	126° - 169°	3:17:36 PM	1.3 s	1 psig	600 lines/mm

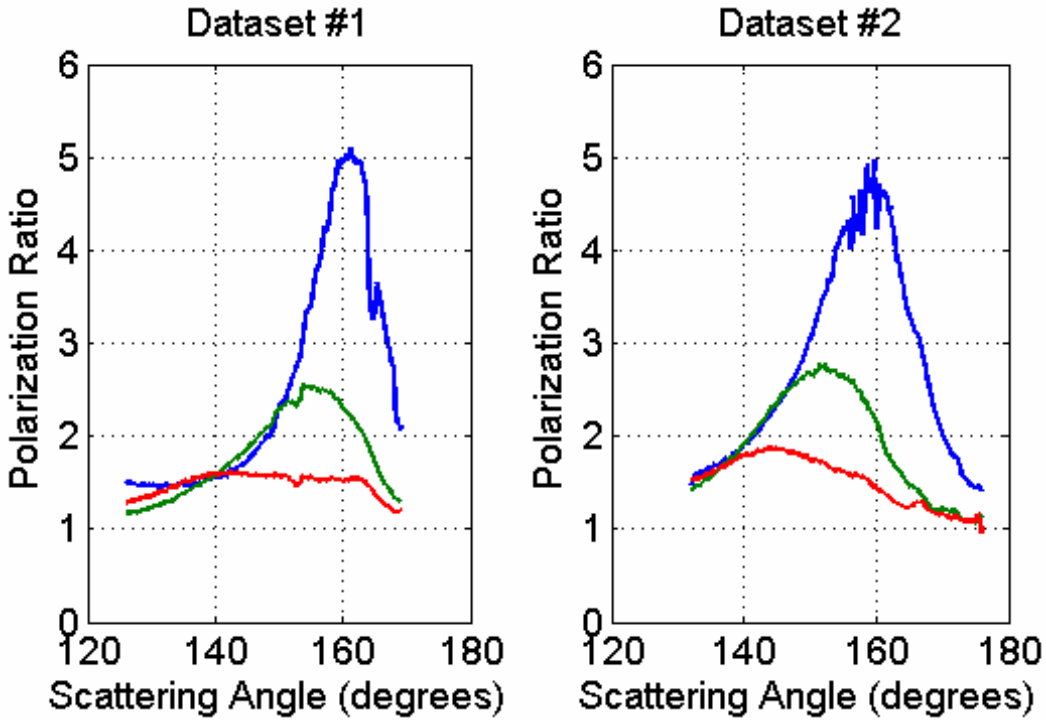


Figure 5-14: Polarization ratio for datasets #1 and #2.

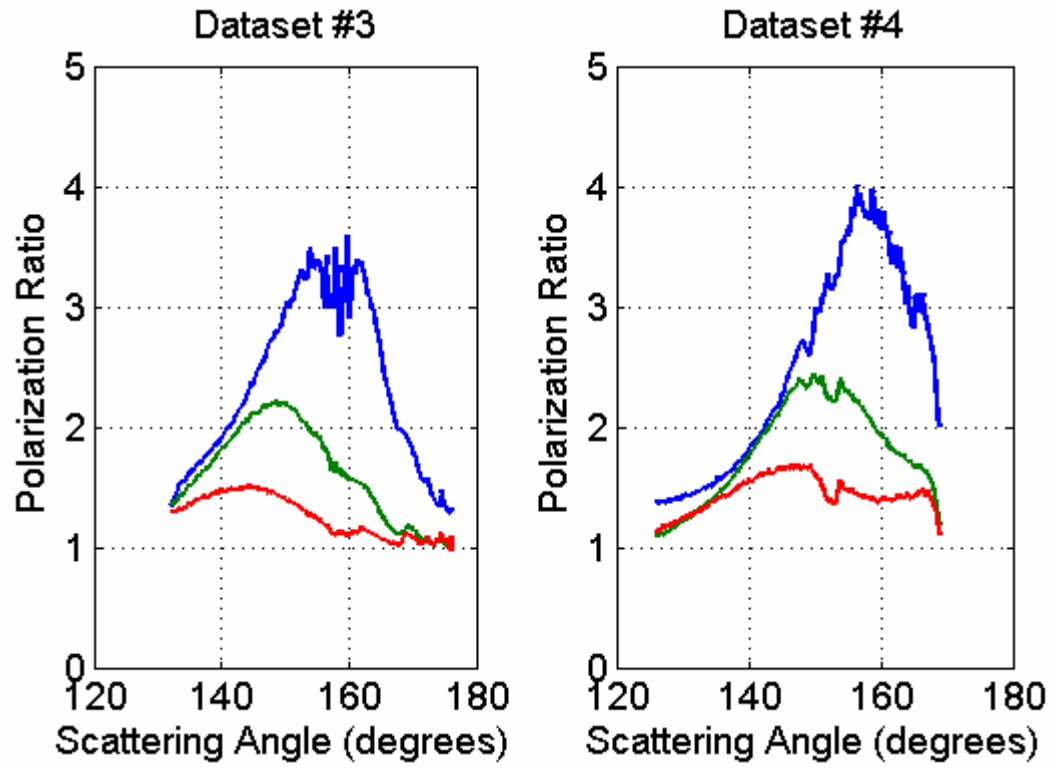


Figure 5-15: Polarization ratio for datasets #3 and #4.

5.2.2 Inversion parameters and results

All four measured polarization ratios are first inverted using the simple two-variable genetic algorithm explained in Section 3.2.1 that produces the geometric mean and geometric standard deviation for a single lognormal probability density function. A single fixed value is used for the refractive index of the particles, requiring the algorithm to load only one look-up table of unit scattering intensities, significantly reducing the time of computation for each generation of the algorithm. The average computation time to convergence for the genetic algorithm is approximately one minute on a Pentium D processor. The inverted lognormal probability density functions retrieved by the genetic algorithm for dataset #1 through dataset #4 are summarized in Table 5-2.

Table 5-2: Summary of two-variable inversion of datasets #1-#4 for EPA fog.

	Geometric Mean Radius, r_g	Geometric Standard Deviation, σ_g
Dataset #1	0.23 μm	1.30
Dataset #2	0.23 μm	1.29
Dataset #3	0.20 μm	1.32
Dataset #4	0.21 μm	1.34

A grid search algorithm was run for a truncated section of the solution space to ensure that the algorithm was converging on the global solution. The grid search varied the lognormal geometric mean from 0.1 microns to 1.0 micron by 0.01 micron steps and varied the geometric standard deviation from 1.01 to 3.0 by 0.01 steps. The truncated solution space is shown in Fig. 5-16, and the geometric mean and geometric standard deviation that was produced by the genetic algorithm inversion for dataset #3. The grid search shows that the highest fitness (or lowest squared error between the measured and modeled polarization ratios) occurs at a geometric mean radius of 0.20 μm and geometric standard deviation of 1.32, which matches the results from the genetic algorithm.

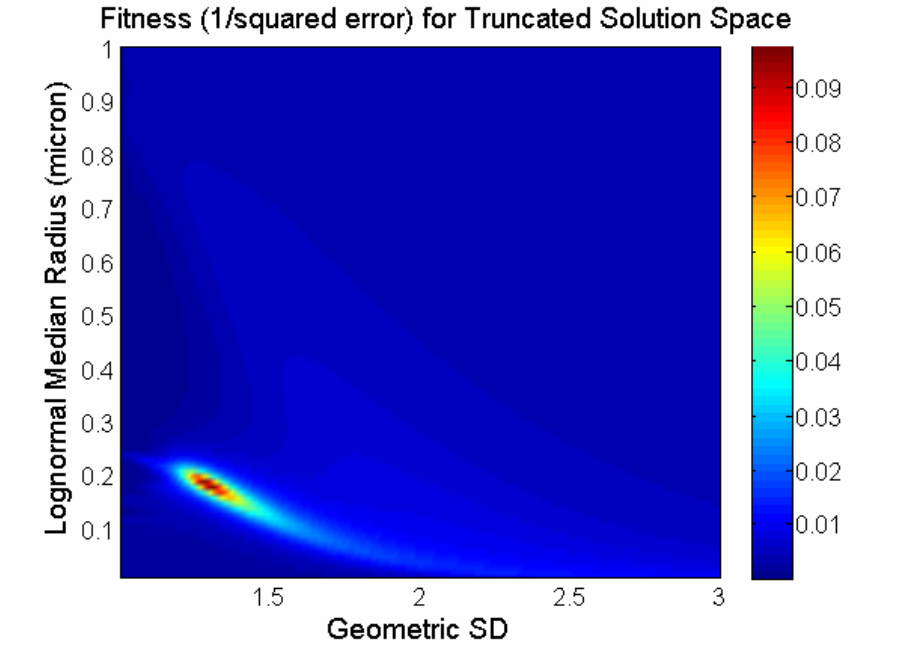


Figure 5-16: Solution space for dataset #3 using a fixed refractive index of 1.47 + i0.001.

The concentration measurements reported by the APS and the CPC are around 10^4 particles/cm^3 as shown in Fig. 5-8. When the concentration is added to the algorithm as a retrievable variable, the concentration that is returned is highly variable (between 10^3 and 10^6 particles/cm^3) because the concentration of the smoke is within a range where the polarization ratio is less sensitive to the molecular scattering contribution (see Chapter 2). The way that the concentration of the particles is determined in the genetic algorithm is based on the contribution of the molecular scattering to the polarization ratio, and when the concentration is high, the molecular scattering contribution is very small, and the polarization ratio changes little with a change in particle concentration.

Another way of determining the concentration of particles is by measuring the extinction of light as it passes through the scattering volume. Power measurements at the three wavelengths were recorded during this experiment using a broadband power meter: however, these measurements should be viewed with a rather skeptical eye. The power meter was mounted on a ring stand at the end of an 8.5 m path, and the laser beams propagating along the path were turned using a mirror which was mounted to a ring stand at the upstream end of the chamber. The ring stands were set on the floor of the EPA tunnel as shown in Fig. 5-3a, and there was a large amount of vibration from the tunnel floor. The active area of the power meter is rather small (1 cm^2), and the lasers could sometimes vibrate back and forth quickly across this active area. The power measurements were recorded by hand based on watching the fluctuations of the power over a few seconds and taking a quick mental average. These power measurements are displayed in Table 5-3 with the resulting extinction coefficient. The geometric mean diameter of the lognormal size distribution retrieved by the genetic algorithm, 0.4 μm, was used to calculate the extinction cross section at the laser wavelengths. The extinction cross sections for a 0.4 μm particle (diameter) for the three wavelengths are: 0.4075 μm^2 for 407 nm, 0.2594 μm^2 for 532

nm, and 0.182 μm^2 for 650 nm. These cross sections are then used to calculate the total particle concentration that would be required to produce the extinction coefficients calculated from the power measurements and the path length of 8.5 m. The calculated concentrations do vary based on wavelength, but this was expected from the data collection method (the so-called 'eye-balling' method). The calculated concentrations (other than the 532 nm horizontal measurement) are within ±20% of the concentration measured by the CPC and do serve as an additional ground-truth for the approximate concentration level of the MDG fog. The optical depth, calculated as the extinction times the path length, is much less than 0.1, indicating that multiple scattering should not be a significant factor in the measurements (van de Hulst, 1957).

Table 5-3: Power measurements to calculate extinction for MDG fog

	Horizontal Polarization			Vertical Polarization		
	407 nm	532 nm	650 nm	407 nm	532 nm	650 nm
Power w/o aerosols (mW)	13.96	14.10	13.5	11.28	14.3	12.89
Power w/MDG fog (mW)	13.3	13.91	13.34	10.8	14.07	12.7
Total Extinction From Power Measurements (1/km)	5.698	0.758	1.403	6.116	1.907	1.747
Particle Concentration Calculated From Power Measurements (#/cm^3)	13,983	2,923	7,707	12,554	7,354	9,599
Average CPC Particle Concentration (#/cm^3)	10, 750			10,750		
Total Extinction Calculated From CPC Concentrations (1/km)	4.38	2.79	1.96	4.38	2.79	1.96

The average concentration measured by the CPC for each dataset (displayed in Table 5-4) is used to scale the lognormal probability density functions to produce particle size distributions

for the four datasets. The particle size distributions are divided by the logarithms of the bin widths to produce a 'normalized' particle size distribution (dN/dlog(d)), shown in Fig. 5-17 for the four datasets. The 'normalized' particle size distributions measured by the APS at the same approximates times as the measured datasets are also shown in Fig. 5-17 for comparison. The lognormal parameters and average concentration used to create the normalized particle size distributions are summarized in Table 5-4 for each dataset.

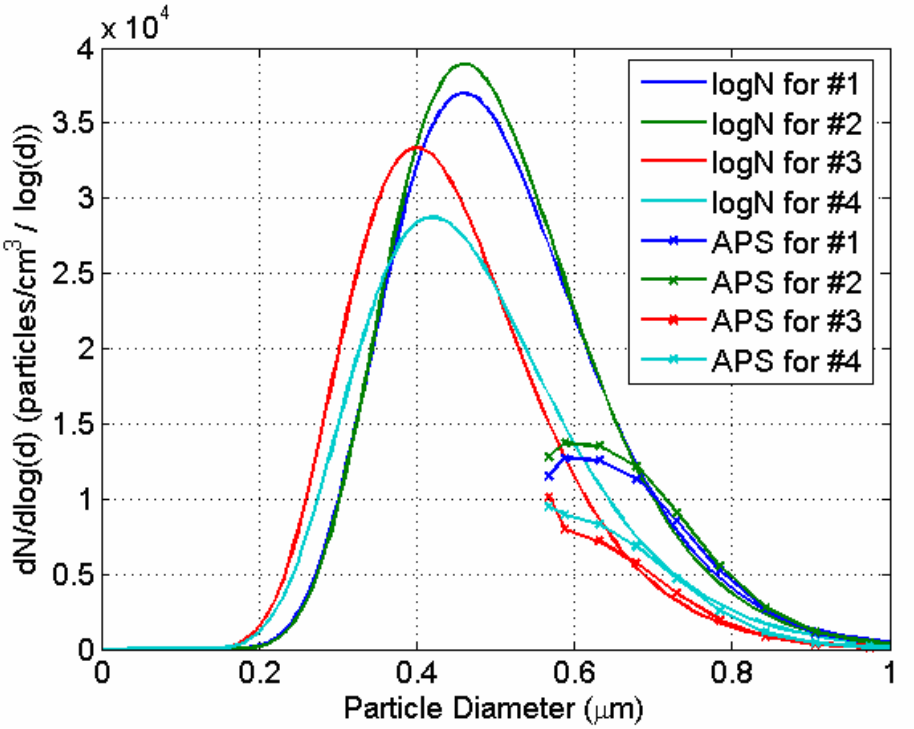


Figure 5-17: Normalized lognormal size distributions inverted from the polarization ratios (solid lines) and the corresponding normalized size distribution measured by the APS (lines with markers).

Table 5-4: Summary of parameters used to calculate normalized particle size distributions shown in Fig. 5-18 for datasets #1-#4 for MDG fog.

	Geometric Mean Radius, r_g	Geometric Standard Deviation, σ_g	Average CPC Concentration, N_T
Dataset #1	0.23 μm	1.30	10,561 #/cm^3
Dataset #2	0.23 μm	1.29	10,790 #/cm^3
Dataset #3	0.20 μm	1.32	10,079 #/cm^3
Dataset #4	0.21 μm	1.34	9,153 #/cm^3

Unfortunately, only a portion of the particles produced by the MDG fog generator fell within the size range of the APS, making it difficult to quantify the total difference in size distribution between the APS and the inversion algorithm. The difference between normalized particle size distributions at particle diameters within the APS range is most likely due to a collection of factors: (1) operating the APS outside of its recommended concentration range; (2) using a single value for the complex refractive index for all three wavelengths in the inversion algorithm, (3) error in the polarization ratio introduced by the variation of retardance of the polarizing beamsplitter as a function of wavelength (the incident light is not perfectly parallel or perpendicular to the scattering plane); and (4) errors introduced into the polarization ratio by the background reflections.

The recommended operating range of the APS and the error in the size distribution caused by 'coincidence' has been previously discussed in Sections 5.1.3 and 5.2. The concentration level of ~10,000 particles/cm^3 is well above the recommended maximum concentration of 1,000 particles/cm^3. A high concentration of particles increases the likelihood that two particles are in the measurement chamber of the APS unit at the same time, called coincidence. A high level of coincidence will skew the size distribution and concentration reported by APS. This is the most likely cause of the large discrepancy between the normalized size distributions for particle diameters between ~0.5 and 0.7 μm, shown in Fig. 5-17.

The remaining sources of error all relate to the measurement and modeling of the polarization ratio. The fit between the measured polarization ratios, and the modeled polarization ratios using the parameters shown in Table 5-4, are shown in Fig. 5-18. The refractive index of the fog fluid is not supplied by the manufacture, but the main ingredient listed on the MSDS sheet is mineral oil. A refractive index of 1.47-*i*0.001 was used in the inversion algorithm for all three wavelengths based on the refractive index information that could be found for mineral oil (Verkouteren, 2010). In reality, the complex refractive index will vary as a function of

wavelength, as shown in Fig. 5-19, with the shorter wavelengths having higher real and imaginary refractive indices.

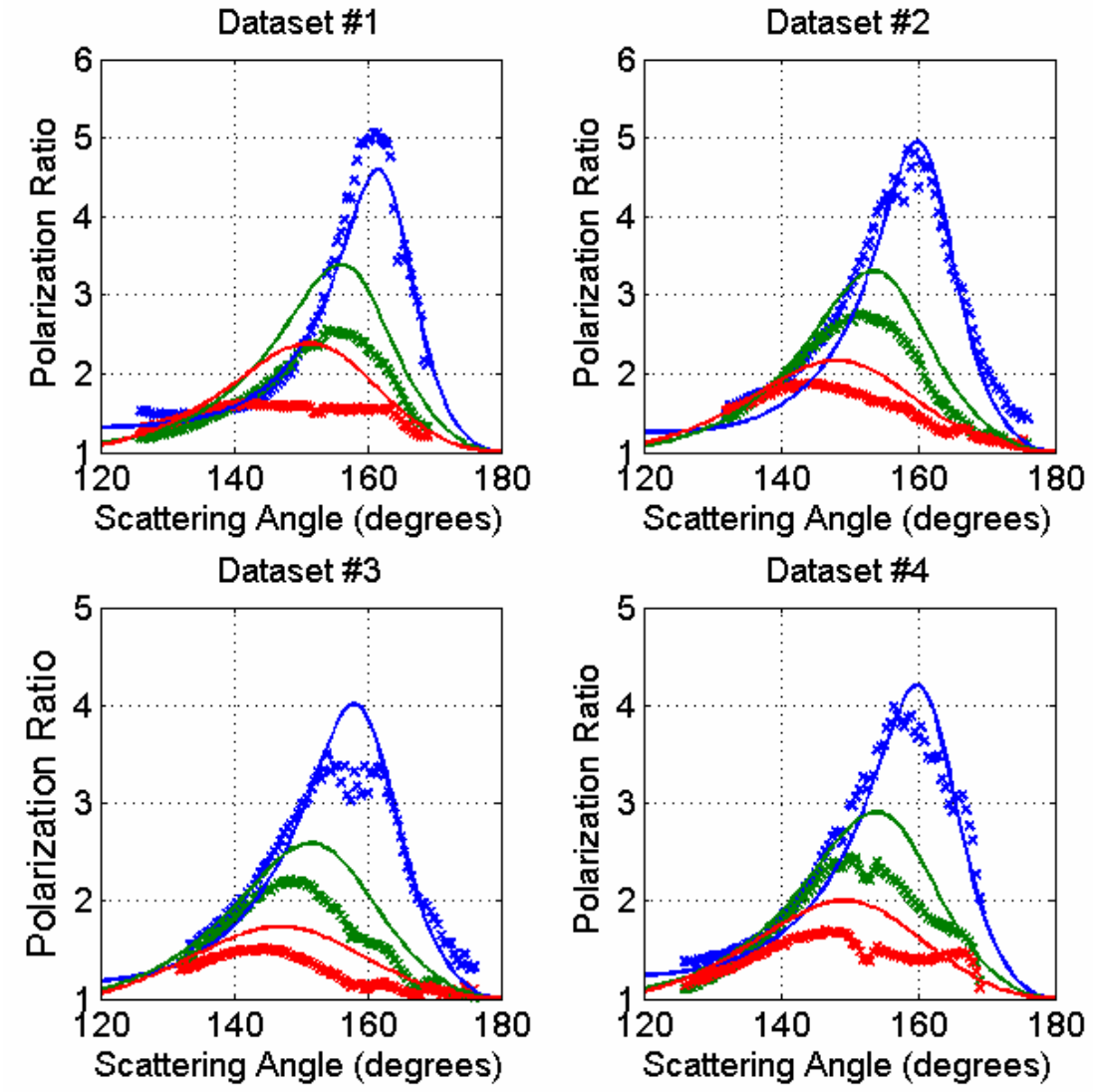


Figure 5-18: Comparison between measured polarization ratio and model polarization ratio using particle size distribution retrieved by the two-variable genetic algorithm for dataset #1through #4.

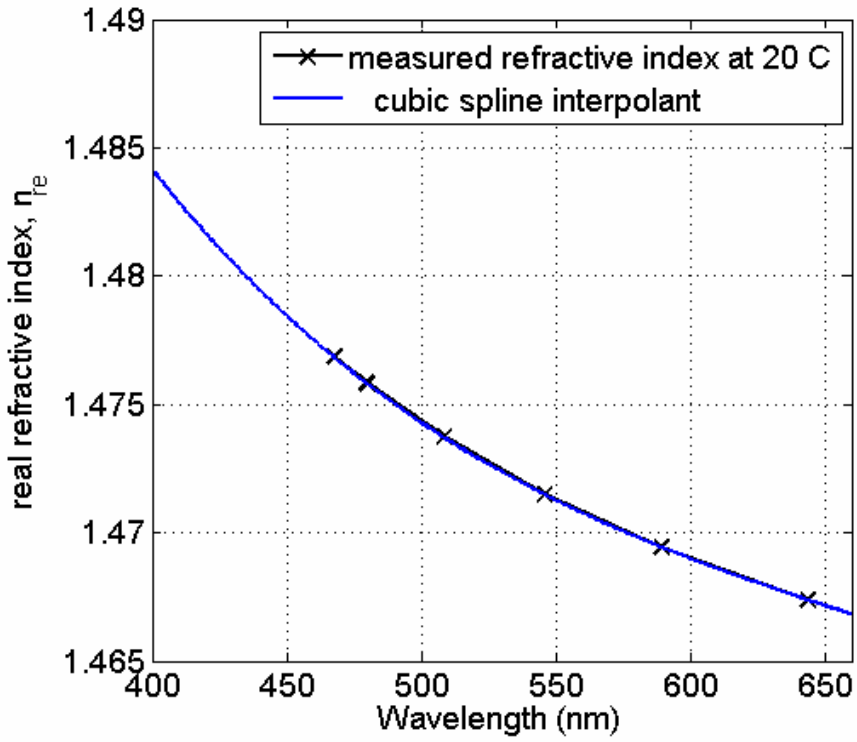


Figure 5-19: Real refractive index for mineral oil as a function of wavelength (Verkouteren, 2010).

The size distribution retrieved by the genetic algorithm was used to explore the squared error fit between the measured and modeled polarization ratio as the complex refractive index varies. Figure 5-20 shows the fitness (inverse of the squared error between the measured and modeled polarization ratio) of the retrieved size distribution as a function of real and imaginary refractive index for dataset #2. The pre-calculated scattering tables generated for the genetic algorithm were used to perform this grid search, therefore the real part of the refractive index varies from 1.43 to 1.53 by 0.005 and the imaginary part of the refractive index assumes values of {0.1, 0.05, 0.01, 0.005, 0.001, 0.0005, 0.0001, and 0}. Fig. 5-20 confirms that a better fit between the measured and modeled polarization ratio is achieved when the complex refractive index varies for each wavelength.

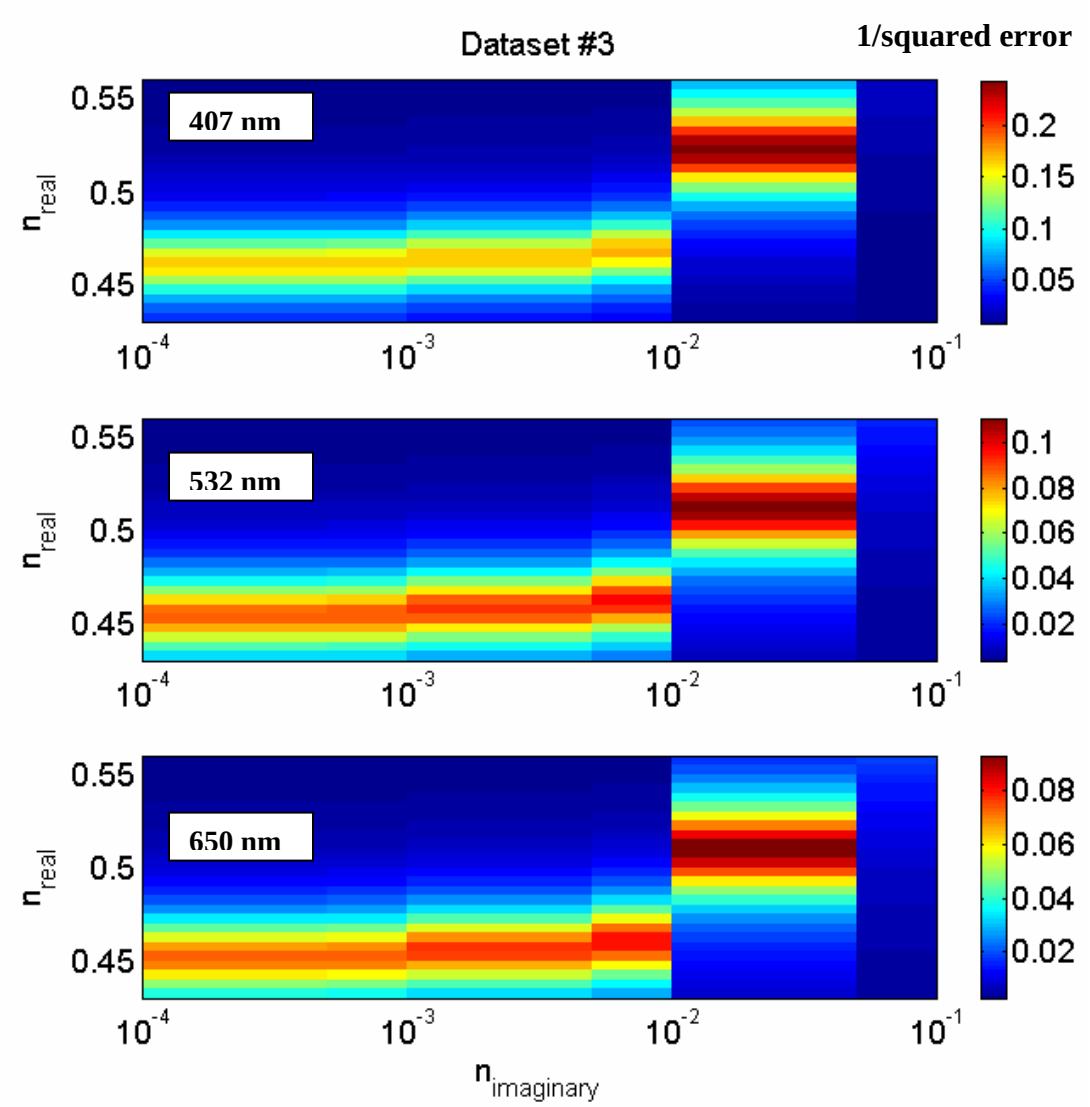


Figure 5-20: Fitness (1/squared error) for modeled and measured polarization ratio for dataset #2 using lognormal size distribution retrieved by genetic algorithm (Table 5-4) as a function of complex refractive index.

A grid search indicates that the best match between measured and modeled polarization ratios for dataset #3 occurs when using the refractive index of 1.535 + i0.05 at 407 nm, and 1.515 + i0.05 at 532 nm and 650 nm. A summary of the complex refractive indices that produce the lowest squared error for each dataset is summarized in Table 5-5. These real refractive indices are higher than expected based on the measured indices for mineral oil shown in Fig. 5-19. The higher refractive indices could be a result of the other ingredients in the fog fluid, or that a

heavier grade of mineral oil was used in the fog fluid than was used for the measurements in Fig. 5-19. The best-fit refractive indices vary slightly between datasets at each wavelength, and is probably a result of the resolution of the grid search and the errors in the measured polarizations ratios introduced by the background reflections. If this grid search were repeated using finer grid spacing for the real and imaginary parts of the refractive index, it is likely that the variation in retrieved indices for the four datasets will be much reduced. This would require the computation of additional scattering intensity look-up tables.

Table 5-5: Summary of complex refractive indices retrieved by the grid search for dataset #3.

	r_g	σ_g	N_T	$n_{re} + in_{im}$ 407 nm	$n_{re} + in_{im}$ 532 nm	$n_{re} + in_{im}$ 650 nm
Dataset #1	0.23 μm	1.30	10,561 #/cm^3	1.525 + i0.05	1.505 + i0.05	1.505 + i0.05
Dataset #2	0.23 μm	1.29	10,790 #/cm^3	1.535 + i0.05	1.515 + i0.05	1.515 + i0.05
Dataset #3	0.20 μm	1.32	10,079 #/cm^3	1.520 + i0.05	1.510 + i0.05	1.510 + i0.05
Dataset #4	0.21 μm	1.34	9,153 #/cm^3	1.535 + i0.05	1.515 + i0.05	1.515 +i0.05

A comparison between the measured and modeled polarization ratios using the retrieved refractive indices and the lognormal size distribution for dataset #3 is shown in Fig. 5-21. The complex refractive indices retrieved by the grid search definitely improve the fit between the polarization ratios, but there is still a noticeable offset between the measured and modeled curves. This offset is most likely a result of the error introduced by the background reflections, particularly in the scattering angle range of 150 to 170 degrees. Figure 5-22 shows an example of what the measured polarization ratios would probably look like if the background reflections were not present in the scattering data.

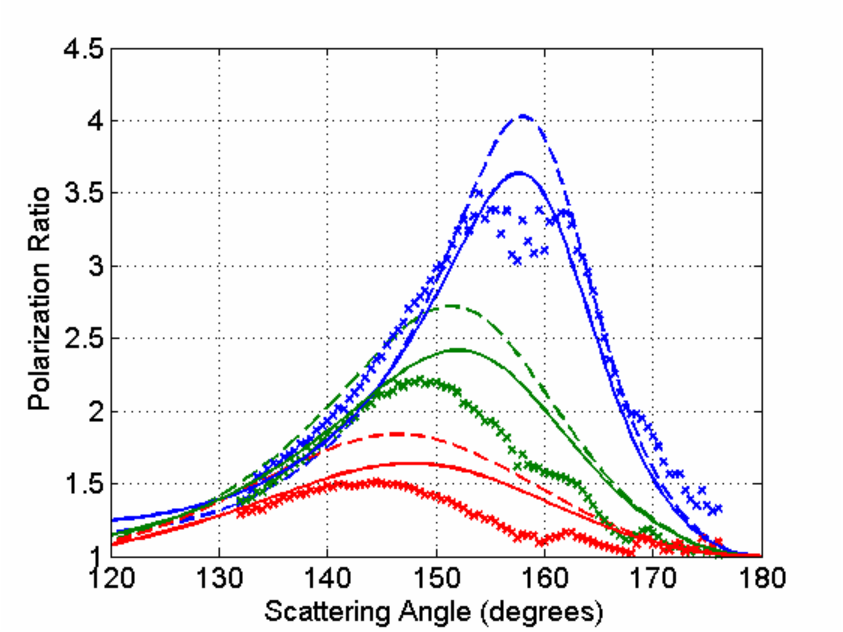


Figure 5-21: Comparison of measured polarization ratios (x) to modeled polarization ratios using a fixed refractive index of 1.47 + i0.001 for all wavelengths (dashed lines) and modeled polarization ratios using refractive index retrieved from grid search (solid lines) for dataset #3.

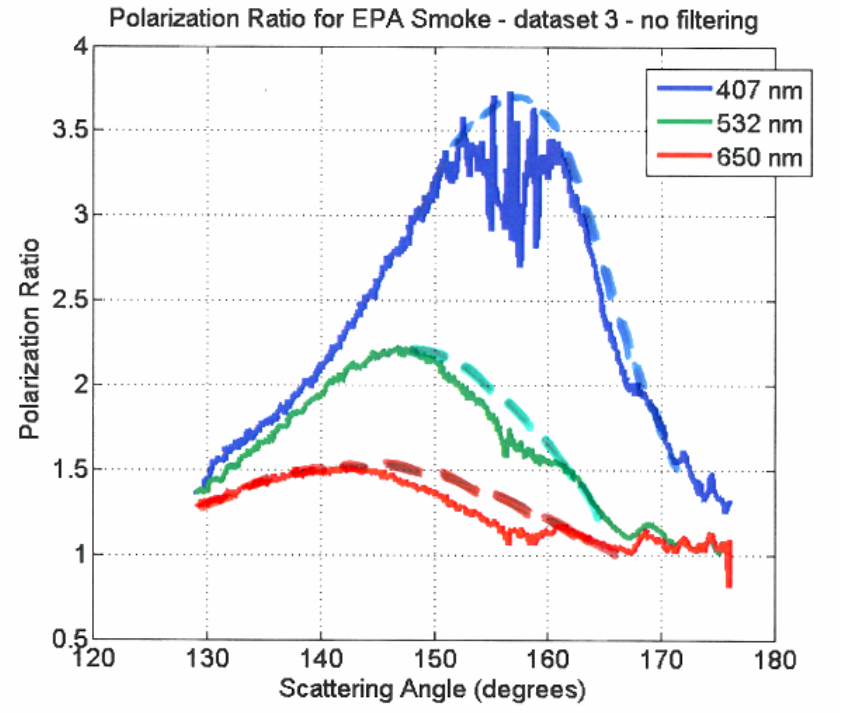


Figure 5-22: Example of possible polarization ratios without errors introduced by background reflections.

The variation in retardance of the polarization beamsplitter as a function of wavelength will also contribute some error to the fit between the measured and modeled polarization ratios. The model is assuming that the incident light is polarized perfectly parallel and perpendicular to the scattering plane for all wavelengths. In reality, there is a slight deviation away from parallel and perpendicular polarizations with respect to the scatter plane, particularly for the 407 nm wavelength. Figure 5-23 shows calculated polarization ratios at the three wavelengths that have been calculated assuming a perfect retardance of 0.5 for all wavelengths (solid lines) and the polarization ratios calculated using the polarization retardances reported in the beamsplitter datasheet (see Fig. 4-2). The curves are calculated using the variable-complex refractive index results for dataset #3 that are tabulated in Table 5-5. The variance in retardation causes a shift in the 407 nm polarization ratio, and virtually no change in the 532 nm and 650 nm polarization ratios, as shown in Fig. 5-23. The error introduced by this slight offset is dominated by the error introduced into the measured polarization ratio by the reflections from the plastic.

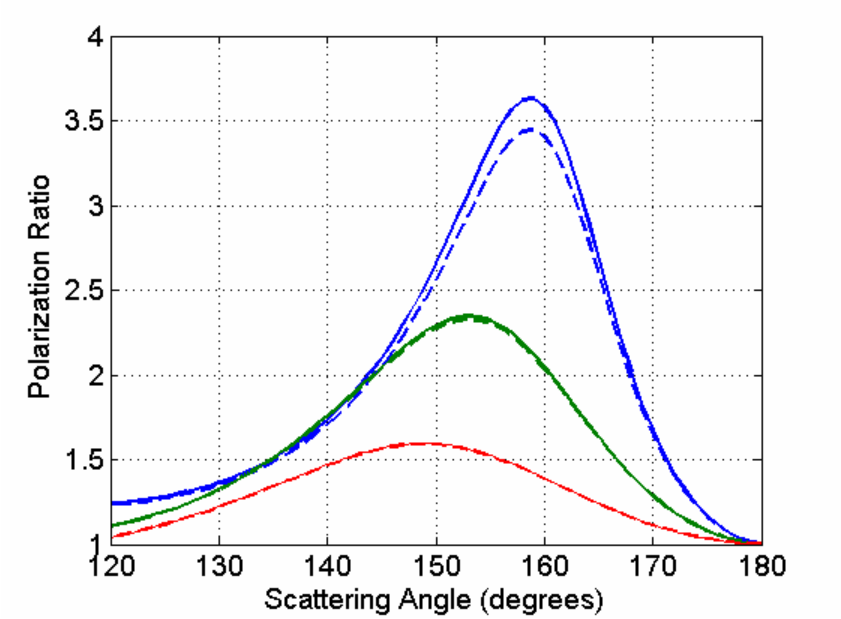


Figure 5-23: Effect of variation in polarization retardance as a function of wavelength using retrieved parameters for dataset #3 in Table 5-5.

5.3 Vibrating Orifice Aerosol Generator

TSI's Vibrating Orifice Aerosol Generator (model 3450) creates highly monodisperse aerosol size distributions using a voltage controlled vibrating orifice. A syringe pump feeds a liquid solution through a small orifice, and the vibration breaks the stream into uniform droplets. The droplet stream passes through a drying column, which prevents the droplets from coagulating and evaporates any volatile portion of the droplets. The VOAG generates primary droplets in the 21- to 48-micrometer range using a standard, interchangeable set of 10- and 20-micrometer nominal diameter orifices. The final diameter of the particle produced by the VOAG is calculated as,

$$D_p = \left(\frac{6QC}{\pi f} \right)^{\frac{1}{3}}, \tag{5-3}$$

where Q is the liquid flow rate in mL/sec, f is the oscillation frequency in Hz, and C is the volumetric concentration of the nonvolatile portion of the solution (VOAG manual). The solution mixture of volatile and non-volatile components used to generate the droplets determines the amount of evaporation and the ultimate particle size.

5.3.1 Producing monodisperse particles

A solution of ethanol alcohol and oleic acid is mixed to produce monodisperse particle size distributions with median diameters of five microns. The VOAG uses a liquid feed rate of 0.16 mL/min and an oscillation frequency of 67 kHz, to produce primary droplet diameters of 42.36 μm. Five micron particles are desired from a 42.36 μm primary droplet, requiring a nonvolatile volumetric concentration of $(5/42.36)^3$, which gives an ethanol to oleic acid mixing ratio of roughly 500:1. Five VOAGs were simultaneously running in the aerosol tunnel, producing

5*67,000=335,000 particles every second. The expected concentration of particles in the wind tunnel can be calculated using the total number of particles produced per second (335,000), the wind speed (2 km/hr), the cross-sectional area of the test tunnel (~3 m x 3.7 m), and the transport efficiency (~30%).

$$N = \frac{335{,}000\,particles}{\sec} \times \frac{3600\sec}{2000m} \times \frac{1}{3m \times 3.7m} \times \frac{1m^3}{10^6\,cm^3} \times 0.3 = \frac{0.016\,particles}{cm^3}$$

The total concentration of the oleic acid droplets as measured by the APS is shown in Fig. 5-24. The blue box indicates the time of measurements for an analyzed dataset and the corresponding APS size distribution for the measurement timeframe is shown in Fig. 5-25.

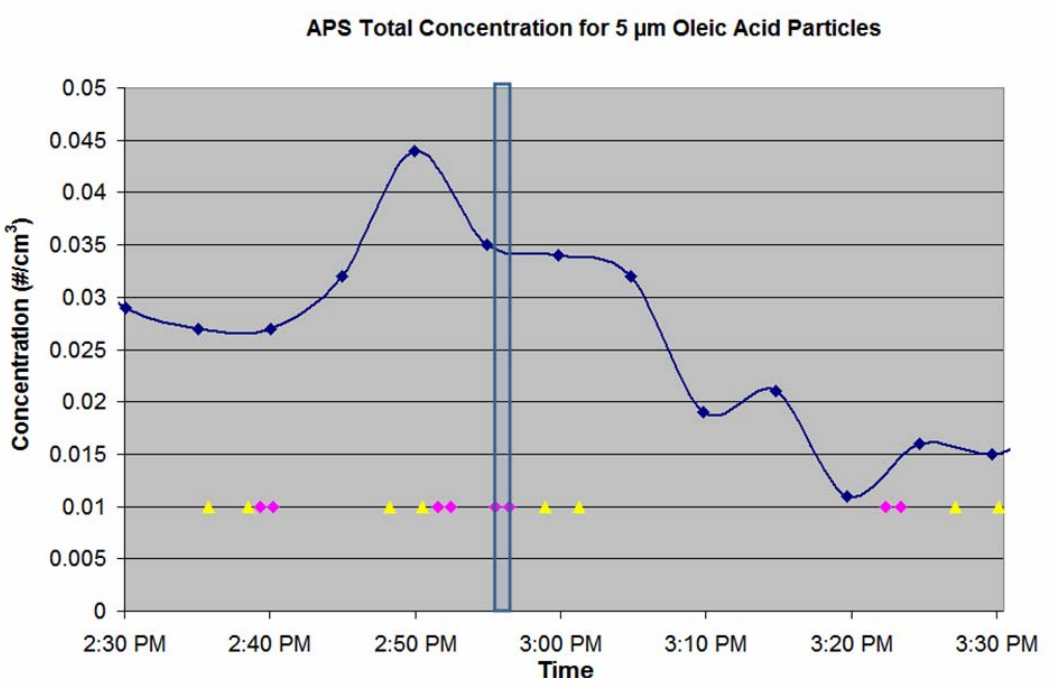


Figure 5-24: Concentration of 5 µm oleic acid droplets as measured by the APS on 23 November. Squares and triangles indicate data images acquired by the two cameras and the blue box indicates the dataset analyzed for this work.

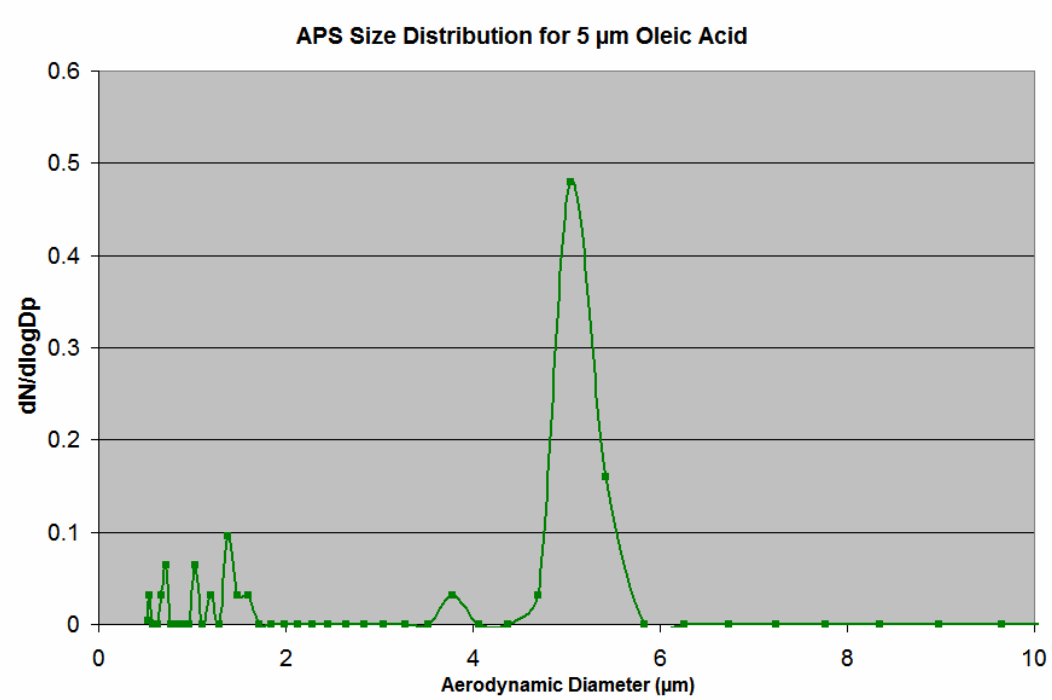


Figure 5-25: Normalized particle size distribution measured by the APS during the collection of the analyzed datasets.

5.3.2 Image processing techniques

The low concentrations of the oleic acid particles requires integration times on the order of half a minute to several minutes for the CCD cameras to collect sufficient signal. Long integration requires an extremely low background light, and steps were taken to minimize stray light in the aerosol tunnel. Black plastic was laid along the top and covered both sides of the transparent window of the HETS section of the aerosol tunnel, and all lights in the work bay where the tunnel is located were turned off. The inside wall of the aerosol tunnel that would be in the field of view of the CCDs was also covered in black plastic to hopefully minimize stray reflections off of this back wall. Unfortunately, this black plastic added an interesting complexity to the analysis of the scattering data by introducing 'rippled' reflections on the hanging folds of the plastic directly behind the laser beams, see Fig. 5-26. The circular rings seen in the scattering

image in Fig. 5-26a are caused by a circular scratch on the grating and add additional error into the measured scattering phase functions.

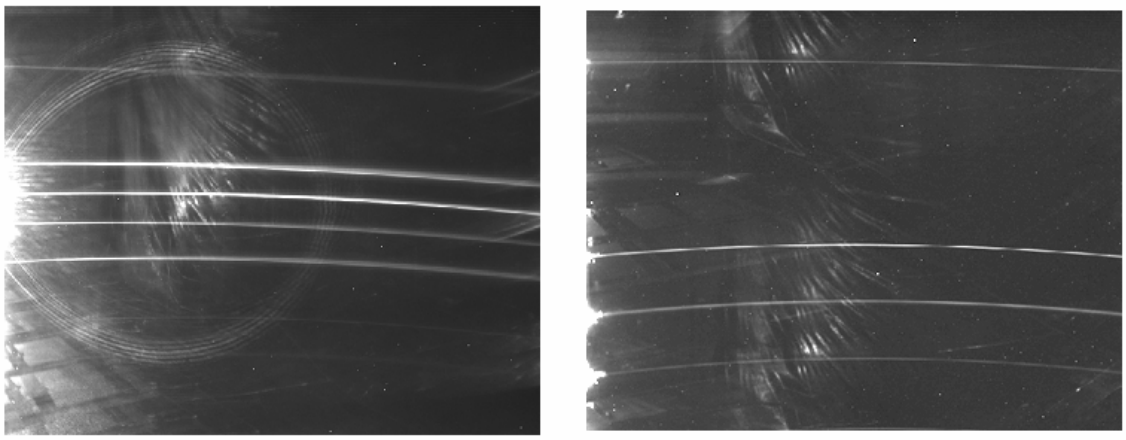


Figure 5-26: Scattering images for oleic acid droplets (a) Camera 1 and (b) Camera 2.

The dark count images are subtracted from the 'raw' images of the frames for polarization perpendicular and parallel to the scattering plane (i.e. the plane containing the laser beam and the imager). Figure 5-27b displays the resulting dark-count-subtracted image for an image of the scattering from the 5 μm particles. Notice that folds in the black plastic on the back wall can clearly be seen in the background of the image, as well as reflections from the metal plates that were along the floor of the tunnel. By imaging through the diffracting grating, the wavelength dependent scattering data has been unfortunately spread across these background reflections. An image interpolation technique is used to attempt to minimize the effect of the reflections in the scattering data. The rows containing the scattering data are removed from the image and an image processing algorithm approach employing neighbor least-squares optimization is used to interpolate the background. The interpolated background image (Fig. 5-27d) is subtracted from the original dark-count-subtracted image (Fig. 5-27b) after adding a constant offset to the whole image to eliminate 'false' zeros. The extraction algorithm uses this

final ‘processed’ image which attempts to retain all of the scattering information and hopefully minimum reflection signal.

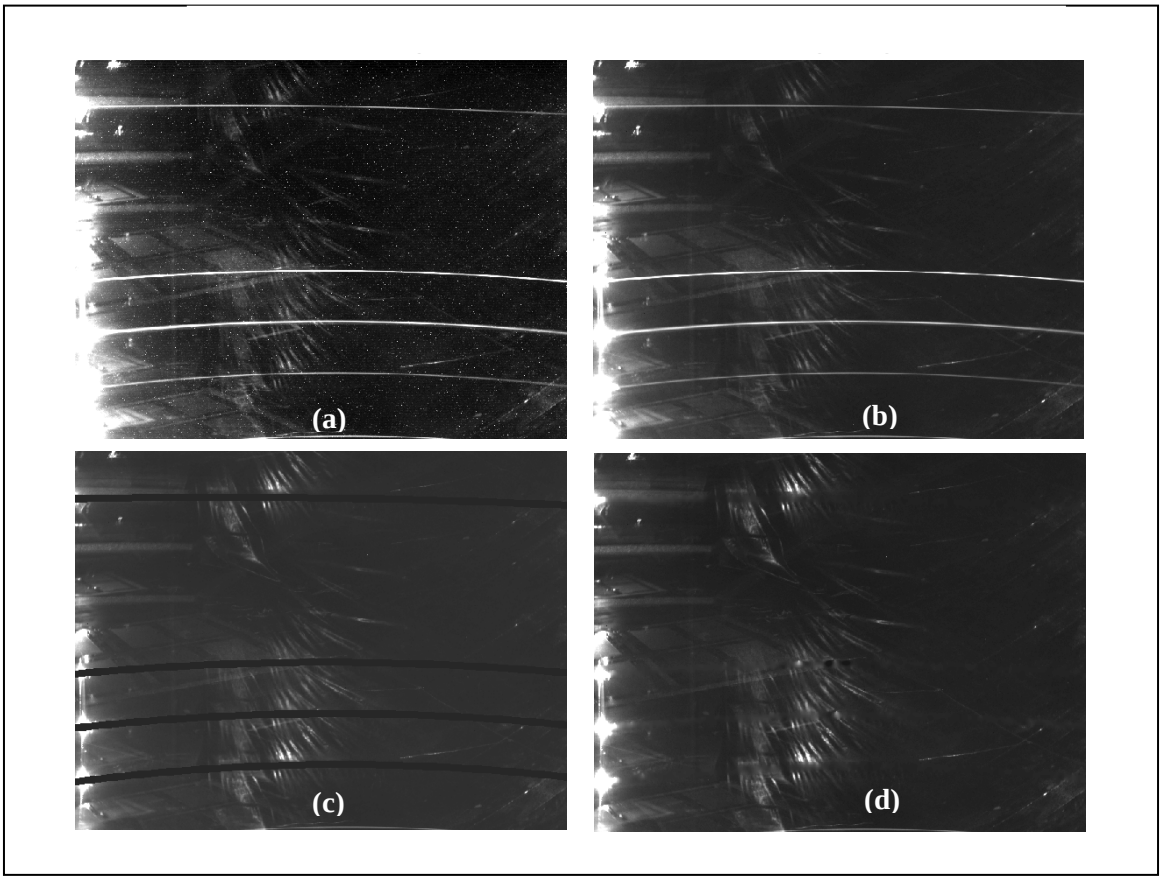


Figure 5-27: (a) ‘raw’ scattering image (b) dark-count subtraction (c) removed scattering from image (d) interpolated background image.

This technique did remove the ripples from the plastic, but it also eliminated scattering information from the images. Fig. 5-28 is zoomed-in view of the interpolated background image and shows the blurred intensity that is spread across the length of the image where the three diffracted beams are located. Subtracting this ‘blurred’ intensity from the raw scattering images completely changes the shape and magnitude of the polarization ratio. Unfortunately, the background reflections cannot be removed from the data, without also altering the scattering intensities generated by the particles. While this is discouraging, it does not mean that the

collected data is completely worthless. These measurements demonstrate the need for future experiments to use a flat black absorption background.

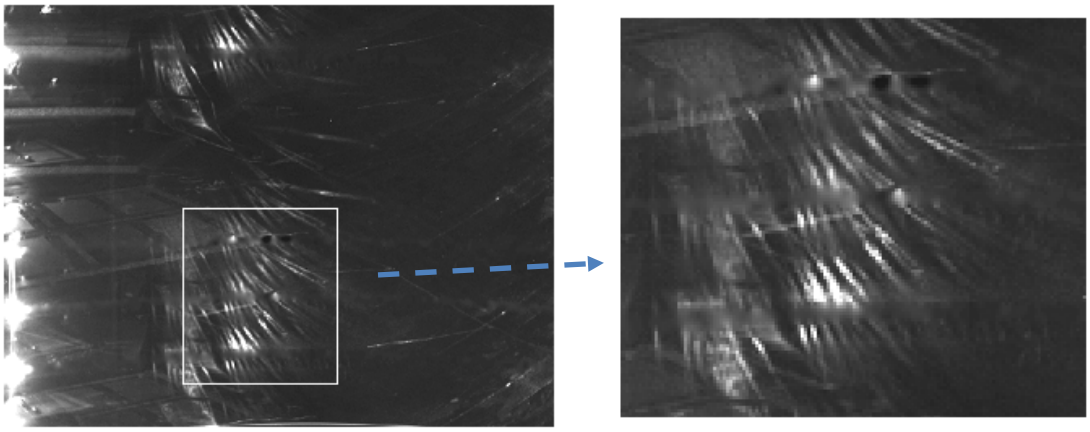


Figure 5-28: Interpolated background image showing blurring of specular reflections.

5.3.3 Polarization ratios

The entire collected range of scattering angles can not be inverted by the algorithm because of the reflections off of the plastic; however, there should still be valuable scattering information in the angles that are not corrupted by background reflections. The normalized size distribution measured by the APS (Fig. 5-25) is converted to a particle size distribution by dividing the normalized concentration by the logarithm of the bin widths and the aerodynamic diameter is converted to particle diameter by dividing by the square root of the density of the oleic acid, 0.895. The particle size distribution is shown in Fig. 5-29 with a 'best-fit' lognormal size distribution that will be used to calculate the model polarization ratio.

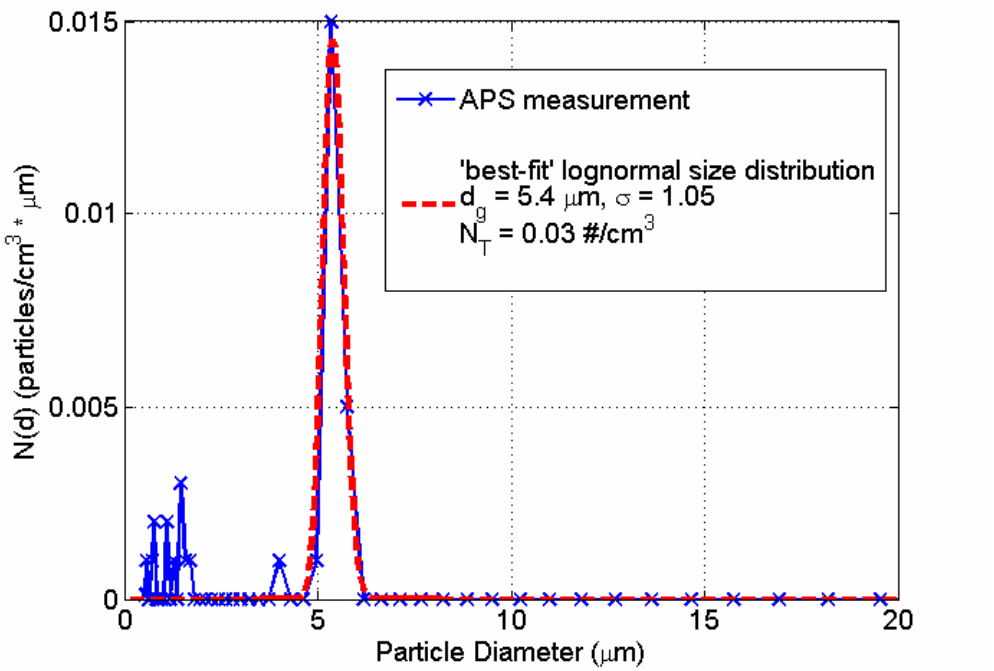


Figure 5-29: Number density size distribution measured by APS for analyzed dataset and 'best-fit' lognormal size distribution.

Figure 5-30 shows the measured polarization ratios for dataset #1 and the theoretical polarization ratio calculated from the APS measured size distribution (5.4 μm, 1.05) at a concentration of 0.03 particles/cm^3. When comparing the measured polarization ratios for dataset #1 to the calculated polarization ratios it becomes clear that the reflections from the black plastic are corrupting the polarization ratios at the scattering angles that contain the most distinct scattering patterns for the lognormal size distribution of oleic acid particles. The general shape of the measured polarization ratios between the angles of ~165 and 170 degrees is similar to the shape observed in the calculated polarization ratios using the APS size distribution, but also could be a result of the background reflections. One significant difference between the theoretical and measured polarization ratios is the offset observed as a shift of the 407 nm measured polarization ratio from the 532 nm, and 650 nm measured polarization ratios. Following this clue, we suspect a second particle mode, a smaller size aerosol contributing to the signal. The genetic algorithm

was used to see if a size distribution could be found to explain this offset between the measured polarization ratios.

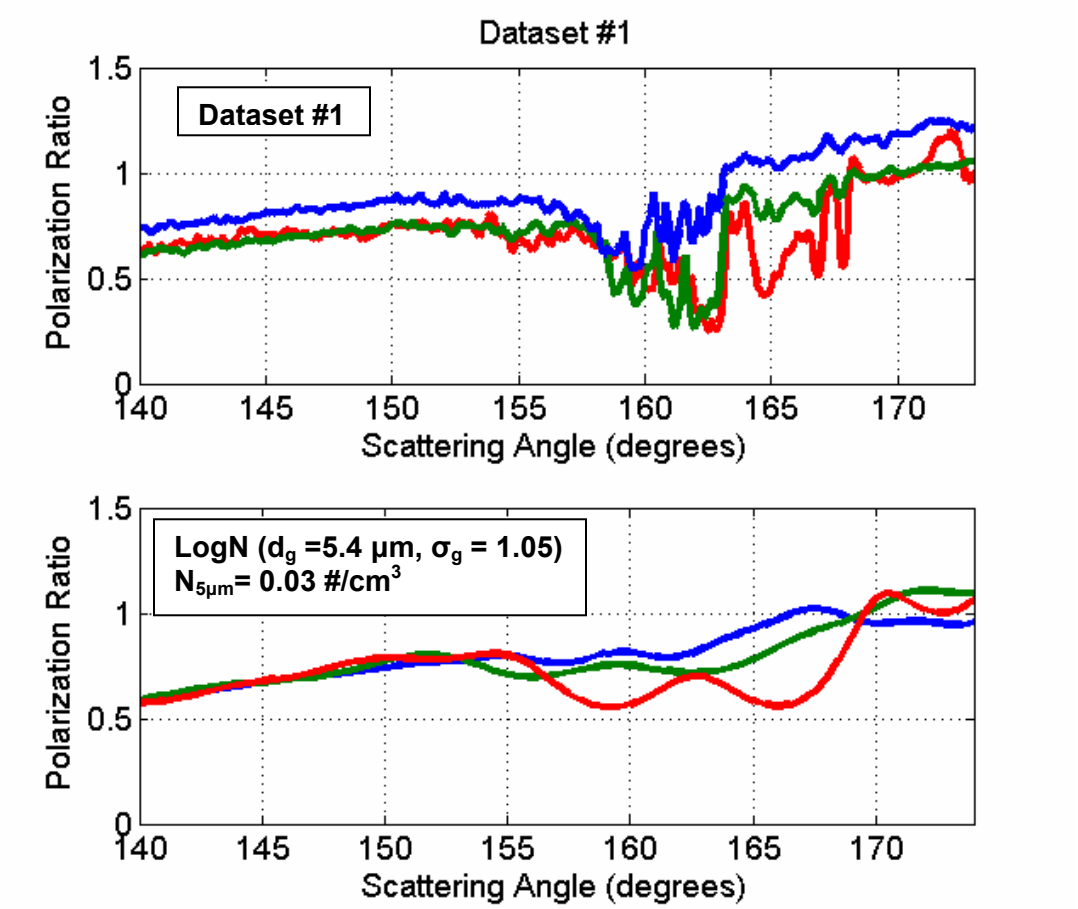


Figure 5-30: Measured polarization ratios for dataset #1 compared with theoretical polarization ratio for lognormal size distribution (d_g = 5.4 µm, σ_g = 1.05) and concentration of 0.03 particles per cm^3.

The genetic algorithm is used to retrieve the geometric mean radius, geometric standard deviation, and concentration of the first mode of a bimodal lognormal particle size distribution that produces the lowest squared error between the measured and modeled polarization ratios. The second mode lognormal distribution is held constant within the genetic algorithm, with a geometric mean diameter of 5.4 µm, a geometric standard deviation of 1.01, and a concentration of 0.03 particles/cm^3. A refractive index of 1.46 + i0 is used for all three wavelengths in order to increase the speed of convergence of the algorithm. Results from the genetic algorithm inversion,

summarized in Table 5-6, indicate that the offset between the polarization ratio curves is most likely caused by a large number density (> 10^4 #/cm^3) of ultrafine particles (~0.18 µm diameter).

Table 5-6: Results for five genetic algorithm inversions of dataset #1.

Geometric mean diameter (µm)	Geometric standard deviation	Concentration (#/cm^3)	Geometric mean radius (µm)	Geometric standard deviation	Concentration (#/cm^3)
0.16	1.35	3 x 10^4	5.4	1.05	0.03
0.22	1.23	1 x 10^4	5.4	1.05	0.03
0.18	1.3	1 x 10^4	5.4	1.05	0.03
0.16	1.34	3 x 10^4	5.4	1.05	0.03
0.18	1.28	2 x 10^4	5.4	1.05	0.03

Subsequent discussions with the director of the EPA aerosol chamber, Russell Weiner, revealed that there are a significant number of smaller particles produced by the VOAGs during the generation of the larger oleic acid droplets. These smaller particles are produced by the 'breaking' of the stream of oleic acid into the dynamic air flow in the tunnel (Chigier and Reitz, 1995). Figure 5-31 is a picture of an operating vibrating orifice and it is possible, with some difficulty, to see the 'haze' created by the small break-off particles around the stream of larger droplets.



Figure 5-31: Picture of operating vibrating orifice from VOAG datasheet (TSI Model 3450 VOAG datasheet). 'Haze' around particle stream could be sub-micron particles.

A bimodal size distribution retrieved by the genetic algorithm is used to calculate polarization ratios at the three wavelengths of 407 nm, 532 nm, and 650 nm, which are shown in

Fig. 5-32. The offset that is seen between the blue wavelength and the other two wavelengths in the measured polarization ratio for dataset #1 is now included in the modeled polarization ratio, indicating that the measured offset is a result of a large concentration of these sub-micron 'break-off' particles.

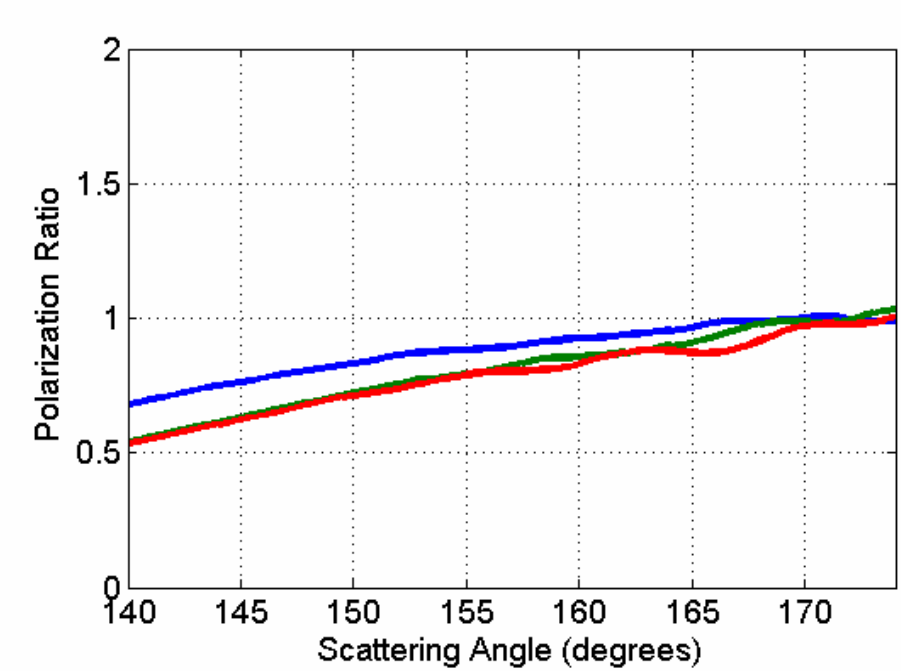


Figure 5-32: Polarization ratio for bimodal lognormal size distribution ($d_{g,1}$=0.18 μm, $\sigma_{g,1}$=1.3, N_{T1}=1 x 10^4 #/cm^3 and $d_{g,2}$ =5.4 μm, $\sigma_{g,2}$ 1.05, N_{T2}=0.03 #/cm^3).

The large number of sub-micron particles that are required to create the offset between the 407 nm polarization ratio and the 532 nm and 650 nm polarization ratios dampen the scattering signature of the five micron particles in the modeled polarization ratios. This knowledge leads to the conclusion that the patterns observed in the measured polarization ratios from 165 to 170 degrees is most likely caused by background reflections, and not the oleic acid droplets. The scattering signature created by the oleic acid droplets are dominated by the strong reflections off of the plastic, and dampened by the scattering from the sub-micron 'break-off' particles.

5.4 Conclusions

The scattering measurements collected in the EPA aerosol wind tunnel provide a unique opportunity to assess the performance of the multiwavelength-multistatic system and the genetic algorithm inversion procedure. The retrieval of the single lognormal size distributions for the case of the MDG fog that so closely matched the size distributions measured by the aerodynamic particle sizer adds a high level of confidence to the technique. The inversion algorithm searched an extremely large solution space and retrieved values within reasonable measurement errors of the point sensors systems, considering the fact that the instruments were operated well outside their recommended concentration range. The ability of the technique to retrieve real refractive indices for the scattering volume, and imaginary indices within certain bounds, is an extreme advantage over the point-measurement systems. The sensitivity of the polarization ratio to the concentration of particles has been explored as a result of these measurements, and the usefulness of extinction measurements and/or absolute magnitude measurements of the scattering phase functions to help quantify concentration has been discussed.

Originally, the monodisperse particle distributions produced by the VOAG were to be used as a solid measure of the accuracy and reliability of the multiwavelength-multistatic technique and the developed inversion algorithm. The low concentration and large size of the oleic acid droplets in relation to the laser wavelengths would be a non-trivial test of the techniques limits. Unfortunately, the presence of the background reflections in the oleic acid data raises some questions when determining the ‘goodness’ of fit between the modeled and measured polarization ratio, because it is difficult to say with certainty which scattering features are results of the particles and which are the background reflections. Additionally, the presence of the ‘break-off’ particles, which are too small for the APS to detect, also adds uncertainty into the ground-truth particle size distribution, which was originally counted on to be highly

monodisperse and completely characterized by the *in situ* point sensor measurements. For these reasons, the oleic acid scattering measurements can not quite be the exclamation point for the multiwavelength-multistatic technique that was originally hoped. That being said, the technique did reveal the presence of the ultrafine particles, prior to confirming their existence with the director of the wind tunnel, and which were completely undetected by the APS. There is hope of repeating this measurement in the not-so-distant future in order to further build upon the insight and confidence in the technique that are results of this first set of measurements. This new level of understanding of the successes and limitations of the system can now be intelligently and confidently applied to the dynamic and complex place that is our atmosphere.

Chapter 6

Atmospheric Aerosol Measurements

The experimental method and inversion algorithms explored in the previous chapters are used to infer characteristics of atmospheric aerosols. A North Carolina State University astronomy site was used as the field site for making the multiwavelength-multistatic aerosol scattering measurements. The astronomy site is located in the middle of horse pastures and there is very little background light pollution making it a nice location for conducting laser scattering measurements. The transmitter was set on a low table, about half of a meter off of the ground, with the lasers propagating down the length of a shallow valley in the middle of the horse pasture. The path was terminated by a target board resting in the back of a pickup truck (the pasture sloped downwards) at a distance of approximately 100 meters. A rope with dangling wires spaced at five meters apart was stretched between two poles along the entire length of the path to aid in determining the angles associated with each pixel in the scattering images. A weather station that recorded temperature, dew point, and humidity was placed about 30 meters away from the transmitter. A condensation particle counter (CPC), TSI model 3007, was placed on the ground under the path of the laser beams, at about three meters distance from the transmitter. It was placed in this location due to the length of the power cord, and to keep the lights from the instrument display out of the field of view of the two cameras. Two cameras were placed at positions to collect scattering signals from overlapping volumes for two overlapping ranges of backscattering angles.

One difficulty encountered during the outdoor tests was the condensation of water onto the transmitter and receiver optics. Figure 6-1 shows the effects of condensation beginning on the diffraction grating. A space heater was then kept constantly blowing on the transmitter optics to

keep them dry throughout the evening and early morning and a handheld hair dryer was used intermittently to dry the camera lenses and diffraction gratings (approximately every 2-3 minutes). The use of the heater and blow dryer minimized the effect of the condensation on the optical elements, but the condensation would occasionally creep into the scattering data. Datasets corrupted by condensation are identified by the dramatic fluctuations in the 650 nm polarization ratio as shown in Figs. 6-1 and 6-2.

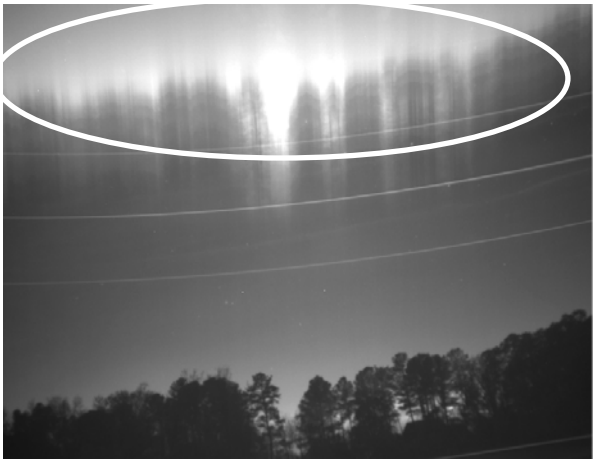


Figure 6-1: Scattering image collected using 600 lines/mm diffraction grating showing condensation on the inside of the grating (streaks inside white oval).

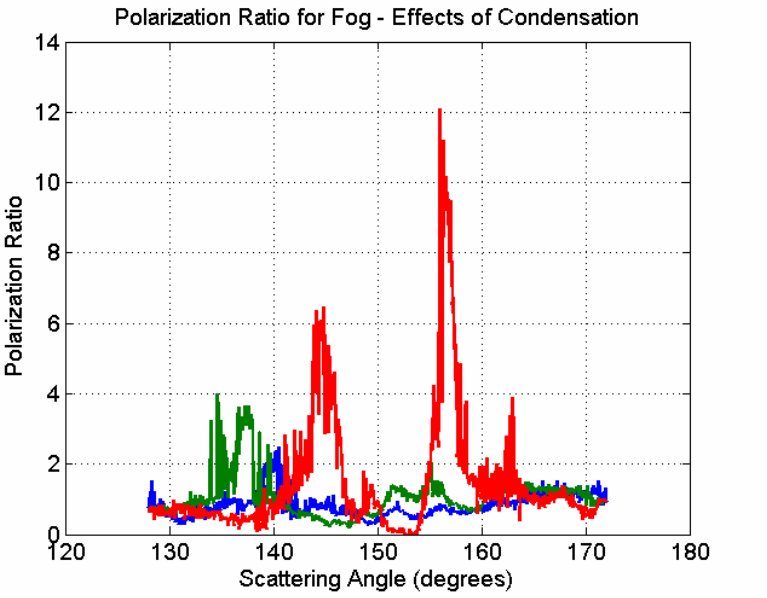


Figure 6-2: Polarization ratio of scattering data altered by condensation collecting on the inside of the diffraction grating.

The night of 20/21 November presented a continuous fluctuation of patchy fog that would progress up the slope of the small valley towards the transmitter. The quickly moving fog made it extremely difficult to acquire scattering images for both incident polarization ratios before the concentration of the fog had changed. Future generations of the multistatic system should automate the rotation of the transmitter polarization and the acquisition of data images to eliminate this difficulty from the data collection process. This concept is discussed further in Chapter 7. Analysis of two polarization ratios measured during two short, relatively stable periods of aerosol concentration collected on this night are presented. The temperature, dew point, and humidity for the night of 20/21 November are shown in Fig. 6-3. Scattering measurements are collected from approximately midnight, which is about the time that the air temperature reached dew point temperature, and fog was observed. The patchy fog continued until about to 2 AM, with the temperature dropping roughly two degrees throughout the time of the scattering measurements. The particle concentration measured by the CPC throughout the course of the measurements is shown in Fig. 6-4, where the approximate collection times of two selected datasets are marked with boxes. The two datasets are roughly an hour apart, with the first dataset collected at 12:50 AM and the second dataset at 1:45 AM. Notice that the measurements are made during periods of brief, relatively stable particle concentrations, with each data point in the graph corresponding to a one minute-averaged concentration measured by the CPC. The weather station recorded no wind throughout the evening, which makes it difficult to explain the patchiness of the observed fog and the large oscillations of the CPC concentration measurements. The analysis of two datasets collected on the night of 20/21 November are presented in the next section to explore the retrieval process of the microphysical properties of atmospheric aerosols from multiwavelength-multistatic data.

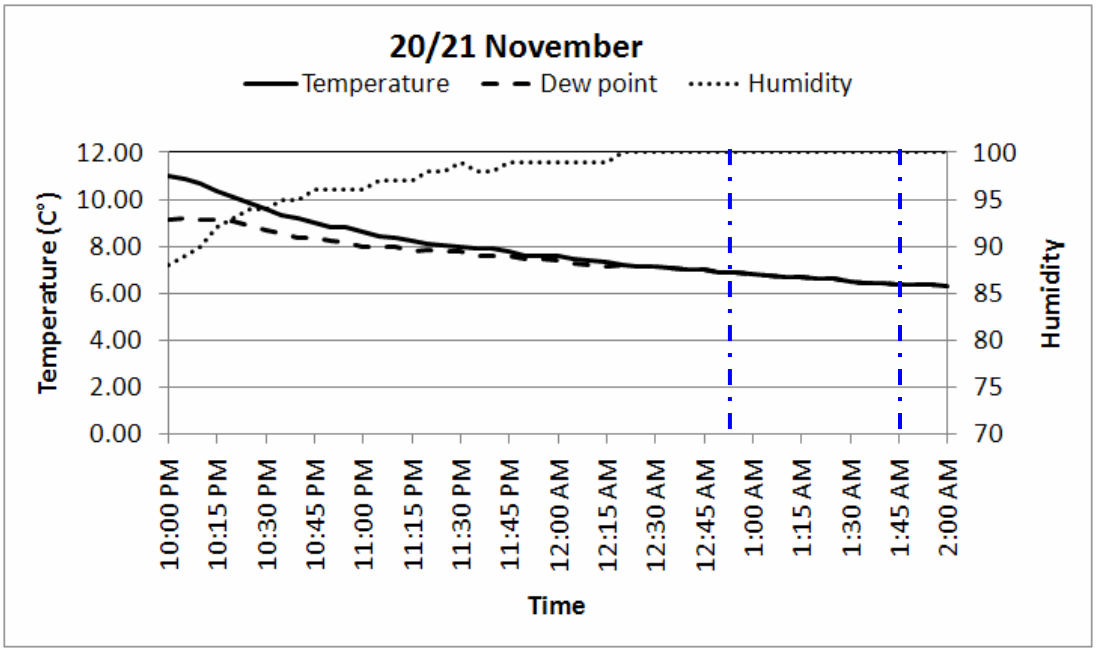


Figure 6-3: Temperature, dew point, and relative humidity for night of 20/21 November. Blue lines show times of data collection for datasets analyzed for this work.

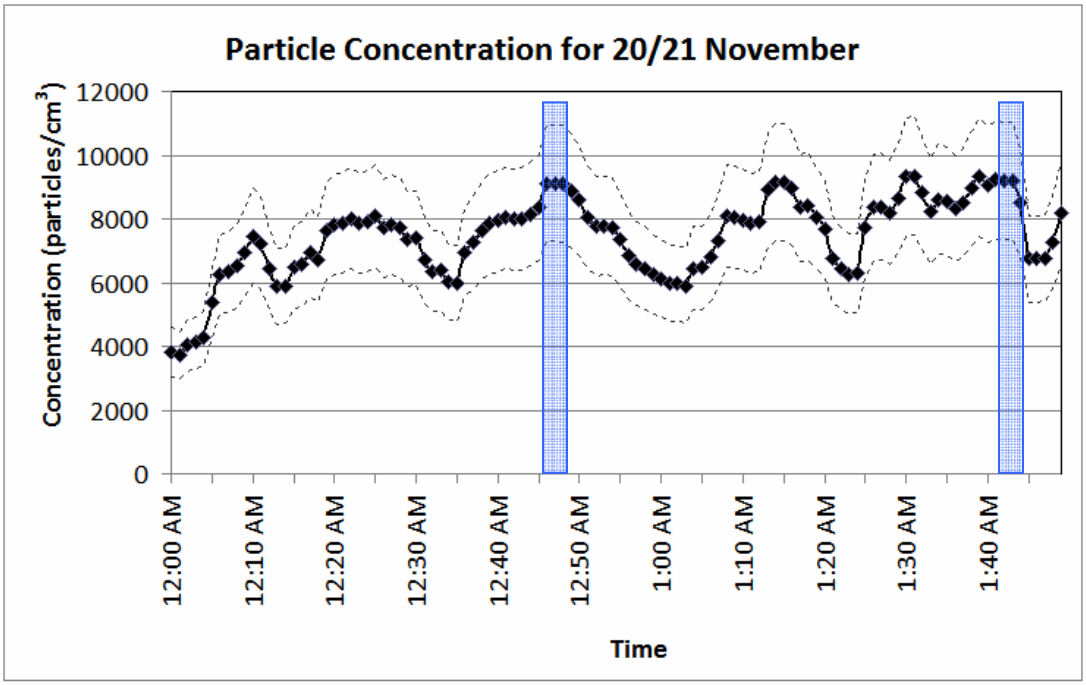


Figure 6-4: CPC concentration for night of 20/21 November with ±20% (dotted lines). Blue boxes indicate times of data collection for analyzed datasets for this work.

6.1 Data Processing

The first analyzed dataset from the evening of 20/21 November was collected at 12:50 AM, when a patchy light fog could be seen along the length of the laser path. The measured scattering intensities for the incident parallel and perpendicular polarizations are shown in Fig. 6-5, and the corresponding polarization ratios are shown in Fig. 6-6. Examination of Fig. 6-5 reveals a cyclic pattern in the measured data that is not typical of the smooth sinusoidal patterns that are characteristic of Mie scattering. These cyclic features in the scattering intensities appear in the polarization ratios as sharp 'drop-offs' in magnitude, which are not consistent with the polarization ratios obtained from fog by Stevens (1996, Chapter 5), Novitsky (2002, Chapter 6), or Park (2008, Chapter 6).

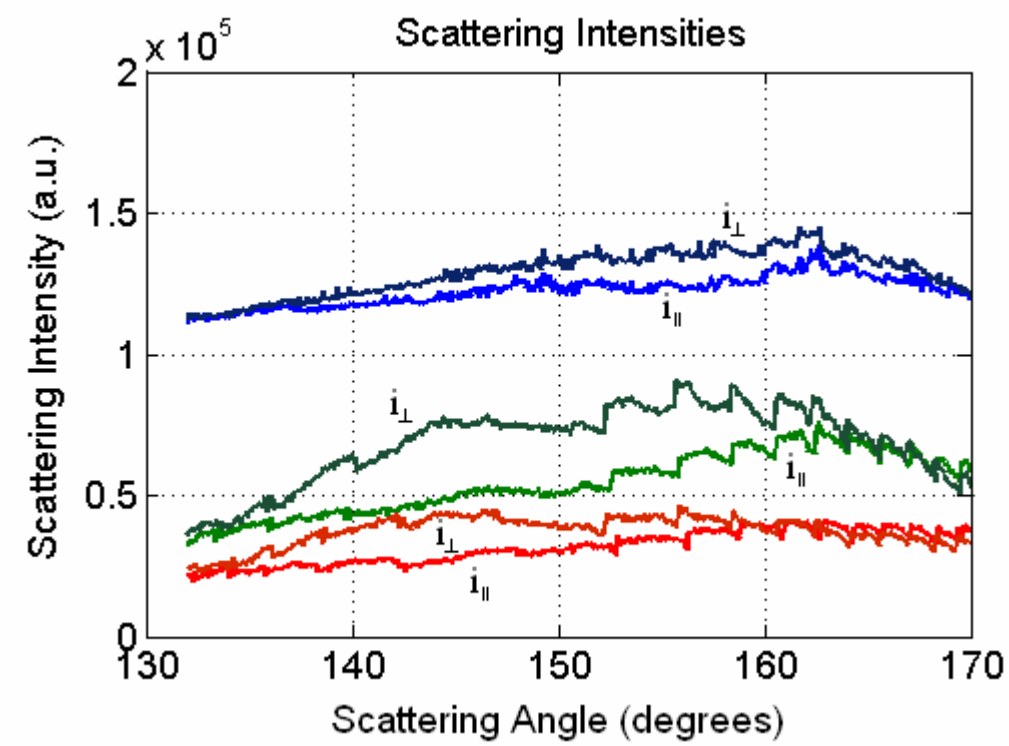


Figure 6-5: Unfiltered measured scattering intensities for fog at 12:50 AM, 20/21 November. The scattering intensities for the 407 nm and 532 nm have been given constant biases to separate the curves from each other.

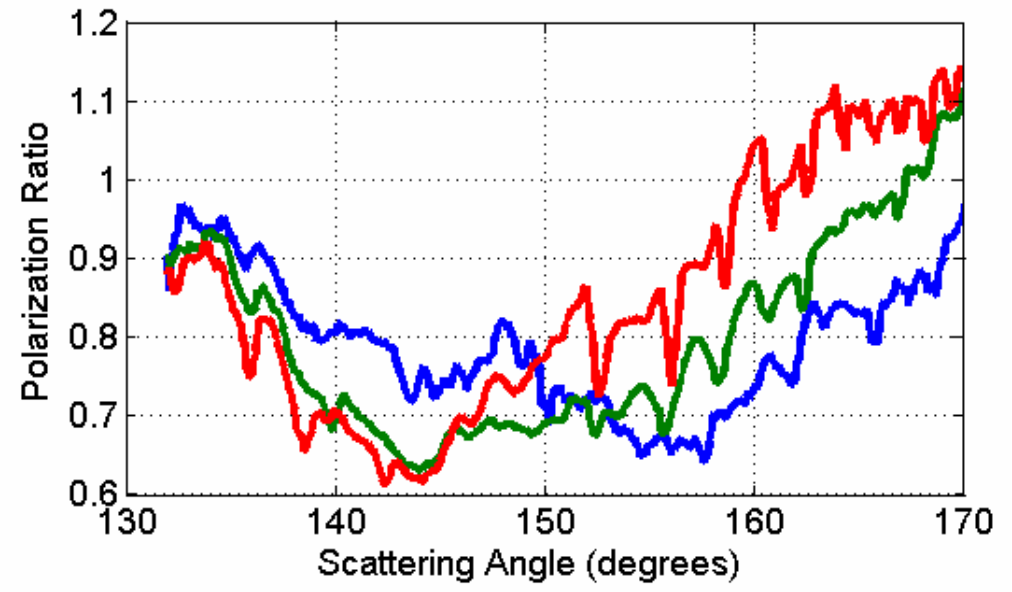


Figure 6-6: Unfiltered polarization ratios for fog at 12:50 AM, 20/21 November.

The data processing procedure is re-examined to determine if the cyclic patterns observed in the scattering intensities can be explained by the integration routines. The data processing algorithm locates the maximum intensity for each wavelength in each column and then adds the pixels above and below this maximum intensity pixel until the value of the pixels drops below a certain percentage of the maximum pixel count. The value of 80% was used to form the measured scattering intensities shown in Figure 6-5 and the polarization ratios shown in Fig. 6-6. The data collected November 21st at 12:50 AM was reprocessed using cut-offs of 50%, 75%, and 90% to determine the effect of the integration cut-off in the data processing routine. Plotted below in Figs 6-7 through 6-9 are the unfiltered scattering intensities calculated using the specified intensity percentage cut-off in the data processing algorithm and the corresponding polarization ratios formed from the ratio of the intensities after a 10-point moving average smooth had been applied.

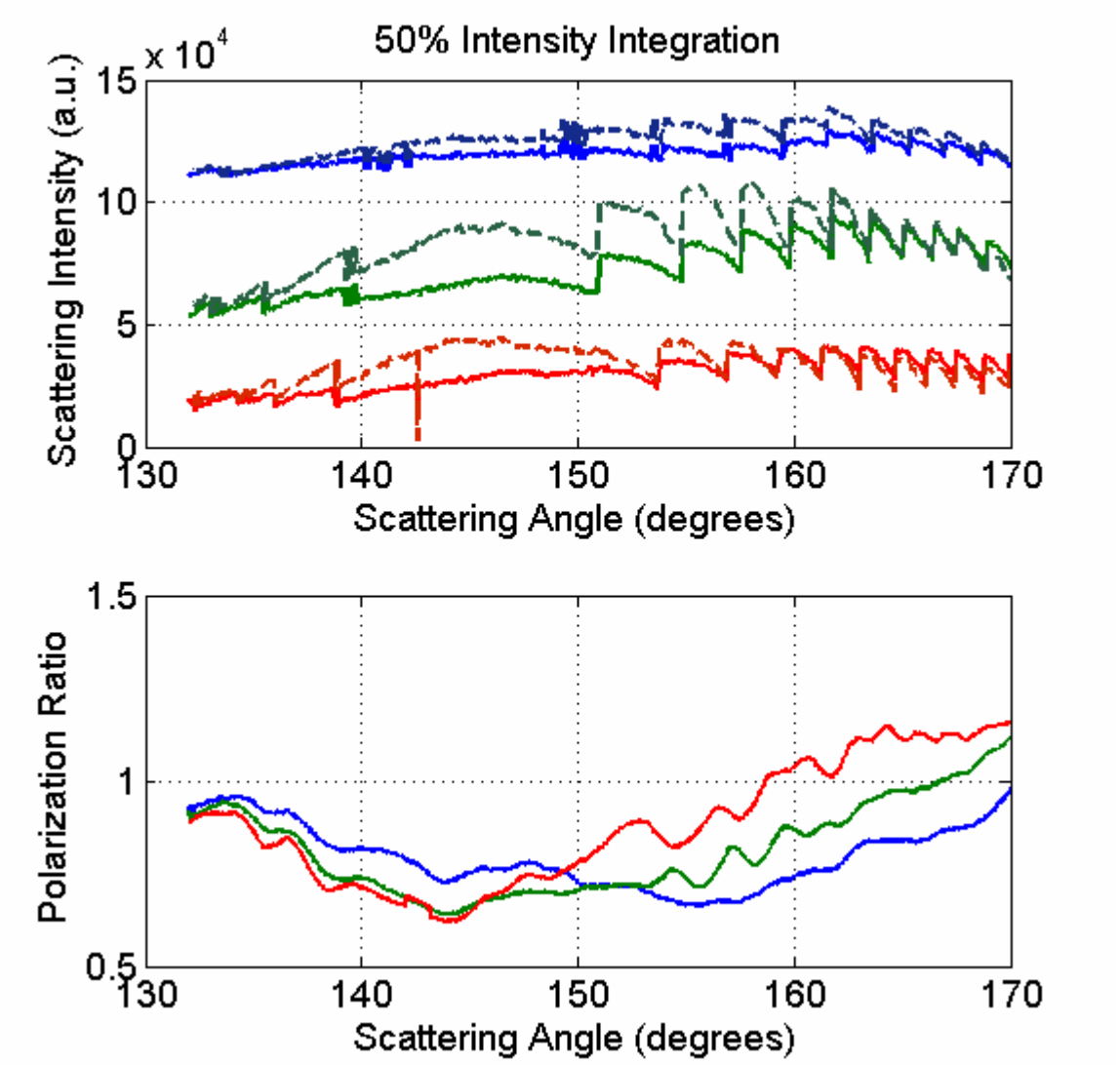


Figure 6-7: Scattering intensities and polarization ratios for data collected 20/21 November at 12:50 AM when using an integration cut-off of 50% of the maximum pixel value.

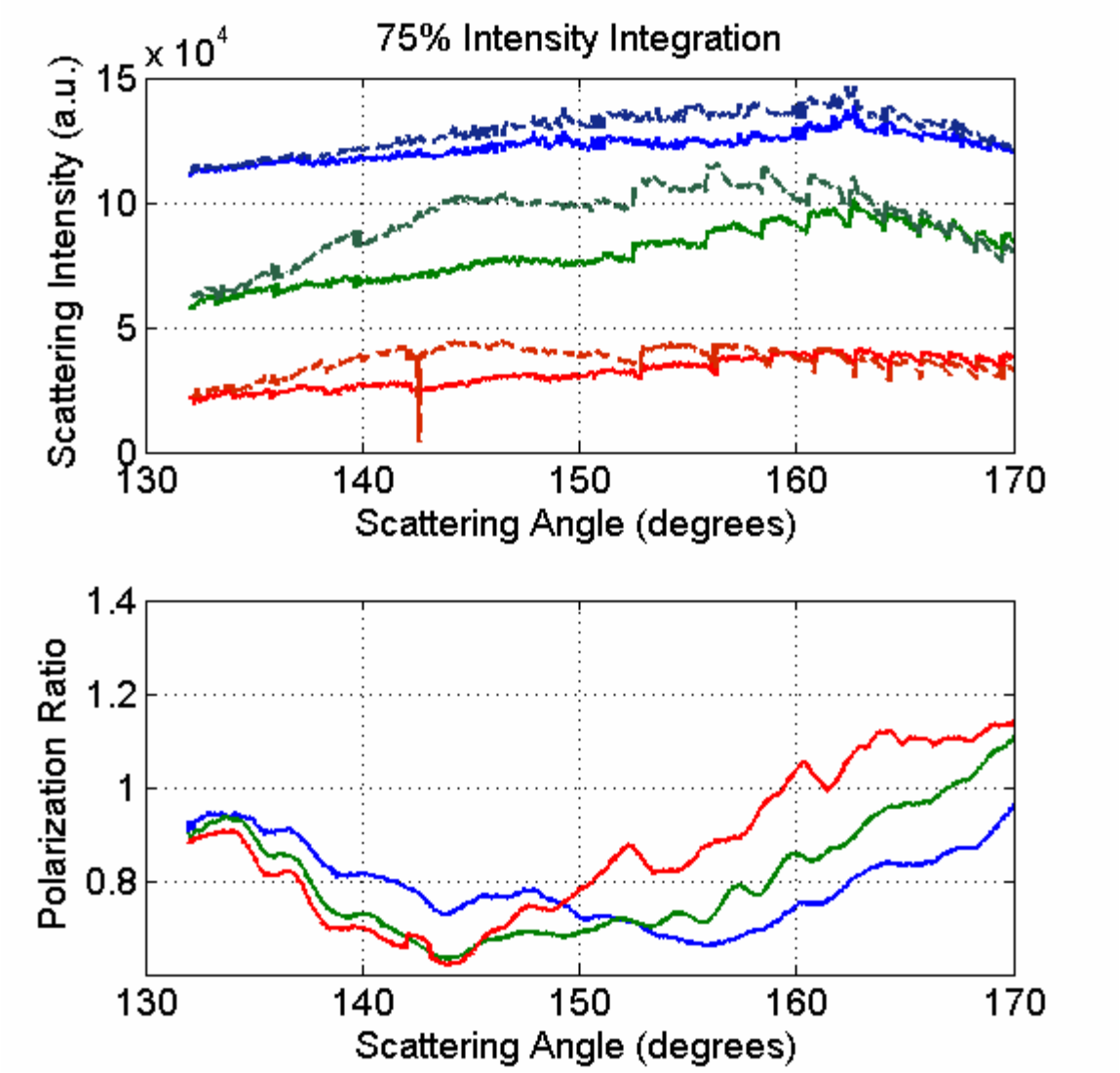


Figure 6-8: Scattering intensities and polarization ratios for data collected 20/21 November at 12:50 AM when using an integration cut-off of 75% of the maximum pixel value.

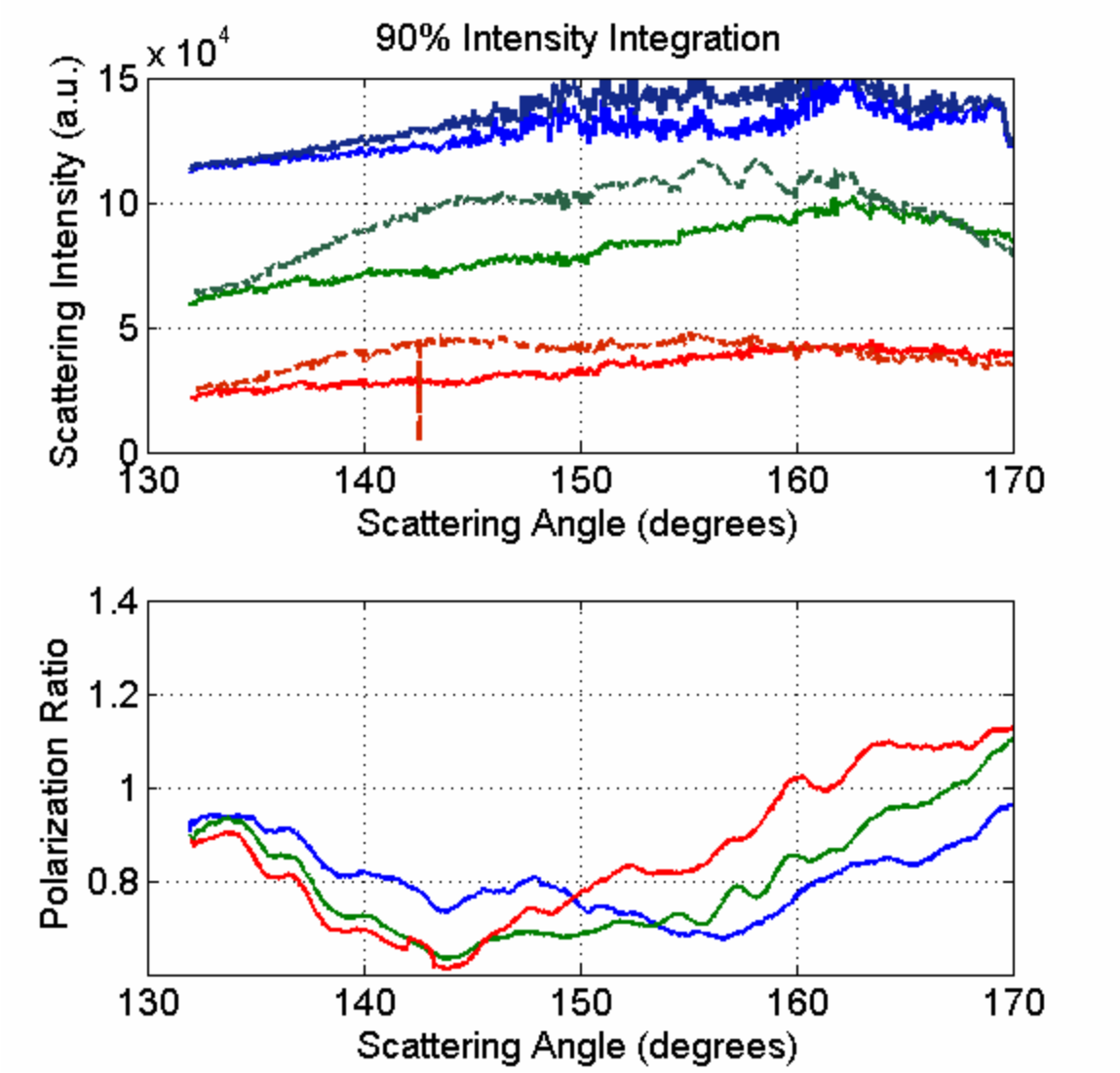


Figure 6-9: Scattering intensities and polarization ratios for data collected 20/21 November at 12:50 AM when using an integration cut-off of 90% of the maximum pixel value.

Inspection of the scattering intensities in Figs 6-7 through 6-9 reveals that the cyclic pattern is more pronounced when integrating fewer rows to obtain the scattering intensities as a function of angle. The transitions at the bottom of the ripples are too sharp to be explained by scattering and they appear to occur at angles where the imaged beams are crossing multiple rows of the CCD array. The curvature of the imaged beams causes the scattered intensities to cross

numerous rows of the CCD array, especially on the right side of the image when the scattered intensity is being collected from longer distances, as shown in Fig. 6-10.

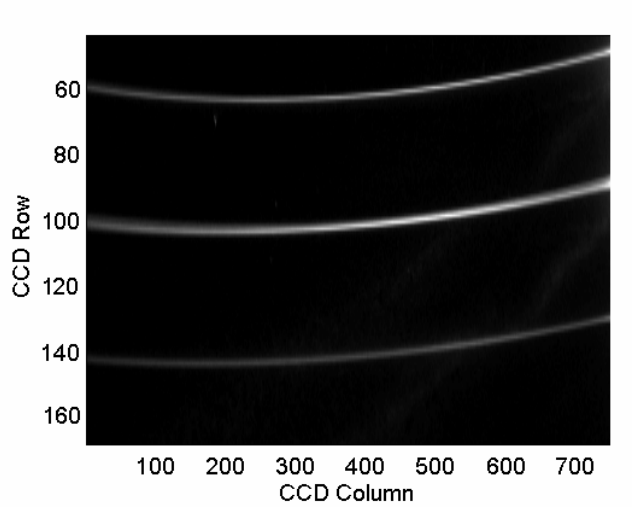


Figure 6-10: Location of diffracted beams on the CCD array

The rippled effect is intensified when fewer rows are used in the integration process due to the discrete nature of the data collected by the CCD array. A cross section of the scattered intensities for the 532 nm wavelength for CCD column 400 is shown in Fig. 6-11.

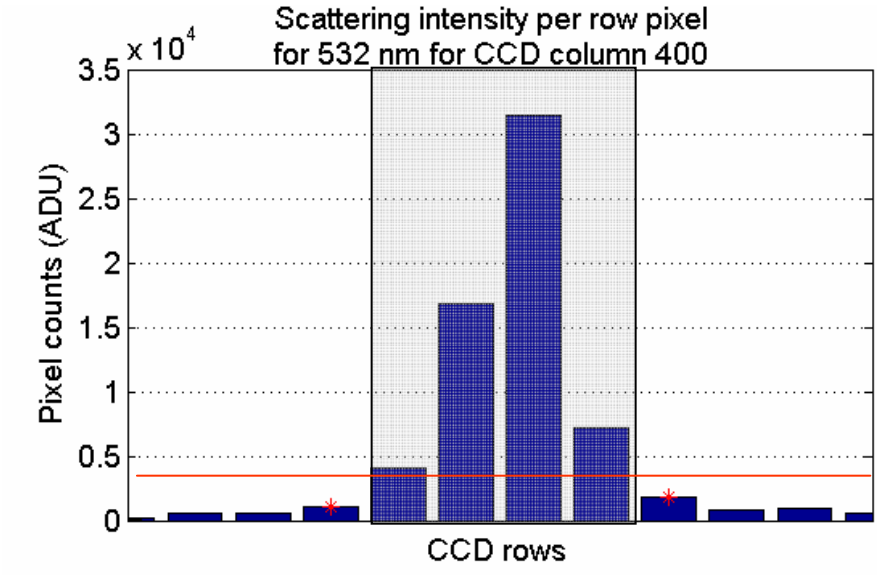


Figure 6-11: Depiction of integration of rows to produce scattering intensity as a function of column

The red line is the threshold that the data processing algorithm uses to determine how many rows to add for each column. The gray box shows the number of rows that are added to produce a total scattering intensity for 532 nm at that particular scattering angle. In this case, the pixel whose value is right at the threshold level is included, but one can imagine if the pixel level was just a little bit less than it would get excluded from the integration and drop the value of the integrated scattering intensity. These drop-offs would be less pronounced if there was a higher sampling resolution of the cross-section of the scattered laser beams. In the higher resolution case, the inclusion or exclusion of a row would have less of an impact on the total integrated scattering intensity. One way that this higher resolution might be accomplished would be to spread the beam using a beam expander. This would distribute the scattered signal across more rows of the CCD array, and the intensity differences between adjacent rows in a column would be less, causing each row to have less of an impact on the overall integrated intensity. Expanding the beam would have the added advantage of interrogating a larger volume of aerosols, increasing the collection of scattering signals from particles that are present in very low concentrations.

The imager used to collect the data is an interline CCD array, meaning that each photodetector in the CCD array has its own transfer circuitry directly next to it, as shown in Fig. 6-12. This transfer circuitry significantly speeds up the transfer rate of data from the CCD array, but also has the effect of creating small ‘dead space’ between adjacent pixels in the array. Microlenses are used to focus most of the light that falls onto each pixel into the photodetectors, as shown in Fig. 6-12. The microlenses vastly improve the collection efficiency of the CCD array, but a small percentage of the light is still lost. The intensity of the scattered beams crossing from one row of pixels to the next causes the efficiency of the microlenses positioned above the photodiodes to change, contributing to the ripples in the scattering intensities and the polarization ratios.

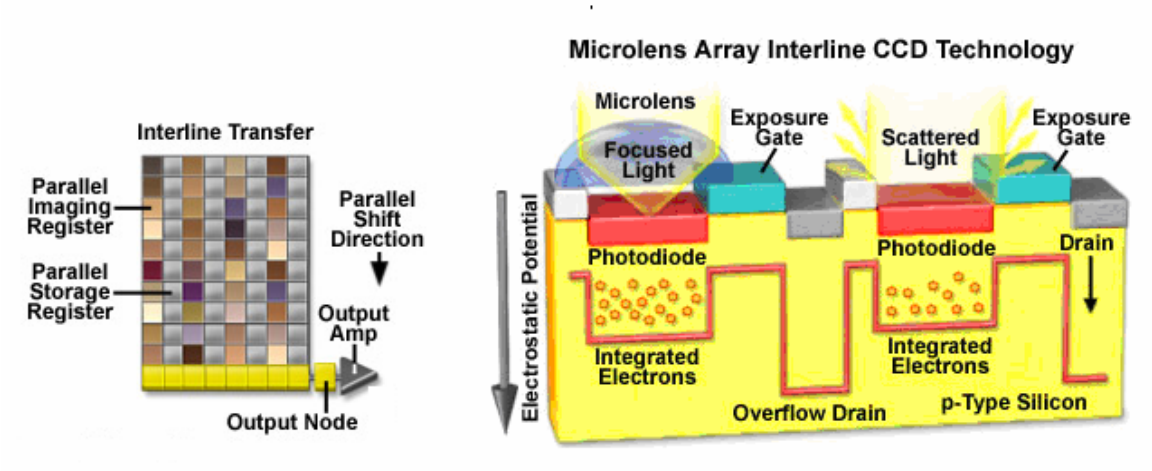


Figure 6-12: Interline CCD architecture (Spring, Fellers, and Davidson, 2000, Figs. 7 and 8).

Figure 6-13 shows the changes to the polarization ratio formed from the measured scattering intensities at 650 nm as the integration threshold level is varied; more rows are included in the integration process as the percentage increases. This figure helps explain the failure of the model to fit all of the ripples in the analyzed datasets presented in the next section. These ripples are essentially noise, and the fact that the inversion algorithm retrieves trimodal size distributions in the presence of these ripples, speaks to the robustness of the algorithm. The ranges of the inversion variables presented in the next section would be considerably reduced if the erroneous ripples could be removed from the polarization ratios.

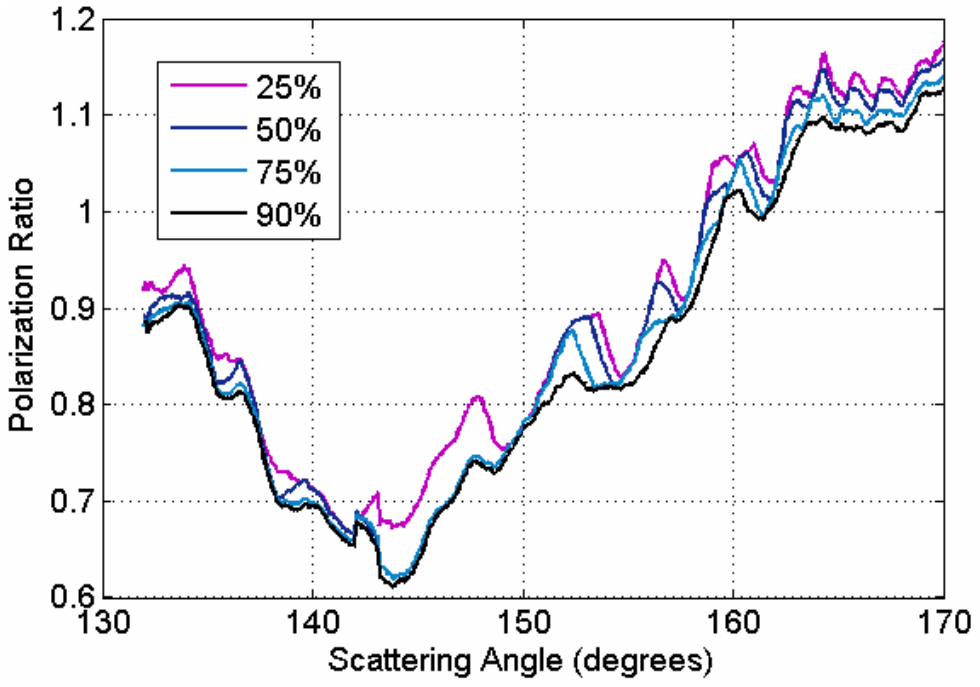


Figure 6-13: Polarization ratio for 650 nm as a function of the number of rows added to calculate the scattering intensity for each scattering angle. The percentage values are the thresholds used in the data processing algorithm to select the number of rows for each wavelength and scattering angle.

6.2 Data Inversion

The first analyzed dataset from the evening of 20/21 November was collected at 12:50 AM, when a patchy light fog could be seen along the length of the laser path. The data was collected using 10 second integration times with the 300 lines/mm grating, and with approximately one minute difference between the beginning of the parallel and the perpendicular scattering data collection periods. The measured scattering intensities calculated using the 90% integration point to minimize the ripples introduced by the interline CCD structure, as discussed in the previous section, are shown in Fig. 6-14. Unfiltered scattering intensities from a second dataset collected approximately an hour later, between 1:43 and 1:45 AM, are shown in Fig. 6-15. The polarization ratios for the two datasets, after applying a 10-point moving average smooth to the collected intensities, are shown in Fig 6-16 for comparison.

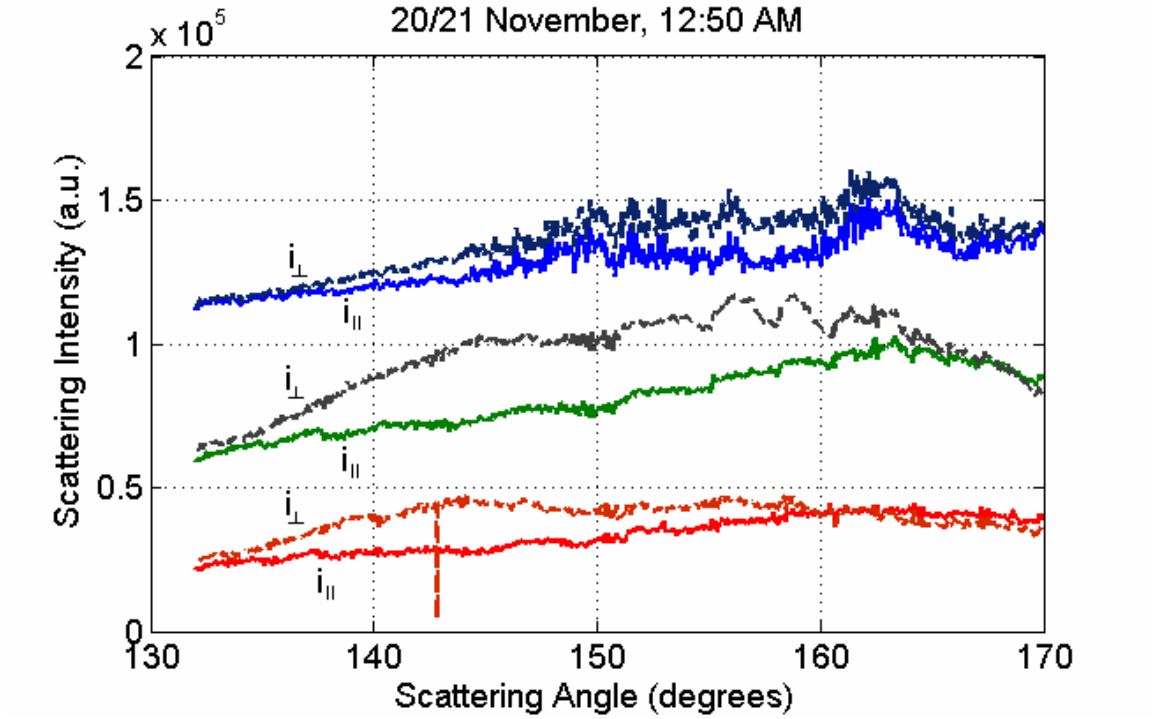


Figure 6-14: Unfiltered scattering intensities for fog at 12:50 AM, 20/21 November.

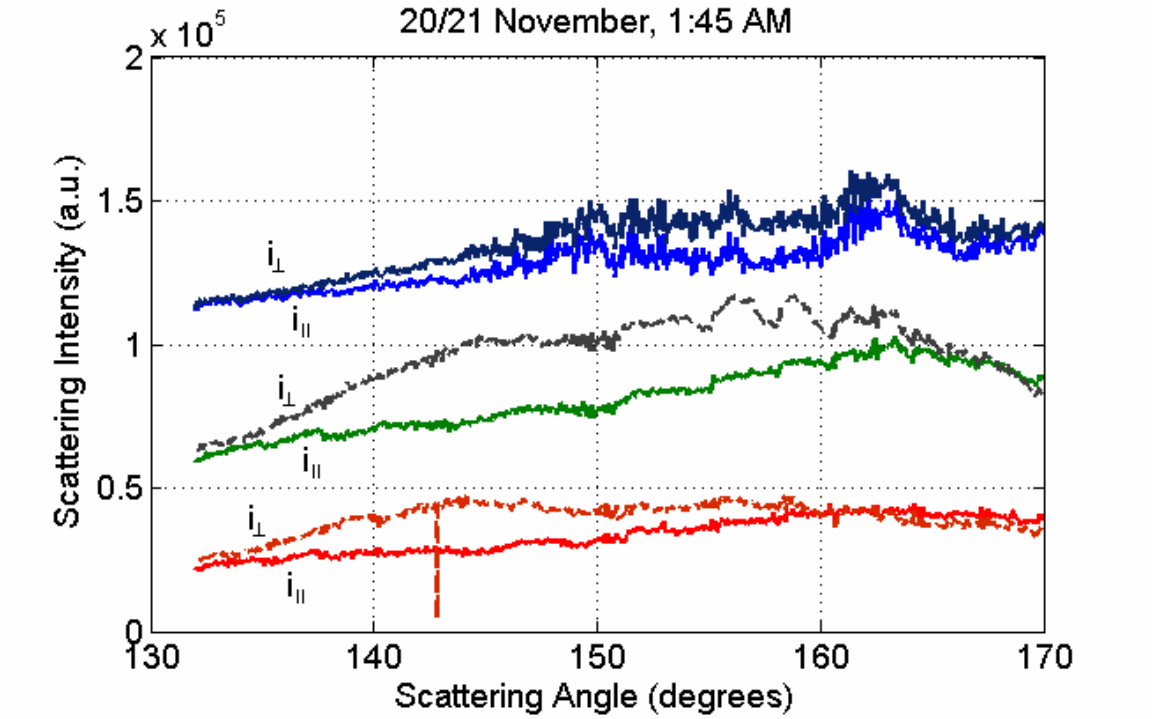


Figure 6-15: Unfiltered measured scattering intensities for fog at 1:45 AM, 20/21 November.

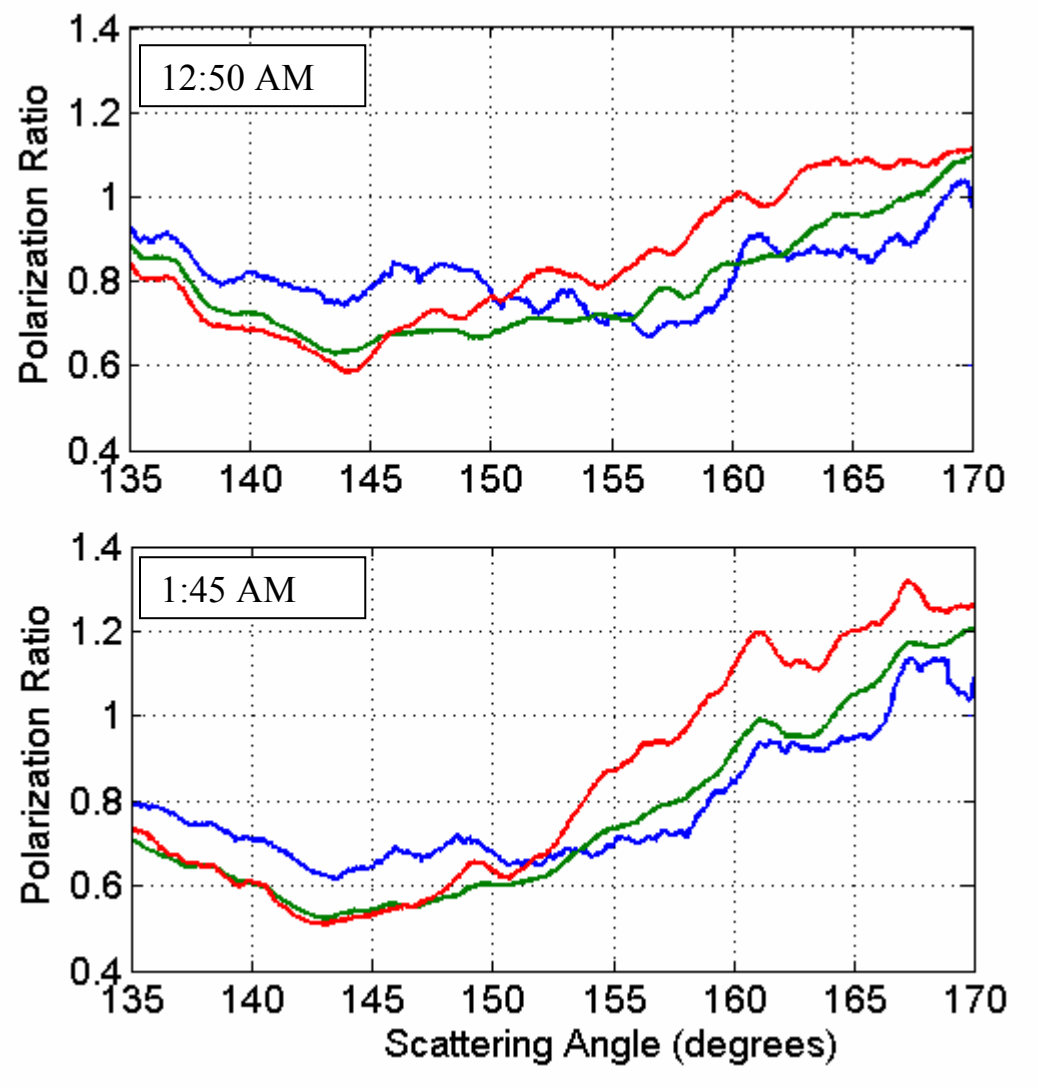


Figure 6-16: Time sequence of polarization ratios collected at two times the evening of 20/21 November.

The genetic algorithm is used to retrieve trimodal lognormal size distributions from the measured data sets. A fixed refractive index is used for all three wavelengths within the algorithm to drastically improve the speed of convergence, as discussed in Chapter 3. The refractive index used for the genetic algorithm inversions of the outdoor scattering data is selected based on the squared error produced by multiple runs of the algorithm on the dataset collected on 20/21 November at 12:50 AM. The algorithm is run repetitively using fixed real refractive

indices from 1.33 to 1.39 by steps of 0.001, and the imaginary refractive index is allowed to assume a discrete value in the set {0, 0.0001, 0.0005, 0.001, 0.005, 0.01, 0.05}. These ranges were selected based on models presented by Shettle and Fenn (1979) for the refractive index of urban and rural aerosols at high relative humidities. A small section of an extensive table of refractive indices for atmospheric aerosols as a function of wavelength and relative humidity presented in the report by Shettle and Fenn (1979) is reproduced in Table 6-1 at the wavelengths and relative humidities of interest for the fog measurements. The average lowest squared error between the modeled and measured polarization ratios produced by the algorithm is used to select the refractive index of 1.35 + i0.001 to use for subsequent inversions of the fog data.

Table 6-1: Reconstructed from Shettle and Fenn (1979, Table 4 and Table 6) showing atmospheric aerosol refractive index used in their model as a function of wavelength and relative humidity.

	Urban Aerosols			Rural Aerosols		
Wavelength (μm)	80% RH	90% RH	99% RH	80% RH	90% RH	99% RH
0.4000	1.416 +0.0316	1.382 +i0.0176	1.344 +i0.00199	1.431 +i0.00286	1.395 +i0.00174	1.348 +i0.000498
0.5500	1.412+ i0.0305	1.377 +i0.0170	1.338 +i0.00187	1.428 +i0.00319	1.391 +i0.00194	1.343 +i0.000323
0.6328	1.411 +i0.0299	1.376 +i0.0166	1.337 +i0.00178	1.420 +i0.00319	1.390 +i0.00194	1.342 +i0.000323

The trimodal lognormal size distributions retrieved by the genetic algorithm for the datasets collected the night of 20/21 November are shown in Table 6-2. The retrieved size distributions that produce the lowest squared error between the measured and modeled polarization ratios for each dataset are indicated by an asterisk in Table 6-2. These retrieved size distributions are used as the starting point for a comprehensive analysis that is done by adjusting each of the inversion parameters and observing the effects on the fit between the model and measured data. The modeled polarization ratios for the dataset collected on 20/21 November at 12:50 AM are compared to the measured polarization ratios in Fig 6-17. The trimodal lognormal

size distribution retrieved by the genetic algorithm in Table 6-2 is used to calculate the modeled polarization ratios and is plotted in the bottom half of Fig. 6-17.

Table 6-2: Inversion results from genetic algorithm for datasets collected the evening of 20/21 November.

Minimum SE	r_{g1} (μm)	σ_{g1}	N_{T1} (#/cm^3)	r_{g2} (μm)	σ_{g2}	N_{T2} (#/cm^3)	r_{g3} (μm)	σ_{g3}	N_{T3} (#/cm^3)
20/21 November 12:50 AM									
0.603	0.05	2.02	12600	0.560	1.25	23	13.3	2.78	0.0141
*0.596	0.06	1.99	14100	0.60	1.15	25	14.3	3.9	0.0141
20/21 November 1:45 AM									
0.729	0.141	1.8	13200	1.37	2.34	17.8	-	-	-
*0.726	0.131	1.86	11600	1.2	2.65	15.8	-	-	-

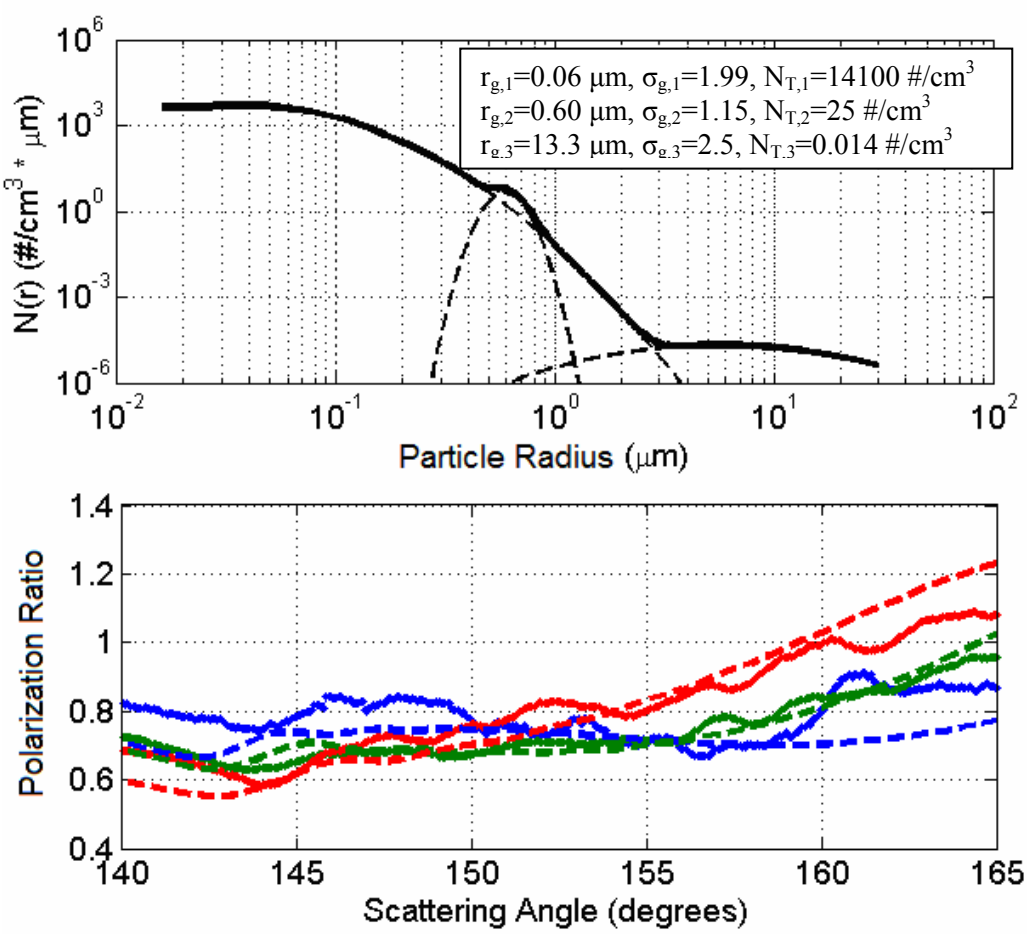


Figure 6-17: (a) Inverted size distribution and (b) modeled (dashed lines) polarization ratios from genetic algorithm using fixed refractive index of 1.35 + i0.001 compared to measured polarization ratios (solid lines) for dataset collected at 12:50 AM, 20/21 November.

A fixed refractive index was used for all three wavelengths to speed the convergence of the inversion algorithm, but in reality the refractive index of the aerosols will vary with wavelength. The refractive index is adjusted independently for each wavelength through visual analysis to optimize the fit for each wavelength between the measured and modeled polarization ratio. Higher real refractive indices tend to lift the modeled polarization ratio curves, while higher imaginary refractive indices flatten the gradient of each curve and decrease the magnitude of the peaks and troughs in the polarization ratios. The complex refractive indices that produce the best fit for each wavelength are: 1.36 + i0.001 for 407 nm, and 1.35 + i0.001 for 532 nm and for 650 nm. Minor adjustments are made to each of the parameters of the trimodal size distribution retrieved by the algorithm to optimize the average fit between the measured and modeled polarization ratios using the varied refractive indices for each wavelength. The concentrations of the first and second modes are slightly lowered and the third mode that was retrieved by the genetic algorithm is removed from the size distribution. The third mode was removed because the dip in the polarization ratio that resulted in the third mode is thought to be a result of shifting concentrations between the two polarization images. There was approximately one minute between the collection of the parallel scattered intensity and the perpendicular scattered intensity in order to accommodate the flipping of the waveplate and a quick drying of the diffraction gratings. The dip is located at the exact same angular location for all three wavelengths which could not be recreated in the calculated polarization ratios. The third mode is removed from the size distribution with little or no detriment to the over-all average fit of the polarization ratios across the range of angles from 145 to 165 degrees. The adjusted fit using a varying refractive index as a function of wavelength and a bimodal lognormal size distribution is shown in Fig. 6-18 with the corresponding bimodal size distribution. A decent average fit over the angle range is achieved for each wavelength. There are some discrepancies between the

modeled and measured polarization ratios that appear to be wavelength dependent. The 532 nm model shows a good fit to the measured data throughout the whole range, while the 407 nm and 650 nm model deviates noticeably from the data in certain spots. The probable cause for these deviations are shifting concentrations of aerosols between the acquired parallel and perpendicular polarized scattering images.

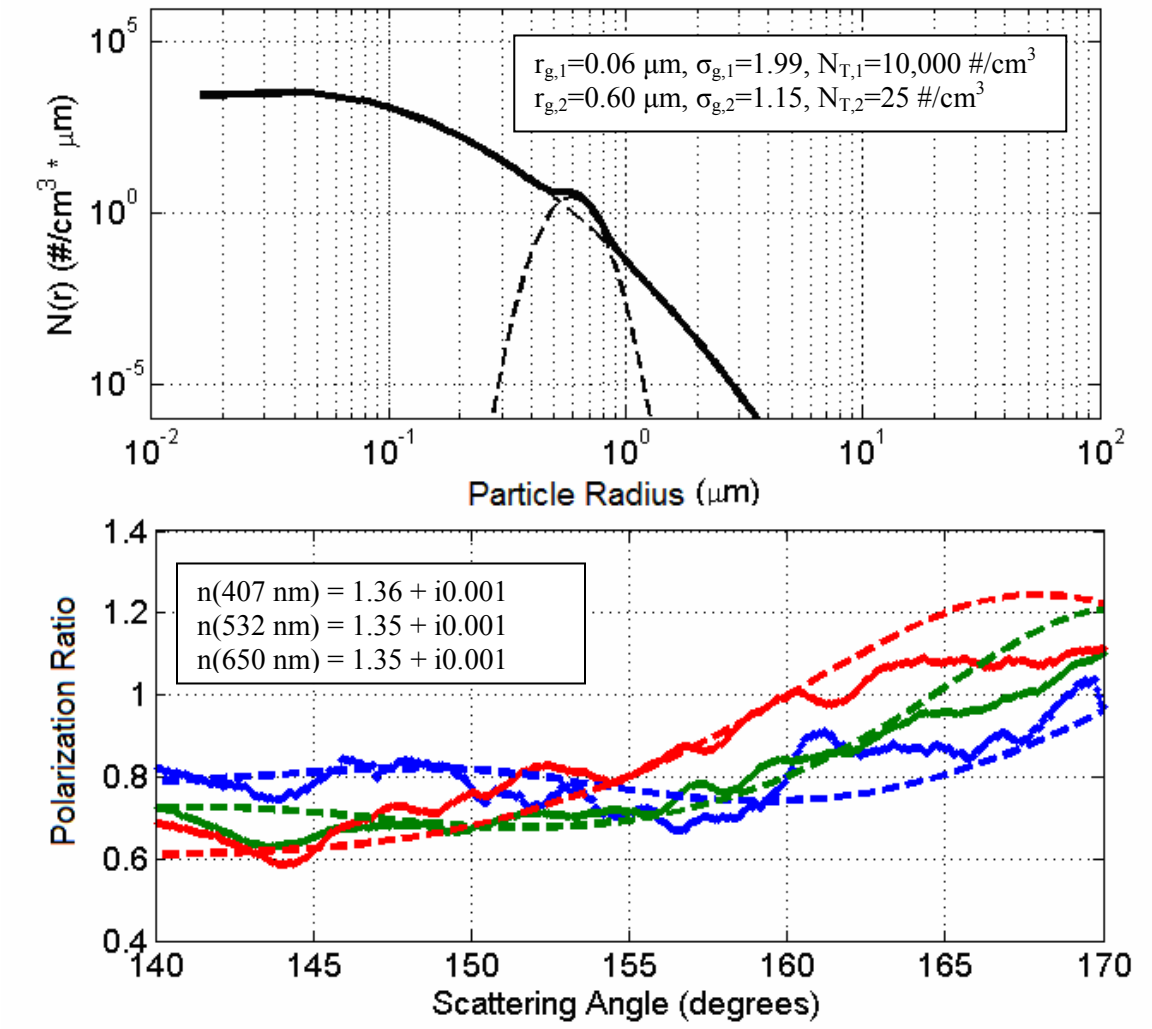


Figure 6-18: (a) Adjusted size distribution to produce the (b) best average fit between modeled (dashed lines) and measured (solid lines) polarization ratios for all wavelengths and angles using variable refractive index as a function of wavelength for dataset collected at 12:50 AM, 20/21November.

In order to explore the range of parameters that produce a decent fit for this dataset, each lognormal parameter is slowly varied while the others are held constant until the modeled polarization ratio can no longer be considered to fit the data. The range of the refractive index is explored first by allowing the real part of the refractive index to vary for all three wavelengths to locate the upper and lower limits that still fit the measured data reasonably well. Figure 6-19 shows a comparison between the measured and modeled polarization ratios for two different sets of refractive indices: (a) shows the upper limits of 1.365 for 407 nm, and 1.355 for 532 nm and for 650nm, and (b) shows the lower limits of 1.350 for 407 nm, and 1.340 for 532 nm and 650 nm. The refractive indices are returned to their 'optimized' values and another parameter in the calculation of the modeled polarization ratios is varied. The modeled polarization ratios are monitored as the concentration, geometric mean radius, and geometric standard deviation of the lognormal distributions are varied, and a minimum and maximum value is retrieved for each parameter that produce a decent fit for all three wavelengths. While each parameter is varied, the other parameters remain fixed to the values shown in the first line of Table 6-3, which are also the parameters used to calculate the modeled polarization ratio in Fig. 6-18. An example of this process is shown in Figure 6-20, which displays the polarization ratio comparisons for the maximum and minimum fine mode concentration values, $N_{T,1}$, that can be considered a decent fit to the measured data. The ranges established for each of the parameters are summarized in Table 6-3 along with the optimized values that produced the best averaged fit. The process is repeated for the second dataset collected the night of 20/21 November at 1:45 AM. The process follows these steps: (1) the size distribution retrieved by the genetic algorithm is used to optimize the refractive index for each wavelength, (2) the parameters of the size distribution are varied to determine the range of values that produce a reasonable average fit, and (3) a comparison is made between the measured and modeled polarization ratios.

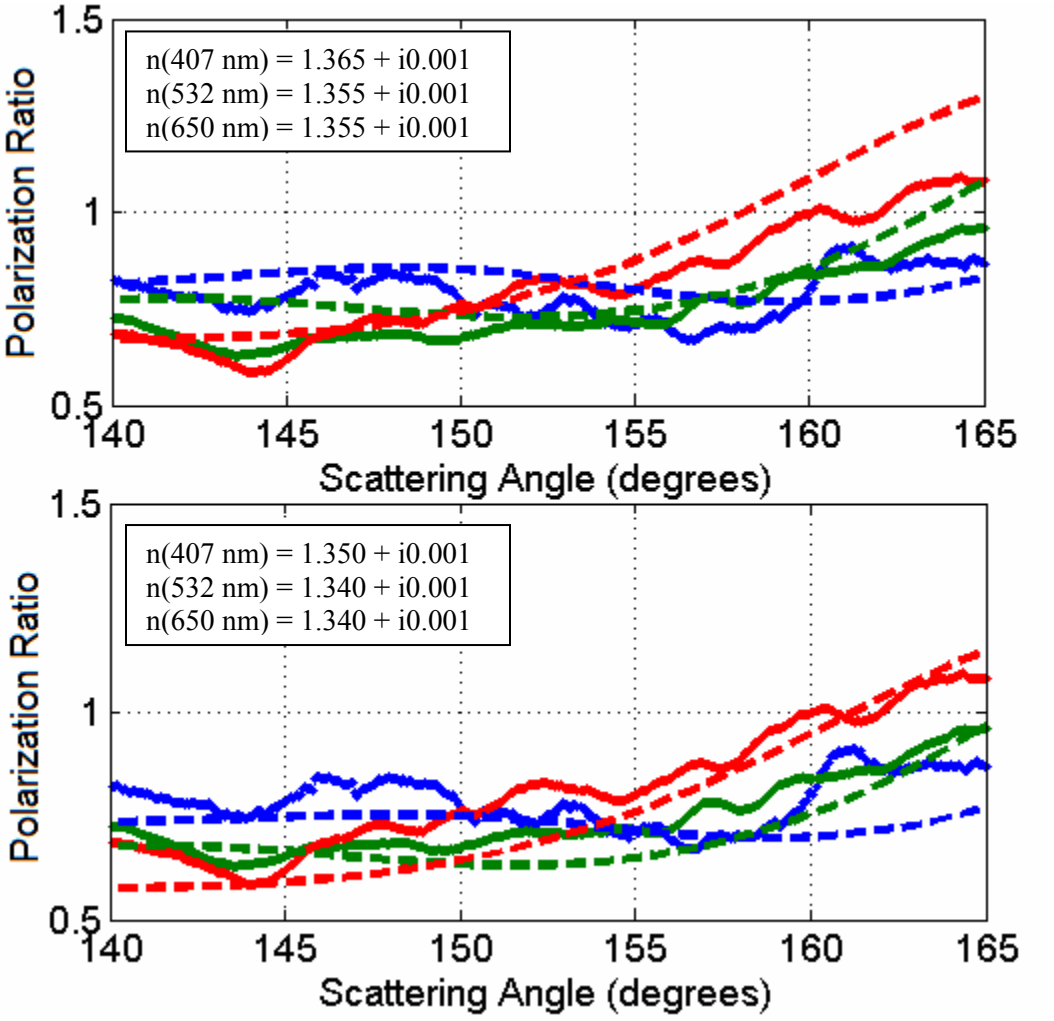


Figure 6-19: Comparison between the measured (solid lines) and modeled (dashed lines) polarization ratios for varying refractive indices for dataset collected at 12:50 AM, 20/21November.

Figure 5-21 shows the optimized size distribution that produces the 'best-fit' between the measured and modeled polarization ratios for the dataset collected at 1:45AM, 20/21November. The refractive indices that produce the best fit to the measured data from 1:45 AM are the same refractive indices that were retrieved from the previous dataset. It was thought that the imaginary part of the refractive index would be less for the second dataset, as more water condensed on the background aerosols, but the modeled polarization ratio fits the data best with

the same imaginary index of 0.001, estimated to be within about ± 0.0005. The ranges for each inversion variable for the second dataset are also summarized in Table 6-3.

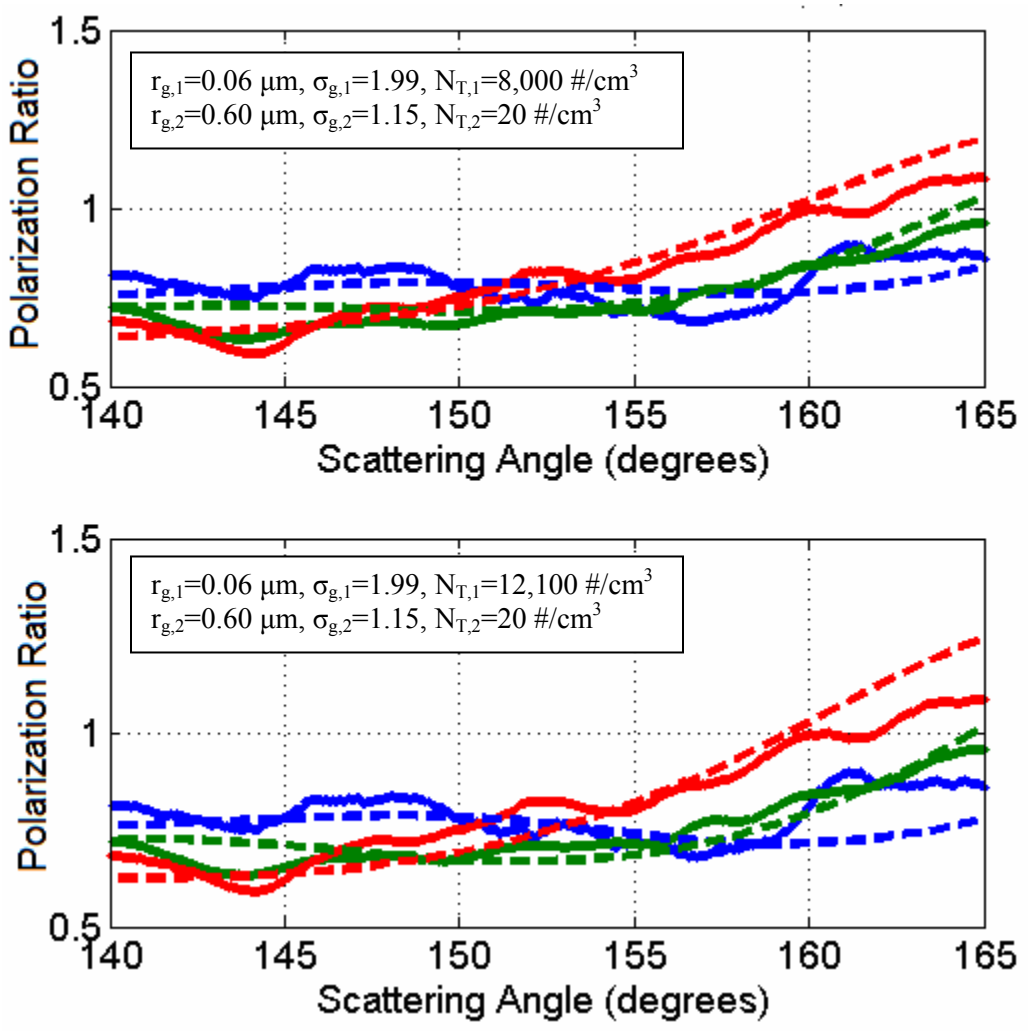


Figure 6-20: Comparison between the measured (solid lines) and modeled (dashed lines) polarization ratios for varying fine mode concentration, $N_{T,1}$, for dataset collected at 12:50 AM, 20/21 November.

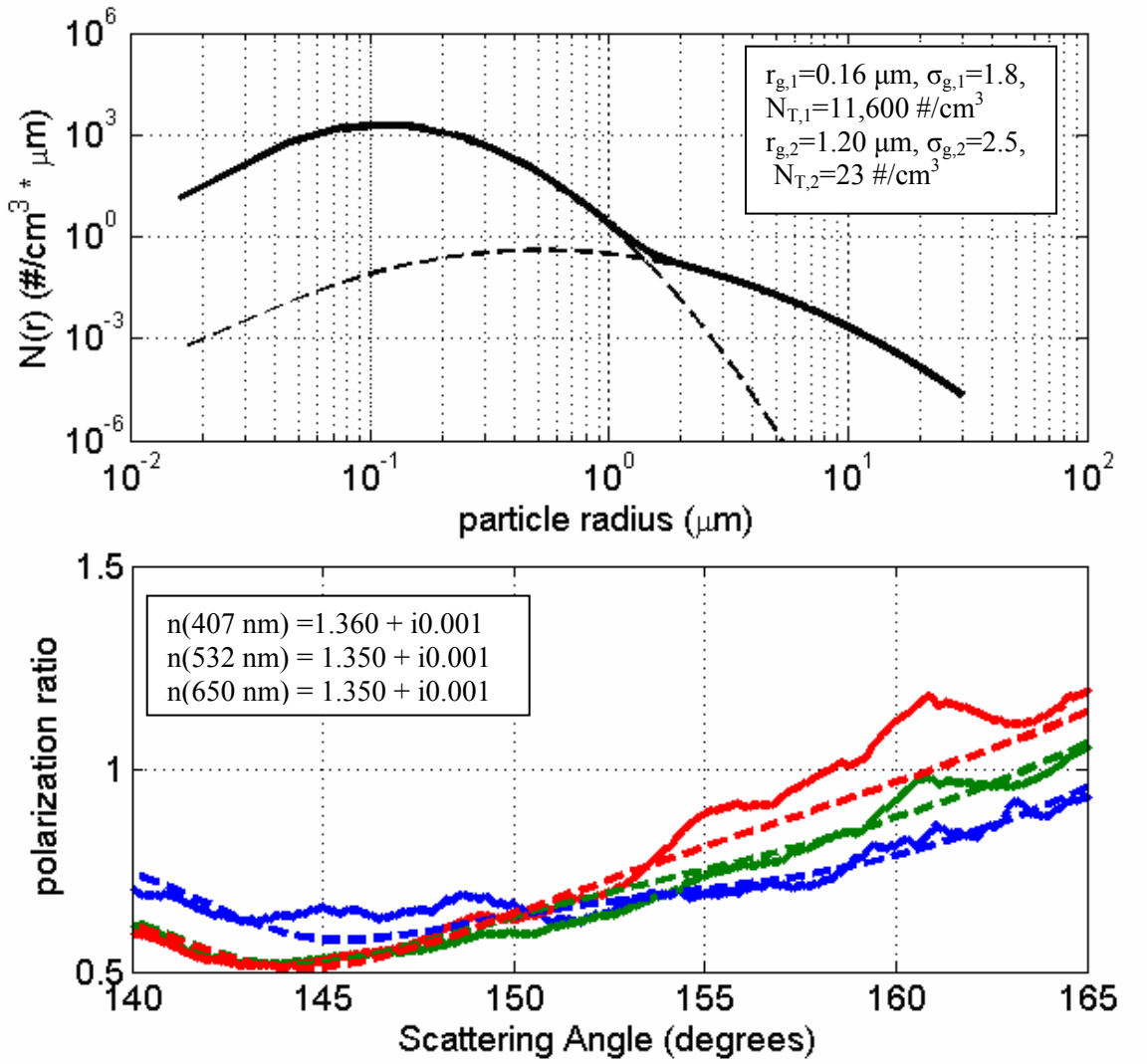


Figure 6-21: (a) Adjusted size distribution to produce the (b) best average fit between modeled (dashed lines) and measured (solid lines) polarization ratios for all wavelengths and angles using variable refractive index as a function of wavelength for dataset collected at 1:45 AM, 20/21 November.

Table 6-3: Ranges of trimodal lognormal parameters using a refractive index of 1.36 + i0.001 for 407 nm, and 1.35+ i0.001 for 532 nm and for 650 nm.

r_{g1} (µm)	σ_{g1}	N_{T1} (#/cm^3)	r_{g2} (µm)	σ_{g2}	N_{T2} (#/cm^3)	r_{g3} (µm)	σ_{g3}	N_{T3} (#/cm^3)
20/21 November, 12:45 AM								
*0.06	1.99	10,000	0.60	1.15	20	-	-	-
0.055-0.070	1.95-2.15	8,000-12,100	0.595-0.615	1.145-1.2	18-22	-	-	-
20/21 November, 1:45 AM								
*0.16	1.8	11,600	1.20	2.5	23	-	-	-
0.155-0.165	1.78-1.82	10,500-12,500	1.18-1.22	2.45-2.55	21-24.5	-	-	-

Figure 6-22 shows a comparison between the two retrieved size distributions from the evening of 20/21 November, along with the integrated total number density for each dataset. The number density is almost exactly the same for both size distributions, at ~11,690 particles/cm^3. Review of the concentrations reported by the CPC for the time frame of the measurement (Fig. 6-4) shows that the concentrations were also extremely similar, with the CPC reporting roughly 9,100 particles/cm^3 for both datasets. The 11,690 particles/cm^3 obtained from the multistatic measurements is slightly higher than the ±20% accuracy concentration of the CPC measurement. This difference is most likely due to the fact that the multistatic concentration is a path-averaged result from data collected on the aerosols farther down the valley than where the CPC was collecting point-measurements of the concentration.

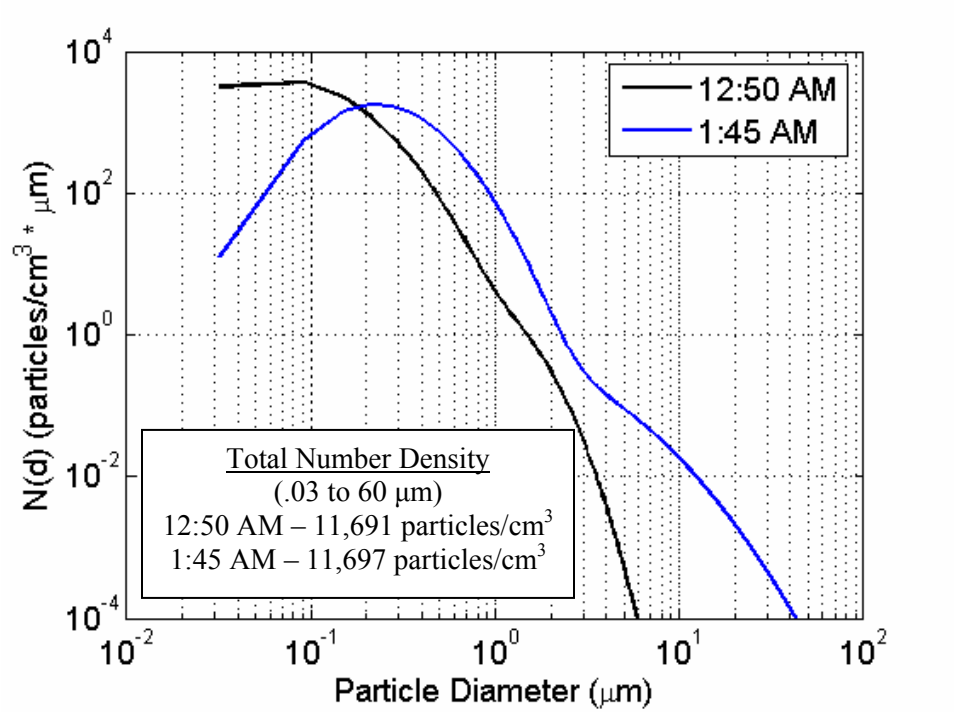


Figure 6-22: Comparison of retrieved size distributions for two datasets summarized in Table 6-3 collected the night of 20/21 November.

The temperature had dropped about one degree between the two analyzed datasets and the geometric mean radius of both lognormal modes grew larger over the hour between measurements. The cooler temperature causes more water vapor to condense out of the air and form onto small fog droplets, which accounts for the increase in geometric mean radius for the second mode of the bimodal distribution. The most probable cause of the increase in the first mode geometric mean radius is the uptake of water throughout the evening by background hygroscopic aerosols, most likely beginning with a nuclei of ammonium sulfate or inorganic material (Shettle and Fenn, 1979).

The visibility range is defined as the path length when the minimum contrast for the eye reaches 2% at 550 nm (Measures, 1984). The visibility range for each of the measurements can be calculated as (Measures, 1984),

$$S = \frac{3.9}{\alpha_{ext}} \tag{6-1}$$

where α_{ext} is the extinction coefficient at 550 nm reported in inverse kilometers. The extinction coefficient at 550 nm and the resulting visibility range for both datasets are reported in Table 6-4. The extinction coefficients are calculated using Mie code as weighted averages of monodisperse particle sizes in the range from 2 nm to 60 μm diameters.

Table 6-4: Extinction coefficients and visibility range for size distributions obtained for datasets collected the evening of 20/21 November.

550 nm α_{ext} (km^{-1})	S (km)
20/21 November, 12:45 AM	
0.3952	9.87
20/21 November, 1:45 AM	
5.4454	0.72

The normalized size distributions retrieved from the multistatic data are compared to published results for dense radiation fog obtained in Albany, New York (Meyer et al, 1979). The

normalized size distributions for the Albany fog were obtained using two Royco optical particle counters, and the visibility was obtained by measuring the ambient extinction using a xenon flash lamp. The normalized particle size distributions shown in Fig. 6-23b were reported for a case of dense radiation fog, whereas the cases studied in this Chapter are more typical of a dense haze. The dense fog is created by the generation of a third mode, reported for the Albany fog, which did not occur on this night of measurements. The comparison is made to highlight the similarities in the shape of the first two modes of our retrieved size distributions and the size distributions reported in the literature as conditions transition from high visibility to low visibility. In both instances, the mean diameter and width of the second mode increased over the time of the measurements.

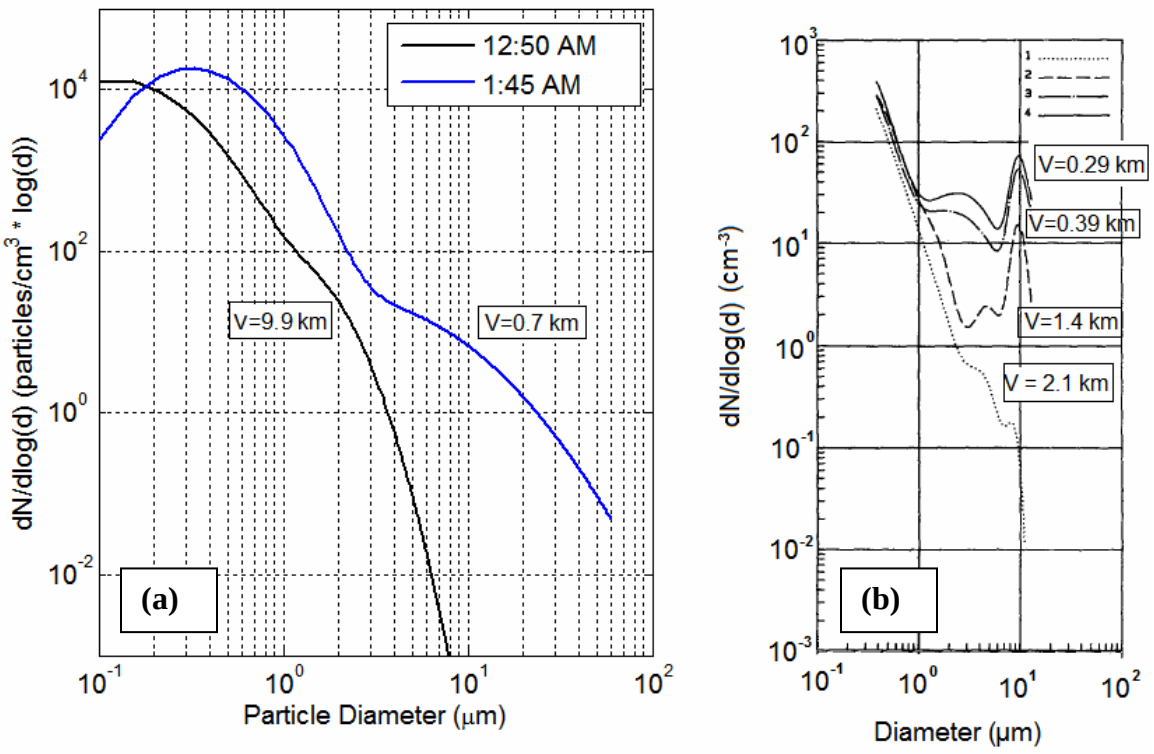


Figure 6-23: Comparison of (a) retrieved normalized size distributions from Raleigh, North Carolina multistatic measurements to (b) published normalized size distributions for radiation fog in Albany, New York obtained using an optical particle counter (Meyer *et al*, 1979).

6.3 Conclusions

Several conclusions can be drawn from comparisons between the modeled and measured polarization ratios and the corresponding retrieved size distributions presented in this chapter. The manner in which the modeled and measured data are presented demonstrate how the multiple wavelengths and range of scattering angles are used together to retrieve a trimodal size distribution that produces the best average-fit for all wavelengths. This measurement and inversion technique retrieves the average microphysical properties of the aerosols along the entire length of the analyzed path. A measurement and retrieval method capable of interpreting these path averaged results, even in the presence of small non-uniformities along the path of the laser, is the ultimate goal of this work. These cases demonstrate where a multiwavelength-multiangular approach has a significant advantage over single wavelength bistatic, or multistatic techniques.

Ranges of the concentration, geometric mean radius, and geometric mean deviation for each of the three lognormal distributions collected under different aerosols conditions (patchy fog and haze) are examined and studied throughout this chapter. The advantage of simultaneously having three wavelengths for analysis became clear during the course of the studies of outdoor fog inversion because of the wide range of parameterized variables within the inversion process. We repeatedly found that it is possible to perform a good match between modeled and measured polarization ratios for a range of angles for the 650 nm and 532 nm wavelengths, but not for the 407 nm. The addition of angularly resolved polarization ratios at a third wavelength, 407 nm, greatly reduces the solution space to a more unique solution. Figure 6-24 shows an example of this point; here the inversion algorithm was limited to the optimization of the fit of measured data at two wavelengths, instead of all three as used throughout the described work. This example shows exceptional fits for both the 532 nm and 650 nm

wavelengths; however, the 407 nm curve has drastically deviated from the measured data, making the validity of the result questionable. The power of the approach presented resides in the ability to simultaneously analyze the information contained in the entire dataset, which greatly increases the confidence of the retrieved results, and reduces the uncertainty of the conclusions.

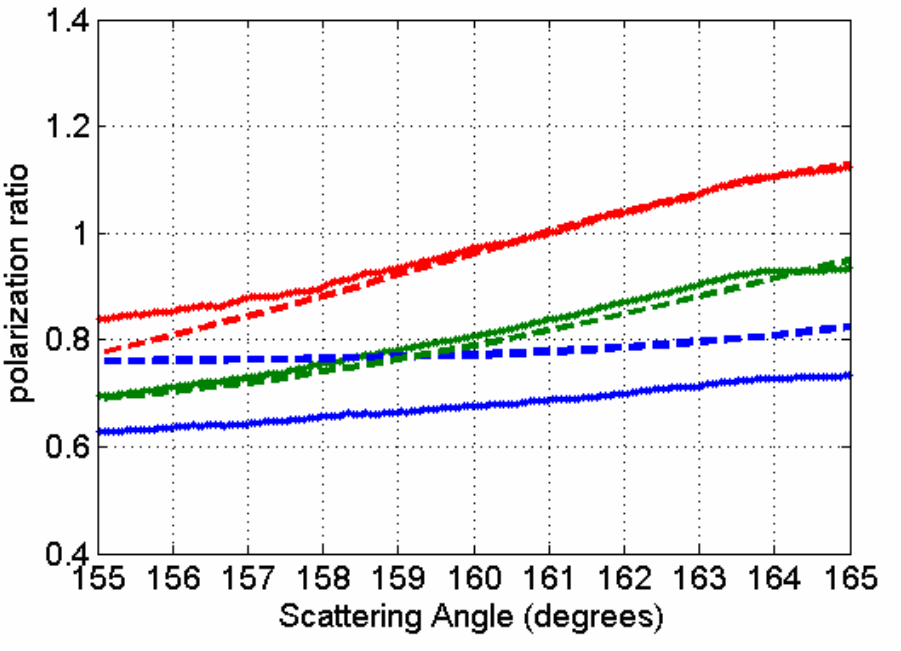


Figure 6-24: Comparison between modeled and measured polarization ratios for fog data collected 21/21 November at 12:55 AM, when the inversion algorithm was only required to interpret data for angularly resolved data on two of three wavelengths.

We have shown in this chapter that although some of the outdoor datasets have notable fluctuations in the measured polarization ratios resulting from the architecture of the CCD array, we are still able to retrieve reasonable results using an averaged-best fit for all three wavelengths, as shown in Figs. 6-18 and 6-21. The retrieved bimodal size distributions are reasonable for the weather conditions observed during the measurements, and the retrieved refractive indices are consistent with results reported by Shettle and Fenn (1979) for urban environments and high humidity (Table 6-1).

The multiwavelength-multistatic technique, coupled with a robust inversion algorithm that performs well in the presence of noise, is a promising approach to aerosol characterization. Knowledge gained from these initial outdoor measurements will be leveraged to design the next generation multistatic sensor. A high-level design concept for this next-generation sensor is discussed in Chapter 7, along with additional applications of this technique beyond the characterization of atmospheric aerosols.

Chapter 7

Future Developments

The Penn State Lidar Lab has been working towards the goal of a standardized multistatic instrument prototype design to monitor and map the properties of atmospheric aerosols. The extension of the technique to multiple wavelengths and the development of an improved inversion algorithm are two significant steps on the path to realizing this standardized instrument. While we are not ready to select the design details of the prototype instrument, we do feel that we can make several suggestions for this development. It is our intention to keep the design as simple and inexpensive as possible, while retaining the ability to provide useful and accurate data.

Diode-pumped Nd:YAG lasers offer the advantages of multiple wavelengths at high peak powers and can simultaneously produce wavelengths of 1064 nm, 532 nm, and 355 nm at high repetition rates. A silicon CCD array can be used to detect all three of these wavelengths, with various varieties (UV, and IR enhanced) available to counteract the reduced quantum efficiency at 355 and 1064 nm, as compared to 532 nm, see Figure 7-1. The differences in spectral response can be managed by the replacement of the diffraction grating by a high-speed automated filter wheel in the receiver setup. The filter wheel can be used to examine each wavelength separately (which eliminates the possibility of higher orders of the 355 nm wavelength interfering with lower order of the 1064nm) and thus each wavelength can be integrated for different periods of time to maximize the signal-to-noise of the system.

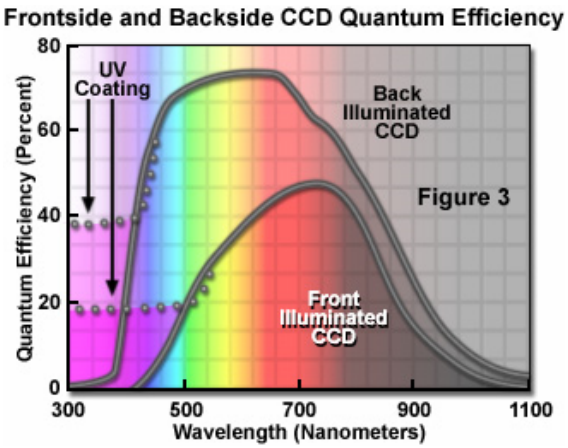


Figure 7-1: Quantum Efficiency of silicon CCD array. (Spring, 2010)

As an alternative to this architecture, dichroic optics could separate the received light into three channels, each being coupled to independent CCD imagers. Similar to the approach developed in this work, this technique provides a way to sample the scattering phase function at three wavelengths simultaneously. One difficulty experienced during our experiments was the changing of aerosol characteristics between polarized scattering images. The polarization of the laser had to be manually changed and the CCD cameras had to be manually operated, all contributing to significant periods of time between scattering images. An improved transmitter design would utilize an automated ferroelectric polarization rotator to quickly change the plane of polarization of the laser and the camera acquisition software can be used to quickly acquire multiple scattering images at each polarization. Essentially, we would trigger the ferro-electric cell and data collection on every Q-switch event of the laser so that every pair of pulses could feasibly be used to perform a polarization ratio. Using lasers with repetition rates in the hundreds of hertz to kilohertz, this approach would be able to accurately quantify a wide range of background atmospheric effects, ranging from wind variations (10s of Hz scale, to turbulence on the kHz scale.) Synchronization of the camera and the laser transmitter would allow fully automated acquisition of scattering images at two polarizations at all three wavelengths and background images. Multiple sets of these scattering images can be averaged to minimize

random noise and increase the signal-to-noise of the collected data. Another important addition to the multistatic system would be the collection of multiwavelength extinction data. This additional information would be used to scale the particle size distributions when the concentration of particles is such that the polarization ratio is insensitive to the molecular scattering contribution (see Chapter 2). Multiwavelength extinction information would also aid in the determination of the complex refractive index of the aerosols.

Although safety is somewhat of a concern for the Nd:YAG fundamental and its harmonics, the high sensitivity of silicon at 532 nm lends to the requirement of a borderline Class IIIa to a minimal Class IIIb laser at this wavelength. With improved optics and thermoelectrically cooled CCD imagers, power requirements would relax to a class IIIa level for 532 nm. With a carefully optimized VIS/UV CCD detector scheme, the same could be true for the 3rd harmonic wavelength. As an alternative to 1064 nm, pulsed fiber laser technology can be used to easily achieve adequate power at 1550 nm. Lasers in this wavelength range are less of a concern for eye safety due to different optical damage mechanisms, and are easy to obtain due to developments in the telecom boom. Indium gallium arsenide (InGaAs) CCD imagers are optimal for measurements 1300 nm to 1550 nm, and while they are more expensive than silicon, their cost is still reasonable.

The system described capitalizes on commercially available components to create a complete multiwavelength- multiangular characterization suite that is capable of atmospheric characterization on the rapid time-scale compatible with background atmospheric fluctuations. The conceptual system would be designed for continuous measurements of the scattering phase function for a range of angles – with the most important angles residing in the backscattering hemisphere from 130 to 175°. The hypothetical prototype wavelengths (Nd:YAG fundamental, second, and third harmonics) mentioned earlier can be inexpensively acquired, and span a wide wavelength region that is most useful for characterizing aerosol particles in the size range of the

fine, accumulation, and course aerosol modes with sized from 10s of nanometers to roughly 10 microns. A system optimized for characterization of micron-sized aerosols only would require NIR to MWIR wavelengths only. Although there is a significant level of synchronization required for a system such as the one described, an operational instrument can be envisioned for various scenarios. The setup is simple, straight forward, and can be built with a limited investment in components.

7.1 Supercontinuum scattering

A supercontinuum laser produces a broadband source that emits a continuous range of wavelengths across a region of the optical spectrum, oftentimes visible wavelengths. Supercontinuum sources are sometimes being to as "white light" lasers. A white-light supercontinuum laser is generated by coupling picosecond 1.064 μm laser pulse through a nonlinear photonic crystal fiber, which broadens the pulse in both time and frequency due to non-linear process of wave mixing. Using a supercontinuum source as the transmitter for the angular scattering measurements would eliminate the need to align multiple, discrete diode lasers and would provided a larger range of different wavelengths for analysis purposes. The wavelength resolution of the system would be dependent on the resolving power of the transmission diffraction grating and conjugate lens focusing of the scattering intensity onto the CCD array. The power of this technique resides in the fact that there are a continuous range of wavelengths available for the remote characterization of aerosols through the measurement of the polarization ratio at a few angles (i.e. at one pixel range). Using such a vast array of wavelengths lends to the determination of the particle characteristics as well as scanning the same particles over all angles using a monochromatic technique.

To perform a cursory demonstration of continuous multiwavelength-multistatic scattering, a supercontinuum source was used while on loan for a few days from a company in Denmark, NKT Photonics A/S. This quasi-CW laser has an output power of 3W distributed across a range from 500 nm to 2 μm. A measured power spectrum of this laser operating at 40% of its maximum power is shown in Fig. 7-2. Scattering measurements from generated fog were made using the supercontinuum source in the small PSU fog chamber described in Chapter 4. Figure 7-3 shows scattering images corresponding to using the three discrete lasers (407 nm, 532 nm, and 650 nm) on the left, and the supercontinuum laser source on the right. Ultimately, the analysis of a large number of closely spaced wavelengths could be used to infer additional characteristics of the aerosols, such as shape. Unfortunately, these scattering measurements were not conducted under ideal conditions. Following the initial laboratory experiments shown in Fig 7-3, we have been successful in developing a parallel effort to demonstrate efficient angularly resolved supercontinuum scattering from aerosols.

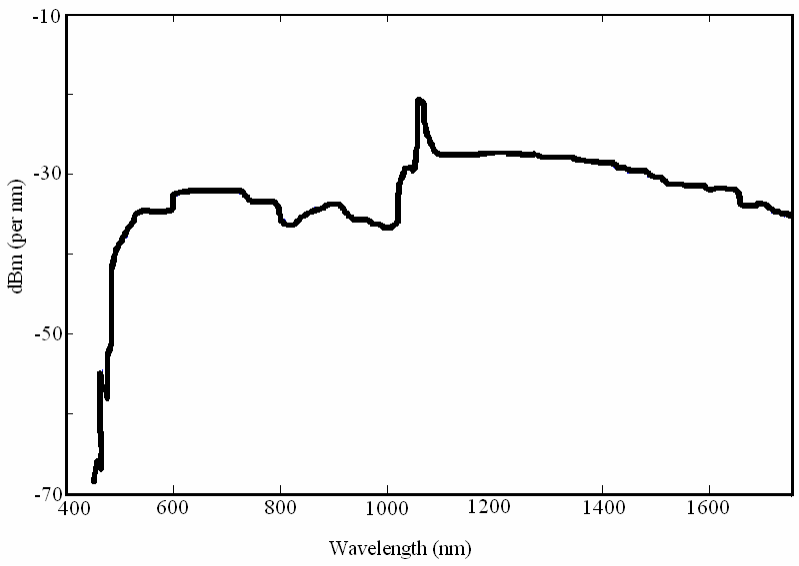


Fig. 7-2: High-power supercontinuum from NTK Photonics (Edwards, 2009)

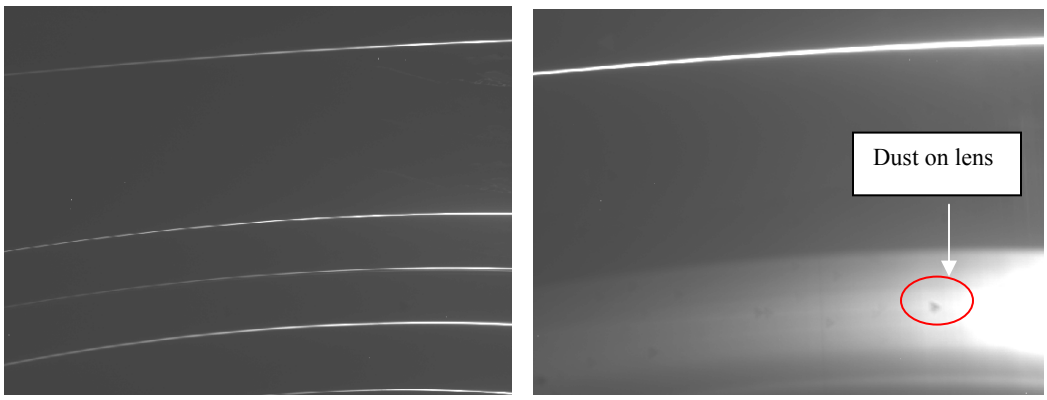


Figure 7-3: Scattering image for (a) 3-λ source and (b) 4W supercontinuum source taken using the same camera

7.2 Elimination of assumed particle size distributions

Using a probability density function to describe particle size distributions is desirable because only two variables are required to fully define each distribution: the geometric mean and standard deviation. The information in the literature that is available on atmospheric aerosol size distributions show trimodal size distributions to be a good assumption; however, it may also be of interest to apply the multiwavelength-multistatic technique to aerosol volumes that are not accurately characterized by predefined size distributions. It would be beneficial to develop an inversion technique that does not assume a predefined distribution, but instead allows the particle size distribution to be defined by the scattering measurements alone. Such an algorithm could operate on a 'binning' principle, where the particle sizes are discretized into size bins that are allowed to assume different concentration levels. The accuracy of the size distribution would then be a function of the resolution of the size bins and the concentration ranges that each 'bin' is allowed to assume. A genetic algorithm was designed that retrieved size distributions based on this concept of 'size-binning', and an example of the results obtained from this algorithm are shown in Fig 7-4. The algorithm used 20 size bins between 1 nm and 2 μm, and 10 bit binary

numbers were used to represent the number density of each size bin, requiring a 200-bit binary number to represent a single size distribution. The area of the size distribution is normalized to one, so actually retrieved size distributions would need to be scaled by the total number concentration of the aerosols. This method increases the number of inversion variables from the two needed to describe a lognormal distribution, to 20 variables, and only covered a small range of particle sizes. For time considerations, this algorithm was not considered as a viable alternative to the assumed trimodal lognormal distribution inversion algorithm. With future improvements in computer technology and the use of multi-core programming, this type of inversion scheme could be extremely beneficial and practical when characterizing size distributions that do not necessarily conform to predefined probability density distributions.

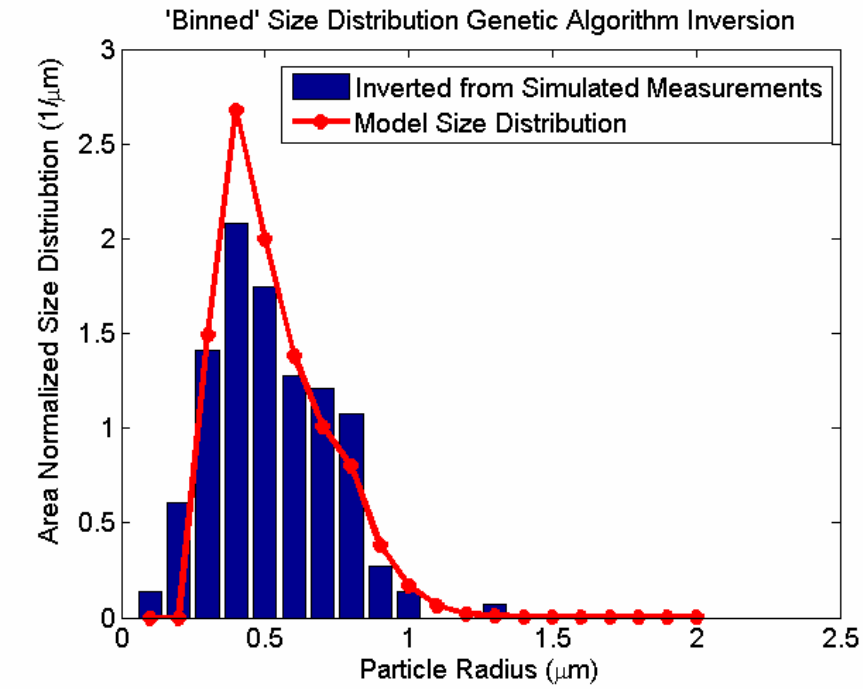


Figure 7-4: Genetic algorithm inversion of size distribution with no pre-defined distribution function.

7.3 Extension to non-spherical particles

All atmospheric aerosols are not spheres. It is reasonable to assume that the fogs and droplets examined in this work are spherical and that Mie scattering equations can be used to describe the scattering of light from these particles. Measurements on desert dust have shown that the scattering phase functions of dust deviate noticeably from those predicated by Mie scattering equations (Horvath et al, 2006), and measurements from ice crystals in cirrus clouds can not be modeled using spheres. The extension of the inversion algorithm to include non-spherical scatterers is the next step for multistatic characterization of aerosols. Preliminary studies have been done on the affects of the shape of the aerosols on the polarization ratio. T-matrix code, a publicly available program (Mishchenko, 2010), written by Michael Mishchenko, Larry Travis, and Daniel Mackowski at NASA Goddard Institute for Space Studies, that computes the scattering phase functions for a volume of homogenous, rotationally symmetric non-spherical scatterers in random orientations. This code was used to calculate the polarization ratios for spheroids. Like the Mie equations, T-matrix equations are direct solutions to Maxwell's equations based on solving specific boundary conditions (Mishchenko *et al*, 2002). In the T-matrix code, a spheroid is characterized by the ratio of the principal semi-axes (a/b) and the radius of a sphere (r_v) having ether the same volume or the same surface area (r_s) (Mishchenko *et al*, 2002). Figure 7-5 shows examples of spheroids with varying a/b ratios.

As a first step to characterizing aerosol shape based on angular scattering measurements, the affect of the shape distributions of particles on the polarization ratio was examined at four wavelengths: 407 nm, 532 nm, 650 nm, and 1064 nm. Figures 7-6 and 7-7 show the polarization ratios as a function of the shape distribution for spheroids The same Gaussian size distribution is used in each calculation, indicating that the equivalent radius (based on volume) of the particles are the same in each of the calculations, with only the a/b ratio of the particles changing. As the

variance of the Gaussian distribution used to model the shape distribution of the particles increases, a larger spread of non-spherical particles are included in the polarization ratio calculations. Analysis of the polarization ratios reveals a decrease in the amplitude of the polarization ratio as the variance of the shape distribution increases with little change in the angular position of the peaks and troughs. This information could be used to determine shape distributions from polarization ratio data. The angular location of the polarization ratio peaks could be used to measure the size distribution while the magnitude of the peaks could be used to extract shape information from the measured data. An extended study is required to determine if these measurements will have sufficient specificity to allow determination of the shape and size distributions. Also further studies will discern if the trend appears across a broad range of situations and can be used to infer characteristics of aerosols from scattering measurements.

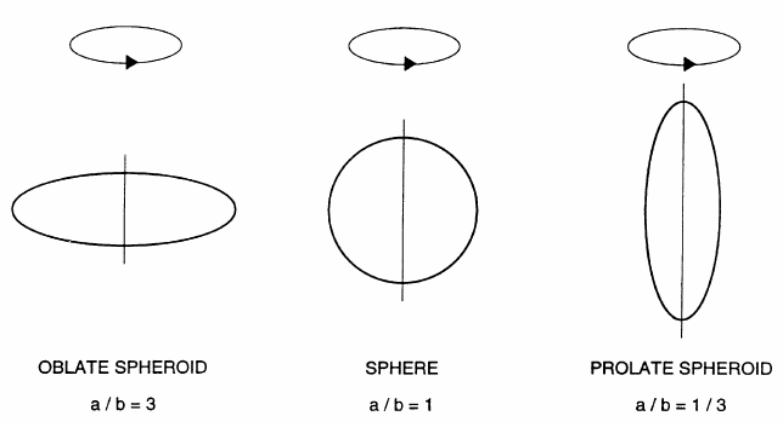


Figure 7-5: Examples of spheroids with varying axial ratios (a/b) (Mishchenko, 2002, Fig. 1)

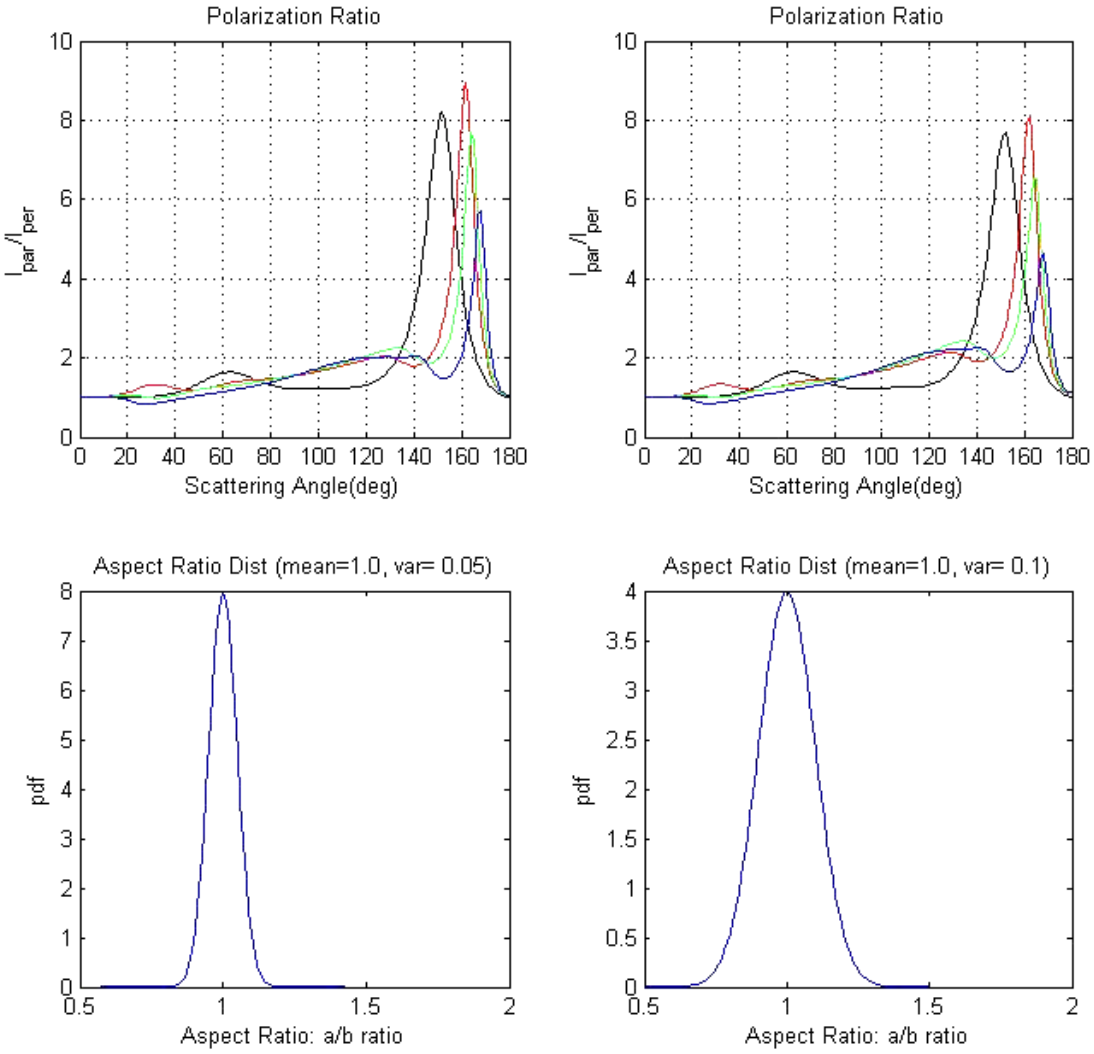


Figure 7-6: Polarization ratios at 1064 nm (black), 650 nm (red), 532 nm (green), and 407 nm (blue), as a function of shape distribution. Gaussian shape distributions were used with the mean and variance shown in the title of each distribution. A fixed Gaussian size distribution was used with a mean radius of 0.5 μm and a variance of 0.05.

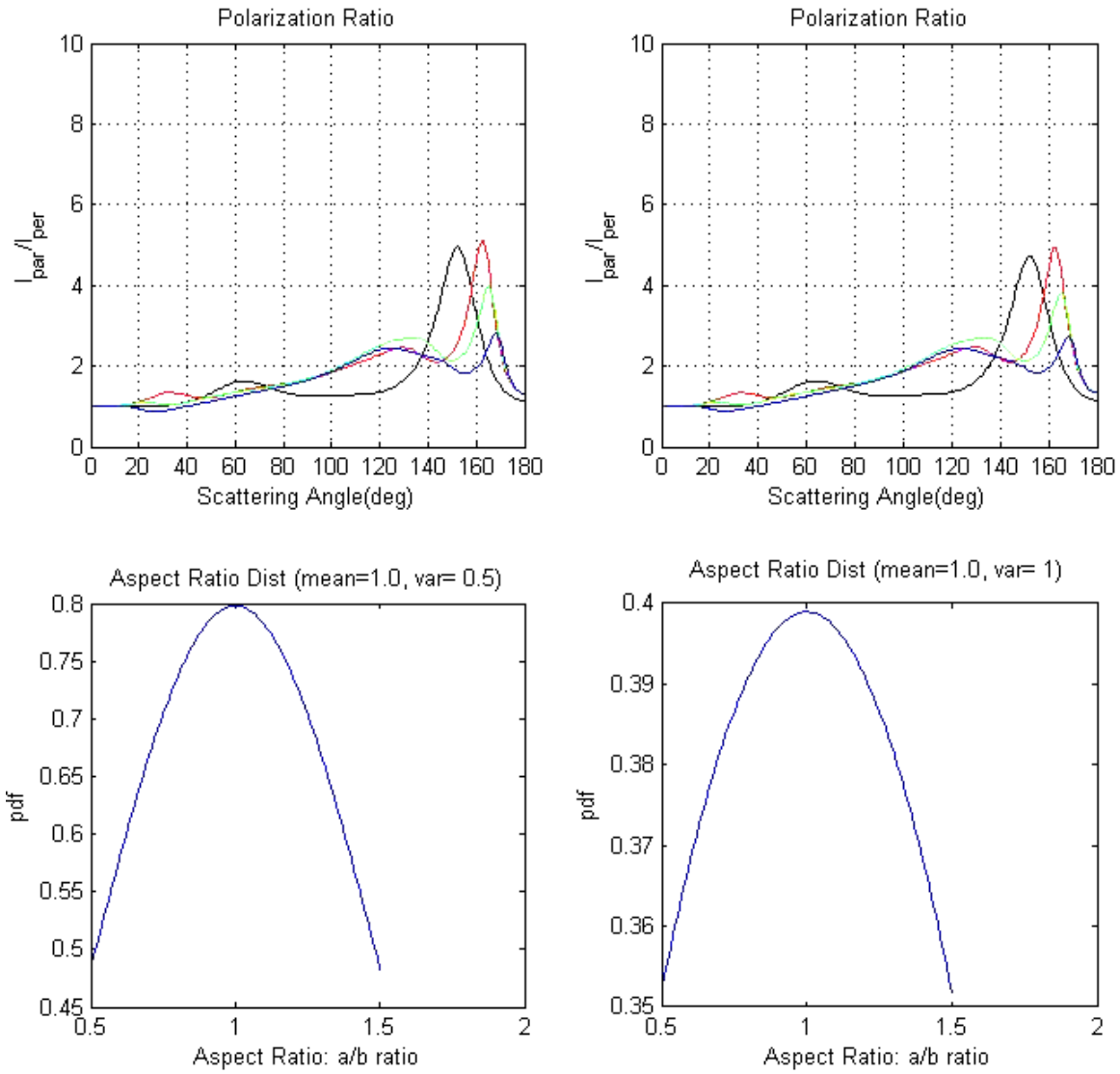


Figure 7-7: Polarization ratios at 1064 nm (black), 650 nm (red), 532 nm (green), and 407 nm (blue), as a function of shape distribution. Gaussian shape distributions were used with the mean and variance shown in the title of each distribution. A fixed Gaussian size distribution was used with a mean radius of 0.5 μm and a variance of 0.05.

Chapter 8

Summary and Conclusions

There is a global need to characterize the microphysical and spatial properties of atmospheric aerosols in order to understand their impact on our climate and our atmosphere. A detailed database of atmospheric aerosol properties from regions around the world is required to develop a global picture of the impact of aerosols and correctly include their effects in climate-forecasting models. The Penn State Lidar Laboratory has been working towards the goal of developing a prototype sensor and a data analysis approach to aid in mapping the spatial and temporal properties of atmospheric aerosols as a tool to develop this database.

A multiwavelength-multistatic transmitter was developed to conduct experimental testing using three visible diode lasers for expanding the capability of multi-static remote sensing to multiple wavelengths. Angular scattering measurements are simultaneously collected at three wavelengths by imaging three co-aligned laser beams through a transmission diffraction grating using a CCD camera. Images of the scattering intensity are collected that contain the parallel and perpendicular polarized (measured with respect to the scattering plane) components, and a polarization ratio of these scattered intensities formed as a function of both wavelength and scattering angle.

The use of the polarization ratio as the principal data, rather than using the scattering phase functions, greatly reduces the complexity of the inversion procedure by removing most of the effects of system non-linearities affecting the data, as well as canceling the variation in the path extinction between the scattering volume and the imager. A study of the polarization ratio, and the proper way to model the polarization ratio using Mie equations, was conducted in order to understand the behavior of the data and to determine the strengths and limitations of this

technique. This knowledge was required in order to design a robust inversion algorithm, which is capable of retrieving aerosol size distributions and refractive indices based on the polarization ratio data. The development of this genetic algorithm led to a conclusion that the number of particle radii included in the calculation of the polarization ratio is important. Erroneous features are present in the calculated polarization ratio when too few particle sizes are used to represent a lognormal size distribution. Polarization ratio calculations presented in Chapter 3 show that ~1,000 particle sizes should be included in analysis of the particle size range (single nanometers to 30 microns) and wavelength combinations (407 nm to 650 nm) used in this work. We find that logarithmic or linear sampling of the particle sizes used in forward calculations produce nearly equivalent polarization ratios for the two cases explored in Chapter 3. We conclude that the next generation of the developed measurement technique would benefit by the use of a linear sampling scheme, as it will be most robust to the large array of particle sizes and distributions encountered in the natural atmosphere. Other applications that also have well defined size distributions in the several micron size range would also benefit from this class of approach. The examination of the simulations further shows that logarithmic sampling would be the ideal choice when primarily concerned with accurate characterization of smaller (sub-micron) particles.

Simulations were also performed to determine the sensitivity of the polarization ratio to changing concentrations of different size particles. The molecular scattering components of the polarization ratio are used to scale the concentration of the lognormal size distributions used to represent the aerosols present in the scattering volume. Accurate aerosol concentrations can be retrieved from the polarization ratio when the concentration of the aerosols are such that both the molecular scattering and the aerosol scattering contribute to the shape of the polarization ratio. This occurs at different concentrations of aerosols depending on their size in relation to the wavelength used for the scattering measurements. Simulations in Chapter 2 establish approximate concentration ranges that can be retrieved from polarization ratio data for ultrafine

particles, fine mode particles, accumulation mode particles, and course mode particles when analyzing scattering measurements from wavelengths in the visible spectrum. It was determined that the polarization ratios obtained from ultrafine particles (diameters in the 10's of nanometers) is entirely insensitive to particle concentration, and wavelengths shorter than 407 nm are required for concentration measurements using the polarization ratio technique. The concentration of the ultrafine particles can be determined from the magnitude of the scattering phase functions when a calibration case of clean air scattering is available. Simulations show that concentrations in range of 100 to 100,000 particles/cm^3 can be accurately retrieved for particles in the 100's of nanometers range, and concentrations in the range of 0.1 to 1,000 particles/cm^3 for micron-sized particles. The retrievable concentration range for large particles, around 10 microns in diameter, is roughly 0.0001 to 10 particles/cm^3. These conclusions are best summarized by considering Table 2-3. Supporting extinction measurements made concurrently with the multiwavelength-multistatic technique can be used to verify the concentrations retrieved from the polarization ratios. When remotely characterizing concentrations well outside the retrievable ranges using the polarization ratio, extinction measurements can be used to determine particle concentrations.

Three main hypotheses related to multiwavelength-multistatic light scattering for aerosol characterization were tested throughout this work. *It was hypothesized that the addition of multiple wavelengths to a previously developed multistatic technique would aid in constraining the solution space of reasonable aerosol size distributions that could be inferred from a single set of angular scattering measurements.* The advantage of multiple wavelengths was realized during analysis of scattering data collected from a low concentration of five micron oleic acid droplets in the EPA Aerosol Wind Tunnel. The offset of the polarization ratio curves between the shortest wavelength of 407 nm, and the 532 nm and 650 nm curves led to the unexpected discovery of a large concentration of ultrafine particles. Discussion with the facility director at the EPA subsequently confirmed that the vibration process used to create each five micron particle also

results in numerous very small 'break-off' particles. Through the analysis of the polarization ratios, specifically the offset between the blue, and green and red curves, we conclude that the developed approach led to the retrieval of a lognormal size distribution for the ultrafine particles, with a mean diameter around 20 nanometers, and a geometric standard deviation of approximately 1.3. The concentration of these particles was on the order of 10^4 particles/cm^3.

The benefit of multiple wavelengths was also highlighted by the analysis of outdoor multiwavelength scattering measurements collected the evening of 20/21 November. Trimodal particle size distributions were retrieved from multiwavelength-multistatic measurements in the presence of rapidly changing outdoor aerosol concentrations by obtaining the best average fit for all three wavelength polarization ratio curves. Analysis of the multiangular measurements at three wavelengths made it possible to identify features in the polarization ratio curves that were due to non-uniformities in concentration along the measurement path, rather than from the particle size distribution. This demonstrates the strength of both the approach and algorithm when it is used for remote characterization of aerosols under non-ideal conditions.

A second hypothesis explored in this work was the ability to retrieve complex refractive index as a function of wavelength from the multiwavelength-multistatic data. Scattering measurements collected from fog generated in the PSU aerosol chamber and in the EPA Aerosol Wind Tunnel were used to explore the effect of the wavelength-dependent refractive index on the fit between measured and modeled polarization ratios. We conclude that the algorithmic result is improved relative to the ground-truth measurement when the refractive index is incorporated as a variable in the inversion procedure. By allowing the refractive index as a function of wavelength to vary, we improve the fit between modeled and measured polarization ratios compared to the fit that is obtained when using a single refractive index for all three wavelengths. The real part of the refractive index was investigate in step sizes of 0.005 and the imaginary part was explored using only 8 different values between 0 and 0.1, due to the time and memory required for each

generated look up table of scattering intensities. A finer resolution of complex refractive indices would most likely improve the fits obtained between measured and modeled polarization ratios beyond what is accomplished in this work.

The third hypothesis explored in the present work is the ability of a stochastic search inversion algorithm to retrieve lognormal size distributions and complex refractive indices from measured scattering data used to form multiwavelength polarization ratios. Prior inversion algorithms designed to retrieve aerosol size distributions from the polarization ratio have used gradient information to minimize the mean-squared error between modeled and measured data. The derivative of the polarization ratio was required for this technique, and it is extremely difficult to obtain (an analytical solution may not exist), particularly when including the complex refractive index as a variable (Novitsky, 2002). Based on the experiences and insight gleaned from the efforts of prior students, it was determined that a stochastic algorithm may provide a better result.

A genetic algorithm (GA) was designed that retrieves lognormal size distributions for up to three particle size distributions simultaneously present in measured polarization ratio data. The algorithm is designed to minimize the squared error between measured polarization data and polarization ratios calculated using the Mie solutions for spherical scatterers built upon Maxwell's equations. Convergence of the genetic algorithm does not necessarily produce the global optimum, as the discrete sampling of the solution space could prohibit the algorithm from being able to select that optimum solution. Repeat runs of the GA often return extremely similar results, indicating that it is finding the most likely area of the global optimum in the solution space. A second algorithm, such as a grid search or a Newton-Rhapson analysis, can be used to locate the solution that produces the smallest error within the smaller solution space. Inversions of simulated data presented in Chapter 3 show that the algorithm returned geometric mean radii and geometric standard deviations within 2% of the correct value (see Table 3-2) when inverting

a single lognormal probability size distribution from simulated polarization ratios that include random Gaussian noise added to decrease the signal-to-noise ratio to 25. Investigation found that the concentrations retrieved from the simulated data showed errors as high as 400% when the polarization ratios were not sufficiently unique. The particle concentrations showed large errors that occur in certain regions of the size/wavelength and number density space. The genetic algorithm performed reasonably well when retrieving results using a single complex refractive index for all three wavelengths when finding the lognormal particle size parameters (Table 3-4). The calculation including the complex refractive index as a variable within the algorithm increased the average time of convergence from one minute to roughly an hour. It was found that little advantage in accuracy is gained by allowing the complex refractive index for each wavelength to independently vary and doing so severely degrades the speed of converge of the algorithm. The necessity of loading a different lookup table of unit scattering intensities for each wavelength/size distribution combination vastly increases the amount of time it takes the algorithm to calculate the fitness of each possible solution that was generated. The addition of six more retrievable variables (a real and imaginary refractive index for each wavelength) requires a much larger population size and a later generation cut-off to obtain convergence of the algorithm. Finally, the algorithm was tested for the case of a trimodal size distribution with a varying refractive index with positive results. Three inversion runs of the algorithm on simulated noisy data (Table 3-7) showed that the algorithm could retrieved a trimodal size distribution and a single complex refractive index that produced a very good fit between the simulated noisy polarization ratios and the forward-calculated polarization ratios (see Figs. 3-13 and 3-14). It is currently much faster to run the algorithm with a fixed refractive index for all three wavelengths, and then use a localized grid search to optimize the complex refractive indices as a function of wavelength, rather than allowing each complex index to vary independently within the algorithm. The algorithm architecture is such that is could easily be adapted to multi-core parallel

processing, which would vastly improve the analysis speed. While the speed of the GA is not currently at a real-time processing level, the algorithm is a vast time-improvement over the 'guess and check' method that we have been forced to use in the past to invert measured polarization ratio data.

The multiwavelength-multistatic technique shows great promise for an atmospheric aerosol characterization technique, particularly in situations where the solution space can be limited by *a priori* knowledge of the scattering volumes size range or composition. Instrument and data collection improvements outlined in Chapter 7 will greatly reduce the uncertainty of the measured polarization ratios and increase the confidence of the size distributions and refractive index results obtained using this technique. Improvements in the speed of the inversion algorithm are also required before his technique could be consistently applied to atmospheric aerosol characterization for an extended period of measurements.

References

Ackerman, A. S., O. B. Toon, D. E. Stevens, A. J. Heymsfield, V. Ramanathan and E. J. Welton (2000). "Reduction of tropical cloudiness by soot," *Science*, vol. 288(5468): pp. 1042-1047.

Albrecht, B. (1989). "Aerosols, cloud microphysics and fractional cloudiness," *Science*, vol. 245: pp. 1227-1230.

Baker, J. (1987). "Reducing bias and inefficiency in the selection algorithm," *Proc. of the Second International Conference on Genetic Algorithms and their Application*, pp. 14-21.

Barkey, B., S. E. Paulson and A. Chung (2007). "Genetic algorithm inversion of dual polarization polar nephelometer data to determine aerosol refractive index," *Aerosol Science and Technology*, vol. 41: pp. 751-760.

Barnes, J. E., S. Bronner, R. Beck and N. C. Parikh (2003). "Boundary layer scattering measurements with a charge-coupled device camera lidar," *Applied Optics*, vol. 42(15): pp. 2647-2652.

Barnes, J. E., N. C. P. Sharma and T. B. Kaplan (2007). "Atmospheric aerosol profiling with a bistatic imaging lidar system," *Applied Optics*, vol. 46(15): pp. 2922-2929.

Bockmann, C. (2001). "Hybrid regularization method for the ill-posed inversion of multiwavelength data in the retrieval of aerosol size distributions," *Applied Optics*, vol. 40(9): pp. 1329-1342.

Bohren, C. F. and D. R. Huffman (1983). Absorption and Scattering of Light by Small Particles. Wiley, New York, NY, pp. 544.

Born, M. and E. Wolf (1980). Principle of Optics. Pergamon Press, New York, NY, pp. 986.

Bucholtz, A. (1995). "Rayleigh-scattering calculations for the terrestrial atmosphere," *Applied Optics*, vol. 34(15): pp. 2765-2773.

Byrne, D. M. (1978). Remote detection of atmospheric particulates using a bistatic lidar, Ph.D. Dissertation, Electrical Engineering Department, University of Arizona.

Chigier, N. and R. D. Reitz (1995). Regimes of Jet Breakup and Breakup Mechanisms (Physcial Aspects). Recent Advances in Spray Combustion:. K. Kuo. America Institute of Aeronautics and Astronautics, Inc., vol. 1**:** pp. 109-136.

Chin, M., R. A. Kahn, L. A. Remer, H. Yu, D. Rind, G. Feingold, P. K. Quinn, D. G. Streets, P. Decola, S. E. Schwartz and R. Halthore (2009). CCSP 2009: Atmospheric Aerosol Properties and Climate Impacts. Mian Chin, R. A. Kahn and S. E. Schwartz, Climate Change Science Program.

Dave, J. V. (1971). "Determination of size distribution of spherical polydispersions using scattered radiation data," *Applied Optics*, vol. 10: pp. 2035-2044.

Davies, C. N. (1974). "Size distribution of atmospheric particles," *Journal of Aerosol Science*, vol. 5: pp. 293-300.

Deepak, A., Ed. (1982). Atmospheric Aerosols, Their Formation, Optical Properties, and Effects. Spectrum Press, Hampton, NJ, pp. 480.

Deirmendjian, D. (1969). Electromagnetic Scattering on Spherical Polydispersions. Elsevier, New York, NY, pp. 290.

Devara, P. C. S. and P. E. Raj (1989). "Remote sounding of aerosols in the lower atmosphere using a bistatic CW helium-neon lidar," *Journal of Aerosol Science*, vol. 20(1): pp. 37-44.

Dubovik, O. and M. D. King (2000). "A flexible algorithm for retrieval of aerosol optical properties from sun and sky radiance measurements," *Journal of Geophysical Research*, vol. 105(20): pp. 673-696.

Edwards, P. S. (2009). Measurement and analysis of atmospheric species using a low power supercontinuum laser, Masters Thesis, Electrical Engineering Department, Penn State University.

Forster, P., P. Ramaswamy, T. Artaxo, T. Berntsen, R. Betts, J. Fahey, J. Haywood, J. Lean, D. C. Lowe, G. Myhre, J. Nganga, R. Prinn, G. Raga, M. Schulz and R. Van Dorland (2007). Changes in Atmospheric Constituents and in Radiative Forcing. Climate Change 2007: The Physical Science Basis. Contribution of Working Group I to the Fourth Assessment Report of the Intergovernmental Panel on Climate Change. S. Solomon, D. Qin, M. Manning, Z. Chen, M. Marquis, K. B. Averyt, M. Tignor and H. L. Miller. Cambridge, UK and New York, NY.

Goldberg, D. E. (1989). Genetic Algorithms in Search, Optimization and Machine Learning. Addison-Wesley Longman Publishing Company, Boston, MA, pp. 432.

Haywood, J. M. and O. Boucher (2000). "Estimates of the direct and indirect radiative forcing due to tropospheric aerosols: a review," *Reviews of Geophysics*, vol. 38(4): pp. 513-543.

Herman, B. M., S. R. Browning and J. A. Reagan (1971). "Determination of aerosol size distributions from lidar measurements," *Journal of Atmospheric Science*, vol. 28: pp. 763-771.

Hodgson, R. J. (2001). "Genetic algorithm approach to the determination of particle size distributions from static light-scattering data," *Journal of Colloid and Interface Science*, vol. 240: pp. 412-418.

Horvath, H., M. Kasahara, S. Tohno, and M. Kacifaj (2006). "Angular scattering of the Gobi Desert aerosol and its influense on radiative forcing," *Journal of Aerosol Science*, vol. 37(10) pp. 1287-1302.

Jaenicke, R. (1993). Tropshperic Aerosols. Aerosol-Cloud-Climate Interactions. P. V. Hobbs. Elsevier. New York, NY, pp. 233.

Junge, C. E. (1955). "The size distribution and aging of natural aerosols as determined from electrical and optical data in the atmosphere," *Journal of Meteorology*, vol. 12: pp. 13-25.

Kelkar, D. N. and P. V. Joshi (1977). "A note on the size distribution of aerosols in urban atmospheres," *Atmospheric Environment*, vol. 11: pp. 531-534.

Kerker (1969). The Scattering of Light and Other Electromagnetic Radiation. Academic Press, New York, NY, pp. 666.

King, M. D. (1982). "Sensitivity of constrained linear inversions to the selection of the lagrange multiplier," *Journal of the Atmospheric Sciences*, vol. 39: pp. 1356-1369.

King, M. D., D. M. Byrne, B. M. Herman and J. A. Reagan (1978). "Aerosol size distributions obtained by inversion of spectral optical depth measurements," *Journal of Aerosol Science*, vol. 21: pp. 2153-2167.

Klett, J. D. (1981). "Stable analytical inversion solution for processing lidar returns," *Applied Optics*, vol. 20: pp. 211.

Kolgotin, A. and D. Muller (2008). "Theory of inversion with two-dimensional regularization: profiles of microphysical particle properties derived from multiwavelength lidar measurements," *Applied Optics*, vol. 47(25): pp. 4472-4490.

Levy, J. (2000). "New Findings Highlight the Significance of Aerosols in the Earth's Climate System." Spotlight Feature Articles Retrieved April 23, 2009, from http://www.oar.noaa.gov/spotlite/archive/spot_aero.html.

Lienert, B. R., J. N. Porter and N. C. P. Sharma (2003). "Aerosol size distributions from genetic inversion of polar nephelometer data," *Journal of Atmospheric and Oceanic Technology*, vol. 20: pp. 1403-1410.

Lienert, B. R., J. N. Porter and S. K. Sharma (2001). "Repetitive genetic inversion of optical extinnction data," *Applied Optics*, vol. 40(21): pp. 3476-3482.

Ligon, D. A., T. W. Chen and J. B. Gillespie (1996). "Determination of aerosol parameters from light-scattering data using an inverse Monte Carlo technique," *Applied Optics*, vol. 35(21): pp. 4297-4303.

Measures, R. M. (1984). Laser Remote Sensing: Fundamentals and Applications. Wiley-Interscience, New York, NY, pp. 521.

Meki, K., K. Yamaguchi, X. Li, Y. Saito, T. D. Kawahara and A. Nomura (1996). "Range-resolved bistatic imaging lidar for the measurement of the lower atmosphere," *Optics Letters*, vol. 21(17): pp. 1318-1320.

Meyer, M., J. Jiusto and G. Lala (1979). "Measurements of visual range radiation-fog (haze) microphysics," *Journal of the Atmospheric Sciences*, vol. 37: pp. 622-629.

Mie, G. (1908). "Contributions to the optics of turbid media, particularly of colloidal metal solutions," *Ann. Physik*, vol. 25: pp. 377-445.

Miecznik, G., R. Illing, S. Petroy and I. N. Sokolik (2005). "Sensitivity metric approach for retrieval of aerosol properties from multiangular and multispectral polarized radiances," *Applied Optics*, vol. 44(20): pp. 4186-4204.

Mishchenko, M. I., L. D. Travis and A. A. Lacis (2002). Scattering, Absorption, and Emission of Light by Small Particles. Cambridge University Press, New York, pp. 480.

Mishchenko, M. I., L. D. Travis and D. W. Mackowski. "T-Matrix Codes for Computing Electromagnetic Scattering by Nonspherical and Aggregated Particles." Retrieved May 19, 2009, from http://www.giss.nasa.gov.

Novitsky, E. J. (2002). Multistatic Lidar Profile Measurements of Lower Tropospheric Aerosol and Particulate Matter Ph.D. Dissertation, Electrical Engineering Department, Pennsylvania State University.

Novitsky, E. J. and C. R. Philbrick (2004). "A multistatic receiver for the monitoring of lower troposphere aerosols and particulate matter". *22nd International Laser Radar Conference*, Matera, Italy: pp. 219-222.

Novitsky, E. J. and C. R. Philbrick (2005). "Multistatic lidar profiling of urban atmospheric aerosols," *Journal of Geophysical Research*, vol. 110(D07S11): pp. 1-10.

Olofson, K. F. G. (2008). Lidar Studies of Tropospheric Aerosols and Clouds, Ph.D. Dissertation, Chemistry and Atmospheric Sciences, University of Gothenburg.

Olofson, K. F. G., G. Witt and J. B. C. Pettersson (2008). "Bistatic lidar measurements of clouds in the Nordic Arctic region," *Applied Optics*, vol. 47(26): pp. 4777-4786.

Parameswaran, K., K. D. Rose and B. V. Krishna Murthy (1984). "Aerosol Characteristics from Bistatic Lidar Observations," *Journal of Geophysical Research*, vol. 89(D2): pp. 2541-2552.

Park, J. H. (2008). Multiple Scattering Measurements using Multistatic Lidar, Ph.D. Dissertation, Electrical Engineering Department, Pennsylvania State University.

Philbrick, C. R. (2003). "Remote sensing of atmospheric properties using lidar," *Proceedings of the International Symposium on Spectral Sensing Research (ISSSR)*, vol. 34: pp. 1-10.

Philbrick, C. R., M. D. O'Brien, D. B. Lysak, T. D. Stevens and F. Balsiger (1996). "Remote sensing using active and passive optical techniques". *Remote Sensing: A Valuable Source for Information*, NATO/AGARD Proceedings on Remote Sensing, Toulouse, France: pp. 8-1 - 8-9.

Philbrick, C. R., T. Wright, M. Snyder, H. Hallen, A. M. Brown, S. Verghese and P. S. Edwards (2010). "Characteristics of atmospheric aerosols using optical remote sensing". *12th Conference on Atmospheric Chemistry, The 90th American Meteorological Society Annual Meeting*, Atlanta, Georgia: pp. 4.2.

Phillips, D. L. (1962). "A technique for the numerical solution of certain integral equations of the first kind," *Journal of the Assoc. Comput. Mach.*, vol. 9(1): pp. 84-97.

Pincus, R. and M. B. Baker (1994). "Effect of precipitation on the albedo susceptibility of clouds in the marine boundary layer," *Nature*, vol. 372: pp. 250-252.

Reagan, J. A., D. M. Byrne and B. M. Herman (1982). "Bistatic LIDAR: A Tool for Characterizing Atmospheric Particulates: Part II- The Inverse Problem," *IEEE Transactions on Geoscience and Remote Sensing*, vol. GE-20(3): pp. 236-243.

Reagan, J. A., D. M. Byrne and B. R. Herman (1982). "Bistatic LIDAR: a tool for characterizing atmospheric particulates: Part I- The remote sensing problem," *IEEE Transactions on Geoscience and Remote Sensing*, vol. GE-20(3): pp. 229-235.

Reagan, J. A., D. M. Byrne, M. D. King, J. D. Spinhirne and B. M. Herman (1980). "Determination of the complex refractive index and size distribution of atmospheric particulates from bistatic-monostatic lidar and solar radiometer measurements," *Journal of Geophysical Research*, vol. 85(C3): pp. 1591-1599.

Seinfeld, J. H. and S. N. Pandis (1998). Atmospheric Chemistry and Physics: From Air Pollution to Climate Change. John Wiley, Hoboken, NJ, pp. 1326.

Shettle, E. P. and R. W. Fenn (1979). "Models for the aerosols of the lower atmosphere and the effects of humidity variations on their optical properties," *Air Force Geophysics Lab*, vol. Environmental Research Paper No. 675: pp. AFGL-TR-79-0214

Spring, K. R. and M. W. Davidson. (2010). "Basic concepts in digital imaging technology: quantum efficiency." Microscopy Resource Center Retrieved June 18, 2010, from www.olympusmicro.com.

Spring, K. R., T. J. Fellers and M. W. Davidson. (2010). "Introduction to charge-coupled devices." MicroscopyU: the source for microscopy education Retrieved June 2, 2010, from http://www.microscopyu.com/articles/digitalimaging/ccdintro.html.

Stevens, T. D. (1996). Bistatic Lidar Measurements of Lower Tropospheric Aerosols Ph.D. Dissertation, Electrical Engineering Department, Pennsylvania State University.

Stevens, T. D. and C. R. Philbrick (1996). "Particle size distributions and extinction determined by a unique bistatic lidar technique," *Geoscience and Remote Sensing Symposium, 1996. IGARSS '96. 'Remote Sensing for a Sustainable Future.', International*, vol. 2: pp. 1253-1256.

Tikhonov, A. N. (1963). "On the solution of incorrectly stated problems and a method of regularization," *Dokl. Acad. Nauk. SSSR*, vol. 151: pp. 501-504.

Twomey, S. (1963). "On the numerical solution of Fredholm integral equations of the first kind by the inversion of the linear system produced by quadratures," *Journal of Assoc. Computer. Mach.*, vol. 10: pp. 97-101.

Twomey, S. (1974). "Pollution and the planetary albedo," *Atmospheric Environment*, vol. 8: pp. 1251-1256.

van de Hulst, H. C. (1981). Light Scattering by Small Particles. Dover Publications, Mineola, New York, pp. 471.

Verkouteren, J. (2010). "Liquid refractive index - mineral oil." Standard reference materials Retrieved May 28, 2010, from https://rproxy.nist.gov/srmors/viewTableH.cfm?tableid=119.

Veselovskii, I., A. Kolgotin, V. Griaznov, D. Muller, U. Wandinger and D. N. Whiteman (2002). "Inversion with regularization for the retrieval of tropospheric aerosol parameters from multiwavelength lidar sounding," *Applied Optics*, vol. 41(18): pp. 3685-3699.

Walters, P. T. (1980). "Practical applications of inverting spectral turbidity data to provide aerosol size distribution," *Applied Optics*, vol. 19: pp. 2353-2365.

Whitby, K. T., R. B. Husar and B. Y. H. Liu (1972). "The aerosol distribution of Los Angeles Smog," *Journal of Colloid and Interface Science*, vol. 39(1): pp. 177-204.

Xu, F., X. Cai, K. Ren and G. Grehan (2004). "Application of genetic algorithm in particle size analysis by multispectral extinction measurements," *China Particuology*, vol. 2(6): pp. 235-240.

Yamamoto, G. and M. Tanaka (1969). "Determination of aerosol size distribution from spectral attenuation measurements," *Applied Optics*, vol. 8: pp. 447-453.

Ye, M., S. Wang, Y. Lu, T. Hu, Z. Zhu and Y. Xu (1999). "Inversion of particle-size distribution from angular light-scattering data with genetic algorithms," *Applied Optics*, vol. 38(12): pp. 2677-2685.

VITA

Andrea M. Brown

Andrea M Brown was born in Hornell, New York in May of 1984. She obtained a dual Bachelor of Science and Masters of Science in Electrical Engineering from The Rochester Institute of Technology in August of 2007. She served as a teaching assistant and lab instructor for courses in the Department of Electrical Engineering while pursuing her Masters degree at Rochester Institute of Technology. She received a Doctorate of Philosophy in Electrical Engineering from The Pennsylvania State University in August of 2010, which she attended on a Clare Boothe Luce fellowship. Her primary research interests are in electromagnetics, optical properties of the atmosphere, and remote sensing. She is currently a member of SPIE, and OSA.